SYNTHESIS AND CHARACTERIZATION OF NANOCOMPOSITES

ELECTROSYNTHESIS AND CHARACTERIZATION OF SUPERPARAMAGNETIC ORGANIC-INORGANIC NANOCOMPOSITE FILMS

By

JUN CAO, B.Eng., M.Eng.

A Thesis

Submitted to the School of Graduate Studies

In Partial Fulfilment of the Requirements

For the Degree

Doctor of Philosophy

McMaster University

Doctor of Philosophy (2008) McMaster University

(Materials Science & Engineering) Hamilton, Ontario

TITLE: ELECTROSYNTHESIS AND CHARACTERIZATION OF SUPERPARAMAGNETIC ORGANIC-INORGANIC NANOCOMPOSITE FILMS

AUTHOR: Jun Cao, B.Eng., M.Eng., (Tsinghua University, Beijing, China)

SUPERVISOR: Dr. M.Niewczas

Dr. I.Zhitomirsky

NUMBER OF PAGES: xx, 233

ABSTRACT

New electrochemical methods were developed to fabricate superparamagnetic organic-inorganic nanocomposites. The methods were based on the electrosynthesis of γ-Fe_2O_3, Mn_3O_4 and $NiFe_2O_4$ *in situ* in a polymer matrix. Various composite materials were developed using new electrochemical strategies, which were based on the use of strong and weak polyelectrolytes and polymer-metal ion complexes. The deposited films were studied by XRD, TG, DTA, SEM and AFM. The results show that cathodic deposits with thickness of several microns can be obtained on various conductive substrates. The results reveal that the weight percentage of inorganic phase in the deposits reduced with the increase of the polymer concentration in the electrochemical bath solution.

The particle size distribution was measured by HRTEM and evaluated by theoretical models interpreting the magnetic measurement data. The two methods are in good agreement with each other. The results show that the average particle sizes of Mn_3O_4 and γ-Fe_2O_3 can be adjusted by the selection of polymers with different functional properties, the polymer concentration in the solutions and annealing temperatures. The particle size distribution in the developed composites followed the lognormal distribution. A double-lognormal distribution was required to interpret the magnetization data of the system containing strong interparticle interactions, and to interpret the double-peak phenomenon observed in the imaginary part of the susceptibility in some nanocomposites.

DC magnetization and AC susceptibility measurements were used to study the relationship between the magnetic properties and the average particle size by studying the

superparamagnetic behavior and ferrimagnetic phase transitions of γ-Fe_2O_3 and Mn_3O_4 nanoparticles in the temperature range of 2 K – 300 K. The results show that the blocking temperature T_B is mainly controlled by the average particle size of the nanoparticles, and increasing the average particle size results in an upward shift of the T_B. One observes no frequency dependence of T_B, which indicates strong interparticle interaction in the nanoparticle assembly, in agreement with the structural results. The results revealed superparamagnetic behavior in Mn_3O_4 nanoparticles below the ferrimagnetic Néel temperature T_N, and that T_B was identified by a peak in the temperature lower than the ferrimagnetic transition peak marked by T_N in the AC measurement. It is found that both T_B and T_N of Mn_3O_4 depend on the average particle size, and reducing the average particle size of Mn_3O_4 from 3.5 nm to 2.8 nm results in a shift of T_B from 14 K to 7 K, and T_N from 36 K to 31 K (bulk Mn_3O_4 T_N = 42 K)

ACKNOWLEDGEMENTS

I would like to express my sincere gratitude to both Dr. Marek Niewczas and Dr. Igor Zhitomirsky for their knowledge, patience and encouragement that have guided me through this work. It is my great honour to have them as my supervisors. Their kindnesses and great personalities have enriched my learning experience in both the academic area and personal life.

Sincerely thanks to my supervisory committee members, Dr. Tony Petric and Dr. David Venus. Their kindly advices during my entire research have made this work more sound and comprehensive.

Appreciation is also given to the technical assistance I have received from faculty and staff throughout my entire experimental work. Especially, I want to thank James Britten, Wenhe Gong, Chris Butcher, Frank Gibbs, Fred Pearson, Andy Duft and Steve Koprich.

Thanks are given to my fellow graduate students who have shown me their trust. Their friendship has made my PhD study a pleasant journey.

I am very grateful for the support from my family. This thesis is dedicated to my parents.

TABLE OF CONTENTS

LIST OF FIGURES

LIST OF TABLES

INTRODUCTION

The research objective of the current work is dedicated to the synthesis and characterization of superparamagnetic organic-inorganic nanocomposites. The broad aim of this work is to develop new electrochemical methods to fabricate superparamagnetic organic-inorganic nanocomposites and to understand the correlation between their structure and the functional properties.

Materials with particle size in the range of 1 - 100 nm exhibit novel electronic, optical, magnetic, and chemical properties [1, 2]. Magnetic nanoparticles have widespread applications in numerous areas, e.g., in ferrofluids, audio speakers, magnetic seals; in biological and biomedical science as biosensors [3, 4], magnetic targeted drug delivery, contrasting agents in magnetic resonance imaging; in magnetic storage media [5] and in color imaging [6]. The study of the properties of these systems is of fundamental importance in terms of the underlying theory, as well as the applications of these materials.

However, for most of these highly specialized applications, there is a practical need to disperse the nanoparticles in nonmagnetic media. This media must prevent the nanoscale magnetic materials from aggregating. Polymer materials are very well suited for these purposes.

Polymers have traditionally been considered as excellent host matrix for composite materials [7-11]. Several advanced polymer composites have been synthesized with a wide variety of inclusions like metals, semiconductors, carbon nanotubes, and magnetic nanoparticles. Many attractive properties of polymers like low density, and transparency

in optical and ultraviolet range, can be utilized along with magnetic and optical properties of nanoparticles. Another effect of these polymer hosts is that they can provide control of the magnetic interactions between particles.

Cathodic electrolytic deposition is an important technique for the fabrication of oxide/hydroxide films. The electrochemical intercalation of inorganic nanoparticles into polymer films is a new strategy for the fabrication of novel nanocomposite materials, containing magnetic nanoparticles in a polymer matrix [7-9]. The advantages of electrodeposition are short processing time, process simplicity, good compositional control and homogeneity. This method produces nanoparticles in situ in a polymer matrix, and the particle size can be controlled by the amount of polymer.

The thesis is organized into five sections including: Literature Review, Experimental Procedures, Experimental Results, Discussion, and Conclusions. The thesis consists of six chapters, specifically focused on the following subjects. The first two chapters are devoted to the literature review: Chapter One on the fundamentals of the magnetic nanoparticles, and Chapter Two on the fundamentals of electrodeposition. In Chapter Three "Experimental Procedures", our experimental approaches to the present research are laid out. In Chapter Four "Experimental Results", the detailed experimental results for some selected materials, containing different polyelectrolytes, are summarized. In Chapter Five "Discussion", the effects of polyelectrolytes on the microstructure, the influence of the microstructure on the magnetic properties and some proposed models of magnetic nanoparticles will be discussed. Conclusions and future work suggestion are presented in the Chapter Six. The references are listed at the end of the thesis.

CHAPTER 1

FUNDAMENTALS OF MAGNETIC NANOPARTICLES

This chapter reviews the fundamentals of magnetic nanoparticles. At the beginning, a short introduction to some concepts of magnetism and magnetic materials is provided. Then, the single-domain particles, magnetic anisotropy and some theoretical models to interpret the magnetic properties of nanoparticles are discussed. At the end of this chapter, some fabrication methods of magnetic nanoparticles are surveyed.

1.1 Magnetism and magnetic materials

1.1.1 Magnetic Units and Nomenclature

There are two magnetic units systems widely used in the scientific references and textbooks. One is Gaussian & cgs units which are very popular among researchers involved in studying this subject, and the other is SI units which are commonly used in the textbooks.

It is known that every material acquires a magnetic moment when it is put in a magnetic field, **H**. The magnetic moment per unit volume is defined as the magnetization **M**. The magnetic flux density, called magnetic induction **B** can be written in the Gaussian & cgs units system as [12]:

$$\boldsymbol{B} = \boldsymbol{H} + 4\pi\boldsymbol{M} \tag{1.1}$$

Magnetic induction B in the SI units system is expressed as:

$$\boldsymbol{B} = \mu_0(\boldsymbol{H}+\boldsymbol{M}), \text{ where } \mu_0 = 4\pi\times10^{-7} \text{ Henries/meter.} \tag{1.2}$$

In the Gaussian & cgs system, the units for the flux density **B** and the field strength **H** are given by **Gauss** (G) and **Oersted** (Oe) respectively, although they have exactly same dimension, which means 1 G = 1 Oe. The magnetization **M** of the material contributes to the flux density as $4\pi\mathbf{M}$. No special name is given for the unit of **M**, so the name "electromagnetic unit of dipole moment" per unit volume or emu/cm^3 is used, called *volume* magnetization. Often $4\pi\mathbf{M}$ is specified instead of **M**, and then it is measured in Gauss as flux density **B**. If **M** (emu/cm^3) is divided by the density (g/cm^3) of the material, it is known as *mass* magnetization, and measured by emu/g. The term **emu** is short for 'electromagnetic unit' and is not a unit in the conventional sense. It is sometimes used as a magnetic moment (1 emu = 1 ergG^{-1}) and sometimes takes the dimensions of volume (1 emu = 1cm^3).

In the SI system, the units for the flux density **B** (**Tesla**, T, equal to Vs/m^2, or Wb/m^2) and for the field strength **H** (A/m) have clearly different dimensions. The volume magnetization **M** (A/m) has the same dimension as **H**. The unit of magnetic moment is Am^2, or Nm/T (J/T) by definition.

We used cgs units to be consistent with the references and our experimental data, and keep in mind that they can be easily converted to SI units.

1.1.2 Magnetic ordering and classification of magnetic materials

Based on the magnetic behaviour in the presence and absence of an external magnetic field, the magnetic properties of materials can be classified into five major groups: diamagnetism, paramagnetism, ferromagnetism, ferrimagnetism, and antiferromagnetism.

In diamagnetic materials, the magnetic moment is zero for each atom unless the magnetic field is applied. The induced magnetization is opposite to the field, which gives a negative susceptibility in the order of 10^{-5} (in CGS units). Superconductors form another group of diamagnets for which susceptibility $\chi \approx -1$. Most elements in the periodic table are diamagnetic, for example Cu, Au, Ag, and Bi, all the inert gases [13].

In paramagnetic materials, there is non-zero magnetic moment for each of the atoms, which is not caused by, and is independent of the magnetic field. In the absence of an applied field, the magnetic moments of the individual atoms are randomly oriented, so that their average is zero. An applied field will partially align the magnetic moments with the magnetic field. It has a positive susceptibility in the order of 10^{-3} to 10^{-5} (in CGS units).

In ferromagnetic materials, unlike the paramagnetic ones, the magnetic moments of the individual atoms interact strongly with each other, and the moments align with each other. This interaction is called exchange interaction, which can be expressed as an exchange energy between spin S_i and S_j. $E_{ex} = -\sum_{ij}{}' J_{ij} S_i S_j$. The coefficients J_{ij} are called the exchange integrals. J_{ij} is positive in ferromagnetic materials, which means parallel spins are preferred, and have a lower energy than antiparallel ones [12]. This parallel arrangement results in a non-zero magnetization, or called spontaneous magnetization even in zero applied field.

In antiferromagnetic and ferrimagnetic materials, the exchange integral J_{ij} is negative, and it tends to align the neighbouring magnetic moments of atoms antiparallel to each other. The exact cancellation of the opposite moments results in zero net magnetization,

which is called antiferromagnetism. A partial cancellation of the magnetic moment leads to a non-zero magnetization in the zero applied field, which is called ferrimagnetism.

Among them, diamagnetic and paramagnetic materials exhibit no collective magnetic interactions and are not magnetically ordered. Ferromagnetic, ferrimagnetic and antiferromagnetic materials exhibit long-range magnetic order below a certain critical temperature and are described as magnetically ordered materials.

1.1.3 Magnetic domains

A magnetic domain defines a region within a material which has spontaneous magnetization. This means that the individual magnetic moments of the atoms are aligned within a magnetic domain. The regions separating magnetic domains are called domain walls where the magnetization rotates coherently from the direction in one domain to that in an adjacent domain.

Magnetic domain theory was developed by Weiss in 1907 [14]. Weiss assumed that there is a certain internal field (molecular field or mean field) in ferromagnets, which tries to align the magnetic moments of the atoms against thermal fluctuations. The magnitude for the Weiss molecular field H_{mf} may be estimated from the Curie temperature T_C because the thermal energy $k_B T_C$ is of the same order of interaction energy $\mu_B H_{mf}$, which gives $H_{mf} \approx 10^7$ Oe for $T_C \approx 10^3$ K, a value close to that observed for iron [15].

Landau and Lifshitz (1935) [16] showed that the domain structure is a consequence of minimizing the total magnetic energy, which includes exchange, anisotropy, and magnetostatic energy. The anisotropy in the magnetic nanoparticles is introduced in the Section 1.2.

Adjacent domains are separated by the domain walls, called Bloch walls, named after Felix Bloch [17], who was the first to study the nature of the transition layer.

The essential idea of the Bloch wall is that the entire change in spin direction between domains does not occur in one discontinuous jump across a single atomic plane, but takes place in a gradual way over many atomic planes, as seen in Fig.1.1. The exchange energy is lower when the change is distributed over many spins. An estimate of the thickness and domain wall energy of the Bloch wall was done by Kittel [15, 18]. The domain wall energy per unit surface area may be estimated as the sum of contributions from exchange and anisotropy energies. The thickness of the domain wall in terms of the number N of atomic planes contained within the wall, and the total wall energy per unit area σ_w are

$$N = \sqrt{\frac{\pi^2 JS^2}{Ka^3}} = \sqrt{\frac{\sigma_{ex}}{\sigma_{anis}}} \qquad (1.3)$$

where $\sigma_{ex} = \frac{\pi^2 JS^2}{Na^2}$, $\sigma_{anis} \approx KNa$, $\sigma_w = \sigma_{ex} + \sigma_{anis} = 2\pi\sqrt{\frac{JKS^2}{a}}$

J is the exchange integral and S is the spin angular momentum measured in units of $h/2\pi$; K is the anisotropy constant and a is the lattice constant. In iron, $N \approx 300$ lattice constants ≈ 100 nm, and $\sigma_w \approx 1$ erg/cm^2.

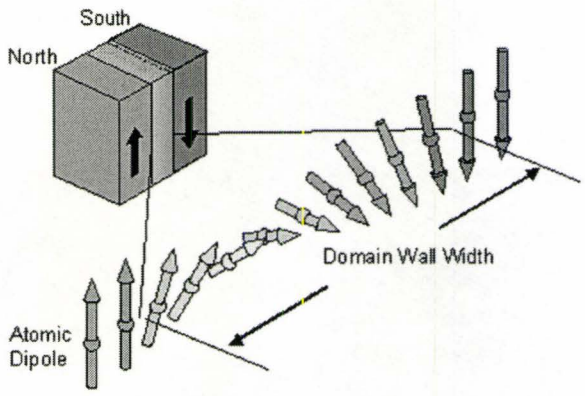

Figure 1.1 Domain wall structure [19]

Further development of domain wall theory was made by Landau and Lifshitz [16], Néel [20], Herring and Kittel [15, 21].

1.1.4 Magnetic transitions

The temperature dependence of the susceptibility of a typical paramagnet is given by the Curie law [22].

$$\chi = \frac{C}{T}, \text{ and } C = \frac{NJ(J+1)}{3k_B}(g\mu_B)^2 \qquad (1.4)$$

where C is the Curie constant, J is the angular momentum quantum number, N is the number of paramagnetic atoms per unit volume, g = -2.002 is the electron g-factor, μ_B is the Bohr magneton, and k_B is the Boltzmann constant.

Ferromagnetic materials become paramagnetic above the Curie temperature, when thermal oscillations in the material are strong enough to overcome the exchange energy between aligned moments. Weiss assumed an internal molecular field in the ferromagnet [22]:

$$H_{mf} = N_W M \qquad (1.5)$$

where N_W is the Weiss coefficient.

For temperatures above the ferromagnetic Curie point, the susceptibility can be expressed by the Curie-Weiss law [22]:

$$\chi = \frac{C}{T-\theta} \tag{1.6}$$

where $\theta = N_W C$ is the paramagnetic Curie point.

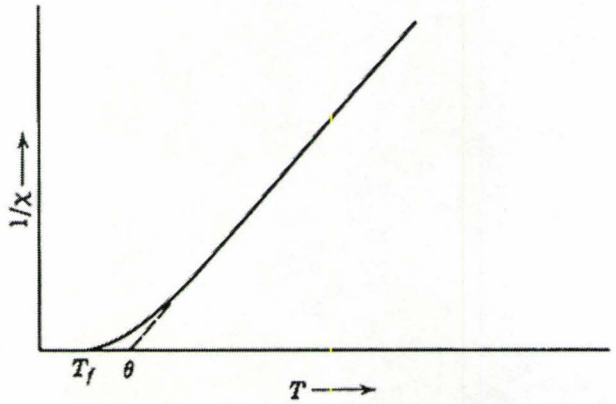

Figure 1.2 Temperature dependence of the inverse susceptibility of a ferromagnet above the ferromagnetic Curie point T_f, θ is the paramagnetic Curie point [22]

The deviation from the Curie-Weiss law is usually observed in the neighbourhood of the Curie point, as shown in Fig.1.2. The intercept of the linear part of the curve with the T-axis is just θ, which does not coincide with T_f, the ferromagnetic Curie point [22].

Antiferromagnetic or ferrimagnetic materials become paramagnetic above the critical temperature, which is called the Néel temperature. Néel extended Weiss's molecular field theory of ferromagnetism, and proposed the two antiparallel magnetic sublattices model for the antiferromagnetic and ferrimagnetic materials. The molecular field H_{mA} or H_{mB} acting on an atom at the sublattice A or B may be written in analogy with Eq.1.5 as [22, 23]:

$$H_{mA} = -N_{AA}M_A - N_{AB}M_B \quad (1.7\text{ a})$$

$$H_{mB} = -N_{BA}M_A - N_{BB}M_B \quad (1.7\text{ b})$$

Then, if a field H is also applied, the field H_A and H_B at an atom on the A and B lattice, respectively, are given by [22]

$$H_A = H - N_{AA}M_A - N_{AB}M_B \quad (1.8\text{ a})$$

$$H_B = H - N_{BA}M_A - N_{BB}M_B \quad (1.8\text{ b})$$

In the case of antiferromagnetism, since the same type of atoms occupy the A and B lattice sites, $N_{AA} = N_{BB} = N_{ii}$ and $N_{AB} = N_{BA}$. N_{AB} is positive because the interaction between nearest neighbours is antiferromagnetic. On the other hand, N_{ii} may be positive, negative, or zero, depending on the particular material.

Above the Néel temperature, the sublattice magnetizations induced by the applied field are given by:

$$M_A = \frac{C}{2T}H_A \quad (1.9\text{ a})$$

$$M_B = \frac{C}{2T}H_B \quad (1.9\text{ b})$$

where $C = \frac{NJ(J+1)}{3k_B}(g\mu_B)^2$

Hence the antiferromagnetic susceptibility [22]

$$\chi = \frac{M}{H} = \frac{M_A + M_B}{H} = \frac{C}{T+\theta}, \quad (1.10)$$

where $C = \frac{NJ(J+1)}{3k_B}(g\mu_B)^2$ and $\theta = \frac{1}{2}C(N_{ii} + N_{AB})$

Eq 1.10 is the generalized Curie-Weiss law.

In the case of ferrimagnetic material, $N_{AB} = N_{BA}$ as before. However, $N_{AA} \neq N_{BB}$ since the sublattices are inequivalent.

Above the Néel temperature, the sublattice magnetizations induced by the applied field are given by [22]:

$$M_A = \frac{C_A}{T} H_A \tag{1.11 a}$$

$$M_B = \frac{C_B}{T} H_B \tag{1.11 b}$$

where $C_A = \sum_i \frac{N_i g^2 \mu_B^2 S_i (S_i + 1)}{3k_B}$ and $C_B = \sum_j \frac{N_j g^2 \mu_B^2 S_j (S_j + 1)}{3k_B}$

The ferrimagnetic susceptibility χ is more conveniently described in its inverse form [22].

$$\frac{1}{\chi} = \frac{T}{C} + \frac{1}{\chi_0} - \frac{\sigma}{T - \Theta} \tag{1.12 a}$$

where $C = C_A + C_B$, $\frac{1}{\chi_0} = \frac{1}{C^2}\left(C_A^2 N_{AA} + C_B^2 N_{BB} + 2C_A C_B N_{AB}\right)$ (1.12 b)

$$\sigma = \frac{C_A C_B}{C^3}\left\{C_A^2 (N_{AA} - N_{AB})^2 + C_B^2 (N_{BB} - N_{AB})^2 - 2C_A C_B \left[N_{AB}^2 - (N_{AA} + N_{BB}) N_{AB} + N_{AA} N_{BB}\right]\right\} \tag{1.12 c}$$

$$\Theta = -\frac{C_A C_B}{C}(N_{AA} + N_{BB} - 2N_{AB}) \tag{1.12 d}$$

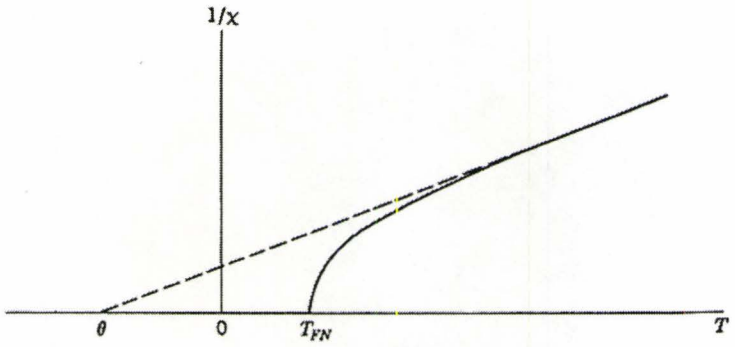

Figure 1.3 Temperature dependence of the inverse susceptibility of a ferrimagnet above the Néel temperature (T_{FN}) according to the molecular field theory. (dashed line is the asymptote of the hyperbola, θ is paramagnetic Curie point) [22]

As shown in Fig.1.3, the graphical representation of Eq 1.12 is a hyperbola. Its asymptote $T \to \infty$ is given by [22]

$$\frac{1}{\chi} = \frac{T}{C} + \frac{1}{\chi_0} \tag{1.13}$$

Defining $\theta = \frac{C}{\chi_0}$ as the paramagnetic Curie point, Eq.1.13 may be written as $\chi = \frac{C}{T+\theta}$. This is again the Curie-Weiss law (Eq.1.10).

The ferrimagnetic Néel temperature T_{FN} can be obtained from Eq.1.14 as [22]:

$$T_{FN} = -\frac{1}{2}\left(C_A N_{AA} + C_B N_{BB}\right) + \frac{1}{2}\left[\left(C_A N_{AA} - C_B N_{BB}\right)^2 + 4 C_A C_B N_{AB}^2\right]^{1/2} \tag{1.14}$$

1.1.5 Spinel ferrites

Spinel structure is named after a natural occurring mineral spinel $MgAl_2O_4$ [24]. The unit cell consists of eight molecules of $MO{\cdot}N_2O_3$. The 32 oxygen ions form a face-centered cubic lattice, which include 64 tetrahedral (A sites) and 32 octahedral interstices

(B sites). The cations occupy only 24 of the interstitial positions, of which there are two distinctly different types [22].

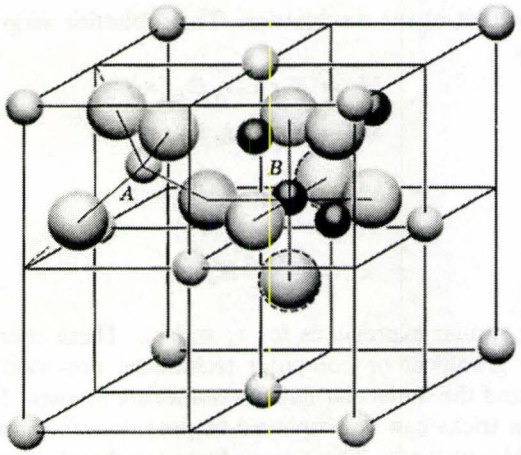

Figure 1.4 A part of the spinel lattice. The large spheres represent oxygen ions, the small light spheres ions in tetrahedral (A) sites and the small dark spheres ions in octahedral (B) site [22].

In a normal structure, the eight divalent (M) ions occupy the A sites and the 16 trivalent (N) ions occupy the B sites, such as $MgAl_2O_4$, $FeCr_2O_4$, $ZnAl_2O_4$.

In a inverse structure, the A sites are occupied by eight trivalent (N) ions, and the B sites by eight divalent (M) ions and eight trivalent (N) ions, such as Fe_3O_4, $NiFe_2O_4$, $CoFe_2O_4$.

A mixed structure of normal and inverse spinels occurs when a certain fraction of trivalent ions occupy A sites while the other fraction occupy the B sites, such as $MnFe_2O_4$.

The interaction between the ions on the sublattices A and B sites are through superexchange. The theory of superexchange interaction was first introduced by Kramers [25], and further developed by Anderson [26] and others. It is an indirect exchange interaction which the magnetic atoms strongly interact magnetically with each other

through the intervening non-magnetic ions. In the spinel structure, the superexchange interaction between two cations via an intermediate oxygen ion is greatest if the three ions are collinear and if their separations are not too great [22].

Spinel ferrites have the general formula $MO{\cdot}Fe_2O_3$ where M is a divalent metal such as Cu, Mg, Co, Ni, Mn, etc. Data for some spinel ferrites are collected in Table 1.1. The cations within the brackets are located at B sites, whereas those to the left of the bracket are in A sites. These cation distributions are made primarily on the basis of X-ray and neutron diffraction measurements. The spin-only values of the magnetic moments expected for these distributions are tabulated in Bohr magnetons for the A and B sites. The theoretical net moment per formula unit is calculated based on the Néel's theory of ferrimagnetism, which is close to the experimental value.

For the spinels in Table 1.1, the predicted net moment is reasonably close to the observed value. The two normal spinels, $ZnFe_2O_4$ and $CdFe_2O_4$, do not exhibit ferrimagnetism. The deviations in other spinel may arise for several reasons. For example, for $NiFe_2O_4$ and $CoFe_2O_4$ the orbital momentum probably is not completely quenched. For $CuFe_2O_4$, it is suggested there is an equilibrium distribution of Cu ions on A and B sites at a temperature T, which means a partly inverted structure [27].

Table 1.1 Saturation moments and Curie temperatures of some spinel ferrites [22]
Magnetic moments are in Bohr magnetons per formula unit for 0 K

Spinel	Moment A Site	Moment B Site	Net moment Theor-etical	Net moment Experi-mental	T_C (K)
$Zn[Fe_2]O_4$	0	5-5	0	Para	
$Cd[Fe_2]O_4$	0	5-5	0	Para	
$Mn_{0.8}Fe_{0.2}[Mn_{0.2}Fe_{1.8}]O_4$	5	5+5	5	4.6	573
$Fe^{3+}[Fe^{2+}Fe^{3+}]O_4$	5	4+5	4	4.1	858
$Fe^{3+}[\square_{1/3}Fe_{5/3}{}^{3+}]O_4$	5	8.3	3.3	3.2	1020
$Fe[CoFe]O_4$	5	3+5	3	3.7	793
$Fe[NiFe]O_4$	5	2+5	2	2.3	858
$Fe[CuFe]O_4$	5	1+5	1	1.3	728
$Mg_{0.1}Fe_{0.9}[Mg_{0.9}Fe_{1.1}]O_4$	4.5	5.5	1.0	1.0	713

1.2 Magnetic nanoparticles

1.2.1 Single domain particles

Multi-domain structure is a result of minimizing the total magnetic energy. This total energy includes magnetostatic energy, the exchange and the anisotropic energy as well as the domain wall contribution. However, there is a critical crystal size, below which a single-domain structure is favourable, since the energy increase due to the formation of domain walls is higher than the energy decrease obtained by dividing the single domain into smaller domains.

The study of single-domain magnetic particles has been an active field of research since the pioneering work of Stoner and Wohlfarth [28], who studied the hysteretic rotation of the magnetization over the magnetic-anisotropy energy barrier under the influence of an applied field, and Néel, who predicted that at nonzero temperature the magnetization can overcome the energy barrier as a result of thermal agitation.

The critical particle size for single domain behaviour has been estimated by Kittel [18] Néel [29] and Stoner and Wohlfarth [28, 30]. For typical magnetic materials the dimensional limit of a single domain is in the range of 10-800 nm, depending on the spontaneous magnetization and on the anisotropy and exchange energies. For spherical crystals the characteristic radius is given by [31]

$$R_{sd}=9E_{\sigma}/\mu_0 M_S^2, \qquad (1.15)$$

where M_S is the saturated magnetization and E_σ is the total domain wall energy per unit area. The critical radius is about 15 nm for iron, 35 nm for Co, 100 nm for NdFeB, and 750 nm for $SmCo_5$.

1.2.2 Magnetic anisotropy in the single domain particles

The term *magnetic anisotropy* is used to describe the dependence of the internal energy on the direction of the spontaneous magnetization of the magnetic nanoparticles, which creates "easy" and "hard" directions of magnetization. In bulk materials, magnetocrystalline and magnetostatic energies are the main sources of anisotropy. In the single domain particles, other kinds of anisotropy can be of the same order of magnitude as these main anisotropies, such as surface anisotropy, strain anisotropy and shape anisotropy [12, 32].

Magnetocrystalline anisotropy

This term originates from spin-orbit coupling and exhibits the same symmetry as in the crystal structure. Two most common symmetries are uniaxial and cubic.

For uniaxial symmetry, the anisotropy of hexagonal crystal is a function of only one parameter, the angle θ between the c-axis and the direction of the magnetization. The energy is symmetric with respect to the ab-plane based on the experiment, so that odd powers of cosθ may be eliminated from a power series expansion for the anisotropy energy. The first two terms are given by [12]

$$E_u = V(K_1 \cos^2\theta + K_2 \cos^4\theta) = V(K_1 m_z^2 + K_2 m_z^4) \qquad (1.16)$$

where z is parallel to the crystallographic c-axis, and **m** is a unit vector parallel to the magnetization vector. The coefficients K_1 and K_2 are constants which depend on the temperature and can be taken from experiments. In principle the expansion may be carried to higher orders, but they are not required, and the K_2 coefficient is negligible.

For cubic symmetry, x, y, z directions are not distinguishable, and cubic crystals are the same after rotating the coordinates so that x is replaced by y etc. Again, odd powers are ruled out and the lowest-order combination which fits the cubic symmetry is $m_x^2 + m_y^2 + m_z^2$, but this is just a constant. Therefore, the expansion starts with the fourth power and is [12]:

$$E_c = V\left[K_1\left(m_x^2 m_y^2 + m_y^2 m_z^2 + m_x^2 m_z^2\right) + K_2 m_x^2 m_y^2 m_z^2\right] \tag{1.17}$$

where the values of K_1 and K_2 are also taken from experiments, and they also depend on the temperature. Cubic materials exist with either sign for K_1. For example, $K_1>0$ in Fe, so that the easy axes are along (100), while for Ni $K_1<0$, and the easy axes are along the body diagonals, (111).

Magnetostatic self-energy and shape anisotropy

Magnetostatic self energy originates from the classical interactions among the dipoles, and is also the reason for shape anisotropy. It can be evaluated as

$$E_M = -\frac{1}{2}\int M \cdot H dv \tag{1.18}$$

where M is the magnetization, and H is the internal field. It may be taken as the interaction of each dipole with the *internal* field H created by the other dipoles, and a

factor ½ introduced in order to avoid counting twice the interaction of A with B, and of B with A.

For a single-domain particle, any nonspherical shape gives rise to shape anisotropy. Here are three examples with different shapes, such as *sphere, cylinder* and *ellipsoid.*

For a *spherical* particle in a uniform field, which is parallel to z, a field H inside is [12]

$$H_{x_{in}} = H_{y_{in}} = 0, H_{z_{in}} = -\frac{M_S}{3}\gamma_B \tag{1.19}$$

So, the integration in Eq. 1.18 leads only to a multiplication by the volume of the sphere. The magnetostatic self-energy of a uniformly magnetized sphere is:

$$E_M = \frac{1}{6}\gamma_B M_S^2 \cdot V \tag{1.20}$$

where $V = \frac{4}{3}\pi R^3$ is the volume of the sphere, and γ_B is the unit conversion factor. For the SI units, $\gamma_B = 1$, while for the Gaussian, cgs units, $\gamma_B = 4\pi$. M_S is the magnetization.

The second example is an *infinite circular cylinder*. When it is uniformly magnetized along the x-axis, and the cylinder axis is defined as z. The internal field H inside the cylinder is [12]

$$H_{x_{in}} = -\frac{M_S}{2}\gamma_B, H_{y_{in}} = H_{z_{in}} = 0 \tag{1.21}$$

The energy *per unit length along z* is

$$E_M = \frac{1}{4}\gamma_B M_S^2 \cdot S \tag{1.22}$$

where $S = \pi R^2$ is the circular end area of the cylinder. If the same cylinder is magnetized along the z-direction, $\boldsymbol{E_M = 0}$.

The third example is the *ellipsoid.* The examples of a sphere and a cylinder are particular cases of a more general theorem about uniformly magnetized ellipsoids. If the ellipsoid is uniformly magnetized, the field inside the ellipsoid can be written [12] as

$$H_{in} = -\gamma_B D \cdot M \tag{1.23}$$

where $\boldsymbol{D}$ is a tensor, called the demagnetization tensor, and the trace of the tensor $\boldsymbol{D}$ is 1. For a sphere all the directions are equivalent, $D_x = D_y = D_z = 1/3$. For an infinite cylinder, $D_z = 0$, $D_x = D_y = 1/2$. They lead to the same results as the above two.

Substituting it into Eq 1.18, the magnetostatic self-energy of a uniformly magnetized ellipsoid, is

$$E_M = \frac{1}{2}\gamma_B \left(D_x M_x^2 + D_y M_y^2 + D_z M_z^2\right) \cdot V \tag{1.24}$$

This is the *shape anisotropy* term.

Surface Anisotropy

There are several contributions to this term, the most important of which was suggested in 1954 by Néel [33], who pointed out the importance of the reduced symmetry at the surface of a ferromagnet. The spin at the surface has a nearest neighbour on one side, and none on the other side, so that the exchange energy there cannot be the same as in the bulk. This is also true at the interface between two different ferromagnets. The easiest case to consider is that of a thin film, because in this case it is possible to calculate each atomic layer. But, it is hard to extend to other geometries. From a phenomenological

point of view, any surface energy term should describe a tendency of the surface spins to be either parallel or perpendicular to the surface.

Magnetostriction and *strain anisotropy*

This anisotropy term is the origin of strain anisotropy. When a ferromagnet is magnetized, it shrinks or expands in the direction of the magnetization. The energy of the internal magnetostriction in a ferromagnetic crystal can be expressed in the same mathematical form as in magnetocrystalline anisotropy.

1.2.3 Superparamagnetism

As we discussed above, the anisotropy energy in a single domain particle is proportional, in a first approximation, to the volume V, $E_B=KV$. Thus, with decreasing particle size the anisotropy energy decreases, and for a particle size lower than a characteristic value, it may become so low as to be comparable to the thermal energy k_BT. This implies that the energy barrier for magnetization reversal may be overcome, and then the total magnetic moment of the particle can thermally fluctuate, like a single spin in a paramagnetic material. Thus the entire spin system may be rotated and the spins within the single domain particles remain magnetically coupled. This is called *superparamagnetism*.

The calculation of the superparamagnetic relaxation time τ of the single domain particles is very important for the understanding of the magnetic behaviour of superparamagnetic materials.

The first τ calculation was done by Néel [34]. For simplicity, he assumed that the magnetic moments of the particles spend all their time in one of the easy directions, and

no time at all at any direction in between, which is well approximated by assumption that $\alpha = \frac{E_B}{k_B T} >> 1$, where E_B is the energy barrier of the particle. He considered only the case of uniaxial symmetry. The expression for the relaxation time:

$$\tau = \tau_0 \exp(\alpha), \text{ with } \alpha = \frac{E_B}{k_B T} >> 1 \qquad (1.25)$$

The original estimation of τ_0 by Néel was 10^{-9} s. It was criticized by W.F.Brown who provided more quantitative description of the relaxation time [35-37]. He considered the magnetic moments of the particles to wiggle around an energy minimum (easy direction) for a while, and described it as a random walk which obeys the Fokker-Planck equation. He tried some analytic approximations and an asymptotic expansion to this differential equation, which is:

$$f_0 = \frac{2K\gamma_0}{M_S}\sqrt{\frac{\alpha}{\pi}} \text{ for } \alpha > 1 \qquad (1.26)$$

Numerical solutions of Brown's model for the case of a uniaxial anisotropy have been modified recently by Coffey [38, 39]

At a specific experimental technique, the value of the measuring time τ_m may be comparable to τ. If $\tau_m >> \tau$, the relaxation appears to be so fast, and the assembly of particles behaves like a paramagnetic system, called superparamagnetic state. On the contrary, if $\tau_m << \tau$, the relaxation appears so slow that quasi-static properties are observed, and the rotation of the spins in the single-domain particles is blocked, or "frozen" by the energy barrier.

The blocking temperature T_B, separating the two states, is defined as the temperature at which $\tau_m = \tau$. Therefore, it is not uniquely defined, but is related to the time scale of the experimental technique. The blocking temperature for a magnetic particle increases with increasing size and for a given size increases with decreasing measuring time. The highest value of T_B is represented by the Curie or Néel temperature at which the transition from the superparamagnetic to the paramagnetic state occurs. The techniques currently used to study the superparamagnetic relaxation are DC magnetization (τ_m around 100 s, depends on the type of magnetometer and procedure), AC susceptibility ($\tau_m = 10^{-1}$ to 10^{-5} s for standard PPMS (Physical Properties Measurement System by Quantum Design) experiments), Mössbauer spectroscopy (time window, 10^{-7} to 10^{-9} s for ^{57}Fe), ferromagnetic resonance ($\tau_m = 10^{-9}$ s), and neutron diffraction (time window, 10^{-8} to 10^{-12} s) [32].

1.2.4 Non-interacting magnetic nanoparticles

Theoretical calculation is based on the framework of the Néel-Brown model. Some systematic studies have been well established on this model [32, 40, 41]. These are used to interpret the relationship between the observed microstructure of magnetic nanoparticles and the experimental data obtained from the magnetic measurements.

In an ideal model, without considering magnetic interparticle interactions, the relaxation time τ of an assembly of the non-interacting magnetic nanoparticles is given by the Néel-Brown model, Eq 1.25, $\tau = \tau_0 \exp[E_B / k_B T]$.

With a specific measuring time (τ_m) of the experimental technique, the blocking temperature T_B, at which $\tau_m=\tau$, separates the two states, the blocking and superparamagnetic states. Using AC susceptibility technique, T_B is expected to move by changing τ_m from 10^{-1} to 10^{-5} second.

$$\ln \tau_m = \frac{E_B}{k_B T} + \ln \tau_0 \tag{1.27}$$

The plot of $\ln \tau_m$ vs. $\frac{1}{T_B}$ gives a straight line with a slope of $\frac{E_B}{k_B}$ and an intercept of $\ln \tau_0$. Both the anisotropy energy E_B and the characteristic relaxation time τ_0 of a particle, which are intrinsic parameters of the assembly, can be experimentally obtained.

If the particles in the assembly are all of the same size, the magnetization versus applied magnetic field curve can be expressed as a Langevin function in the superparamagnetic state:

$$M = M_S L\left(\frac{\mu H}{k_B T}\right) = M_S\left[\coth\left(\frac{\mu H}{k_B T}\right) - \frac{k_B T}{\mu H}\right] \tag{1.28}$$

where M_S (emu/cm^3) is the volumetric saturation magnetization, L denotes the Langevin function $L = \coth x - \frac{1}{x}$, and $\mu=M_S V$ is magnetic moment per particle. By fitting the magnetization curve with the Langevin function, M_S and μ can be calculated.

However, the nanoparticle assembly inevitably contains a distribution of particle sizes. R.W.Chantrell and coworkers [42] considered a lognormal distribution function in the system, and derived the equations to calculate the magnetic diameter of a particle (D_{Vm}) and a standard deviation (σ) by the sum of the contributions from each particle:

$$D_{Vm} = \left(\frac{18k_B T}{\pi M_S'} \sqrt{\frac{\chi_i}{3\varepsilon M_S'} \frac{1}{H_O}} \right)^{\frac{1}{3}} \quad (1.29\text{ a})$$

$$\sigma = \frac{1}{3} \sqrt{\ln\left(\frac{3\chi_i H_O}{\varepsilon M_S'} \right)} \quad (1.29\text{ b})$$

$$\mu = M_S' V = 3k_B T \sqrt{\frac{\chi_i}{3\varepsilon M_S'} \frac{1}{H_O}} \quad (1.30)$$

where M_S' (emu/cm^3) is the volumetric saturation magnetization of the bulk material, ε is the volumetric particle fraction. χ_i is the initial susceptibility of the system, and the relationship between M and 1/H for the large H regime should be a straight line, which can be extrapolated linearly to the M = 0 axis at a point $1/H_0$.

For a uniform particle size σ=0, it follows from Eq 1.29 b that $\chi_i = \frac{\varepsilon M_S'}{3} \cdot \frac{1}{H_0}$. From the measured values of χ_i or $1/H_0$, it is possible to make two estimates of the diameter D_i and D_u from Eq 1.29 a by substituting $1/H_0$ by χ_i or vice versa.

$$D_i = \left(\frac{18k_B T}{\pi} \cdot \frac{\chi_i}{\varepsilon M_S'^2} \right)^{\frac{1}{3}} \quad (1.31)$$

$$D_u = \left(\frac{6k_B T}{\pi M_S'} \cdot \frac{1}{H_0} \right)^{\frac{1}{3}} \quad (1.32)$$

If the system has a distribution of particle size, the two diameters will differ, and in general, $D_i > D_u$, since χ_i is more sensitive to the larger particles, whilst the approach to saturation is more sensitive to the smaller particles [42].

D.Yu.Godovsky and coworkers [43] have derived an equation specifically for polymer nanocomposite materials based on Chantrell's method [42]. Knowing that $\varepsilon M_S' = M_S$ and $\varepsilon = \frac{\rho_c}{\rho_m} \cdot \frac{c}{c+1}$, where M_S is volumetric saturation magnetization of the nanocomposite, ρ_c and ρ_m are the densities of the composite and pure magnetic materials respectively, and c is weight ratio of magnetic materials to the polymer, then by substitution of D_i in Eq 1.31 by volume V:

$$V = \frac{3k_B T}{M_S^2} \cdot \chi_i \cdot \frac{\rho_c}{\rho_m} \cdot \frac{c}{c+1} \tag{1.33}$$

Because of the existence of a nonmagnetic surface layer on the particle, called the magnetic dead zone, it is important to note that all the above diameters calculated from Chantrell's method are the magnetic diameter of the particle D_{Vm}, which is smaller than the physical diameter of the particle D_{Vp} obtained by TEM observation [42]. The nonmagnetic surface layers may be formed from interface chemical reaction between the dispersant and the particles, the surface spin canting (like in ferrite) [44-47], or the surface oxidation (like in metal) [48, 49]. This also explains why M_S of a nanocomposite system is always less than $\varepsilon M_S'$, which is the expected value of the saturation magnetization of the nanocomposite.

In spite of the discrepancy between D_{Vm} and D_{Vp}, particle size is an important parameter in terms of evaluating different theoretical models for interpreting magnetic data. Moreover, the average particle size can be adjusted by changing electrodeposition parameters. Ultimately, this will lead to optimization of the microstructure and magnetic properties of the nanocomposite films.

We attempted to calculate the magnetic sizes of the particles (D_{Vm}) and standard deviation (σ) using Eq.1.29 and Eq.1.30, assuming a lognormal particle size distribution in our experiments. Also, we can simply estimate D_{Vm} by fitting the magnetization curve to the Langevin function, or by calculating any of Eq.1.31, Eq.1.32, or Eq.1.33 if we assume an identical particle size.

In many instances, the lognormal distribution is selected. However the Gaussian distribution function is also used to describe the distribution of particle sizes found in ferrofluids. K.O'Grady and coworkers [50] compared these two cases and their results showed that the lognormal distribution can be used as a good approximation, even when the particle diameters obey a Gaussian distribution if the standard deviation of the distribution is small, i.e., $\sigma<0.35$. Therefore the lognormal distribution may be favourable since integration over the distribution function leads to simple analytical expressions.

In our experimental work, the average particle size of the particles (D_{Vp}) and standard deviation (σ) were obtained from TEM observations.

1.2.5 Interacting magnetic nanoparticles

Our results described below show that magnetic interparticle interaction must be considered in organic-inorganic nanocomposite films.

Shtrikman and Wohlfarth [51, 52] proposed a phenomenological model to the problem. They considered two cases, corresponding to weak and strong interactions, respectively.

In the weak interaction regime, they added an additional interaction energy term to the energy barrier $\mathbf{E_{B0}}$ of a noninteracting particle with a volume V and a no-relaxing

(intrinsic) magnetisation $\mathbf{M_{nr}}$, expressed as $H_i M_{nr} V$, where $\mathbf{H_i}$ is a phenomenological interaction field. To proceed to an interaction assembly of such particles, H_i can be further replaced by a statistical mean field of a particle assembly, $H_i \tanh\left(\frac{H_i M_{nr} V}{k_B T}\right)$.

Hence the energy barrier E_B of a particle is expressed as:

$$E_B = E_{B0} + M_{nr} V H_i \tanh\left(\frac{H_i M_{nr} V}{k_B T}\right) \tag{1.34}$$

$H_i \tanh\left(\frac{H_i M_{nr} V}{k_B T}\right)$ can be estimated as $(H_i^2 M_{nr} V)/(3k_B T)$ when $\frac{H_i M_{nr} V}{k_B T} \ll 1$ for the weak interaction. This leads to: $\frac{E_B}{k_B T} = \frac{E_{B0}}{k_B (T - T_0)}$ with $T_0 = \frac{(H_i M_{nr} V)^2}{3 k_B E_{B0}}$. It is valid only if $T_0 \ll T$. Hence the temperature dependence of the relaxation time of weakly interacting magnetic nanoparticles becomes:

$$\tau = \tau_0 \exp\left[\frac{E_{B0}}{k_B (T - T_0)}\right] \text{ with } T_0 = \frac{(H_i M_{nr} V)^2}{3 k_B E_{B0}} \tag{1.35}$$

This is the Vogel-Fulcher law, which was first suggested by Tholence [53] to fit the frequency dependence of T_f (freezing temperature) in spin glasses.

In the strong interaction regime, another model is suggested where the actual volume of the particle is replaced by an effective volume that increases when the temperature is lowered. With an effective energy barrier $E_{Beff} = K_{eff} V_{eff}$, this model leads to:

$$\tau = \tau_0 \exp\left[\frac{E_{Beff}}{k_B T_0 g\left(\frac{T}{T_0}\right)}\right] \text{ with } g(t) = t(t-1)^{1/2} \tag{1.36}$$

It is a slightly different form to the Vogel-Fulcher law for which g_{VF}=t-1, and only holds for $T_0<T\leq 2T_0$.

Following the approach of Shtrikman and Wohlfarth, J.L.Dormann and coworkers quantified the effect of the interactions, and built up the Dormann-Bessais-Fiorani (DBF) model [52, 54]. This model accounts for interparticle interactions by a statistical calculation of the dipolar energy for a disordered assembly of particles with a volume distribution and easy axes in random orientation. This model, valid for weak and medium interaction strengths, concludes that the interactions lead to an increase of the energy barrier. This interaction anisotropy energy term has uniaxial symmetry, in agreement with the symmetry of dipolar interactions, and can be expressed by

$$E_{B\text{int}} \sim M_{nr}^2 V \sum_j a_j L\left(\frac{M_{nr}^2 V a_j}{kT}\right) \tag{1.37}$$

where L denotes the Langevin function, $a_j = \frac{\langle V\rangle\left(3\cos^2\xi_j - 1\right)}{d_j^3}$, where ξ_j and d_j correspond to an angle parameter of special orientation and to the distance of particle j with respect to an origin particle, respectively.

If limiting the interactions to the nearest neighbours, which represents about 90% of the total interaction effect, the effective energy barrier (E_B) of an interacting particle with volume V and non-relaxing (intrinsic) magnetization M_{nr} is:

$$E_B = E_{B0} + n_1 a_1 M_{nr}^2 V L\left(\frac{a_1 M_{nr}^2 V}{k_B T}\right) \tag{1.38}$$

where n_1 is the average number of nearest neighbours, $a_1 \approx \frac{C_V}{\sqrt{2}}$ where C_V is the volume concentration of the particles in the sample, and $\boldsymbol{L}$ is the Langevin function.

Energy barrier E_B (Eq 1.38) can be approximated in two conditions: weak and medium interactions, according to $\frac{a_1 M_{nr}^2 V}{k_B T_B}$, where T_B is the blocking temperature related to the volume V. For $\frac{a_1 M_{nr}^2 V}{k_B T_B} \leq 1$, which corresponds to weak interactions or high T values

$$E_B \approx E_{B0} + n_1 \frac{(a_1 M_{nr}^2 V)^2}{3 k_B T} \tag{1.39}$$

In this weak interaction approximation, the relaxation time (Eq 1.25) is approximately given by the Vogel-Fulcher (VF) law (Eq 1.35).

For $\frac{a_1 M_{nr}^2 V}{k_B T_B} \geq 2$, which corresponds to medium interactions or low T values

$$E_B \approx E_{B0} - n_1 k_B T + n_1 a_1 M_{nr}^2 V \tag{1.40}$$

In this case, the relaxation time (Eq 1.25) becomes

$$\tau = \tau_0 \exp(-n_1) \exp\left(\frac{E_{B0} + n_1 a_1 M_{nr}^2 V}{k_B T} \right) \tag{1.41}$$

Hence, by plotting the $\log_{10}\tau_m$ versus $1/T_B$ from (Eq 1.41), we obtain a quasi-straight line, with increased slope and intercept of the $\log_{10}\tau_m$ axis shifted by $-n_1/2.30$ with respect to the case without interactions.

Dormann and coworkers studied the dynamical properties of γ-Fe_2O_3 nanoparticles, dispersed in a polymer, by AC susceptibility measurements [55]. The variation of the average blocking temperature as a function of the measuring time can be satisfactorily described by this model.

1.2.6 Experimental characterization of magnetic nanoparticles

The transition from ferromagnetism to superparamagnetism is a dynamic process which is characterized by the relaxation time. There are numerous methods to study the assembly of the magnetic nanoparticles, including measurements of field cooled (FC) and zero field cooled (ZFC) magnetizations at low field, magnetization under moderate and high fields, AC susceptibility, Mossbauer spectroscopy without and with applied field, ferromagnetic resonance, neutron diffraction and etc. Here we focus on the DC magnetization (FC and ZFC) and AC susceptibility.

DC magnetization experiments are widely used for characterizing magnetic nanoparticle assemblies. They provide the static susceptibility and point out the irreversible properties below the blocking temperature. The experimental procedure includes field-cooled (FC) and zero-field-cooled (ZFC) magnetization.

The FC magnetization curve is obtained by cooling the sample in the presence of a magnetic field to the minimum temperature T_{min} and measuring the magnetization of the sample while increasing the temperature to T_{max}.

The ZFC magnetization curve is obtained by cooling the sample in the zero magnetic field to T_{min} and measuring the magnetization of the sample in the presence of a magnetic field while warming up to T_{max}.

The superparamagnetic behaviour of the nanoparticle assembly is indicated by a ZFC peak and splitting of the ZFC and FC curves. The temperature at which the ZFC and FC curves diverge corresponds to the temperature commonly referred to as breaking temperature, i.e., the blocking temperature of the largest particles within the particle size distribution. The peak in the ZFC curve occurs at the average blocking temperature of the nanoparticle assembly.

Wenger and Mydosh [56] found that the peak depends on concentration and field. Using Brown's formula of the relaxation time in the presence of a magnetic field, they calculated the effects of an external magnetic field on the blocking temperature. Their numerical calculations showed a power law dependence of the blocking temperature on the field of the form H^2 for low field ($H \ll H_K$) and $H^{2/3}$ for high fields [57].

The concentration dependence of the ZFC peak indicates the influence of the interparticle interaction in the nanoparticle assembly. El-Hilo et al. showed that the contribution of the interaction energy is equivalent to increase the energy barrier of the individual particle, so that the temperature of the ZFC peak increases at higher concentration [58, 59].

Above the blocking temperature, the magnetic properties of the nanoparticle assembly are described as superparamagnetic. Therefore, the assembly has Curie behaviour in the case with no interparticle interaction, and Curie-Weiss behaviour with interparticle interaction. Curie-Weiss-like variation of the initial susceptibility of magnetic fluids was observed and discussed by O'Grady, Chantrell and et al [60, 61].

AC susceptibility is proven to be a very useful tool for studying dynamical properties of magnetic nanoparticles. A small AC magnetic field is applied in the frequency range 10-10,000 Hz, inducing a time-dependent moment in the sample. The advantage of the small magnetic field (~5 Oe) allows the initial susceptibility at H→0 to be measured. Moreover, it only slightly modifies the barrier energy (the variation is proportional to H^2) [56], and therefore a good approximation of the relaxation time value in the absence of the applied field can be obtained.

According to Gittleman [62] the complex susceptibility of an assembly of isolated single-domain particles is given by:

$$\chi = \frac{\chi_0 + i\varpi\tau\chi_1}{1 + i\varpi\tau} \tag{1.42}$$

The real part is given by $\chi' = \chi_1 + \frac{\chi_0 - \chi_1}{1 + (\varpi\tau)^2}$ (1.43)

And the imaginary part is given by $\chi'' = \varpi\tau\left(\frac{\chi_1 - \chi_0}{1 + (\varpi\tau)^2}\right)$ (1.44)

χ' as a function of temperature shows a characteristic peak at T_{max} which is consistent with the superparamagnetic behavior of nanoparticles. One can compare the T_{max} to the blocking temperature T_B defined as the temperature at which the relaxation time is equal to 1/f. In an assembly of nanoparticles which shows a size distribution, the average blocking temperature $\langle T_B \rangle$ is related to T_{max} as:

$$T_{max} = \beta \langle T_B \rangle \tag{1.45}$$

where β is a constant dependent on the form of the particle size distribution [62].

The analysis of the frequency dependence of T_{max} allows one to check the models describing the temperature dependence of the relaxation time, for instance, the Néel-Brown model, and to derive the related parameters, such as τ_0 and the energy barrier E_B.

Dormann et al [54, 63] studied the frequency dependence of T_{max} of noninteracting ferrimagnetic γ-Fe_2O_3 particles in the frequency range 2×10^{-2}-10^4 Hz. The frequency dependence of T_{max} was found to follow an Arrhenius law with $\tau_0 \sim 10^{-10}$ s. It was the first time to clearly prove this law for noninteracting particles in a large frequency range.

T_{max} was found to increase with particle concentration. Dormann et al [52, 55, 64, 65] further analyzed the frequency dependence of T_{max} in the frequency range 2×10^{-2}-10^4 Hz for γ-Fe_2O_3 particles dispersed in a polymer matrix with different volume concentration, which introduced weak, median or strong interparticle interaction. The results were satisfactorily explained by the model proposed by the authors, which describes the effect of interparticle interaction on the relaxation time by means of a statistical calculation of the dipolar energy. The parameters that govern the relaxation time, such as the number of first neighbours per particle, interparticle distance, were deduced.

1.3 Fabrication of Magnetic Nanoparticles

Recent advances in chemical synthesis and the characterization of magnetic nanoparticles were reviewed by Willard and et al. [66]. Various solution chemistry techniques used to synthesize nanoparticles, including precipitation, borohydride reduction, hydrothermal, reverse micelles, polyol, sol-gel, thermolysis, photolysis, sonolysis, multisynthesis processing and electrochemical techniques, were surveyed.

One common procedure to prepare nanoparticles is the decomposition of organometallic precursors. Rockenberger and coworkers prepared spheres of nanosized γ–Fe_2O_3 by injecting the iron cupferron complex ($FeCup_3$) into trioctylamine at 300 °C [67]. This method was further expanded to the synthesis of transition metal oxide nanoparticles, such as Cu_2O and Mn_3O_4, by using metal cupferronates M^xCup_x (M: Cu^{2+}, Mn^{2+}).

Sun [68, 69] and coworkers reported a convenient organic phase process for making monodisperse Fe_3O_4 nanoparticles through the reaction of $Fe(acac)_3$ and a long-chain alcohol. Their further experiments indicated that this reaction could be readily extended to the synthesis of MFe_2O_4 nanoparticles (with M = Co, Ni, Mn, Mg, etc.) by simply adding a different metal acetylacetonate precursor to the mixture of $Fe(acac)_3$ and 1,2-hexadecane diol. Fe_3O_4 and related MFe_2O_4 nanoparticles (with M = Co and Mn as two examples) with sizes tunable from 3 to 20 nm in diameter. The process involves high-temperature (up to 305 °C) reaction of metal acetylacetonate with 1,2-hexadecane diol, oleic acid, and oleylamine. The size of the oxide nanoparticles can be controlled by varying the reaction temperature or changing metal precursors. Alternatively, with the smaller nanoparticles as seeds, larger monodisperse nanoparticles up to 20 nm in diameter can be synthesized by seed-mediated growth. The nanoparticles can be dispersed into nonpolar or weakly polar hydrocarbon solvent, such as hexane or toluene. The hydrophobic nanoparticles can be transformed into hydrophilic ones by mixing with a bipolar surfactant, tetramethylammonium 11-aminoundecanoate, allowing preparation of aqueous nanoparticle dispersions.

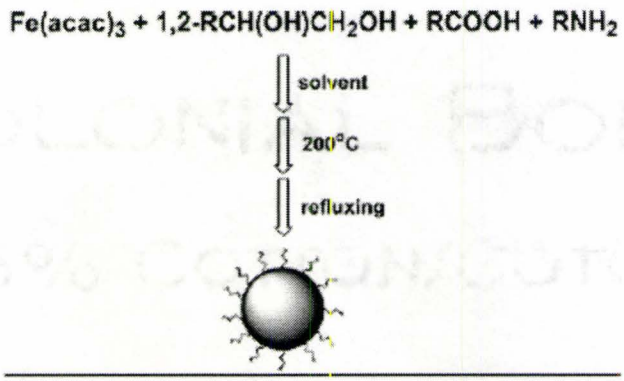

Figure 1.5 Scheme of synthesis of 4 nm Fe_3O_4 nanoparticle seeds

Sukhorukov [10, 11] synthesized magnetic ferrite nanoparticles inside the hollow polyelectrolyte capsules. The capsules were assembled by layer-by-layer (LbL) method which consisted of alternative adsorption of oppositely charged polyelectrolyes. The capsule wall, made of polyelectrolyte multilayers of poly(styrenesulfonate) (PSS) and poly(allylamine hydrochloride) (PAH), is permeable for small ions but not for polymers. To perform particle synthesis exclusively in the capsule interior, capsules were loaded with PAH. The inorganic ions penetrate capsule walls and face a higher pH generated by PAH inside the capsule, forming oxide particles. $CoFe_2O_4$, $ZnFe_2O_4$, $MnFe_2O_4$ and magnetite were synthesized inside the capsules of 10 μm diameter.

Pascal and coworkers [70] prepared 3–8 nm iron oxide nanoparticles from a sacrificial iron electrode in an aqueous solution of dimethylformamide (DMF) and cationic surfactants. The size was directly controlled by the imposed current density, and the resulting particles were stabilized as a colloidal suspension by the use of cationic

surfactants. The size distributions of the particles were narrow, with the average sizes varying from 3 to 8 nm.

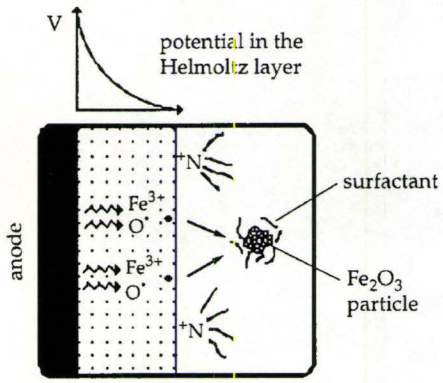

Figure 1.6 Formation of stabilized γ-Fe_2O_3 nanoparticles

Dierstein et al. [71] used a similar strategy to prepare metal oxides. This technique is termed 'electrochemical deposition under oxidising conditions' (EDOC). Mixed oxides and oxide mixtures (ZnO; Mn_3O_4, CuO; Fe_2O_3, SnO_2, In_2O_3, ZrO_2, NiO; Co_3O_4, $CoFe_2O_4$, In_2O_3/SnO_2 etc.) in the nanometre range with narrow particle size distribution were obtained.

Cathodic electrolytic deposition is an important technique for the fabrication of oxides/hydroxides films.[9] The electrochemical intercalation of inorganic nanoparticles into polymer films is a new strategy for the fabrication of novel nanocomposite materials, containing magnetic nanoparticles in a polymer matrix. The advantages of electrodeposition are short processing time, process simplicity, good compositional

control and homogeneity. This method produces nanoparticles in situ in a polymer matrix, and the particle size can be controlled by the amount of polymer. Our research work is based on this method.

CHAPTER 2

FUNDAMENTALS OF ELECTRODEPOSITION

This chapter describes the fundamental aspects of the electrodeposition pertinent to the present work. Electrodeposition, which refers to electrophoretic deposition (EPD) or electrolytic deposition (ELD) in the current context, is widely used to prepare thin film and coatings of metals, ceramics, polymers and organoceramics [9, 72].

Electrophoretic deposition (EPD) is a process, in which charged colloidal particles, suspended in a suitable polar solvent migrate under the influence of an electric field and deposit on an electrode. The colloidal particles that can form stable suspensions and carry charges include ceramics, metals and polymers (polyelectrolytes) [9, 73]. The solvent can be either aqueous or non-aqueous, or a mixture of both.

Cathodic electrolytic deposition (ELD) is a process in which metal ions or complexes are hydrolyzed by an electrogenerated base to form oxide, hydroxide or peroxide deposits on the cathodic substrates. Important hydrolysis reactions for the base generation include reduction of water, nitrate ions and dissolved O_2, which result in the accumulation of colloidal particles at the electrode [9].

Ceramic and organoceramic thin films are important functional materials in various devices. Electrodeposition of ceramic materials can be performed by cathodic or anodic methods. However, anodic deposition has limited utility regarding possible materials to be deposited by this method and substrates used for deposition. Cathodic deposition has important advantages for industrial application. Two processes are commonly used to prepare ceramic coatings by cathodic electrodeposition: the electrophoretic process

(EPD), which is based on the use of suspensions of ceramic particles, and the electrolytic process (ELD), which starts from solutions of metal salts (Fig. 2.1). Comprehensive recent reviews covered materials science aspects, kinetics and applications of EPD [73-76] and ELD [77-79]. The distinguishing features of the two methods were compared in [77, 80]. EPD is an important tool for the preparation of thick ceramic films (Fig. 2.2). ELD enables the formation of nanostructured thin ceramic films.

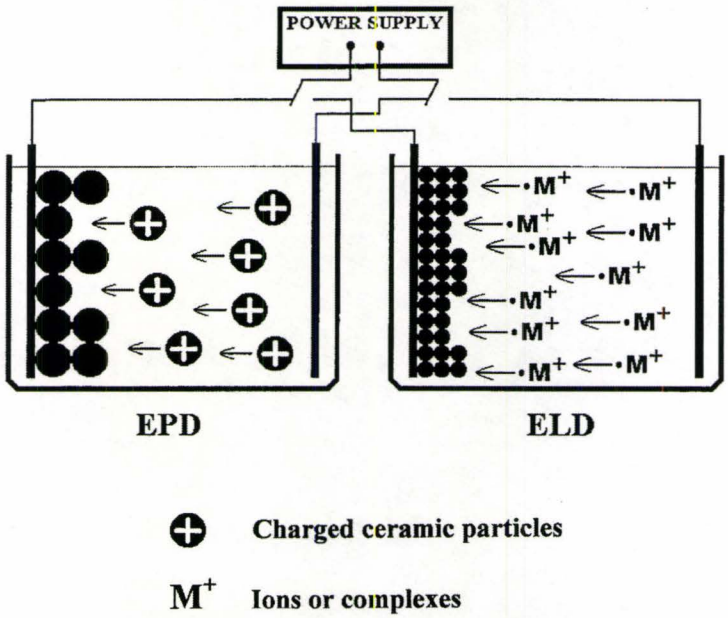

Figure 2.1 Schematic of cathodic electrophoretic deposition (EPD) and electrolytic deposition (ELD), showing electrophoretic motion of positively charged ceramic particles and ions (M^+), followed by hydrolysis of the ions to form colloidal nanoparticles and coagulation of the particles to form EPD and ELD deposits.

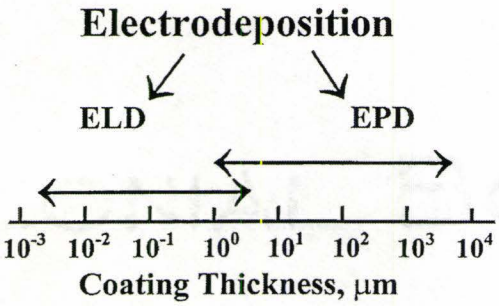

Figure 2.2 Thickness of coatings deposited using ELD and EPD.

A novel method of electrodeposition of organoceramic materials is based on heterocoagulation of charged ceramic and polyelectrolyte particles. Recent experimental and theoretical studies have also highlighted the importance of the electric field, electrode reactions and other factors that influence the coagulation of particles near the electrode surface.

Further description of the deposit formation mechanism of EPD and ELD includes classical Derjaguin-Landau-Verwey-Overbeek (DLVO) theory of colloidal stability, transport phenomena and electrode reactions, which are introduced in the sections 2.2-2.5.

2.1 Polyelectrolytes

Polyelectrolytes is a class of macromolecules that contains charged functional groups, which, when dissolved in a suitable polar solvent (generally water), can acquire a large number of elementary charges [81]. Some common examples of polyelectrolytes include proteins, nucleic acids, polyacrylic acid and polystyrene sulfonate.

Polyelectrolytes may be categorized in different ways [81]:

As for the architecture of macromolecules, polyelectrolytes may be grouped into linear, branched, and cross-linked chains or into homo- and copolymers.

As for the electrochemical considerations, polyelectrolytes can be divided into anionic and cationic polyelectrolytes. The anionic polyelectrolytes carry the electrolyte groups such as –COOH and $–SO_3H$, which can dissociate into negatively charged polyions (polyanions) and positively charged protons (H^+). The cationic polyelectrolytes carry the electrolyte groups, such as $–NH_2$, which can bind a proton, yielding positively charged polyions (polycations). Polyampholytes are macromolecules that bear both anionic and cationic groups and that are positively charged at low pH and negatively at high pH. They are neutral at isoelectric pH, where the amount of positive charge equals the amount of negative charge [81].

In the current work, only cationic polyelectrolytes have been used in the co-deposition of polyelectrolytes and inorganic nanoparticles. Some examples of cationic polyelectrolytes, including poly(ethylene imine) (PEI), poly(allylamine hydrochlorie)

(PAH), chitosan (CHIT), poly(4-vinyl-pyridine) (P4VPy) and poly(diallyldimethylammonium chloride) (PDDA), have been illustrated in Fig. 2.3 [82].

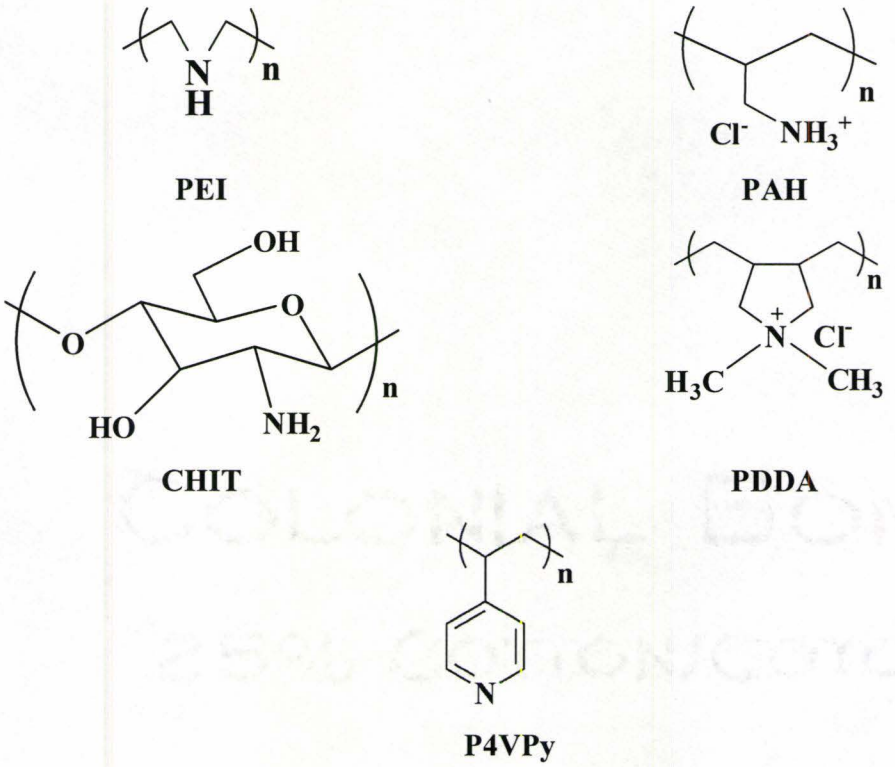

Figure 2.3 Cationic polyelectrolytes: poly(ethylene imine) (PEI), poly(allylamine hydrochlorie) (PAH), chitosan (CHIT), poly(4-vinyl-pyridine) (P4VPy) and poly(diallyldimethylammonium chloride) (PDDA) [82]

There are strong and weak polyelectrolytes. The strong polyelectrolytes acquire spontaneously full charges, and the degree of dissociation of the ionic groups is nearly pH independent. The weak polyelectrolytes are only partially charged when dissolved in pure solvent, the degree of ionization is determined by the solution pH, which can be titrated to full charge with a strong base, such as NaOH, or acid, such as HCl.

Among the cationic polyelectrolytes listed above, PDDA is a strong polyelectrolyte because of the quaternary amino group. The degree of dissociation of the ionic groups of

PDDA is nearly pH independent in a wide pH range below pH 13. PEI, PAH, P4VPy and chitosan are weak polyelectrolytes, containing amine groups [82].

PEI is a polybase. The amine groups in the branched PEI exist in primary, secondary and tertiary form in the approximate ratio of 1:2:1 with a branching site every 3–3.5 nitrogen atoms along any given chain segment [83, 84]. The primary amine groups, which are the chain terminating units, are the most basic and chemically reactive. The pH of an aqueous solution containing 1 wt.% PEI is about 11 and at this pH the PEI molecule has no charge [85, 86]. PEI adsorbs protons in the acidic solutions and becomes charged positively, according to the reaction:

$$PEI + H_3O^+ \rightarrow PEI\text{-}H^+ + H_2O \qquad (2.1)$$

The degree of protonation depends on the amount of acid added.

Significant interest has been generated in the application of PAH for the polymer-mediated synthesis, surface modification of nanoparticles, and thin film deposition [87, 88]. The PAH macromolecules are positively charged below pH 8 [88]. The interest in PAH is stimulated by the fact that PAH facilitates the room temperature crystallization of complex metal oxides. [10]

Chitosan is a natural cationic polysaccharide that can be produced by alkaline N-deacetylation of chitin [89]. Important properties of this material, such as chemical resistance, biocompatibility, advanced mechanical, antimicrobial, and thermal properties, have been utilized in biotechnology [90, 91]. Water soluble and positively charged chitosan can be prepared by the protonation of amine groups in acidic solutions [92, 93]:

$$CHIT + H_3O^+ \rightarrow CHIT\text{-}H^+ + H_2O \qquad (2.2)$$

The properties of chitosan in solutions depend on the molecular weight, the degree of deacetylation, pH and ionic strength. At pH 6.5, the primary amine groups of chitosan become deprotonated. As a result of the decreasing charge with the pH increase, dissolved chitosan usually flocculates at pH above 6.5 [92, 93].

Poly(4-vinyl-pyridine) (P4VPy) is a weak cationic polyelectrolyte. It was found [94] to form polychelates with Cu^{2+}, Zn^{2+}. Partially protonated P4VPy can be obtained by adding an appropriate amount HCl into polymeric solution [95].

A very promising and emerging area in the application of polyelectrolytes is the electrosynthesis of hybrid organic-inorganic nanocomposite films, which contain inorganic nanoparticles *in situ* inside a polymer matrix. Electrophoretic deposition (EPD) of polyelectrolytes and electrolytic deposition (ELD) of metal oxides or hydroxides have been combined to synthesize this type of nanocomposite films [8, 82].

2.2 Particle interactions

The basis for our understanding of the interaction between colloids particles is the classical DLVO (Derjaguin, Landau, Verwey and Overbeek) theory [96, 97]. This theory states that the total pair interaction between colloidal particles consists of two parts, the Coulombic double-layer repulsion and van der Waals' attraction. The total energy V_T of interaction of two isolated, identically charged particles may be defined as:

$$V_T = V_A + V_R \tag{2.3}$$

The attractive energy V_A of the London-van der Waals' interaction between two spherical particles can be expressed by:

$$V_A = -\frac{A}{6}\left(\frac{2}{s^2-4}+\frac{2}{s^2}+\ln\frac{s^2-4}{s^2}\right) \tag{2.4}$$

where A is the Hamaker constant and s = 2 + H/a, with H the shortest distance between the two spheres and a is the particle radius. If H « a, Eq 2.4 can be simplified to:

$$V_A = -A\frac{a}{12H} \tag{2.5}$$

The repulsive energy V_R is:

$$V_R = 2\pi\varepsilon\varepsilon_0 a\psi^2 \ln\left(1+e^{-\kappa H}\right) \tag{2.6}$$

where ε is the dielectric constant of the solvent, ε_0 is the vacuum dielectric permittivity, ψ is the surface potential, 1/κ is the Debye length:

$$\kappa = \left(\frac{e_0^2\sum n_i z_i^2}{\varepsilon\varepsilon_0 kT}\right)^{1/2} \tag{2.7}$$

where e_0 is the electron charge, k is the Boltzmann constant, T is the absolute temperature, n_i is the concentration of ions with valence z_i. Repulsion between colloidal particles is directly related to the diffuse layer charge on the particles.

The DLVO theory describes the potential energy curve for pair interaction, as shown in Fig. 2.4a. When the diffuse-layer repulsion is sufficiently high compared to the van der Waals' attraction, the total energy of particle interaction exhibits a maximum. This is the energy barrier to particle coagulation.

The thickness of the double layer (characterized by the Debye length, 1/κ) is very sensitive to the electrolyte concentration [96]. The DLVO theory explains the existence of a critical electrolyte concentration (flocculation value) for coagulation, decreasing with

the valence of the electrolyte ions of a charge opposite to that of the colloidal particles (rule of Schulze and Hardey [96]). It was demonstrated that the potential energy peak decreases as the electrolyte concentration increases. As the energy barrier disappears, coagulation becomes possible Fig. 2.4b. Flocculation by ions compressing the double layer also follows the Hofmeister series [96].

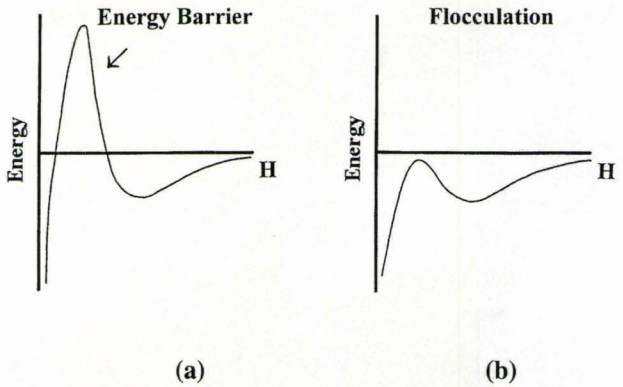

Figure 2.4 Total interaction energy between spherical particles as a function of interparticle separation according to the DLVO theory

Within the series of ions of the same charge, the flocculation value increases in the order:

NH_4^+, K^+, Na^+, Li^+; and

Ba^{2+}, Sr^{2+}, Ca^{2+}, Mg^{2+}

Therefore, a negatively charged sol is flocculated by large cations at a smaller concentration than by small cations of the same valency. The flocculation value was found to be in the range 20-200 mM for monovalent ions, 0.3-3 mM for divalent ions, and 0.003-0.1 mM for trivalent ions [96]. Flocculation values are affected by sol concentration, temperature, particle size of the colloid, and chemical nature of the sol.

2.3 Solvents

The solvent used in electrodeposition should dissolve both inorganic salts and polyelectrolytes. It can be either aqueous or non-aqueous (Table 2.1). ELD needs a sufficient amount of water for base generation in cathodic reactions. However, adsorbed water in green deposits leads to shrinkage and cracking during drying. Non-aqueous solvent have the advantage of avoiding the electrolysis of water, and thus avoiding the gas evolution which prevents forming a uniform adherent deposit. Mixed methyl alcohol-water and ethyl alcohol-water solution were found to be preferable in order to reduce cracking and porosity in the electrolytic deposits [78]. The addition of alcohols to aqueous solutions reduces the total dielectric constant of the solvent, and the thickness of the double layer decreases with decreasing dielectric constant of the solvent, and thus reduces the solubility of the deposits and promotes particle coagulation.

Solvents used in EPD should be inert with respect to the powder. Organic liquids are superior to water as a suspension medium for EPD. A variety of non-aqueous organic solvents (Table 2.1) are commonly used in ELD and EPD.

Table 2.1 Examples of solvents used for electrodeposition

Solvent	Method of deposition	Deposited material
Water	ELD	Al_2O_3-Cr_2O_3 [98], ZnO [99]
	EPD	Al_2O_3 [100]
Dimethylformamide	ELD	Y_2O_3 [101], TiO_2 [102]
Methyl alcohol-water	ELD	TiO_2, RuO_2- TiO_2 [103]
Ethyl alcohol-water	ELD	CeO_2 [104], SnO_2
	EPD	$CaSiO_3$[105]
Isoporpyl alcohol	EPD	Hydroxyapatite [106, 107]
Isoporpyl alcohol[a]	ELD	$YBa_2Cu_3O_{7-x}$ [108]
Ethyl alcohol-acetylacetone	EPD	MgO, Al_2O_3 [109]
Glacial acetic acid	EPD	PZT [110]
Ethyl alcohol	EPD	Al_2O_3, ZrO_2 [111]
Dichloromethane	EPD	β-alumina [112]
Acetone	EPD	YSZ [113]
Acetylacetone	EPD	YSZ [113]
Cyclohexanone	EPD	YSZ [113]
Methyl ethyl ketone	EPD	Al_2O_3 [114]
Toluene-ethyl alcohol	EPD	Al_2O_3 [114]

PZT, lead zirconate titanate; and YSZ, yttria-stabilized zirconia
[a]Solvent contained small amount of water

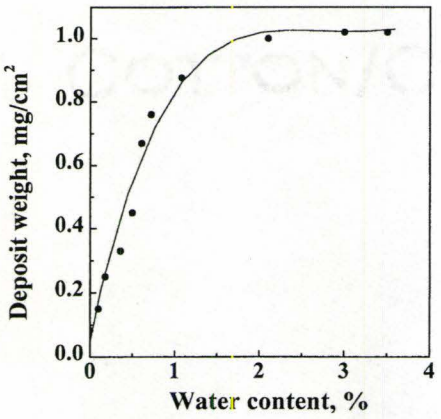

Figure 2.5 Deposit weight of ELD films versus water content in 0.005 M $ZrOCl_2$ solutions in mixed ethyl alcohol-water solvent, current density 5 mA/cm^2, deposition time 5 min.

Fig.2.5 shows the deposit weight for electrolytic zirconia films versus water content in mixed ethyl alcohol-water solvent. A sharp increase in deposit weight was observed when the water content increased up to 2 wt%. However, adsorbed water in green deposits leads to shrinkage and cracking during drying. Non-aqueous solvents prevent the deposit from hydrating. It is known that methanol is capable of extracting non-bridging hydroxo groups and free water [115]. Mixed methyl alcohol-water and ethyl alcohol-water solutions were found to be preferable in order to reduce cracking and porosity in the electrolytic deposits [103]. The addition of alcohols to aqueous solutions reduces the total dielectric constant of the solvent, and thus reduces the solubility of the deposits. It is in this regard that deposition experiments performed in mixed methyl alcohol-water solutions indicate a significant enhancement of the deposition rate [116]. Repulsion between colloidal particles formed near the electrode is related to the diffuse-layer charge on the particles. The thickness of the double layer decreases with decreasing dielectric constant of the solvent, promoting particle coagulation.

The charge on a colloidal particle could originate from solvents. Alcohols are known to behave as proton donors and are important for particle charging. A mixture of solvents may also be useful to achieve particle charging [109]. The addition of alcohols to aqueous suspensions of titania-containing electrolyte resulted in a shift of the isoelectric point (i.e.p.) towards higher pH values, or the absence of i.e.p. The experimental results [117] indicate that the dielectric constant of the mixed solvent could be the factor that governs the shift of i.e.p.

2.4 Electrophoretic mobility

Two different theories of electrophoresis were developed for rigid particles and for polyelectrolytes [118-121]. The theories of electrophoresis were applied for a single isolated particle and for colloidal particles in concentrated suspensions [118-123].

The velocity v of a particle in an electric field E is given by:

$$v = \mu E \tag{2.8}$$

where μ is the electrophoretic mobility. The electrophoretic mobility μ of a rigid colloidal particle can be derived from Biesheuvel's work [118].

$$\mu = \frac{2\varepsilon\varepsilon_0\zeta}{3\eta} f(\kappa a) \tag{2.9}$$

where ζ is the zeta potential and η is the viscosity of the liquid. The function $f(\kappa a)$ is 1 for $\kappa a \ll 1$ and 1.5 for $\kappa a \gg 1$. So, for particle radium a « 1/κ (Debye length), the electrophoretic mobility μ is given by Hückel formula:

$$\mu = \frac{2\varepsilon\varepsilon_0\zeta}{3\eta} \tag{2.10}$$

For a » 1/κ, the electrophoretic mobility μ is given by Smoluchowski equation:

$$\mu = \frac{\varepsilon\varepsilon_0\zeta}{\eta} \tag{2.11}$$

The electrophoretic mobility of a spherical polyelectrolyte, in which fixed charges are distributed at a uniform density ρ_{fix}, can be derived form the equation [120]:

$$\mu = \frac{\rho_{fix}}{\eta\lambda^2}\left[1+\frac{2}{3}\left(\frac{\lambda}{\kappa}\right)^2\frac{1+\frac{\lambda}{2\kappa}}{1+\frac{\lambda}{\kappa}}\right] \tag{2.12}$$

where $\lambda = (\gamma/\eta)^{1/2}$, and γ is the frictional coefficient of the polyelectrolyte.

In contrast to Eq 2.9 for the electrophoretic mobility of a rigid particle, Eq 2.12 does not include the ζ potential.

Ohshima [119-121] proposed a general electrophoresis theory for the electrophoresis of polyelectrolyte-coated spherical colloidal particles, which unites two different theories: the theory for rigid spheres and that for spherical polyelectrolytes. When a rigid particle is coated by a layer of polyelectrolyte of thickness *d*, the general mobility expression is given by:

$$\mu = \frac{\varepsilon\varepsilon_0}{\eta}\frac{\Psi_0/\kappa_m + \Psi_{DON}/\lambda}{1/\kappa_m + 1/\lambda}f\left(\frac{d}{a}\right) + \frac{\rho_{fix}}{\eta\lambda^2} \tag{2.13}$$

where Ψ_0 is the potential at the boundary between the polyelectrolyte and the surrounding solution, and Ψ_{DON} is the Donnan potential:

$$\Psi_0 = \Psi_{DON} + \frac{2n^\infty kT}{\rho_{fix}}\left\{1-\left[\left(\frac{\rho_{fix}}{2ze_0n^\infty}\right)^2+1\right]^{1/2}\right\} \tag{2.14}$$

$$\Psi_{DON} = \frac{kT}{ze_0} \ln\left\{ \frac{\rho_{fix}}{2ze_0 n^{\infty}} + \left[\left(\frac{\rho_{fix}}{2ze_0 n^{\infty}} \right)^2 + 1 \right]^{1/2} \right\} \tag{2.15}$$

where k is Boltzmann's constant, T is the absolute temperature, e_0 is the elementary electrical charge, and κ_m is the Debye-Hückel parameter of the polyelectrolyte layer:

$$\kappa_m = \kappa \left[1 + \left(\frac{\rho_{fix}}{2ze_0 n^{\infty}} \right)^2 \right]^{1/4} \tag{2.16}$$

$$f\left(\frac{d}{a}\right) = \frac{2}{3}\left[1 + \frac{1}{2(1+d/a)^3} \right] \tag{2.17}$$

The function f(d/a) tends to 1 as d/a $\rightarrow$ 0, whereas it becomes 2/3 as d/a $\rightarrow \infty$ [119]. In the limit a $\rightarrow$ 0, the particle becomes a spherical polyelectrolyte.

Theoretical studies have been carried out on electrophoresis in concentrated suspensions [122-124]. The effects of particle interactions and fluid motions associated with the individual particles were addressed. It was demonstrated that in the limit of thin double layers around the particles (κa » 1), the electrophoretic mobility is described by the Smoluchowski formula. However, as the double layer thickness increases, the electrophoretic mobility decreases sharply and becomes strongly dependent on the particle volume fraction φ. The electrophoretic mobility decreases with increasing φ by overlapping of the electrical double layers around the particles. A general theory has recently been developed for the electrophoretic mobility of soft particles in concentrated suspensions [122, 123]. It was established that the φ dependence of the electrophoretic

mobility is negligible for d << a, whereas for d >> a, the mobility strongly decreases with increasing φ.

2.5 Cathodic reactions

Various cathodic reactions could result in a local pH increase at the cathode surface [78, 125-132]. Chemical reactions which consume H^+ are discussed in [126, 127]. These reactions bring about a small increase in pH at the electrode surface [126, 127]:

$$H^+ + e^- \rightarrow H_{ad} \text{ or } H_{abs} \quad (2.18)$$

$$2H^+ + 2e^- \rightarrow H_2 \quad (2.19)$$

$$NO_3^- + 2H^+ + 2e^- \rightarrow NO_2^- + H_2O \quad (2.20)$$

$$NO_3^- + 10H^+ + 8e^- \rightarrow NH_4^+ + 3H_2O \quad (2.21)$$

Cathodic reactions [78, 125, 130] that generate OH^- include the reduction of water, dissolved oxygen, nitrate and perchlorate ions:

$$2H_2O + 2e^- \rightarrow H_2 + 2OH^- \quad (2.22)$$

$$O_2 + 2H_2O + 4e- \rightarrow 4OH^- \quad (2.23)$$

$$NO_3^- + H_2O + 2e^- \rightarrow NO_2^- + 2OH^- \quad (2.24)$$

$$NO_3^- + 7H_2O + 8e^- \rightarrow NH_4^+ + 10OH^- \quad (2.25)$$

$$ClO_4^- + H_2O + 2e^- \rightarrow ClO_3^- + 2OH^- \quad (2.26)$$

$$ClO_4^- + 4H_2O + 8e^- \rightarrow Cl^- + 8OH^- \quad (2.27)$$

These reactions consume H_2O to produce OH^- ions, resulting in an appreciable pH increase near the cathode surface.

Lee and Crayston [129] utilized superoxide O_2^- and tertiary alcohols to generate OH^- ions. Oxygen undergoes reduction:

$$O_2 + 2e^- \rightarrow O_2^- \quad (2.28)$$

Then superoxide reacts with water to give OH^- ions:

$$2O_2^- + H_2O \rightarrow O_2 + HO_2^- + OH^- \quad (2.29)$$

The reduction of tertiary alcohols [129] generates OH^- via the following reaction:

$$ROH + 2e^- \rightarrow R^- + OH^- \quad (2.30)$$

In methyl alcohol solutions the following reactions were considered:

$$2H^+ + 2CH_3OH + 2e^- \rightarrow 2H_2O + C_2H_6 \quad (2.31)$$

$$2CH_3OH + 2e^- \rightarrow 2OH^- + C_2H_6 \quad (2.32)$$

The reduction of H_2O_2 produces OH^- ions via the following reaction [133]:

$$H_2O_2 + 2e^- \rightarrow 2OH^- \quad (2.33)$$

The difference between the solution pH and that in the layer adjacent to the electrode increases with increasing current density and decreases with increasing temperature [134, 135]. Near-electrode pH data (reference) obtained at various current densities [135] indicate that the rate of pH change accelerates in the range 1-10 mA/cm^2. Stirring of solutions was found to delay the onset of alkali formation at the cathode surface. In cathodic ELD, the bulk pH is acidic, whereas the surface pH was reported to be up to 11-12 [134, 135]. The high pH could be constant over the first 100-200 μm from the cathode surface [134, 135].

2.6 Electrolytic deposition of materials

2.6.1 Electrosynthesis and coagulation of particles

The particle formation kinetics and deposit composition are influenced by solvent, additives, temperature and current density [78, 79, 136-152]. In the cathodic electrolytic deposition process, the cathodic reactions in Eqs. (2.18-33) result in a significant increase in pH value near the cathode. The hydrolysis of water and some other cathodic reactions (Eqs. (2.22-27)), which consume water and produce OH^-, result in significant increase in pH value near the cathode [126-128, 130-132].Various cationic species could be hydrolyzed to form colloidal particles of oxides, hydroxides or peroxides by electrogenerated base near the cathode [137, 139, 147]. It was shown that electrosynthesis is similar to the wet chemical method of powder processing that makes use of electrogenerated base instead of alkali [79]. Hydrolysis reactions result in the accumulation of colloidal particles near the electrode.

The coagulation of colloidal particles on the cathode can be explained by DLVO theory of colloidal stability [79]. DLVO theory explains the existence of a critical electrolyte concentration (flocculation value) for coagulation of colloidal particles, below which the suspension is stable and above which it is kinetically unstable. The flocculation value decreases with the valence of the electrolyte ions of a charge opposite to that of the colloidal particles (rule of Schulze and Hardey). The flocculation of colloidal particles near the cathode, which results in the deposit formation, could be enhanced by the electric field, electrohydrodynamic flows, and pressure from the new formation particles [79].

2.6.2 Co-deposition of materials

Co-deposition of various cationic species has been the subject of intense research activity [136, 146, 153, 154]. The use of peroxoprecursors was found to improve co-deposition of some species, and complex oxide compounds were deposited [147, 149, 151, 152]. The method of electrodeposition of RuO_2-TiO_2 films is based on the independent deposition of Ru and Ti species using different precursors. P and Si species cannot be deposited alone from aqueous solutions, but readily co-deposit with Ca species [79, 136, 146]. Various chemical reactions are discussed in [136, 146]:

$$10Ca^{2+} + 6PO_4^{3-} + 2OH^- \rightarrow Ca_{10}(PO_4)_6(OH)_2 \quad (2.34)$$

$$3Ca^{2+} + 2HPO_4^{2-} + 2OH^- \rightarrow Ca_3(PO_4)_2 + 2H_2O \quad (2.35)$$

P species could also co-deposit with Mg species:

$$3Mg^{2+} + 2HPO_4^{2-} + 2OH^- \rightarrow Mg_3(PO_4)_2 + 2H_2O \quad (2.36)$$

The effect of lanthanide ions on the electrodeposition of cobalt oxyhydroxide and manganese oxide was investigated by Matsumoto et al [141]. It was established that the lanthanide ions suppress the electrodeposition of these compounds.

2.7 Electrophoretic deposition of materials

2.7.1 Mechanisms of deposit formation

The mechanisms of EPD have been discussed in numerous publications [73-75, 77, 155-164]. One hypothesis is that charged particles undergo reactions at the electrode, which neutralize them. However, deposit formation was observed on a porous diaphragm

[156] and a dialysis membrane [75] placed between the electrodes. According to [74, 75] , particle/electrode reactions are not involved in EPD and ceramic particles do not immediately lose their charge on being deposited. It was observed that reversal of the electric field strips off the deposited layer [74]. However, alumina particles were deposited using alternating current at frequency of 10 kHz [100]. An electrode reaction model for the deposition of oxide particles was developed by Koura et al.[165]. The experimental data presented by Zhang and Lee [166] indicate that ceramic particles act as the charge carrier and promote the circulation of electric current in suspensions.

According to Hamaker and Verwey [158], the formation of a deposit by electrophoresis is similar to formation of the sediment due to gravitation. It was supposed that applied electric field exerts sufficient force to overcome particle mutual repulsion. The field strength (E) required to supply this force (F) was found to be [156, 167]:

$$E = 2F / 3\varepsilon\xi a \qquad (2.37)$$

Calculated values of the field strength are in agreement with the values observed for some materials [156]. Verwey and Overbeek [167] pointed out that the applied electric field strength in EPD is generally too low to overcome particle mutual repulsion, but great enough to bring about the high particle concentration near the electrode. The electrical resistance of this layer is very high, and as a result the voltage drop and electric field in the layer are also very high. The critical field strength could be achieved in concentrated suspension near the electrode surface [167]. However, the accumulation theory [162] cannot explain the deposition of monolayers [168, 169] or electrophoretic seeding of diamond particles [170].

Koelmans and Overbeek proposed an electrochemical mechanism of deposit formation [162]. Deposit formation is caused by flocculation introduced by the electrolyte formed by the electrode reaction Eq. (2.32). The critical time t* in the flocculation theory [162] could be interpreted as the time required to build up a critical electrolyte concentration. The following relation was proposed:

$$t^*=qV^2\sigma^{-2} \qquad (2.38)$$

where q is a coefficient, V is the voltage applied, and σ is the specific conductance of the suspension.

In several experiments [156, 171-177] EPD of ceramic particles was performed in the presence of electrolytes and polyelectrolytes. These additives are adsorbed on the particles to create positive charges and stabilize the suspensions. The additives are also important for the deposition of uniform and adherent deposits. EPD of ceramic particles could be associated with electrolytic deposition of hydroxides or alkoxides, which form an adhesive matrix [156, 177]. The adhesive materials promote particle coagulation and bind the particles to the substrate. Therefore, the binder materials may enhance the effect of the van der Waals' force. The water content and electrolyte concentration in the bath are very important for the deposition process. It was supposed [159] that reduction of water Eq. (2.22) generates OH^-, resulting in a pH increase near the cathode substrate. It is important to note that electrode blocking by the deposited particles could also result in an additional pH increase in the vicinity of the cathode [178]. When the water content of the suspension is very low (< 1%), the alkoxide is formed, which is converted to the hydroxide at higher water concentrations [156, 177]. Excess water, above ~10 wt.%, was

detrimental because it resulted in excess hydrogen evolution and high bath conductivity. However, experiments with a porous diaphragm [156] and a dialysis membrane [75] placed between the electrodes indicate that electrode reactions are not essential for EPD.

An electrocoagulatory mechanism of deposit formation is based on a polarization attraction of particles to the electrode [134]. Sarkar and Nicholson [75] developed a mechanism of deposition based on double-layer distortion on application of an electric field. They suggested that the double layer becomes thinner ahead of the particle, thus facilitating particle coagulation. Further investigations by De and Nicholson showed that this mechanism is not correct [179]. They proposed a mechanism [179] based on a local pH increase near the cathode surface.

2.7.2 Contributions of different mechanisms

Understanding of the EPD mechanisms is crucial to the development of advanced coatings. It is important to discuss the contributions of the proposed mechanisms at different stages of electrophoretic deposition. Interparticle forces, electrode reactions, solvents and additives influence all stages of the deposition process. The ability to deposit monolayers or separate particles suggests that particle electrode interactions could result in deposit formation. It is in this regard that deposition of ceramic particles could be achieved under open circuit conditions. Electrostatic attraction has been used to deposit alumina and mullite coatings [180]. It is supposed that the mechanism of seeding of diamond particles cathodic substrates [170] is related to the discharge of the H^+ ions [165] adsorbed on the particles. These ions were created in a keto-enol reaction [165]. However, electrophoretic diamond seeding could also be performed on anodic substrates

[181, 182]. Diamond particles spontaneously acquire a negative surface charge in water and some organic solvents [181, 182]. Valdes et al. [182] considered electrophoretic diamond seeding as a combination of electrophoretic transport and electrochemisorption of diamond particles. It was shown that the diamond particles deposited by the sedimentation process cluster together and are non-adherent to the substrate [181]. In contrast, electrophoretic seeding resulted in adherent and non-agglomerated particles. Turning again to [134] and [183], it should be noted that deposition of individual particles could be achieved via polarization attraction of the particles to the electrode.

Grillon et al. [184] supposed that when a particle comes into contact with the substrate or an already deposited particle, it can no longer move, due to electrical neutrality. It was concluded [184] that local electric fields prevent the formation of a continuous layer, resulting in porous deposits. However, particle motion parallel to the electrode surface was reported in [183, 185-187]. Moreover, continuous 2-D layers of colloidal particles were formed [169, 183, 185-187]. Van der Waals' force [167, 188] and long-range attraction forces [183, 185-187, 189-191] discussed above could result in particle coagulation and the formation of 2-D layers.

Electrophoretic motion of ceramic particles results in accumulation of the particles at the electrode. According to [134, 156-159, 162, 167, 171, 172, 188], three basic mechanisms of particle coagulation in the formation of electrophoretic deposits can be distinguished: electrocoagulation, accumulation and electrochemical coagulation. Electrohydrodynamic flows [186], arising from electrode reactions, geometrical confinement effect [191, 192], capillary interactions [193], long-range attraction forces

and other interactions [134, 185, 189-192, 194-208] discussed above influence the particle coagulation.

Colloidal stability could be influenced by non-uniformity of the zeta potential on colloidal particles [209]. It is reasonable to expect that when ceramic particles come into contact with particles already deposited, the local lyosphere distortion and thinning mechanism proposed by Sarkar and Nicholson [75] could contribute to particle coagulation. Another important phenomenon to be considered in connection with the alternative mechanism proposed by De and Nicholson [179] is a local pH increase near the cathode surface. As stated above, various chemical reactions Eqs. (2.18-33). could result in a local pH increase. The reactions could result in a moderate pH increase in non-aqueous solutions, whereas water-consuming reactions Eqs. (2.22-27) result in an appreciable pH increase near the cathode surface.

In the mechanism proposed in [179], the discharge-depletion of H^+ in ethyl alcohol solvent induces the suspension pH to increase towards the isoelectric point of Al_2O_3 and facilitates particle coagulation. However, as pointed out in [79], charge reversal can be expected at higher pH, and colloidal particles can be peptized by OH^-. It is in this regard that EPD of ceramic particles in aqueous suspensions was performed mainly on anodic substrates [76]. As pointed out above, adding cationic polyelectrolytes could result in a considerable shift of the particle isoelectric point. PEI is a cationic polyelectrolyte. However, in the region pH > 11, PEI carries no charge, promoting particle coagulation. Cathodic deposits could be prepared from aqueous suspensions containing PEI additive [77].

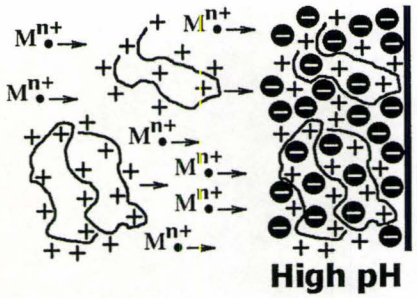

(a)

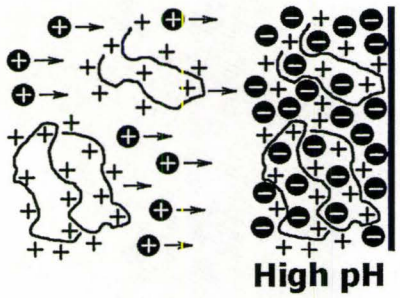

(b)

Figure 2.6 Formation of organoceramic deposits using (a) ELD and (b) EPD of ceramic particles

2.8 Electrodeposition of organoceramic materials

2.8.1 Method based on ELD of ceramic particles and EPD of polyelectrolytes

The feasibility of cathodic electrodeposition of organoceramic materials based on oxides or hydroxides and charged polymers (PDDA, PEI) has recently been demonstrated [77]. The method developed in [77] is based on EPD of polymers and ELD of ceramic materials Fig. 2.6a. Various organoceramic films based on PDDA were studied [210-214]. Electrodeposition was performed from solutions of metal salts containing PDDA.

PDDA is a cationic polyelectrolyte (Fig. 2.3). The electrophoretic mobility of polyelectrolytes is given by Eq. 2.12. PDDA maintains a positive charge under basic

conditions. However, no electrophoretic deposition of PDDA films was achieved from aqueous PDDA solutions. It is important to note that electrophoresis is related to the motion of charged particles towards the electrode, but it is not responsible for the interfacial phenomena related to deposit formation. Cathodic deposits were obtained after addition of chloride or nitrate salts of Zr, Ce, Gd, Y, Fe, Ni, Cu, Co and La to PDDA solutions. Deposit weight increased with increasing salt concentration at a constant level of PDDA, as shown in Fig. 2.7. The pH in the bulk solution was low, whereas cathodic reactions resulted in a significant increase in pH value near the cathode [210-214]. Therefore, colloidal particles formed near the electrode were negatively charged. In this case, film formation was achieved via heterocoagulation of oppositely charged PDDA and colloidal particles of oxides or hydroxides formed near the cathode Fig. 2.6a. However, as pointed out in [210-214], the attraction of polyelectrolytes and colloidal particles could be electrostatic or non-electrostatic. This interaction is a complicated phenomenon, influenced by the pH, ionic strength and electric field.

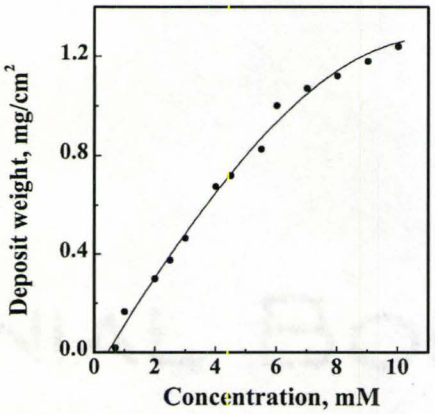

Figure 2.7 Deposit weight versus $ZrOCl_2$ concentration in aqueous solutions containing 1g/l PDDA, current density 10 mA/cm^2, deposition time 6 min

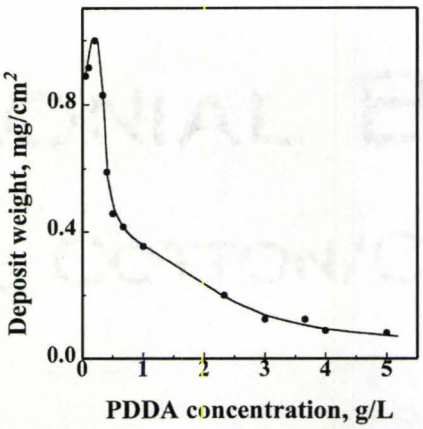

Figure 2.8 Deposit weight versus PDDA concentration in aqueous 0.005 M $ZrOCl_2$ solutions, current density 5 mA/cm^2, deposition time 10 min

The amount of organic phase in the deposits was evaluated from the results of thermogravimetric analysis [211, 212]. An important finding was that deposit composition could be controlled by varying PDDA concentration in solutions. The amount of the organic phase in zirconia-PDDA deposits was found to be in the range 0-70 wt.%. The deposit weight was also traced as a function of PDDA concentration at constant concentrations of metal salts [211, 213]. The deposit weight increased with PDDA concentration (C_{PDDA}) .to a maximum [211, 213] at low C_{PDDA}, as shown in Fig. 2.8. It was suggested that PDDA serves as an electrolyte in compressing the double layer of ceramic particles formed near the electrode, resulting in particle flocculation and increasing the deposition process efficiency. Moreover, PDDA acts as a binder, providing better adhesion of the deposits. At PDDA concentrations beyond the maximum, the deposit weight dropped off continuously. It was suggested that when C_{PDDA} increases, PDDA particles accumulated near the electrode provide a shielding effect, preventing the formation of colloidal particles of metal hydroxides. As a result, the deposition efficiency

of both organic and inorganic phases decreased. It should be noted again that no deposit formation was observed from pure aqueous PDDA solutions. The deposit weight of organoceramic deposits could be controlled by variation of the deposition time Fig. 2.9.

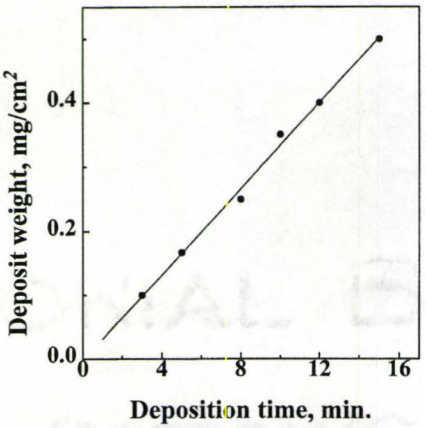

Figure 2.9 Deposit weight versus deposition time for 0.005 M $ZrOCl_2$ + 1 g/l PDDA solutions at current density of 5 mA/cm^2

Fig.2.10 shows cross-sections of organoceramic deposits on graphite substrates. The feasibility of electrochemical intercalation of charged polymers into electrolytic deposits is of significant importance for the further development of electrolytic deposition of ceramic materials. The critical thickness of ELD deposits achievable without crack formation could be increased up to 1-2μm using PDDA with inherent binding properties. Small additives of PDDA act as a binder, preventing cracking and increasing adhesion of the deposit. At higher concentrations of PDDA, organoceramic deposits can be obtained [211].

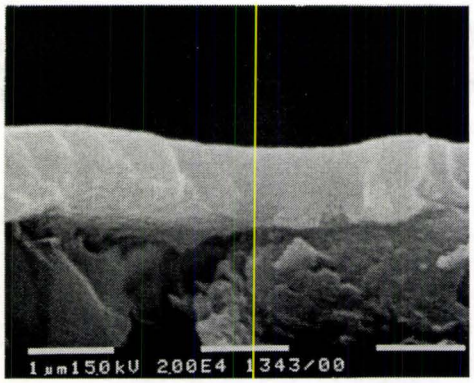

(a)

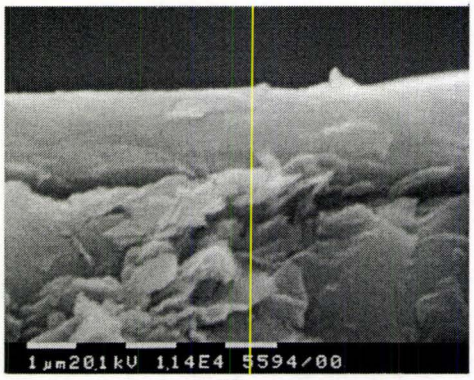

(b)

Figure 2.10 SEM pictures of organoceramic films on graphite substrates prepared from: (a) 0.005 M $ZrOCl_2$ + 1g/l PDDA; and (b) 0.01 M $CeCl_3$ + 1g/l PDDA solutions.

2.8.2 Method based on EPD of ceramic particles and polyelectrolytes

Another method of electrodeposition of organoceramic films is based on EPD of ceramic particles and EPD of polyelectrolytes. Ceramic particles may become positively or negatively charged, depending on the pH. The pH of the suspension should be lower than the isoelectric point of the oxides. In this case, the particles are positively charged and the electric field provides their motion towards the cathodic substrate. However, a charge reversal is expected at high pH near the cathodic substrate. The negatively charged

oxide particles compensate positive charges of polyelectrolytes near the electrode (Fig. 2.6b).

2.8.3 Other electrochemical strategies

There are other electrochemical strategies for cathodic electrodeposition of organoceramic materials based on ELD and EPD of ceramic materials. Electrophoretic deposition of ceramic particles together with adsorbed neutral or charged polymers could result in deposits comprising the two types of materials [77, 174, 215, 216]. PVA is a neutral polymer. Cathodic electrodeposition of PVA films was performed from aqueous PVA solutions containing small additives of boric acid or borax [213]. The method used for PVA deposition is based on a local pH increase and formation of borate ions $B(OH)_4^-$ near cathode, followed by crosslinking of PVA molecules by the borate ions and PVA gelling. Electrode reactions are not directly involved in deposit formation and electrochemical deposition of PVA is not a Faradic process. However, experimental data presented in [213] indicate that deposit weight increases proportionally with deposition time. Moreover, higher deposit weights were obtained for PVA-boric acid solutions at higher current density. It is suggested that the deposition efficiency is dependent on pH, which in turn depends on the rate of base generation in cathodic reactions. SEM observations indicate that uniform and adherent deposits were obtained [213]. EPD and ELD were used for intercalation of ceramic particles into growing polymer films to form organoceramic deposits.

RESEARCH OBJECTIVES

The current work was dedicated to the synthesis and characterization of superparamagnetic organic-inorganic nanocomposites with the focus on advanced magnetic oxides with spinel structures, such as γ-Fe_2O_3, Mn_3O_4 and $NiFe_2O_4$. The broad aim of this work was to develop new electrochemical methods to fabricate superparamagnetic organic-inorganic nanocomposites and to understand the correlation between their structure and the functional properties.

The research was focused on three specific areas. The first goal was to develop novel electrodeposition methods for the fabrication of nanocomposite materials and to understand the effect of strong and weak polyelectrolytes and polymer-metal ion complexes on the deposition mechanisms and material structures of fabricated films. The second goal was to study the structural properties of the deposited film, especially the particle size distribution and the crystal structure of the nanoparticles, and to understand how to tailor these properties by changing electrodeposition conditions and annealing temperature. The third goal was to investigate the relationship between the structural properties of the deposited films and their magnetic properties.

These research objectives were achieved by means of experimental approaches using range of techniques for characterization of structure and properties of materials combined with theoretical efforts using existing models.

CHAPTER 3

EXPERIMENTAL PROCEDURES

As it was stated in the Chapter One and Chapter Two, the current work involved electrochemical fabrication of nanocomposites and characterization of their properties by various techniques. The objective of this chapter is to describe the conditions under which the work has been done.

Electrochemical Deposition

Commercial purity metal chlorides: such as $FeCl_3 \cdot 6H_2O$ (Aldrich), $NiCl_2 \cdot 6H_2O$ (Alfa Aesar), and $MnCl_2 \cdot 4H_2O$ (Aldrich), and commercially available cationic polyelectrolytes: such as polyethylenimine (PEI) (80% ethoxylated, M_W 70,000, Aldrich), poly(allylamine hydrochloride) (PAH) (M_W 70,000, Aldrich), chitosan (Mw 200,000, Aldrich), poly(diallyldimethylammonium chloride) (PDDA) (M_W 400,000-500,000, Aldrich) and poly(4-vinyl-pyridine) (P4VPy) (M_W 60,000, Aldrich) were used as starting materials for the solutions. The metal chlorides and polyelectrolytes were dissolved in the ethanol-water solvent, in which the electrodeposition was conducted. The starting electrochemical solutions in Table 3.1 show different combinations of metal chlorides and polyelectrolytes used to produce various inorganic-organic nanocomposite films.

Table 3.1 Composition of the electrochemical solutions

Polyelectrolytes (g/l)		Ethanol-water (Volume ratio)	$FeCl_3$ (mM)	$MnCl_2$ (mM)	$NiCl_2$ (mM)	Appeared in the thesis
PAH	0-0.5	70:30	5			4.1.1
	0.5-1.0	70:30		5		4.1.2
PEI	0.5-2.0	90:10		5		4.2.1
	0.4	95 (methanol):5	5		2.5	4.2.2
	1.0	95 (methanol):5	5	2.5		4.2.3
Chitosan*	0.2-0.3	70:30	5			4.3.1
	0.2	70:30		5		4.3.2
PDDA	0.1-0.3	70:30	5			4.4.1
P4Vpy	0.5	70:30	5			4.4.2

*Chitosan with a degree of deacetylation of about 85% was dissolved in 1% acetic acid water to get a 0.6 wt% solution and then used for the electrochemical solution.

The electrochemical cell for deposition included a cathodic substrate centered between two parallel platinum counter-electrodes. The nanocomposite films were deposited on Pt foils (50mm × 50mm × 0.1mm), graphite plates (50mm × 6mm × 1mm), or carbon fiber felt (Lydall) (50mm × 30mm × 0.5mm) cathodes by a galvanostatic method at a current density range of 1-5 mA/cm^2. The current efficiency during the electrodeposition could not be determined because the process is non-faradaic. To maintain a thin layer of base environment near the cathode, the solutions can not be

stirred during electrodeposition of the film. The deposition time was varied in the range 0.5- 5 min.

Electrodeposition of inorganic oxide nanoparticles was achieved by cathodic electrolytic deposition (ELD). In this method, metal ions or complexes were hydrolyzed by an electrogenerated base to form oxide or hydroxide deposits on cathodic substrates. Hydroxide precursors can be converted to the corresponding oxides by heat treatment. The current work has been focused on the spinel-structured simple transition metal oxides, i.e., Fe_3O_4, γ-Fe_2O_3 and Mn_3O_4, and complex metal oxides, such as NiO/Fe_2O_3 ($NiFe_2O_4$) and MnO/Fe_2O_3 ($MnFe_2O_4$).

Electrodeposition of polyelectrolytes was achieved by electrophoretic deposition (EPD), in which charged polyelectrolytes, dissolved in a liquid medium, migrate in an electric field and deposit on the electrode.

Combined methods, which were based on the EPD of polyelectrolytes or polymer–metal ion complexes and cathodic electrosynthesis of inorganic materials, were used to obtain the inorganic nanoparticles *in situ* in the polyelectrolyte matrix. This method prevents agglomeration of nanoparticles, and enables preparation of thick oxide films and organic-inorganic nanocomposites. Cathodic deposits of various thicknesses in the range of up to several microns were obtained on Pt and graphite substrates.

The films obtained were studied subsequently by various experimental techniques. The crystal structures of the nanocomposite films were characterized by the techniques such as X-ray diffraction analysis (XRD), thermogravimetric and differential thermal analysis (TG-DTA), scanning electron microscope (SEM), high resolution transmission

electron microscopy (HRTEM), and atomic force microscopy (AFM). The magnetic properties of the nanocomposite films were characterized by Quantum Design® PPMS-9T (Physical Properties Measurement System 9 Tesla). AC susceptibility, hysteresis loops, and DC magnetization utilizing zero-field-cooling (ZFC) and field-cooling (FC) procedures were measured. The following chapter, Experimental Results, is organized in such a way that it includes structural and magnetic characterization of the nanocomposite films.

X-ray Diffraction

The crystal structure of an inorganic phase was determined by X-ray diffraction on a Nicolet 12 automated diffractometer using monochromatized Cu Kα radiation at a scanning speed of 0.5 °/min.

TG-DTA

The decomposition, crystallization, and reaction of organic and inorganic phases in the composite films were studied by thermogravimetric and differential thermal analysis (TG-DTA). The thermoanalyzer (Netzsch STA-409) was operated in air between room temperature and 1200 °C at a heating rate of 5 °C/min.

Electron Microscopy

A Field Emission Gun Scanning Electron Microscope (SEM) JEOL JSM-7000F was used to study the film morphology.

The JEOL JSM-7000F is equipped with a Schottky type Field Emission Gun (FEG) filament which offers high resolution (1.2 nm @ 30 keV and 3.0 nm @ 1 keV) and large probe currents at small probe diameter to meet the needs for the characterisation of nano-

structures. A multi-purpose specimen chamber, motorized specimen stage, one-action specimen exchange and an ideal geometry for techniques such as EDS, EBSD and e-beam lithography are also features of this instrument.

Cross-sections of the nanocomposite films were prepared. First, the film was deposited onto a mechanically polished graphite substrate (50mm×6mm×1mm). Then, the deposited substrate was quenched in liquid nitrogen for 30 seconds. Finally, its edge was cut and the crack propagated gently by a blade. By the quenching process, a clean and straight cross section could be obtained.

A Field Emission Gun Scanning Transmission Electron Microscope (STEM) JOEL 2010F was used to obtain atomic resolution images and particle morphology. The JOEL 2010F was operated at acceleration voltage 120 keV or 200 keV.

The TEM samples were deposited directly on the carbon fibre felt substrate made of 6 μm carbon fibre. A 3 mm diameter specimen was punched afterwards from the deposited carbon fibre felt by a puncher. Deposited films were well attached to the carbon fibres and were used in TEM studies without further processing.

Atomic Force Microscopy

Atomic Force Microscopy (AFM) was used to characterize the surface roughness of fresh deposit films. Description of the techniques can be found in the other literature [217, 218], and thus, only the basic principles are summarized here.

The AFM consists of a microscale cantilever with a sharp tip at its end that is used to scan the specimen surface. The cantilever is typically Si or Si_3N_4 with a tip radius of curvature of the order of nanometers. When the tip is brought into proximity of a sample

surface, forces between the tip and the sample lead to a deflection of the cantilever (mechanical contact force, Van der Waals forces, capillary forces, chemical bonding, electrostatic forces, magnetic forces), which is measured usually by a laser. The AFM can be operated in a number of modes, depending on the application, and in the present study, the AFM was operated in taping mode, which means the tip oscillates in the vertical direction.

Care has to been taken in the sample preparation. The film was electrodeposited on a mechanically polished stainless steel substrate at a current density 2 mA/cm^2. Higher current densities are not favorable because they may induce strong gas evolution and non-uniform deposition on the substrate. A 3 mm diameter specimen was subsequently punched from the substrate by a puncher.

Magnetic Measurements

Magnetic properties were measured by a Quantum Design® PPMS-9T within temperature range from 1.8 K to 400 K.

DC magnetiation measurements were performed using the extraction magnetometer option. Zero-field-cooled (ZFC) and field-cooled (FC) magnetization measurements were carried out in the following way. The sample was demagnetized at 300 K, then cooled to 2 K in zero external field and after the temperature of the sample reached 2 K the field was turned on. The magnetization was measured in the applied field during heating the sample to 300 K. Subsequently, the sample was cooled in the magnetic field down to 2 K and the magnetization was measured during cooling. The divergence of FC and ZFC

curves allowed us to study the blocking temperature and its dependence upon the applied field. The applied field used in this work was either 200 Oe, or 500 Oe.

AC susceptibility [219] measurements were carried out by applying AC magnetic field with the amplitude 5 Oe and the frequency in the range 10-10,000 Hz. The temperature of the sample was scanned from 2 K to 300 K and the measurements were carried out every 1 K between 2 K-50 K and every 5 K between 50 K and 300 K. AC magnetic susceptibility χ, is a complex property which includes an in-phase real component χ' and an out-of-phase imaginary component χ". These components were evaluated automatically by the system at each measurement point. In this way, the dynamic properties, such as temperature dependence of the relaxation time τ could be determined. The results provided an insight into the relaxation processes of magnetic nanoparticles.

Magnetic hysteresis loops were measured in a sweep mode in a temperature range from 2 K to 298 K. The external field sweep rate was 10 Oe/sec in 1 T range, or 100 Oe/sec in 9 T range. This data was used to evaluate coercive force, remanence magnetization and saturation magnetization of the materials.

CHAPTER 4

EXPERIMENTAL RESULTS

This chapter presents all the experimental results obtained in the current work. The results were categorized into four sections by focusing on different polyelectrolytes, such as PAH, PEI, Chitosan, and other strong and weak polyelectrolytes. Each section was further divided into some subsections that described the specific simple oxides, such as γ-Fe_2O_3, and Mn_3O_4, or complex oxides, such as NiO/Fe_2O_3 ($NiFe_2O_4$), and MnO/Fe_2O_3 ($MnFe_2O_4$). The results were focused on two main aspects: structural characterization and magnetic properties.

4.1 Nanocomposites based on PAH

4.1.1 Electrodeposition of γ-Fe_2O_3 using PAH

The detailed description of electrodeposition of γ-Fe_2O_3 using PAH was published by the present author in the journal *Materials Chemistry and Physics, 96 (2006) 289–295,* entitled "Electrodeposition of composite iron oxide – poly(allylamine hydrochloride) films"

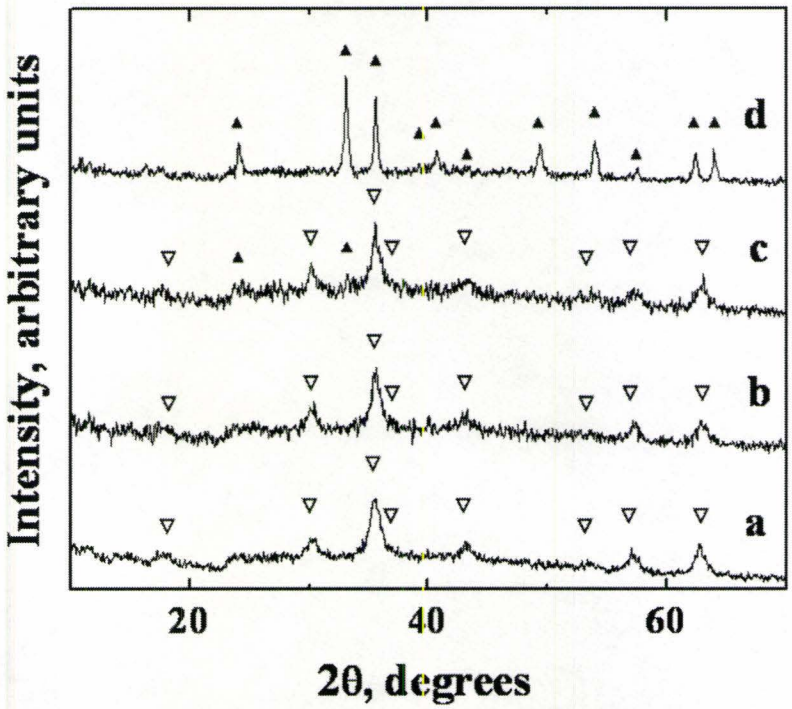

Figure 4.1 X-ray diffraction patterns of the deposits prepared from 5 mM $FeCl_3$ solutions: (a) as prepared and after annealing at (b)200, (c) 400 and (d)500 °C. ∇ - γ-Fe_2O_3 (JCPDS file 39-1346), ▲ - α-Fe_2O_3 (JCPDS file 33-664).

The deposits were analyzed by XRD before and after annealing in the air at different temperatures. Fig.4.1 shows X-ray diffraction patterns of the deposits prepared from pure $FeCl_3$ solutions. The fresh deposits and those annealed at 200 °C exhibited peaks, which can be attributed to γ-Fe_2O_3 or Fe_3O_4. However, it is difficult to distinguish between γ-Fe_2O_3 and Fe_3O_4 due to the similar spinel structure of the both phases and peak broadening attributed to small particle size. Moreover, the two phases can form solid solutions. Small peaks of α- Fe_2O_3 appeared on the X-ray diffraction patterns at 400 °C in

addition to the peaks of the spinel phase. After annealing at 500 °C the X-ray diffraction pattern showed peaks of α- Fe_2O_3.

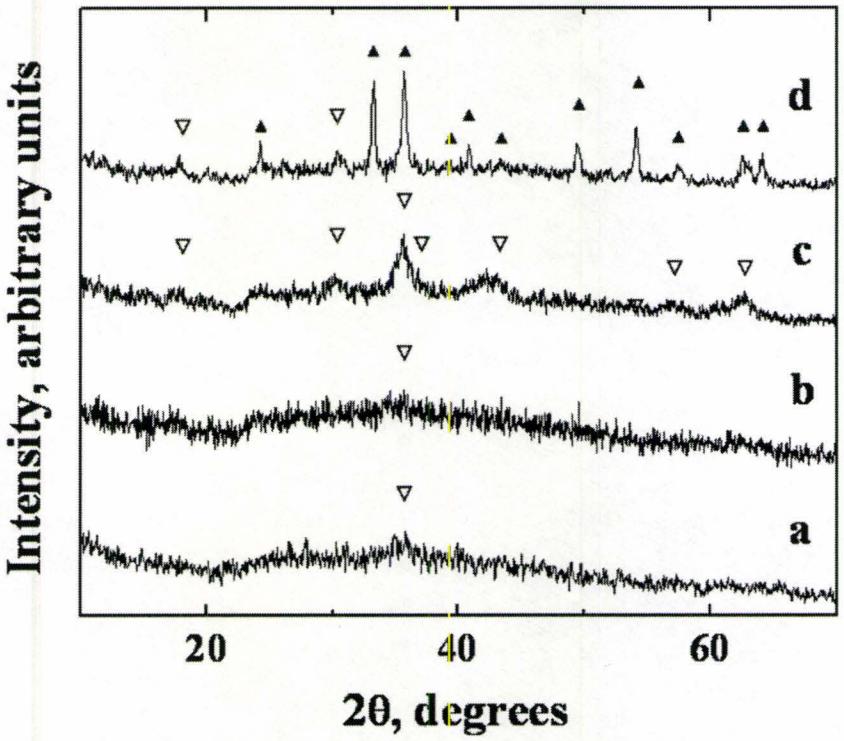

Figure 4.2 X-ray diffraction patterns of the deposits prepared from 5 mM $FeCl_3$ solutions containing 0.5 g/l PAH: (a) as prepared and those annealed at (b) 200, (c) 300 and (d) 400 °C. ∇ - γ-Fe_2O_3 (JCPDS 39-1346), ▲ α-Fe_2O_3 (JCPDS 33-664)

Fig.4.2 shows X-ray diffraction patterns of the deposits prepared from 5mM $FeCl_3$ solutions containing 0.5 g/l PAH. The fresh deposits and those annealed at 200 °C showed a small peak around 2Θ = 36°. At 300 °C peaks of spinel iron oxide phase were observed. The XRD pattern of the sample annealed at 400 °C exhibited small peaks of the spinel phase in addition to the major peaks of α- Fe_2O_3.

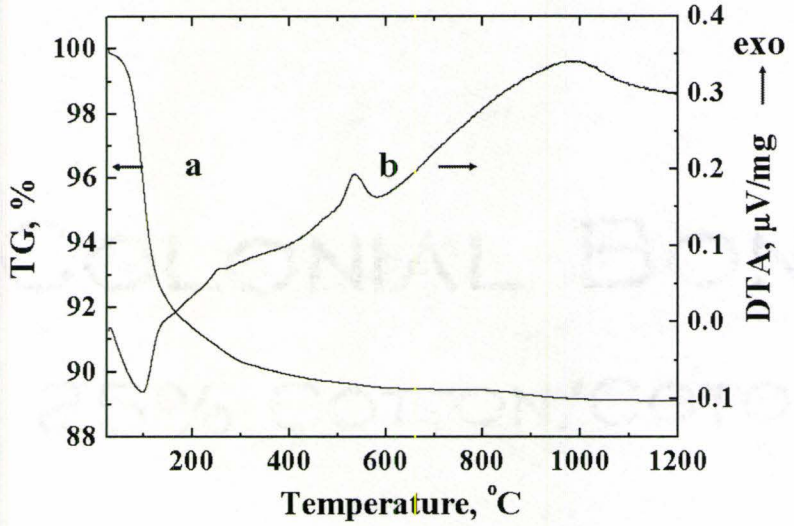

Figure 4.3 TG (a) and DTA (b) data for the deposits prepared from 5 mM $FeCl_3$ solutions.

Fig.4.3 shows the TG and DTA data for the deposits prepared from the $FeCl_3$ solutions without PAH. A sharp reduction of sample weight was recorded below 150 °C, followed by a more gradual weight change. No appreciable weight loss was observed at temperatures exceeding 400 °C. The total weight loss at 1200 °C was found to be 10.9 wt%. The observed weight loss can be attributed to the liberation of the adsorbed water. On the basis of the TG data it can be suggested that the deposition process results in the formation of γ-Fe_2O_3. Weight gain, which can be attributed to the $Fe_3O_4 \rightarrow \alpha$-$Fe_2O_3$ transformation, was not recorded.

DTA data showed a broad endotherm at ~ 100 °C and an exotherm around 550 °C. The observed endotherm is associated with weight loss. The exotherm can be attributed to the γ-$Fe_2O_3 \rightarrow \alpha$-$Fe_2O_3$ transformation.

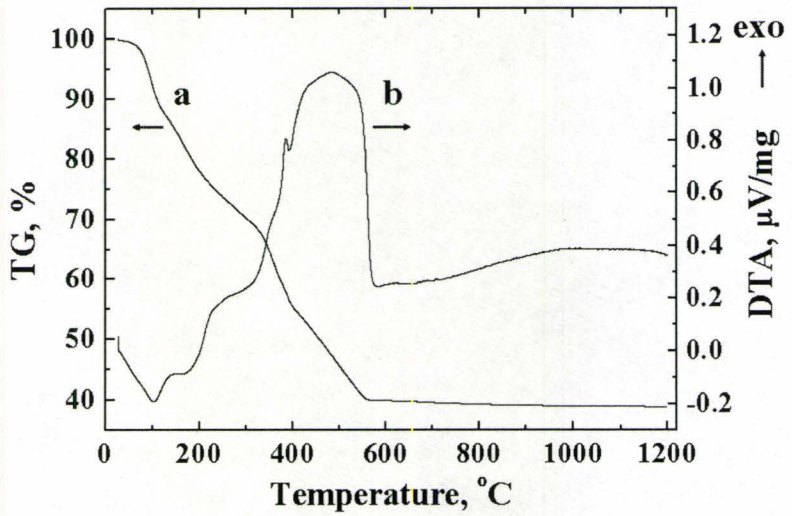

Figure 4.4 TG (a) and DTA (b) data for the deposits prepared from 5 mM $FeCl_3$ solutions, containing 0.5 g/l PAH.

TG data for the deposits prepared from 5mM $FeCl_3$ solutions containing 0.5 g/l PAH showed several steps in the weight loss below 550 °C (Fig.4.4 a). The total weight loss at 1200 °C was found to be 61.1 wt%. The total weight loss at 1200 °C for this deposit (Fig.4.4) exceeded significantly the weight loss for the deposit prepared from pure $FeCl_3$ solution (Fig.4.3). These results indicate co-deposition of iron oxide and PAH. The additional weight loss is attributed to burning out of an organic phase. The DTA data for the deposits prepared from 5mM $FeCl_3$ solutions containing 0.5 g/l PAH (Fig.4.4) showed a broad endotherm in the range below 200 °C and exotherm in the range 350-550 °C. The endotherm is associated with weight loss. The exotherm can be attributed to burning out of PAH and the γ-$Fe_2O_3 \rightarrow \alpha$-$Fe_2O_3$ transformation.

The results of the TG are used to calculate the amount of an organic phase in the composite films. When considering the composite material as a mixture of organic and inorganic components, the weight percentage of γ-Fe_2O_3 in the deposits prepared from the 5 mM $FeCl_3$ containing 0, 0.2, 0.3 and 0.5 g/l PAH was 89.1%, 62.0%, 52.5% and 38.9%, respectively.

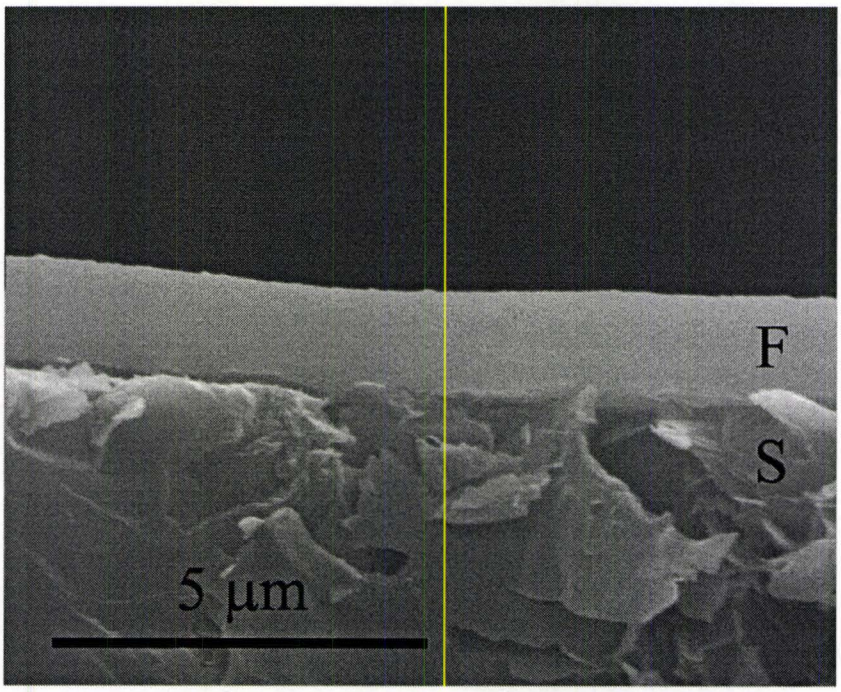

Figure 4.5 SEM picture of a sectioned film (F) obtained from a 5 mM $FeCl_3$ solution, containing 0.5 g/l PAH on a graphite substrate (S).

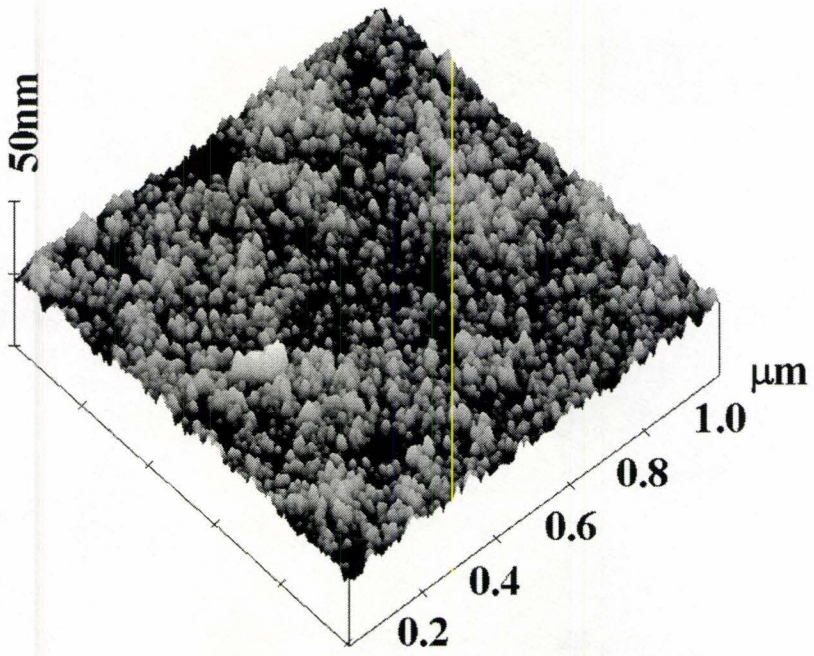

Figure 4.6 AFM image of the film prepared from 5 mM $FeCl_3$ solution containing 0.5 g/l PAH at a current density of 2 mA/cm^2.

Composite films of various thicknesses in the range of up to several micrometers were obtained on Pt and graphite substrates by the variation of the deposition time and current density. Fig.4.5 shows a SEM picture of a composite iron oxide – PAH film on a graphite substrate. It was observed that electrodeposition results in uniform films. Surface roughness of the films was studied using AFM. Fig.4.6 shows the AFM image of the film prepared at a current density of 2 mA/cm^2. The root-mean-square (rms) surface roughness of the film was found to be 1.6 nm.

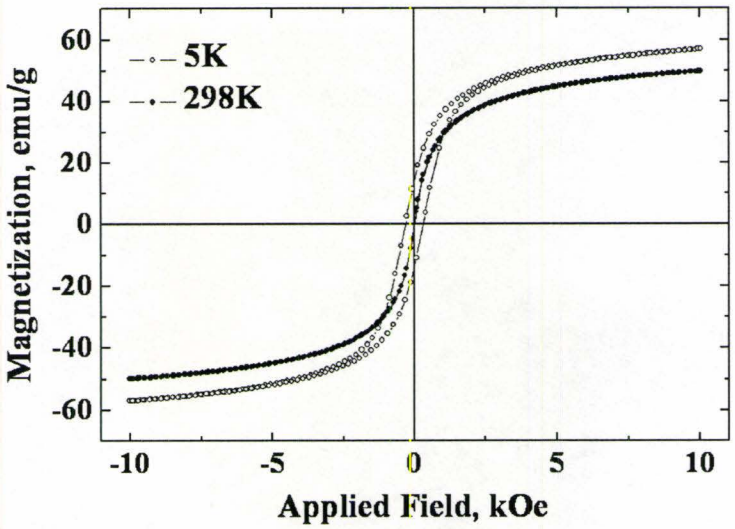

Figure 4.7 Magnetization versus applied field for the deposits prepared from 5 mM $FeCl_3$ solutions.

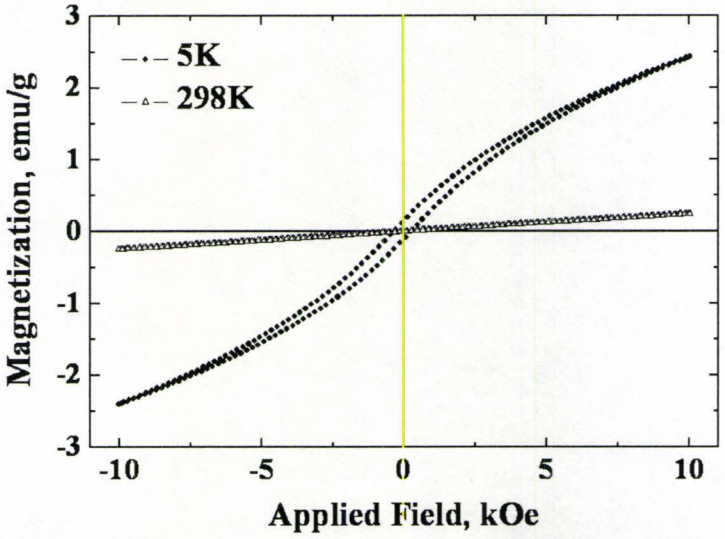

Figure 4.8 Magnetization versus applied field for the deposits prepared from 5 mM $FeCl_3$ solution containing 0.5 g/l PAH.

Fig.4.7 shows typical magnetization versus magnetic field dependencies for the deposits prepared from $FeCl_3$ solutions without PAH. The magnetization data obtained in the low field range indicated a hysteresis behaviour at 5 K. In contrast no magnetic hysteresis was observed at room temperature. The magnetization curve recorded at room temperature showed zero remanence and zero coercivity. These data are consistent with superparamagnetic behaviour of the nanoparticles. Plots of magnetizations versus magnetic field for the composite films showed hysteresis behaviour at 5K (Fig.4.8). However, nearly linear behaviour was observed at 298K.

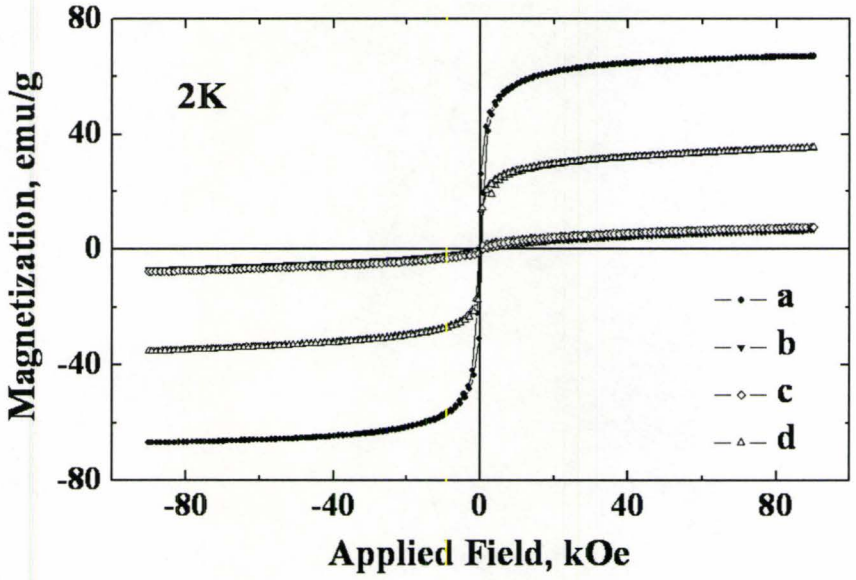

Figure 4.9 Magnetization versus applied field for the deposits prepared from 5 mM $FeCl_3$ solutions without PAH (a) and containing 0.5 g/l PAH (b, c, d): as prepared (a,b) and after annealed at 200 °C (c) and 300 °C (d).

Fig.4.9 compares the magnetization curves at 2 K obtained in field range up to 90 kOe for the iron oxide deposits and composite films. The saturation magnetization was found to be ~ 60 emu/g for the deposits prepared from 5 mM $FeCl_3$ solutions. The composite films prepared from 5 mM $FeCl_3$ solutions containing 0.5 g/l PAH showed lower magnetization. However, annealing of the films at temperatures above 200 °C increased significantly the saturation magnetization, which was found to be ~25 emu/g after heat treatment at 300 °C.

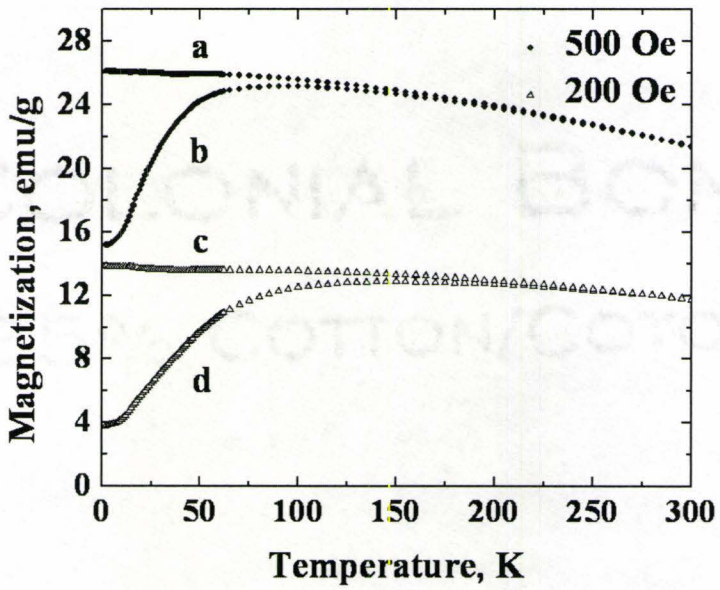

Figure 4.10 DC magnetization for the deposit prepared from the 5mM $FeCl_3$ solutions: field cooling (a,c) and zero field cooling (b,d).

Fig.4.10 shows DC magnetization of the deposits prepared from 5 mM $FeCl_3$ solutions. A separation of the ZFC and FC curves was observed at low temperatures. ZFC

curves exhibited broad cusps. The ZFC and FC curves obtained at 200 and 500 Oe superimposed at temperatures above 250 K and 175 K, respectively.

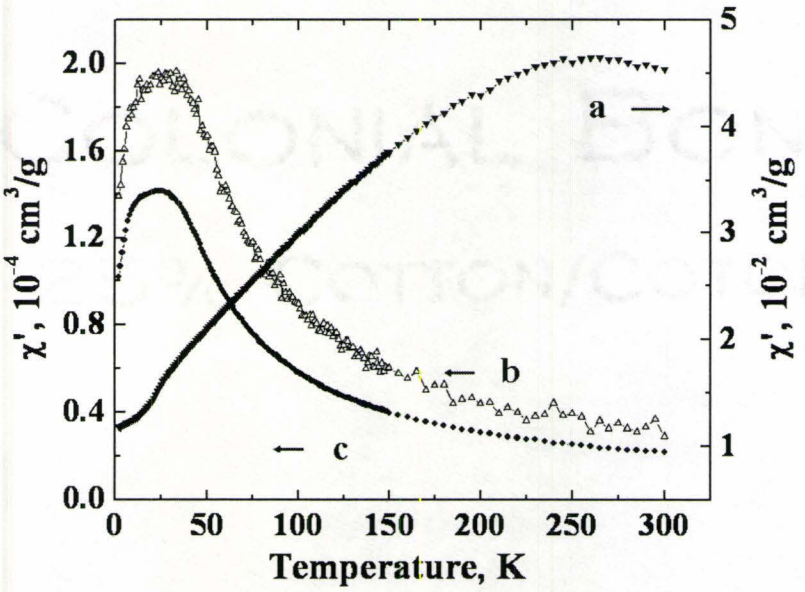

Figure 4.11 Real part χ' of AC magnetic susceptibility versus temperature at a frequency of 10 Hz for the deposits prepared from the 5 mM $FeCl_3$ solutions without PAH (a) and containing 0.2 (b) and 0.3 (c) g/l PAH .

Real part of AC susceptibility of the deposits prepared from 5 mM $FeCl_3$ solutions exhibited a broad maximum around $T_m \sim 260$ K, which can be attributed to the superparamagnetic relaxation (Fig.4.11). In contrast, composite films, prepared from the solutions containing higher amounts of PAH exhibited maximum of the real part of AC susceptibility at lower temperatures. The experimental results for as-prepared composite films (Figs.4.11 and 4.12) indicate that T_m decreases with increasing PAH concentration

in the solutions. The annealing of the films at temperatures of 200 and 300 °C increased T_m as shown in Fig.4.12.

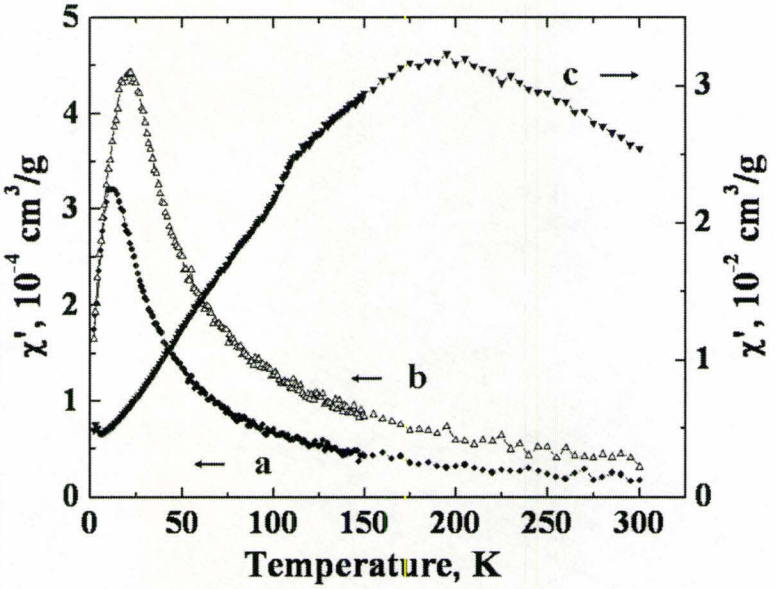

Figure 4.12 Real part χ' of AC magnetic susceptibility versus temperature at a frequency of 10Hz for the deposits prepared from the 5mM $FeCl_3$ solutions containing 0.5 g/l PAH: as-prepared (a) and after annealed at 200 °C (b) and 300 °C (c) for 1 hour

4.1.2 Electrodeposition of Mn_3O_4 using PAH

Cathodic electrodeposition was used to prepare magnetic Mn_3O_4 nanoparticles *in situ* in a polyelectrolyte PAH matrix at room temperature. In this section, the structural characterization and magnetic properties of Mn_3O_4 - PAH nanocomposite films were discussed.

Structural characterization of Mn_3O_4 - PAH nanocomposite

The deposits were analyzed by X-Ray diffraction before and after annealing in air at different temperatures for one hour. Fig.4.13 shows X-ray diffraction patterns of the deposits prepared from 5 mM $MnCl_2$ solution containing 0.5g/l PAH. The as-prepared deposit exhibited small broadened peaks belonging to Mn_3O_4 (Hausmannite, JCPDS file #24-0734). After annealing at 200 °C and 300 °C, Mn_3O_4 phase was mainly detected, and the XRD pattern was sharpened because of grain growth. Further results from high resolution TEM and magnetic measurements confirmed the presence of Mn_3O_4 phase. The deposits annealed at 400 °C and 500 °C showed pure Mn_2O_3 structure (JCPDS file #41-1442).

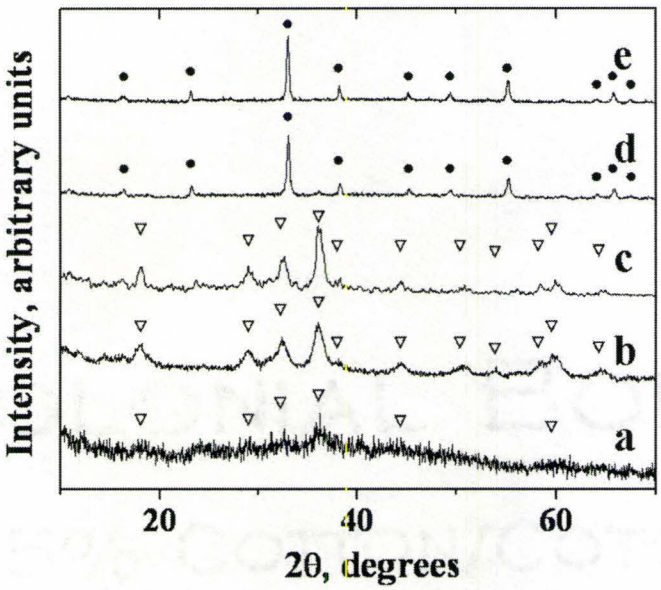

Figure 4.13 X-ray diffraction patterns for the deposits prepared from the 5 mM $MnCl_2$ solution containing 0.5 g/l PAH, (a) as prepared and those annealed at (b) 200 (c) 300 (d) 400 (e) 500 °C for 1 hour. • -Mn_2O_3 (JCPDS 41-1442), ∇ -Mn_3O_4 (JCPDS 24-0734)

Fig.4.14 shows TG and DTA curves for the deposits prepared from 5 mM $MnCl_2$ solutions containing 0.5 and 1.0 g/l PAH. The TG data of both samples (Fig 4.14 a, b) showed total weight loss of 39.6% and 52.1% of the initial weight, respectively. Both samples showed several steps in the weight loss in the temperature range up to 1200 °C. The data indicate that most of the weight loss occurs below 530 °C. The weight loss at 530 °C was 38.9% and 50.1% for the deposit from 0.5 g/l and 1.0 g/l PAH, respectively. Further increase of the temperature gained 1.1 wt% and 0.2 wt% for the deposit from 0.5 g/l and 1.0 g/l PAH, respectively, in the temperature range 530-680 °C. Another 1.8% weight loss occurred for both samples in the temperature range 930-970 °C. No weight changes were observed in the range 970-1200 °C. The corresponding DTA data (Fig.4.14

c, d) showed two endotherms around 100 °C and 950 °C, and exotherms in the range of 200-680 °C.

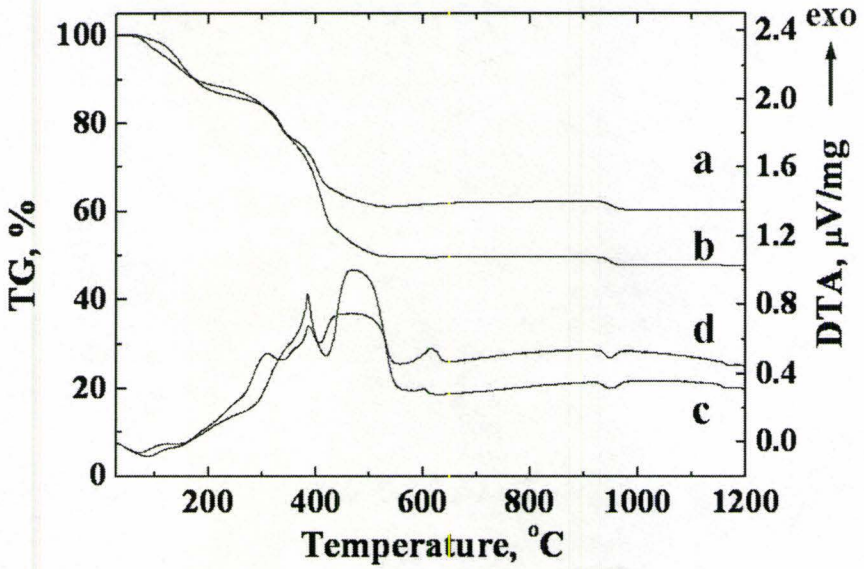

Figure 4.14 TG (a, b) and DTA (c, d) data for deposits prepared from the 5 mM $MnCl_2$ solutions containing (a, c) 0.5g/l and (b, d) 1.0g/l PAH

A relationship between the observed exothermic and endothermic effects in DTA data and the steps in TG data were studied. The endotherm around 100 °C can be attributed to the liberation of the adsorbed water. The exotherms can be related to the burning out of the polymer. The weight gain in the temperature range 530-680 °C in Fig.4.14 can be attributed to the oxygen uptake due to the phase transition from Mn_3O_4 to Mn_2O_3. The weight loss in the temperature range 930-970 °C in Fig.4.14 can possibly be related to the phase transition from Mn_2O_3 to Mn_3O_4.

Composite films with various thicknesses in the range up to several micrometers were obtained on the Pt and graphite substrates by changing the deposition time and current density. Fig.4.15 shows SEM observations of the cross-section of Mn_3O_4–PAH film deposited on graphite substrates. Uniform films were observed.

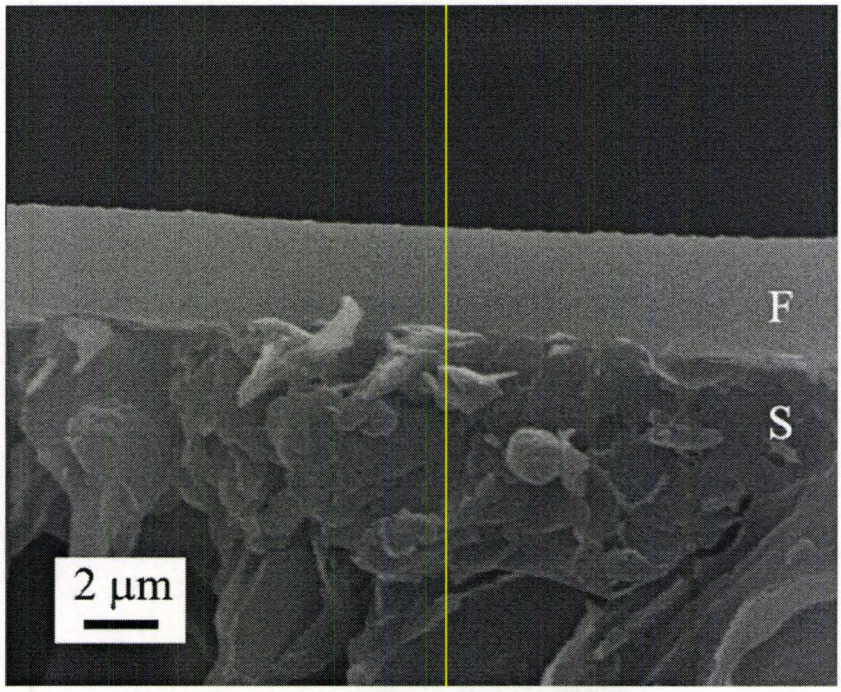

Figure 4.15 SEM cross-sections of the films (F) deposited on the graphite substrate (S). The deposits were obtained from the 5 mM $MnCl_2$ solutions containing 0.5g/l PAH

Fig.4.16 shows high resolution TEM (HRTEM) image of the nanocomposite deposit obtained from the 5 mM $MnCl_2$ solutions containing 0.5 g/l PAH. It was visible that Mn_3O_4 nanoparticles were embedded in a polymer matrix. The average particle size counted from numerous images gave 4.6 ± 1.0 nm.

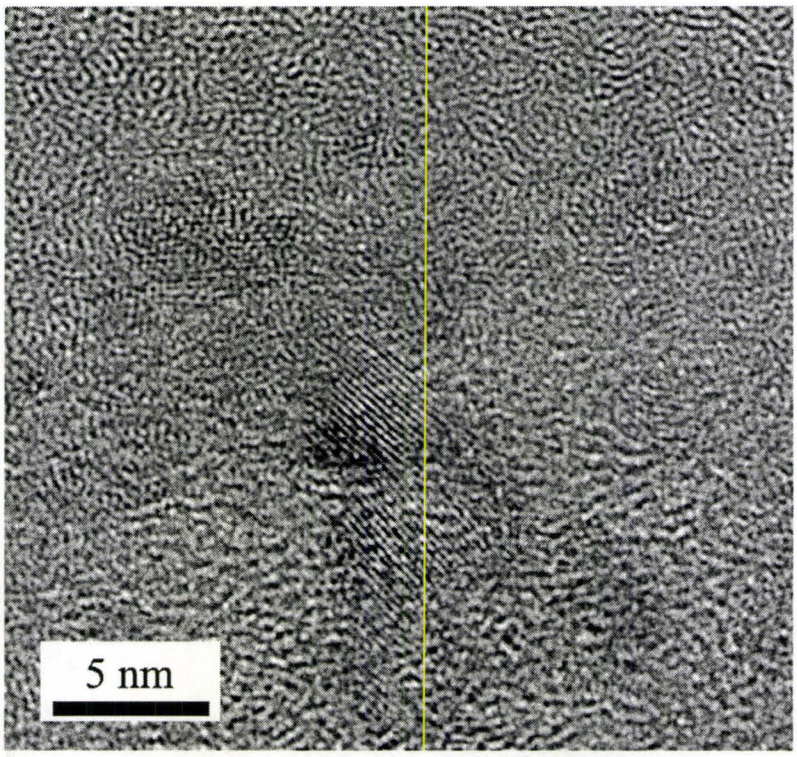

Figure 4.16 HRTEM images for the deposits prepared from the 5 mM $MnCl_2$ solutions containing 0.5g/l PAH

Fig.4.17 shows TEM image of the deposit prepared from the same sample. It contained the nanorods with the diameters of 2 - 4 nm and the lengths of tens of nanometres in the polymer matrix. HRTEM of one of the nanorods (inset in Fig.4.17) showed the lattice fringes of crystalline Mn_3O_4. The formation of nanorods together with smaller particles of different shapes might result in the abnormal behaviour in the magnetization loop observed in the Mn_3O_4-PAH-0.5g-RT deposit.

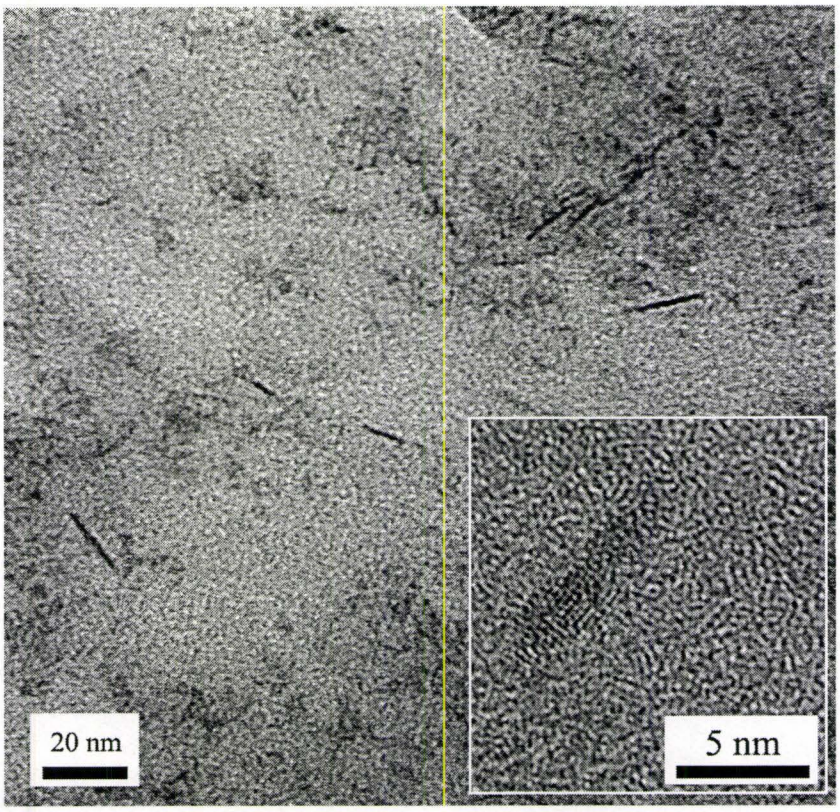

Figure 4.17 TEM image showing the nanorods in the deposits prepared from the 5 mM $MnCl_2$ solutions containing 0.5g/l PAH (inset is a HRTEM image, which shows one of the nanorods)

Magnetic properties of Mn_3O_4 - PAH nanocomposites

For convenience, in the following chapters, the fresh deposit prepared from the 5 mM $MnCl_2$ solution containing 0.5g/l PAH is labelled as *Mn_3O_4-PAH-0.5g-RT*, and those annealed at 200, 300 °C, etc, for 1 hour as *Mn_3O_4-PAH-0.5g-200*, *Mn_3O_4-PAH-0.5g-300* etc.

Fig.4.18 shows magnetization as a function of magnetic field curves at the temperatures 2 K, 5 K, 20 K and 50 K for the Mn_3O_4-PAH-0.5g-RT. Below the ferrimagnetic Néel temperature (T_N = 42 K), Mn_3O_4 nanoparticles show ferrimagnetism

with remnant magnetization and coercive force decreasing with increase of temperature. Above the 42 K, only paramagnetic behaviour was observed.

In Fig 4.18, sharp changes in the magnetization loops were observed in the vicinity of the switch in the applied field direction in the hysteresis loops measured at 2 K, 5 K and 20 K. This jump of the curves may be caused by the magnetic reversion of the smallest particles in the system.

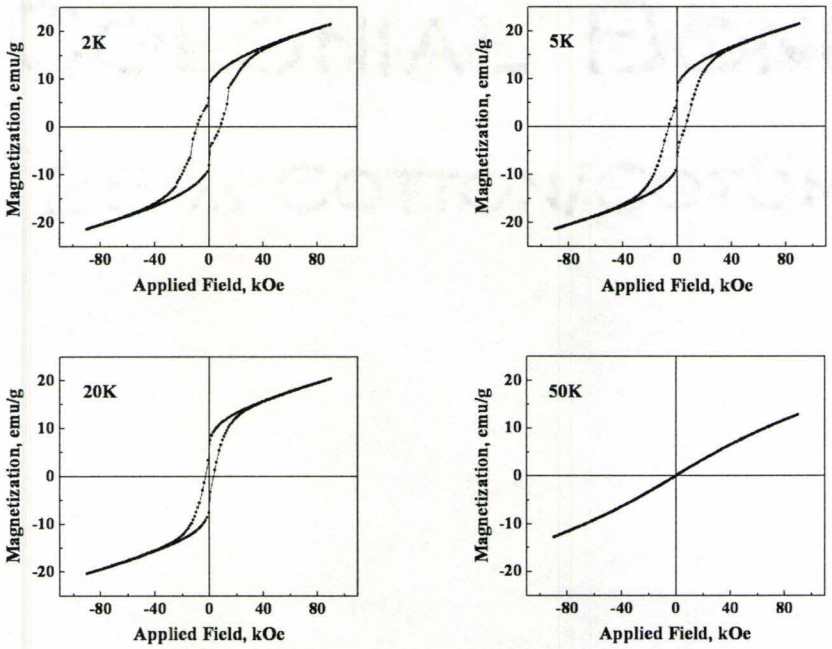

Figure 4.18 Magnetization versus applied field in 9 T range at temperatures 2, 5, 20 and 50 K for the Mn_3O_4-PAH-0.5-RT

Fig.4.19 shows the temperature dependence of field cooling (FC) and zero field cooling (ZFC) magnetization of the Mn_3O_4-PAH-0.5g-RT sample, which were measured at 200 Oe and 500 Oe. The ferrimagnetic-paramagnetic transition is characterized by a divergence between FC and ZFC curves at Néel temperature T_N close to 42 K, where the

maximum in ZFC exists. The Néel temperature obtained from T_{max} of ZFC curves was 36 K and 37 K for the applied field of 200 Oe and 500 Oe, respectively.

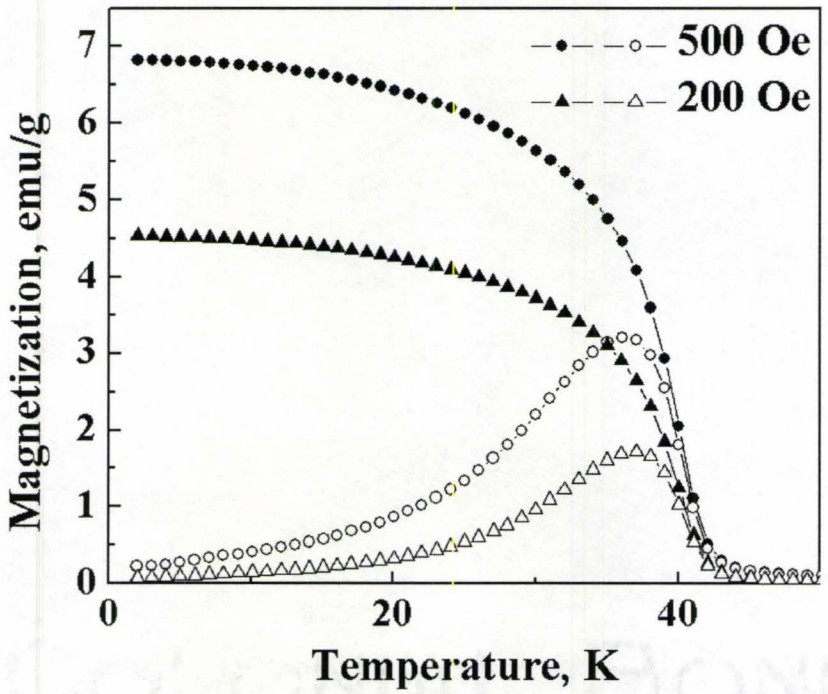

Figure 4.19 Temperature dependence of FC (solid) and ZFC (open) magnetization measured at 200 Oe (triangle) and 500 Oe (circle) for the Mn_3O_4-PAH-0.5g-RT

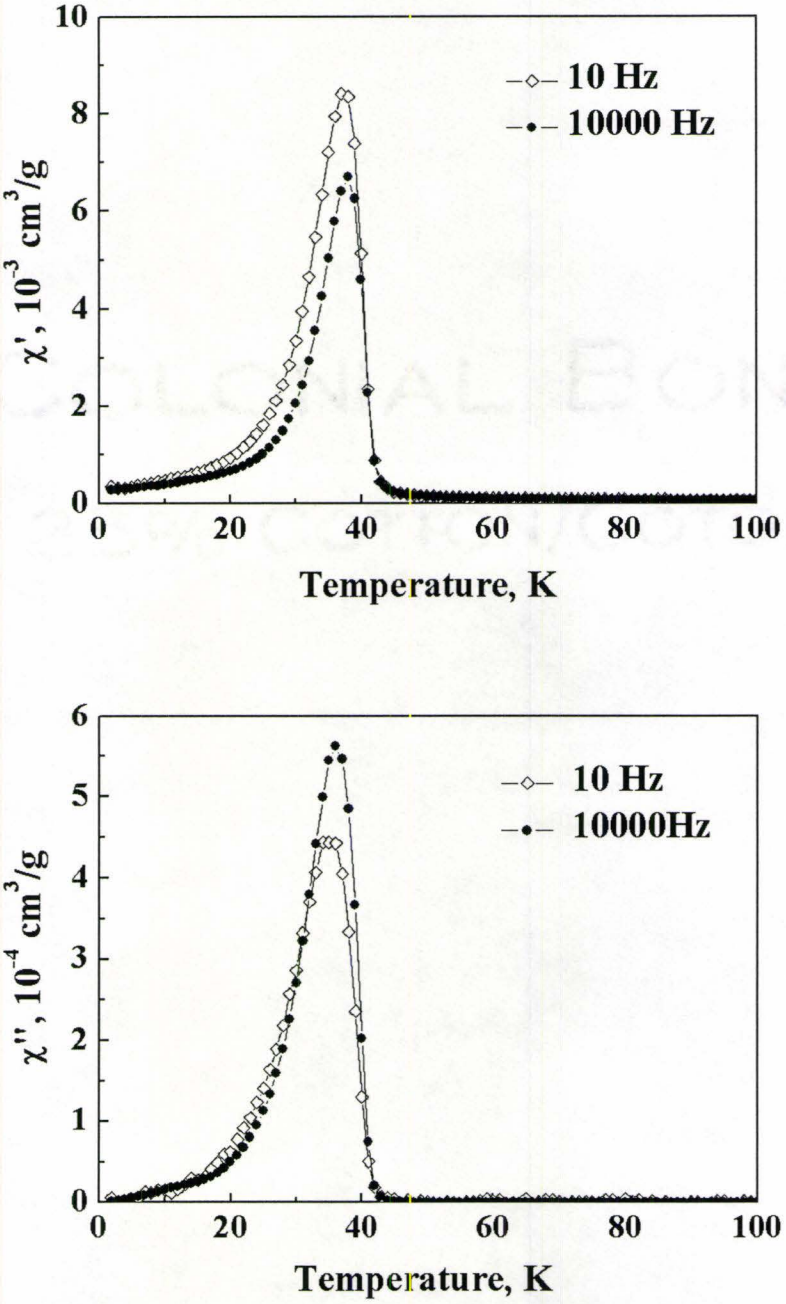

Figure 4.20 Real and imaginary parts of AC complex susceptibility ($\chi=\chi'-i\chi''$) for Mn_3O_4-PAH-0.5g-RT

The real and imaginary parts (χ' and χ'') of the AC complex susceptibility for the Mn_3O_4-PAH-0.5g-RT are shown in Fig.4.20. On the increase of the temperature, the real and imaginary parts of the AC susceptibility increased with a maximum at T_{max} and then decreased. The Néel temperature T_N, marked by T_{max}, was found to be 37 K at 10 Hz and 38 K at 10 kHz, which was slightly lower than T_N = 42 K of the bulk materials.

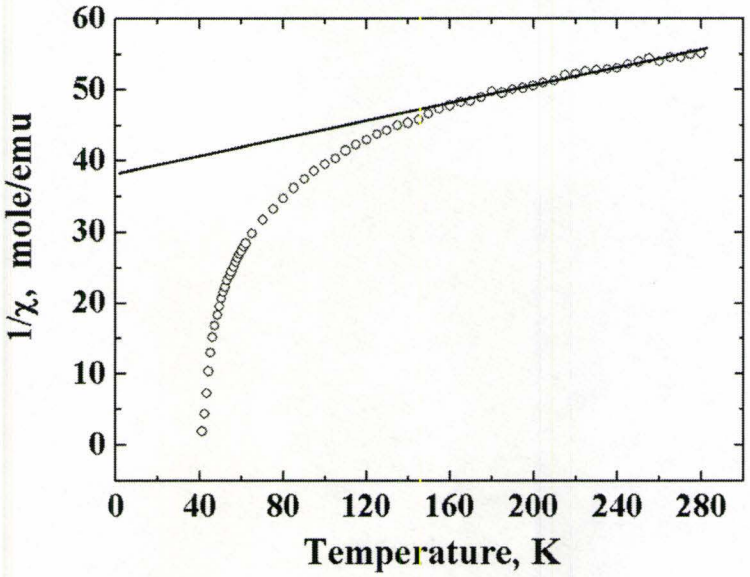

Figure 4.21 Temperature dependence of the inverse susceptibility in the paramagnetic range for Mn_3O_4-PAH-0.5g-RT. Solid line is the best fit of Eq.1.13

The temperature dependence of χ of a ferrimagnetic material in the paramagnetic region is approximated as $\frac{1}{\chi} = \frac{T}{C} + \frac{1}{\chi_0}$ (Eq. 1.13) in the high temperature region.

For the sample Mn_3O_4-PAH-0.5g-RT, the temperature dependence of the inverse susceptibility in paramagnetic region, measured in a field of 500 Oe, is shown in Fig.4.21

as a plot of $1/\chi$ versus temperature. The fitting of the linear region of $1/\chi$ (150 K to 300 K) to Eq.1.13 is also shown in Fig.4.21 as the solid line with the following parameters, $1/\chi_0 = 37.7$ and $C = 15.62$, which gave a paramagnetic Curie point $\theta = 589$ K. This value is close to the experimental values of T_a=640 K reported by others [220, 221].

The Curie constant $C = \dfrac{\mu_0 N_A \mu_{eff}^2 \mu_B^2}{3k_B T}$ 4.1

Where N_A is Avogadro's number, μ_{eff} is measured in Bohr magnetons per formula unit. In cgs units, where the molar susceptibility χ_m is measured in emu/mol, the Curie constant is related to μ_{eff} as follows:

$$\mu_{eff} = 2.827\sqrt{C} \qquad 4.2$$

From Eq.4.2, the μ_{eff}/formula gave 11.2 μ_B/formula from our experiments. This value of μ_{eff} is in agreement with results of other works [222].

Mn_3O_4-PAH-0.5g-200

Fig.4.22 shows magnetization as a function of magnetic field curves at the temperatures 2K, 5K, 20 K and 50 K for the Mn_3O_4-PAH-0.5g-200 composite. Below the ferrimagnetic Néel temperature (T_N = 42 K), the Mn_3O_4-PAH-0.5g-200 showed ferrimagnetism. The remnant magnetization and coercive force were reduced with the increase of the temperature. Above the 42 K, only paramagnetic behaviour was observed. There was no sharp change in the hysteresis loops in this sample, which is different from the previous one. This difference can be explained by the fact that the annealing changes the morphology of the Mn_3O_4-PAH-0.5g composite.

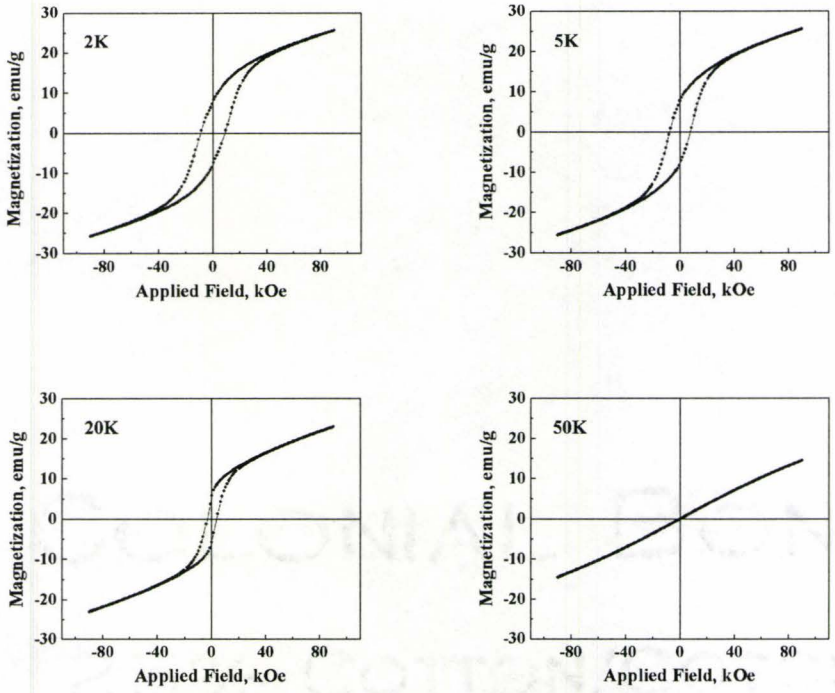

Figure 4.22 Magnetization versus applied field in 9 T range at temperatures 2K, 5 K, 20K and 50 K for the Mn_3O_4-PAH-0.5g-200

Fig.4.23 shows the temperature dependence of field cooling (FC) and zero field cooling (ZFC) magnetization of the Mn_3O_4-PAH-0.5g-200. The ferrimagnetic Néel temperature T_N obtained from T_{max} of ZFC curves was 37 K for both the fields of 200 Oe and 500 Oe. Above T_{max}, FC was superimposed with ZFC into one line in paramagnetic region following Curie-Weiss law.

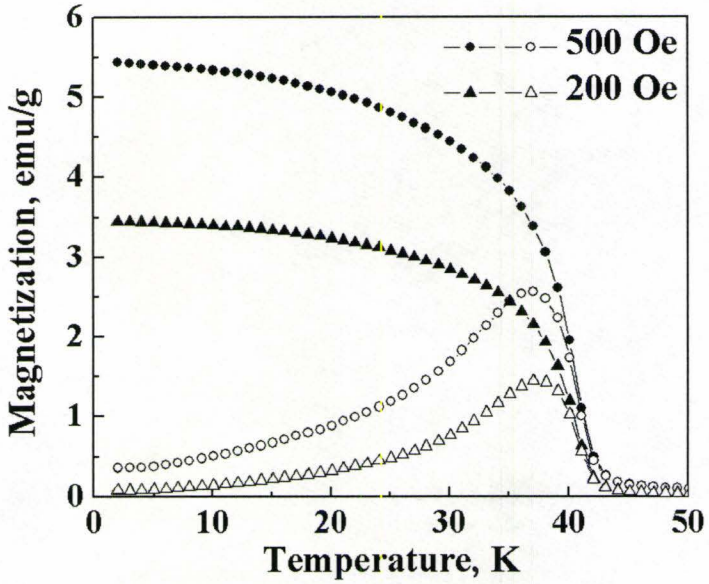

Figure 4.23 Temperature dependence of FC (solid symbols) and ZFC (open symbols) magnetization measured at 200 Oe (triangle) and 500 Oe (circle) for the Mn_3O_4-PAH-0.5g-200

Figure 4.24 shows temperature dependence of real and imaginary parts (χ' and χ'') of the AC complex susceptibility for the Mn_3O_4-PAH-0.5g-200 sample. T_{max} in the real part of AC susceptibility curve at particular frequency indicates Néel temperature T_N of the sample. These measurements gave T_N=39 K in the frequency range of 10 Hz - 10 kHz, showing no frequency dependence. There was no superparamagnetic transition peak below T_N.

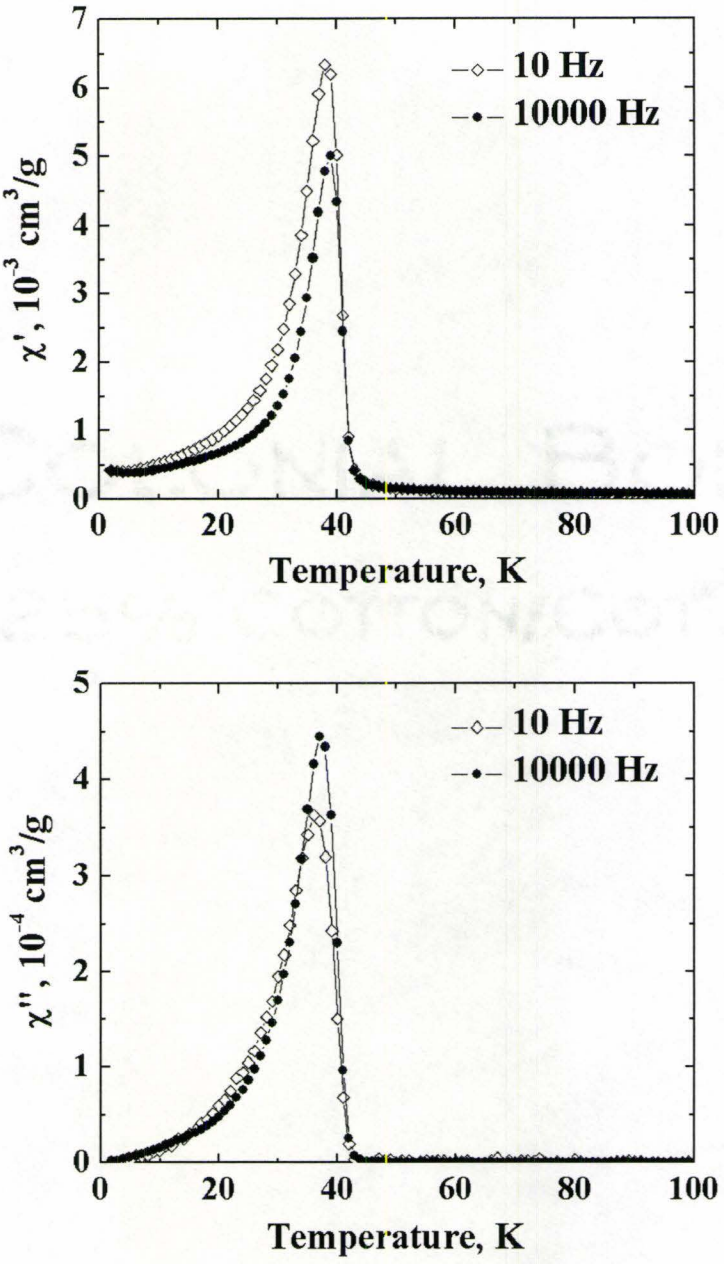

Figure 4.24 Real and imaginary parts of AC complex susceptibility ($\chi=\chi'-i\chi''$) for the Mn_3O_4-PAH-0.5g-200

4.2 Nanocomposites based on PEI

Polyethylenimine (PEI) is a polybase when dissolved in aqueous solution. The pH of an aqueous solution containing 1 wt% PEI was found to be about 11 and at this pH the PEI molecule has no charge. PEI adsorbs protons in the acidic solutions and becomes charged positively through protonation of the secondary amine groups in acidic solutions, according to the reaction [223]:

$$[\text{-CH}_2\text{-CH}_2\text{-NH-}]_n + H_3O^+ \rightarrow [\text{-CH}_2\text{-CH}_2\text{-NH}_2^+\text{-}]_n + H_2O \qquad 4.5$$

PEI has a positive charge over a wide pH range below pH 11, however the charges decrease with increasing pH. Therefore the high pH value at the cathode surface reduces electrostatic repulsion of PEI macromolecules and promotes their deposition on the cathodic substrates. It is known that PEI macromolecules acquire a positive charge as a result of complex formation with metal ions such as Ni^{2+}, Co^{2+}, Mn^{2+} and Fe^{3+}. Electric field provides the electrophoretic motion of the polymer-metal ion complexes towards the electrode surface. It is suggested that these ions participate in cathodic reactions to form nanoparticles of metal oxide/hydroxides. Free metal ion species, which are not complexed by PEI also exist in solutions and contribute to the electrosynthesis of the inorganic phase [82].

4.2.1 Electrodeposition of Mn_3O_4 using PEI

5mM $MnCl_2$ solution containing 0.5-2 g/l PEI in ethanol-water (10 vol% water) solvent were prepared for electrodeposition. When the $MnCl_2$ dissolved in ethanol-water solution, it had no color. It turned to light brown after adding of PEI. It is suggested that a complex between manganese ions and PEI forms in the solution, giving the color change. The electrodeposition was conducted at a current density range of 1-5 mA/cm^2. The deposition time was varied from 0.5 to 5 min to obtain various film thicknesses.

Structural characterization of Mn_3O_4 - PEI nanocomposite

X-ray diffraction patterns of the deposits prepared from 5 mM $MnCl_2$ solution containing 0.5g/l PEI are shown in Fig.4.25. XRD of fresh deposits exhibited their amorphous nature (Fig.4.25 a). After annealing at 200 °C and 300 °C, the deposits showed small peaks belonging to Mn_3O_4 (hausmannite, JCPDS) phase. The peak broadening can be caused by small particle size. Deposits annealed at 400 °C and 500 °C exhibited peaks attributed to Mn_2O_3 structure.

Fig. 4.26 shows X-ray diffraction patterns of the deposits obtained from solution containing 1.0 g/l PEI. XRD pattern of the fresh deposit (Fig.4.26 a) showed amorphous phase. After annealing at 200 and 300 °C, XRD patterns showed small peaks belonging to Mn_3O_4 (hausmannite, JCPDS) phase. The deposit annealed at 400 °C showed additional peaks attributed to Mn_2O_3 structure. The results indicate the phase transition from Mn_3O_4 to Mn_2O_3. Only the Mn_2O_3 phase appeared at higher annealing temperatures at 500 °C and 600 °C.

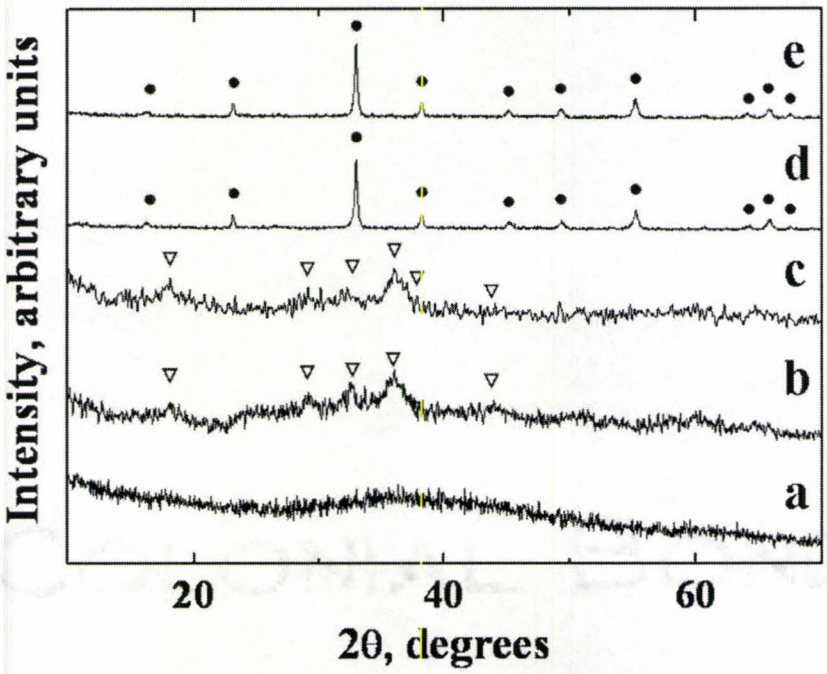

Figure 4.25 X-ray diffraction patterns for the deposits prepared from the 5 mM $MnCl_2$ solution containing 0.5 g/l PEI, (a) as prepared and those annealed at (b) 200 (c) 300 (d) 400 (e) 500 °C for 1 hour. • -Mn_2O_3 (JCPDS file 41-1442), ∇ -Mn_3O_4 (JCPDS file 24-0734)

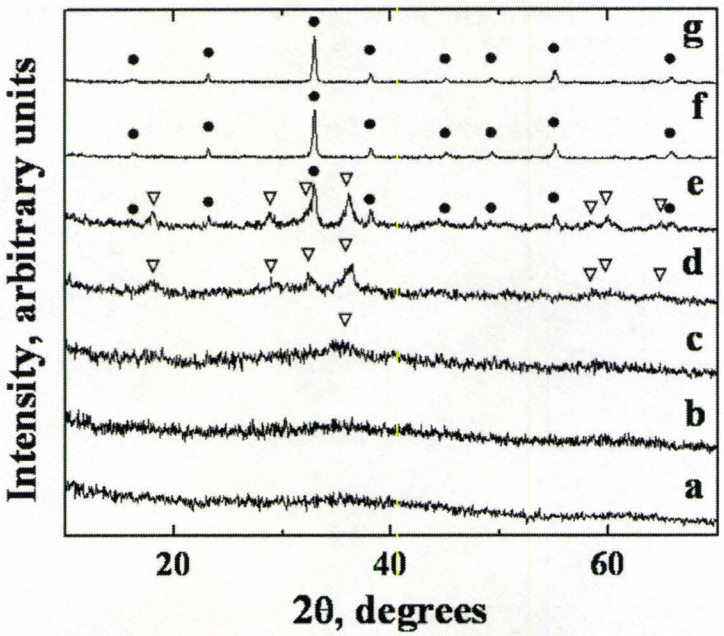

Figure 4.26 X-ray diffraction patterns for the deposits prepared from 5 mM $MnCl_2$ solution containing 1.0 g/l PEI, (a) as prepared, and those annealed at (b) 100 (c) 200 (d) 300 (e) 400 (f) 500 and (g) 600 °C for 1 hour. •-Mn_2O_3 (JCPDS file 41-1442), ∇ -Mn_3O_4 (JCPDS file 24-0734)

Fig.4.27 shows TG/DTA of the deposits prepared from the 5 mM $MnCl_2$ solutions containing 0.5 g/l, 1.0 g/l, and 2.0 g/l PEI, respectively. The TG data (Fig.4.27 a, b, c) indicated that most of the weight loss occurred below 420 °C. The weight loss at 420 °C was 37.7%, 47.8%, and 60.2% weight percentage of the initial sample weight for the three deposits obtained from the solution containing 0.5 g/l, 1.0 g/l, and 2.0 g/l PEI, respectively. Further increasing the temperature, there was a weight gain of 0.9%, 0.9%, and 0.4% in the temperature range 450-550 °C, and a weight loss of 1.6%, 2.7%, and 1.5% in 930-970 °C for the three deposits, respectively. The total weight losses at 1200

°C were 38.4%, 49.6%, and 61.3% of the initial sample weight for the three deposits obtained from the solution containing 0.5 g/l, 1.0 g/l, and 2.0 g/l PEI, respectively. The corresponding DTA data (Fig.4.27 c, d, e) showed two endotherms around 100 °C and 950 °C, and exotherms in the range of 200-550 °C.

A combination of DTA thermal peaks and weight changes in TG data suggests that the endotherm around 100 °C can be attributed to the liberation of the adsorbed water, and the exotherms can be related to the burning out of the polymer. The weight gain in the temperature range 450-550 °C can be attributed to oxygen uptake due to the phase transition from Mn_3O_4 to Mn_2O_3. The weight loss in the temperature range 930-970 °C can be caused by the phase transition from Mn_2O_3 to Mn_3O_4.

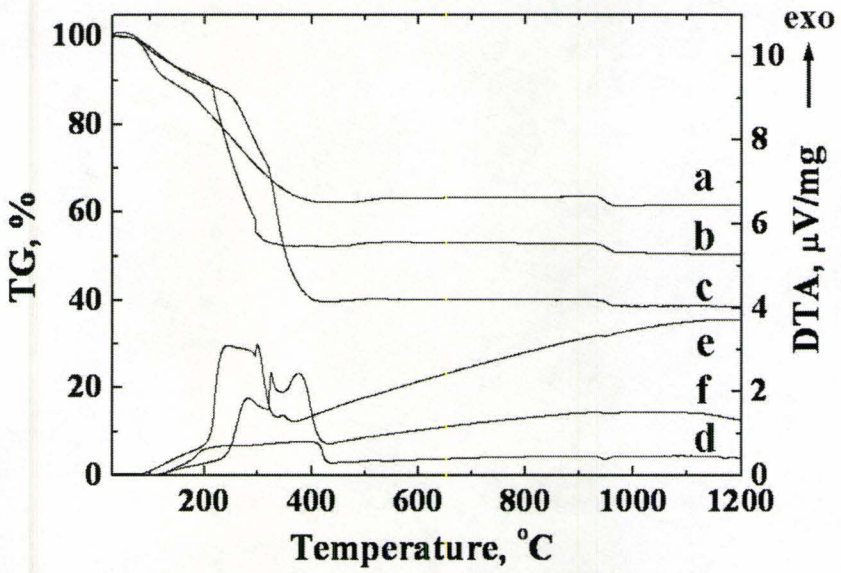

Figure 4.27 TG (a, b, c) and DTA (d, e, f) data for deposits prepared from the 5 mM $MnCl_2$ solutions containing (a, d) 0.5g/l, (b, e) 1.0g/l, and (c, f) 2.0 g/l PEI

Composite films with various thicknesses in the range up to several micrometers were obtained on Pt and graphite substrates by changing the deposition time and the current densities. Fig.4.28 shows SEM observations of the cross-section of Mn_3O_4–PEI films deposited on graphite substrates at a current density of 2 mA/cm^2 for 5 min. It was observed that electrodeposition resulted in uniform films and good adhesion.

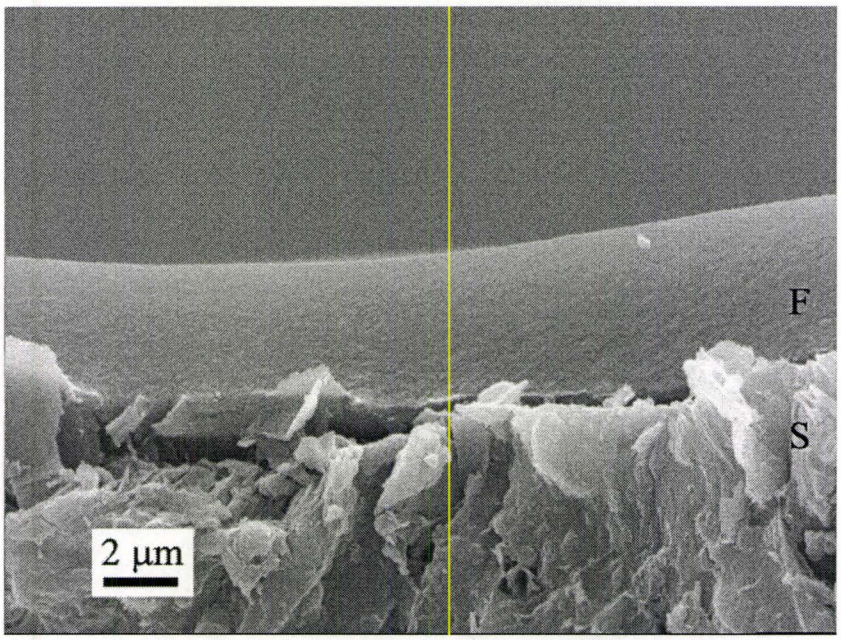

Figure 4.28 SEM cross-sections of the films (F) deposited on the graphite substrate (S). The deposits were obtained from the 5 mM $MnCl_2$ solutions containing 0.5g/l PEI at a current density of 2 mA/cm^2 for 5 min..

Fig.4.29 shows high resolution TEM (HRTEM) images of the nanocomposite deposits obtained from the 5 mM $MnCl_2$ solutions containing 0.5 g/l PEI. It was found that Mn_3O_4 nanoparticles were randomly distributed in the polymer PEI matrix and atomic fringes overlapped with each other in some areas, indicating that there might be magnetic interactions among Mn_3O_4 nanoparticles, and the agglomeration of the particles can not

be avoided. The average particle size measured from numerous images gave an average diameter of 3.0±0.2 nm.

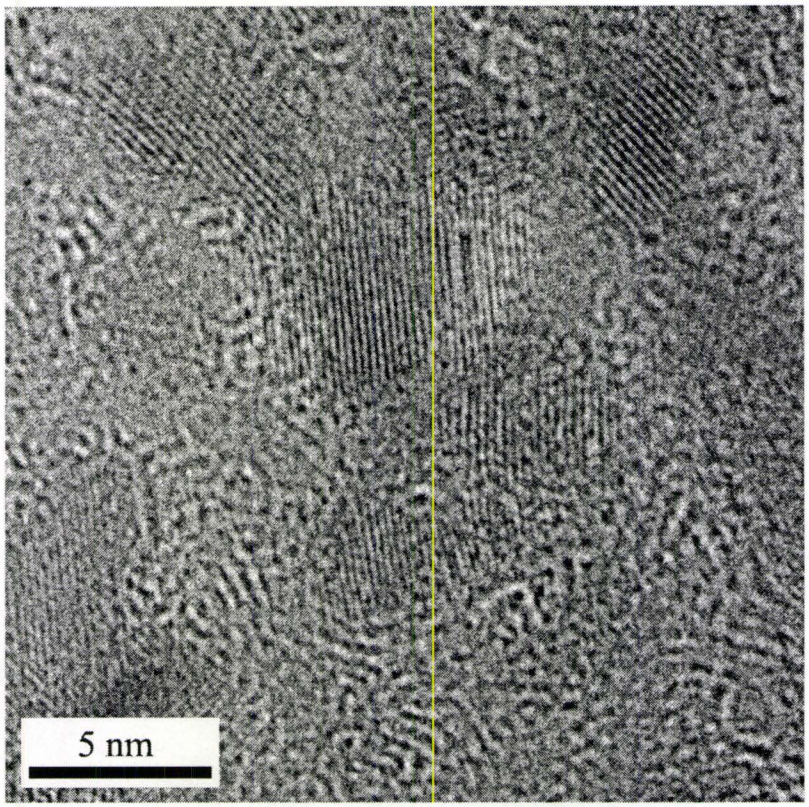

Figure 4.29 HRTEM of deposit from 5 mM $MnCl_2$ solution containing 0.5g/l PEI

Magnetic Properties of Mn_3O_4 - PEI nanocomposite

For convenience, in the following chapters, the fresh deposit prepared from the 5 mM $MnCl_2$ solutions containing 0.5 g/l PEI was labeled as Mn_3O_4-PEI-0.5g-RT, and those annealed at 200 °C, and 300 °C for 1 hour as Mn_3O_4-PEI-0.5g-200, and Mn_3O_4-PEI-0.5g-300.The fresh deposit from the 5 mM $MnCl_2$ solutions containing 1.0 g/l PEI was labeled as Mn_3O_4-PEI-1.0g-RT, and those annealed at 200 °C, and 300 °C for 1 hour as Mn_3O_4-PEI-1.0g-200, Mn_3O_4-PEI-1.0g-300, and etc.

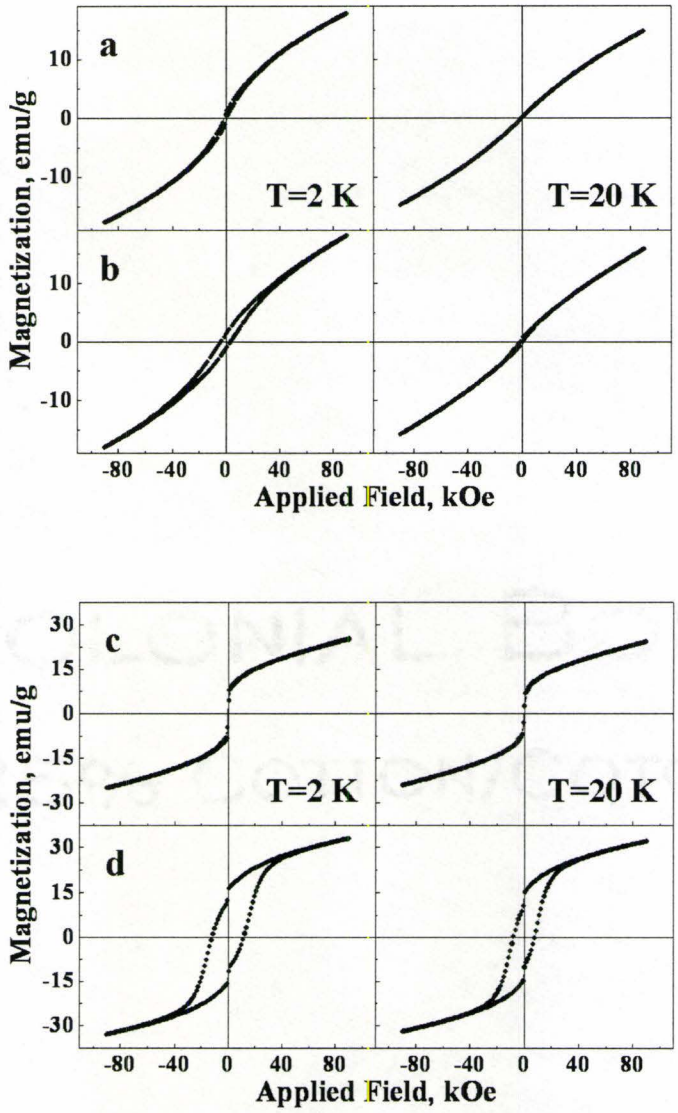

Figure 4.30 Magnetization versus applied field in 9 T range at temperatures 2 K and 20 K for the deposits prepared from the 5 mM $MnCl_2$ solution containing (a) 1.0 g/l PEI and (b, c, d) 0.5 g/l PEI, in which (b) as prepared and (c, d) annealed at 200 and 300 °C

Fig.4.30 shows magnetization versus applied field in 9 T range at the temperatures 2 K and 20 K for the Mn_3O_4-PEI-1.0g-RT, Mn_3O_4-PEI-0.5g-RT, Mn_3O_4-PEI-0.5g-200, and Mn_3O_4-PEI-0.5g-300 samples labelled as (a), (b), (c), and (d), respectively. At 2 K, all the

samples exhibited ferrimagnetism. The remnant magnetization M_r and coercive force H_C were reduced at 20 K, which indicated the thermal energy disturbs the stable magnetization and decreases the magnetization reversal energy. Superparamagnetic behaviour was observed for the Mn_3O_4-PEI-1.0g-RT and Mn_3O_4-PEI-0.5g-RT at 20 K, where it showed zero M_r and zero H_C. Further experiments on the DC magnetization and AC susceptibility gave more solid evidence.

Fig.4.31 shows the temperature dependence of field cooling (FC) and zero field cooling (ZFC) magnetization measured at 200 Oe for these four samples. The ferrimagnetic transition is characterized by a divergence between FC and ZFC curves. The T_N is marked by the T_{max} on the ZFC curves, which is close to 42 K of the bulk Mn_3O_4. The T_N was observed at 26 K, 35 K, 38 K and 42 K for (a), (b), (c), and (d) samples, respectively. A secondary maximum was observed for samples a and b at temperatures of 3 K and 10 K, respectively. This phenomenon, which was also observed in the AC susceptibility characteristics, is most likely caused by superparamagnetic relaxation due to the extremely small particle sizes. It is known that in Mn_3O_4 nanoparticles, superparamagnetic behaviour can be observed only if the superparamagnetic blocking temperature T_B is lower than the ferrimagnetic Néel temperature T_N.

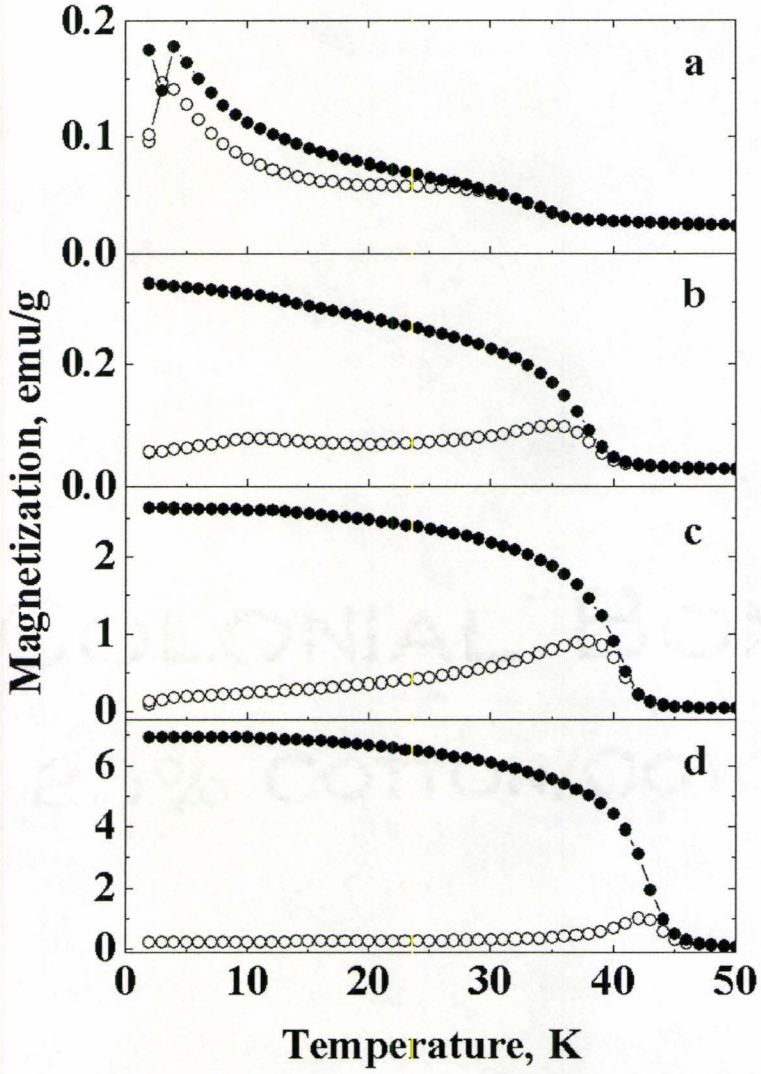

Figure 4.31 Temperature dependence of FC (•) and ZFC (○) magnetization measured at 200 Oe for the deposits prepared from the 5 mM $MnCl_2$ solutions containing (a) 1.0 g/l PEI and 0.5g/l PEI (b, c, d), (b) as prepared and (c, d) annealed at 200 and 300 °C

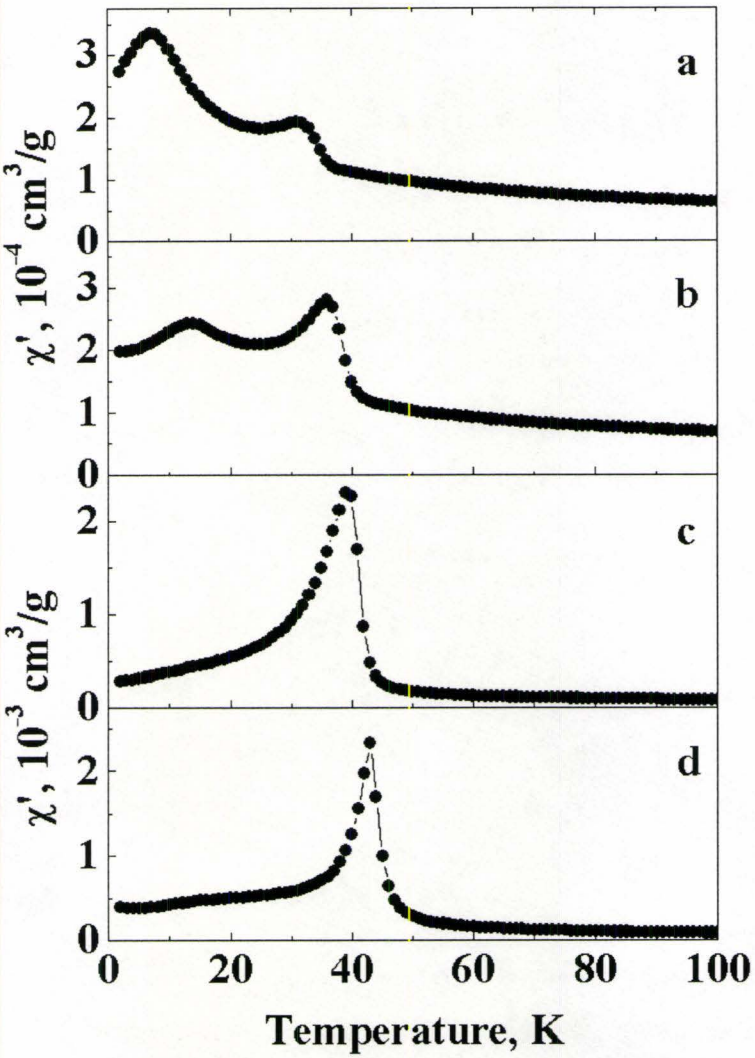

Figure 4.32 Real parts of AC magnetic susceptibility versus temperature at 10 kHz for the deposits prepared from the 5 mM $MnCl_2$ solution containing (a) 1.0 g/l PEI and (b, c, d) 0.5 g/l PEI, in which (b) as prepared and (c, d) annealed at 200 and 300 °C

Fig.4.32 shows the real parts (χ') of AC susceptibility versus temperature at 10 kHz for the Mn_3O_4-PEI-1.0g-RT, Mn_3O_4-PEI-0.5g-RT, Mn_3O_4-PEI-0.5g-200, and Mn_3O_4-PEI-0.5g-300 samples. The Néel temperature T_N was characterized by a relaxation peak

at T_{max}, giving a T_N value of 31 K, 36 K, 39 K, and 43 K for the samples (a) to (d). A secondary peak was observed in the fresh deposits, Mn_3O_4-PEI-1.0g-RT, and Mn_3O_4-PEI-0.5g-RT (samples (a) and (b), Fig.4.32 a, b) at the temperatures of 7 K and 14 K, respectively. It can be caused by the superparamagnetic relaxation marked by the blocking temperature T_B.

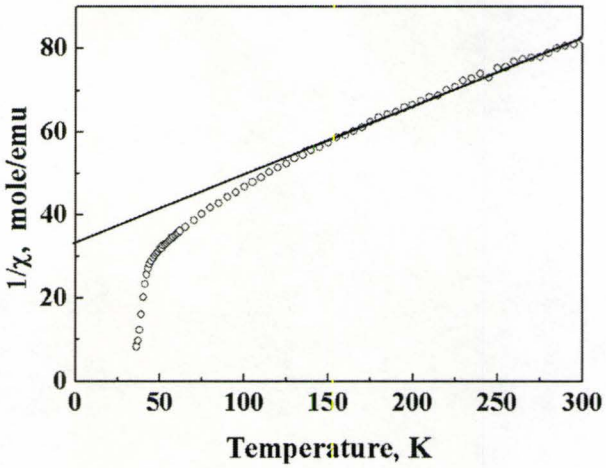

Figure 4.33 Temperature dependence of the inverse susceptibility in the paramagnetic range for the deposits prepared from the 5 mM $MnCl_2$ solutions containing 0.5g/l PEI. Solid line is the best-fit to Eq.1.13

The temperature dependence of the inverse of susceptibility $1/\chi$ in the paramagnetic region for sample Mn_3O_4-PEI-0.5g-RT is shown in Fig.4.33. The measurements were taken in a field of 500 Oe. The fitting of the linear region of $1/\chi$ (150 K to 300 K) to a linear approximation $\frac{1}{\chi}=\frac{T}{C}+\frac{1}{\chi_0}$ (Eq.1.13) with the parameters, $1/\chi_0$ = 33.9 and C = 6.14 is shown as the solid line on the graph. The analysis gave a paramagnetic Curie point θ = 208 K.

4.2.2 Electrodeposition of $NiFe_2O_4$ using PEI

In the previous investigations [224], cathodic electrosynthesis of the composite films consisting of Ni/Fe hydroxide and polyethylenimine (PEI) were developed. In the current work, the characterization of the magnetic properties of Ni/Fe complex oxide was being carried out.

The deposits were analyzed by X-ray diffraction before and after annealing in air at different temperatures for one hour. In Fig.4.34, XRD patterns of the as prepared deposit indicated their amorphous nature (Fig.4.34 a). After annealing at 300°C and 400°C, the deposit showed small broadened peaks belonging to the spinel structured $NiFe_2O_4$ phase (JCPDS file #10-325) (Fig.4.34 b, c). The peak broadening is caused by small grain size. The X-ray diffraction patterns of deposits annealed at 600 °C and 800 °C showed that they have $NiFe_2O_4$ structure (Fig.4.34 d, e). The intensity of the peaks increased with increasing temperatures, which infers the growth of the crystal size.

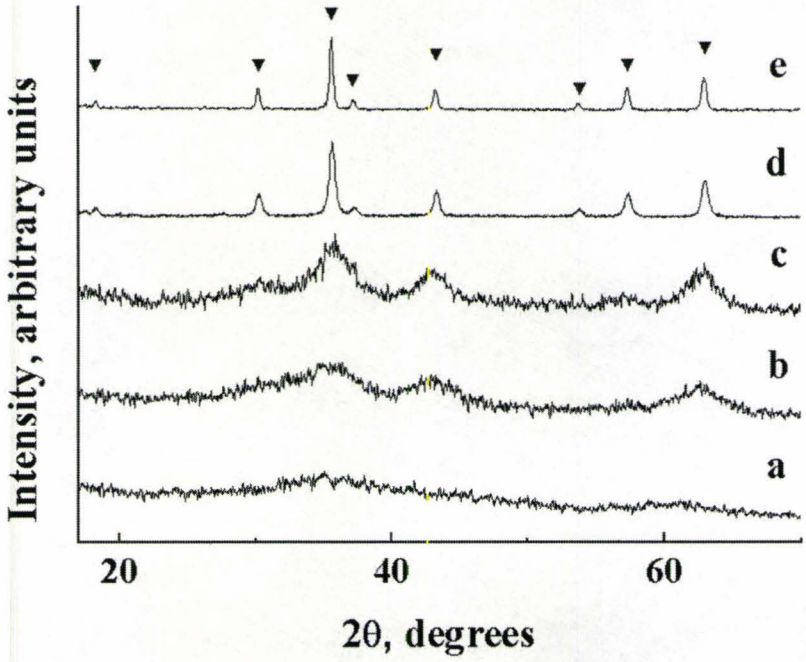

Figure 4.34 X-ray diffraction of the deposit from 5 mM $FeCl_3$ and 2.5 mM $NiCl_2$ solutions containing 0.4 g/l PEI, as prepared (a) and those annealed at 300 (b), 400 (c), 600 (d), and 800 °C (e) for 1 hour. ▼- $NiFe_2O_4$, JCPDS file #10-325.

The SEM surface image of the deposit sintered at 600 °C is shown in Fig.4.35. An interesting observation regarding the deposit microstructure was that it consisted of submicron rods with the length of about 1 μm and the diameter of less than 0.1 μm.

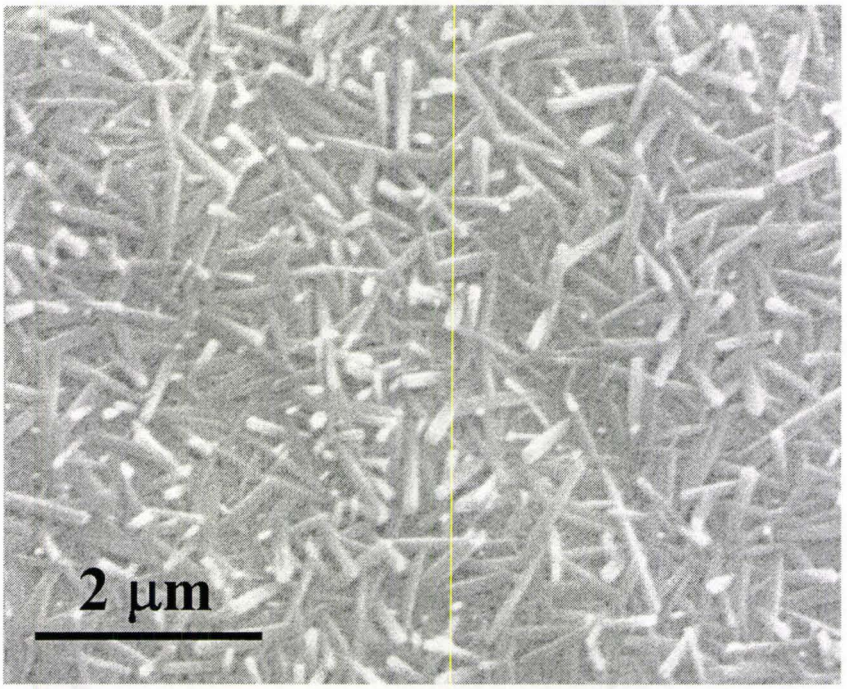

Figure 4.35 SEM image of the deposits prepared from 5 mM $FeCl_3$ and 2.5 mM $NiCl_2$ solutions containing 0.4 g/l PEI on silver wire substrate and annealed in air at 600 °C for 1 hour

Magnetic properties of $NiFe_2O_4$ nanostructures

Magnetic properties were studied with a Quantum Design PPMS-9 System for the deposits prepared from the 5 mM $FeCl_3$ and 2.5 mM $NiCl_2$ solutions containing 0.4 g/l PEI after annealed at 600 °C and 800 °C for 1 hour. For convenience, in the following chapters, they were labeled as $NiFe_2O_4$-PEI-600 and $NiFe_2O_4$-PEI-800, respectively.

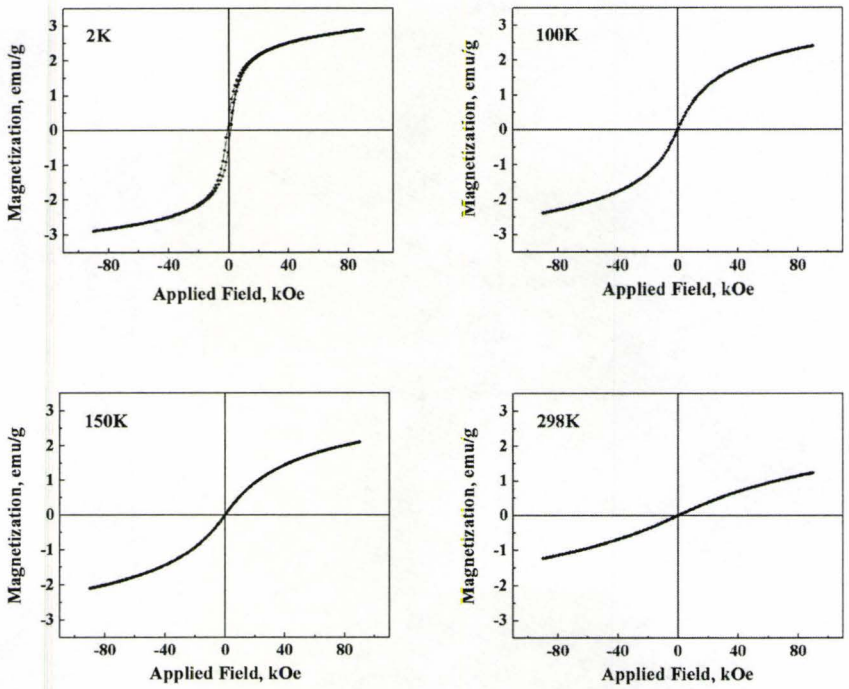

Figure 4.36 Magnetization versus the applied field in 9 T range measured at temperatures of 2 K, 100 K, 150 K and 298 K for the deposits obtained from 5 mM $FeCl_3$ + 2.5 mM $NiCl_2$ solutions containing 0.4 g/l PEI after annealing at 600 °C for 1 hour.

Figure 4.36 shows the magnetization versus high applied field in 9 T range measured at different temperatures for the $NiFe_2O_4$-PEI-600. At a temperature of 2 K, the magnetization data showed ferrimagnetism with non-zero remnant magnetization and non-zero coercive force. When the measuring temperature increased to 100 K and above, no hysteresis loop was observed and the curves showed zero remanence and zero coercivity. This suggested that the sample was superparamagnetic at temperature of 100 K and above. The magnetization of the sample decreased with increasing temperature and did not saturate even at the maximum applied field of 9 Tesla.

Zero remanence and zero coercivity are observed in the superparamagnetic state for very small particles because thermal fluctuations can prevent the existence of a stable magnetization. Below the blocking temperature, magnetic particles become magnetically frozen, and as a result, remanence and coercivity appear on the plot of magnetization as a function of applied field.

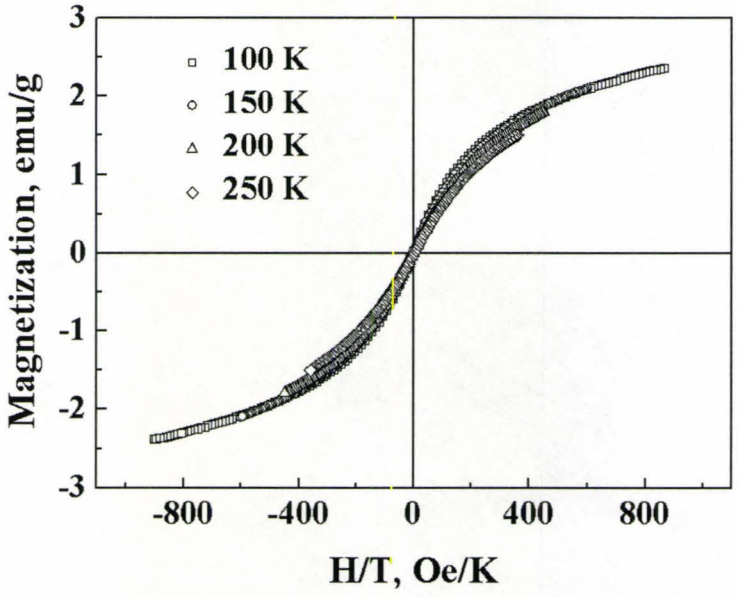

Figure 4.37 Magnetization versus temperature normalized field in the superparamagnetic state for the deposits annealed at 600 °C

Fig.4.37 shows the magnetization behavior versus temperature normalized field (H/T) for the $NiFe_2O_4$-PEI-600 at temperatures higher than the blocking temperature. In the superparamagnetic state, the magnetization curves obtained at different temperatures can be superimposed in a plot of M=f(H/T). As shown in Fig.4.37, the magnetization versus H/T plots between 100 K and 250 K were almost ideally superimposed, and only small

deviations from the superimposed line were observed for characteristics obtained at higher temperatures 200 K and 250 K

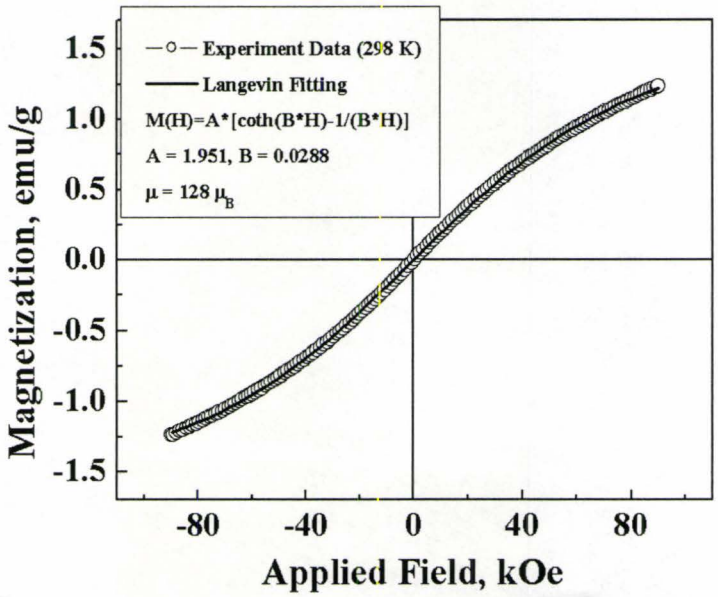

Figure 4.38 Magnetization versus applied field in 9 T at temperature of 298 K. The solid line represents the best fit of the experimental data using Langevin function

In order to evaluate the magnetic moment per particle μ, two approaches were used. In the first approach, the magnetization versus applied field in the superparamagnetic state was fitted by the Langevin function, as shown in Fig.4.38:

$$M = M_S L\left(\frac{\mu H}{k_B T}\right) = M_S\left[\coth\left(\frac{\mu H}{k_B T}\right) - \frac{k_B T}{\mu H}\right] \qquad 4.6$$

where M is magnetization in emu/g, M_S is saturation magnetization taken as 1.95 emu/g in this case, μ is magnetic moment per particle, k_B the Boltzmann constant and T the absolute temperature. It showed almost ideal Langevin-type behaviour of the

paramagnetic materials, which gave μ = 128 μ_B per particle (μ_B is Bohr magneton) at 298 K (Fig.4.38).

Alternatively, the magnetic moment per particle μ was estimated using the relationship derived by Chantrell and coworkers for ferrofluids:

$$\mu = 3k_B T\sqrt{\frac{\chi_i}{3M_S}\frac{1}{H_0}} \qquad 4.7$$

where χ_i is the initial susceptibility of the magnetization (emu/gOe), M_S is the saturation magnetization (emu/g). The initial susceptibility χ_i was found from linear fitting of M versus H curve in zero field region (Fig.4.39 a). Values of M_S and $1/H_0$ are obtained from plotting the magnetization versus the inverse of the applied field (1/H) at the high field regime, where the relationship was linear (Fig.4.39 b). The value of the M_S is obtained by extrapolating the linear fitting of the experimental data to zero value of 1/H, i.e., M_S=M(1/H$\rightarrow$0). On the other hand $1/H_0$ is obtained by extrapolating to zero magnetization, i.e., $1/H_0$=1/H(M$\rightarrow$0). For the case of magnetization measured at 298 K shown in Figure 6 for which the initial susceptibility $\chi_i = 2.069*10^{-5}$ emu/gOe, M_S = 1.85 emu/g and $1/H_0 = 3.30*10^{-5}$ Oe^{-1}, the magnetic moment per particle was obtained as μ = 148 μ_B. These two approaches matched very well with each other. Small deviation is expected because Chantrell's model takes account of the particle size distribution whereas the Langevin function assumes identical particle size.

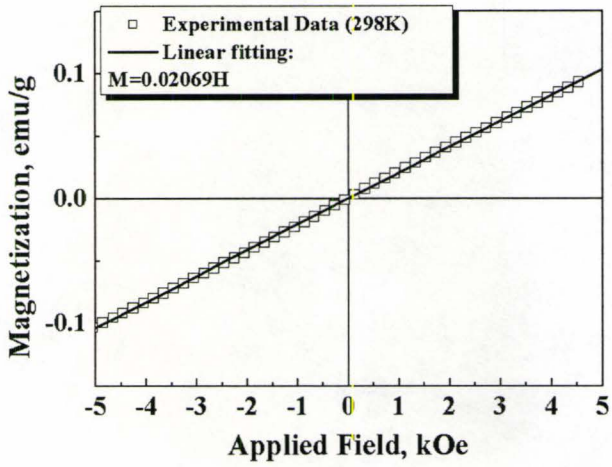

(a)

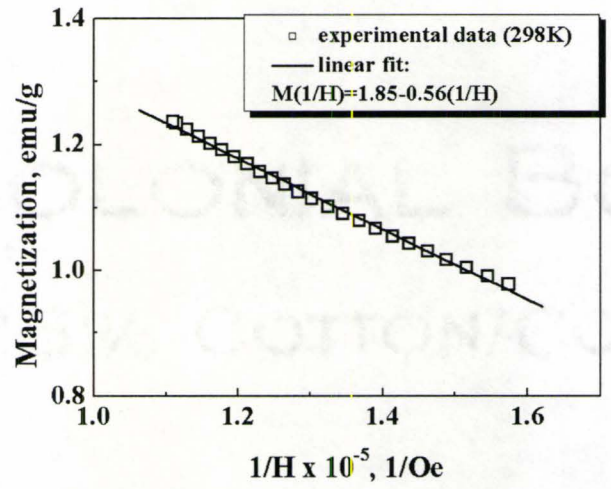

(b)

Figure 4.39 Chantrell's model to obtain the magnetic moment per particle: (a) the initial susceptibility obtained from the linear fitting of M versus H. (b) linear fitting of M versus 1/H. Both magnetization curves were measured at 298 K.

Magnetization curves versus applied field in 1 T range measured at different temperatures for the $NiFe_2O_4$-PEI-600 are shown in Fig.4.40. The magnetization curves showed hysteresis loops at temperatures of 2 K and 5 K, while they vanished at the

temperature 10 K and above. The coercive force at temperatures of 2 K and 5 K was found to be 870 Oe and 270 Oe, respectively. The remnant magnetization was 0.21 emu/g and 0.08 emu/g at temperatures of 2 K and 5 K.

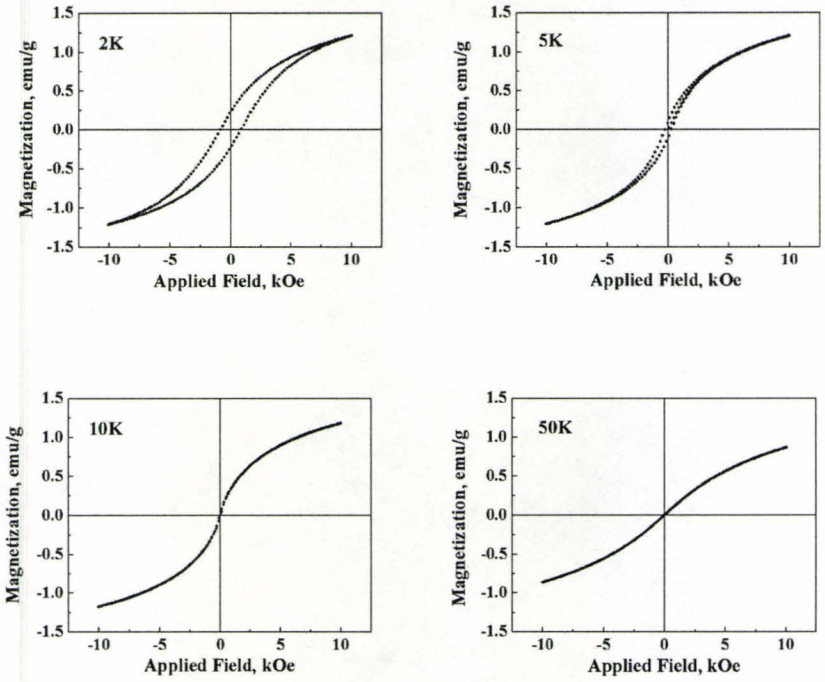

Figure 4.40 Magnetization versus applied field in the 1 T range measured at temperatures of 2, 5, 10 and 50 K for the deposit prepared from 5 mM $FeCl_3$ and 2.5 mM $NiCl_2$ solutions containing 0.4 g/l PEI after annealing at 600 °C

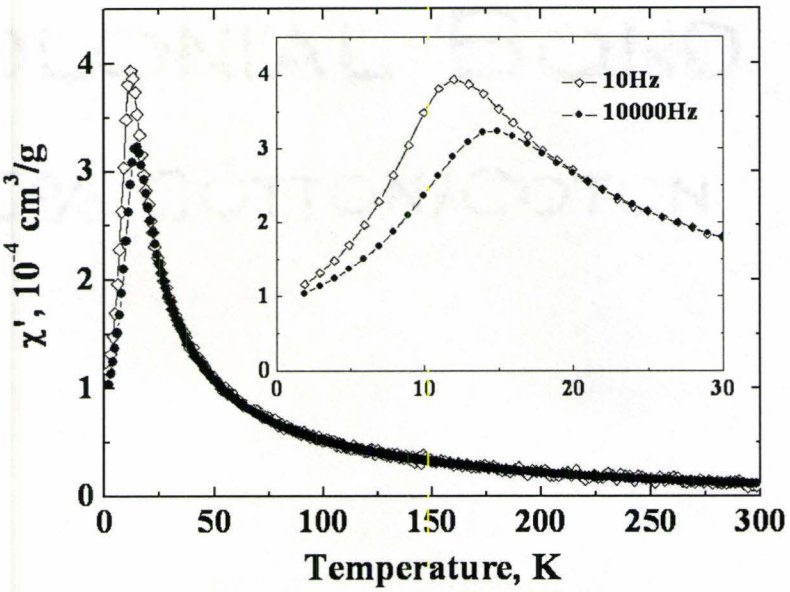

Figure 4.41 Temperature dependence of the real part (χ') of AC susceptibility measured at frequencies between 10 Hz and 10 kHz for the deposit prepared from 5 mM $FeCl_3$ and 2.5 mM $NiCl_2$ solutions containing 0.4 g/l PEI after annealing at 600 °C.

Fig.4.41 shows the temperature dependence of the real part χ' of the complex AC susceptibility, which was also measured in the frequency range 10 Hz to 10 kHz. The peaks in the real part (χ') of AC susceptibility arise from the superparamagnetic relaxation, and the T_{max} in the curve corresponds to the blocking temperature T_B. As frequency changes, the curves split from each other at a temperature below T_{max} and slightly above it, while they are superimposed in the $T > T_{max}$ region, in which superparamagnetic behavior is observed. As the frequency is increased, T_{max} shifts to higher temperature, and T_B obtained from the real part (χ') of AC susceptibility was 12 K and 15 K at 10 Hz and 10 kHz, respectively. Relatively weak frequency dependence of blocking temperature was observed in these nanocomposites.

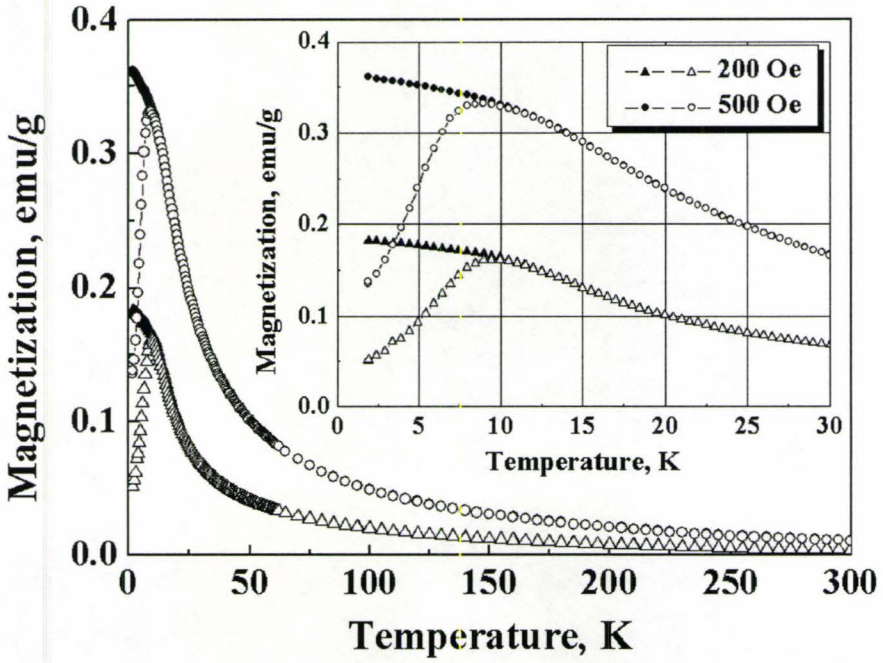

Figure 4.42 Temperature dependence of FC (solid symbols) and ZFC (open symbols) of DC magnetization measured at 200 Oe (triangle) and 500 Oe (circle) for the deposit prepared from 5 mM $FeCl_3$ and 2.5 mM $NiCl_2$ solutions containing 0.4 g/l PEI after annealing at 600 °C for one hour. The inset is the low temperature region.

DC magnetization was investigated for the $NiFe_2O_4$-PEI-600. Fig.4.42 shows temperature dependence of zero-field-cooled (ZFC) and field cooled (FC) DC magnetization curves measured at low magnetic fields of 200 Oe and 500 Oe. On increasing the temperature from 2 K to 300 K, ZFC magnetization increased with a maximum at T_{max} and then decreased, while FC magnetization decreased with temperature over the whole temperature regime. At temperatures below T_{max}, FC magnetization diverged from the ZFC curve and the two curves merged and followed one superimposed characteristic at temperatures slightly higher than T_{max}, for a given applied

field, as shown in Fig.4.42. It is believed that the system is in a superparamagnetic state when FC and ZFC curves superimpose. Increasing the magnetic field caused the T_{max} of the ZFC magnetization to be shifted towards lower temperatures. As indicated in the inset of Fig.4.42, T_{max} was 9.5 K and 9.0 K for an applied field of 200 Oe and 500 Oe, respectively.

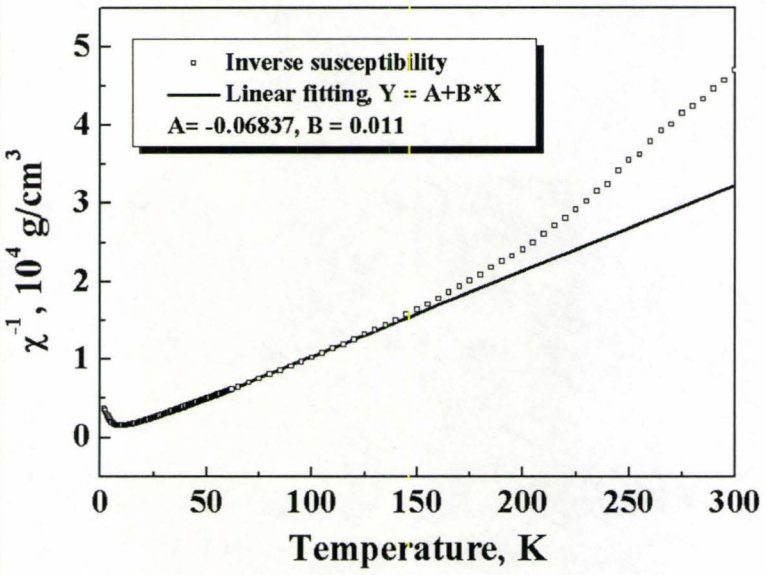

Figure 4.43 Inverse magnetic susceptibility as a function of temperature obtained from the ZFC curve measured at 500 Oe (From Fig.4.42 open circle)

Fig.4.43 represents inverse magnetic susceptibility (g/cm^3) as a function of temperature for the ZFC curve measured at the low field of 500 Oe. In the superparamagnetic regime where FC and ZFC curves merge, the temperature dependence of the inverse susceptibility is given by a linear relationship [225]:

$$\frac{1}{\chi} = \frac{T - \Theta_{SP}}{C} \qquad 4.8$$

Where Θ_{SP} is the superparamagnetic constant, and the Curie constant $C = \langle V \rangle M^2(T)/3k_B$ for low applied field, M(T) is saturation magnetization at temperature T, and $\langle V \rangle$ is the average volume of particles.

In Fig.4.43, a straight line was not obtained, and deviation from linear behaviour was observed in the high temperature region in the superparamagnetic state. The deviation could be due to M(T) thermal variation. A correction for $1/\chi$ data can be done by using the M(T)/M(0) ratios deduced from magnetization data, then a straight can be expected [225].

Magnetic properties of the deposits prepared from 5 mM $FeCl_3$ and 2.5 mM $NiCl_2$ solutions containing 0.4 g/l PEI after annealing at 800 °C showed very different behavior.

Fig.4.44 shows magnetization versus high applied field in the 9 T range measured at 2, 100, 150 and 298 K for the deposits annealed at 800 °C. All the curves showed hysteresis loops, which were marked by non-zero coercive force H_C and remnant magnetization M_r. The magnetization of the sample decreased with increasing temperature, and it was saturated in the applied field range of 9 Tesla. The saturation magnetization reached 45 emu/g and 41 emu/g at 2 K and 298 K, respectively.

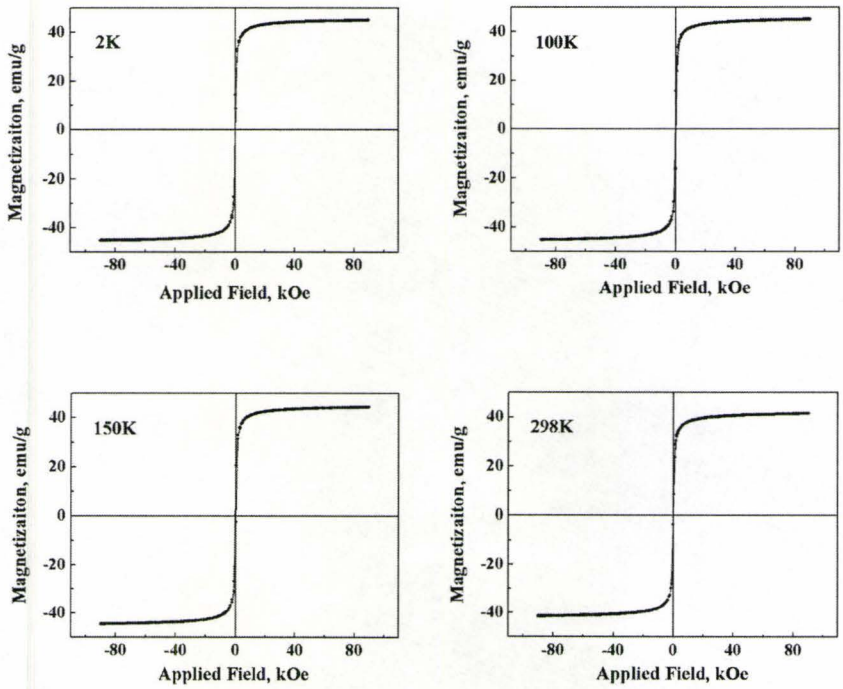

Figure 4.44 Magnetization versus applied field in the 9T range measured at 2, 100, 150 and 298 K for the deposit prepared from 5 mM $FeCl_3$ and 2.5 mM $NiCl_2$ solution containing 0.4 g/l PEI and after annealing at 800 °C.

One explanation for the difference in the magnetization versus applied field data between the deposits annealed at 600 °C and 800 °C can be the particle size difference. The deposit annealed at 600 °C consists of submicron rods with a length of about 1 μm and diameter of less than 0.1 μm. On the other hand the deposit annealed at 800 °C contains a larger particle size, which is beyond the critical size required to determine its superparamagnetic behavior at room temperature.

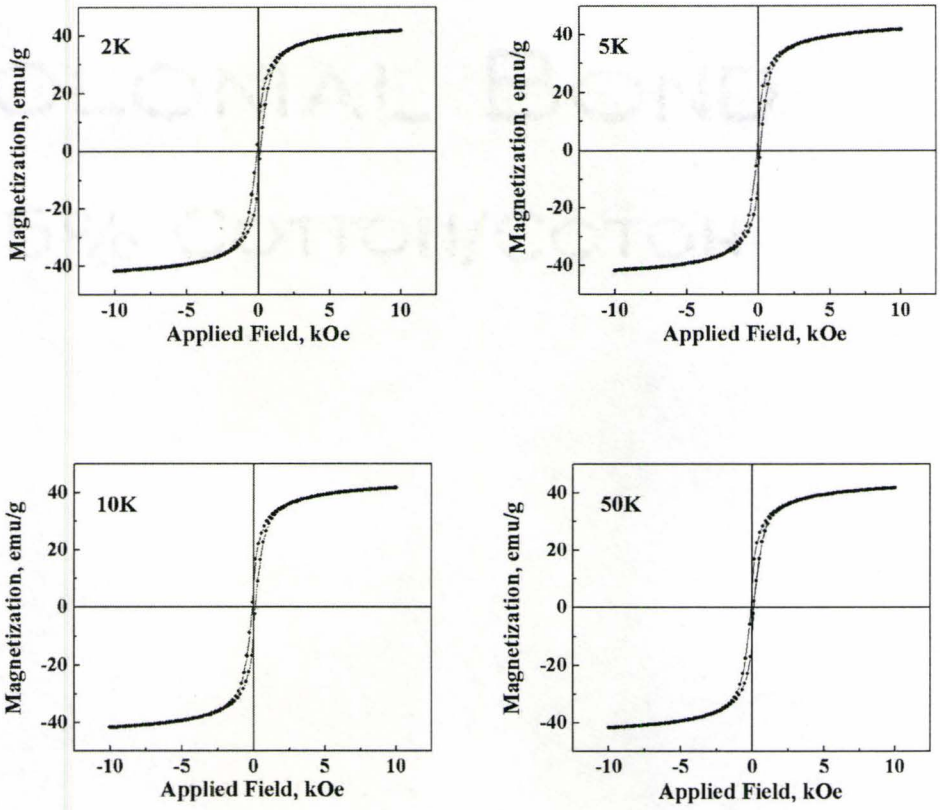

Figure 4.45 Magnetization versus applied field in the 1 T range measured at 2, 5, 10 and 50 K for deposits from 5 mM $FeCl_3$ and 2.5 mM $NiCl_2$ solutions containing 0.4 g/l PEI after annealing at 800 °C

Magnetization curves versus applied field in 1 T range measured at different temperatures for the deposit annealed at 800 °C are shown in Fig.4.45. The magnetization curves show hysteresis loops at all the temperatures up to 298 K. The coercive force is found to be much smaller than in the previous sample, with a value of about 100 Oe at temperatures of 2 K. The remnant magnetization is about 2.5 emu/g at the temperature of 2 K.

Fig.4.46 shows the temperature dependence of the real part χ' of the complex AC susceptibility, which is measured in the frequency range between 10 Hz and 10 kHz for the deposit annealed at 800 °C. The data show no peaks corresponding to the superparamagnetic relaxation up to room temperature.

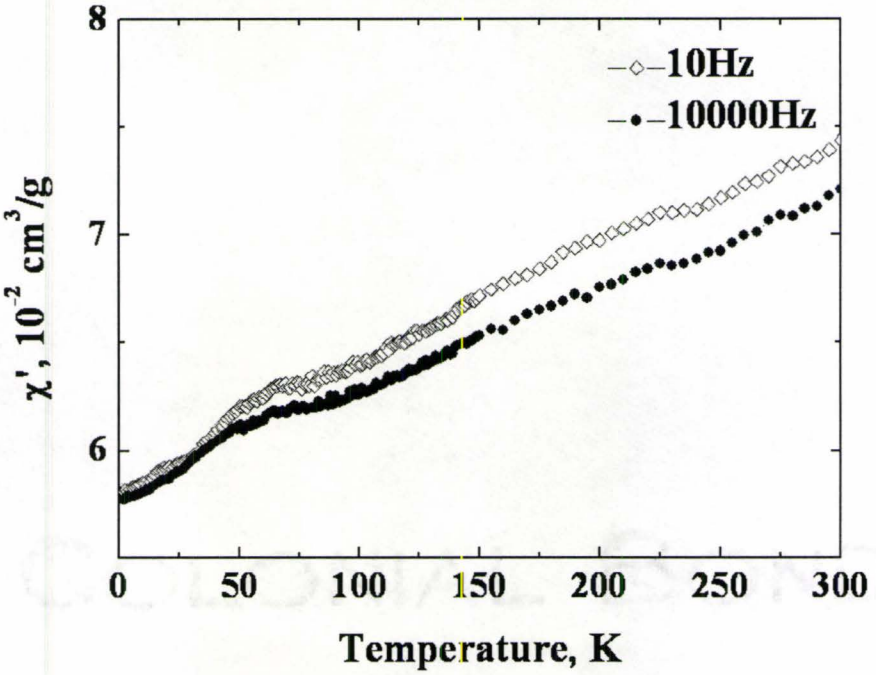

Figure 4.46 Temperature dependence of real part (χ') of AC susceptibility measured at frequencies of 10 Hz and 10 kHz for the deposit prepared from 5 mM $FeCl_3$ and 2.5 mM $NiCl_2$ solution containing 0.4 g/l PEI after annealing at 800 °C.

Fig.4.47 shows the temperature dependence of ZFC and FC magnetization in low applied fields of 200 Oe and 500 Oe for the deposit annealed at 800 °C. In the temperature range from 2 K to 298 K, FC magnetization (Fig.4.47 a, c) decreases with increasing temperature, and FC magnetization diverges from the ZFC curve over the whole temperature regime.

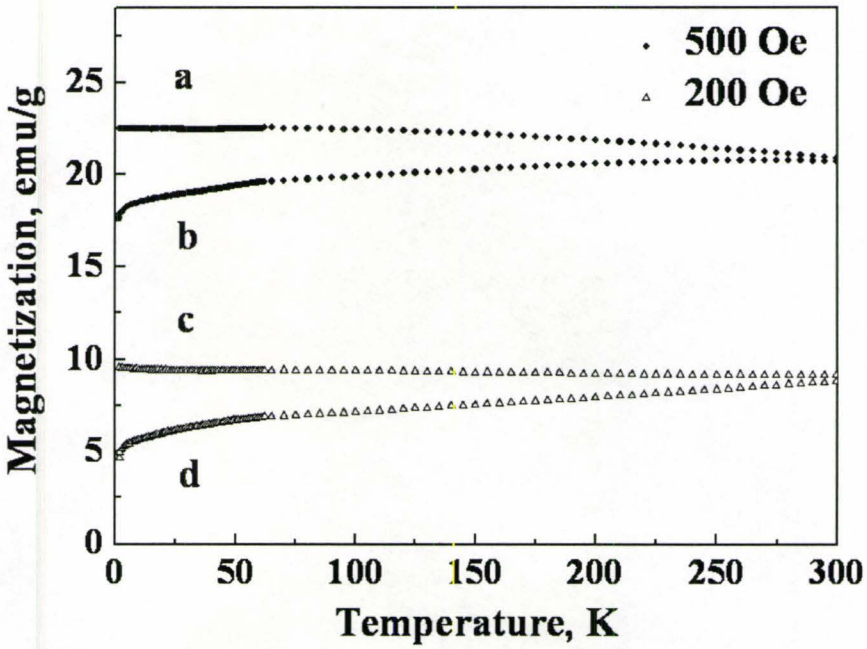

Figure 4.47 Temperature dependence of FC (a, c) and ZFC (b, d) magnetization measured at 200 Oe and 500 Oe for the deposit prepared from 5 mM $FeCl_3$ and 2.5 mM $NiCl_2$ solutions containing 0.4 g/l PEI after annealing at 800 °C.

4.2.3 Electrodeposition of $MnFe_2O_4$ using PEI

Electrodeposition was performed from 5 mM $FeCl_3$ and 2.5 mM $MnCl_2$ solutions containing 1.0 g/l PEI at a current density in the range of 1 - 5 mA/cm^2 for a deposition time of 0.5 - 5 min. X-ray diffraction is used to study the phase content in the deposits after annealing at different temperatures of 800 °C, 1000 °C and 1200 °C for 1 hour. As visible in Fig.4.48, the phase content changes from Mn_2O_3, Mn_2O_3 / Fe_2O_3 mixture to the pure $MnFe_2O_4$ spinel phase for sample annealed at 800 °C, 1000 °C to 1200 °C.

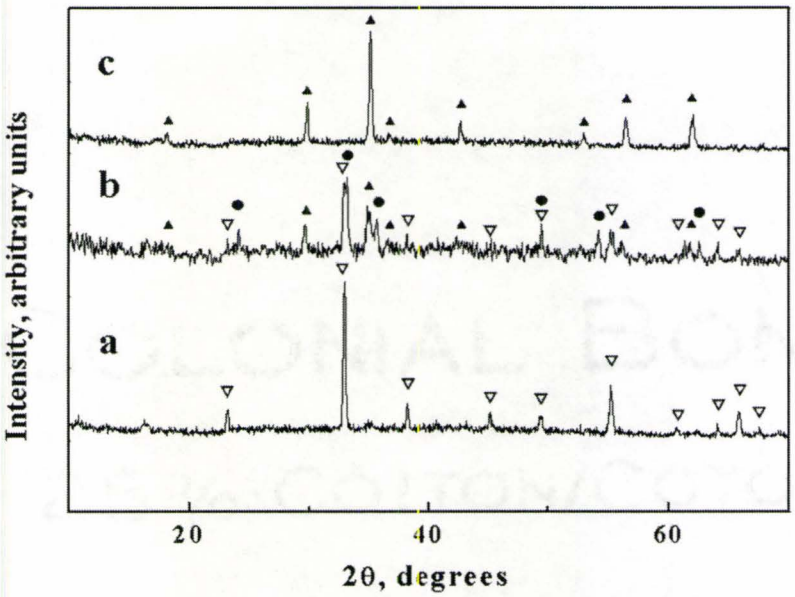

Figure 4.48 X-ray diffraction pattern for deposits prepared from 5 mM $FeCl_3$ and 2.5 mM $MnCl_2$ solutions containing 1.0 g/l PEI after annealing at (a)800, (b)1000 and (c)1200 °C for 1 hour. ▲-$MnFe_2O_4$, ● -α-Fe_2O_3, ∇ -Mn_2O_3

The deposit annealed at 800 °C has been studied by the Energy Dispersion Spectroscopy (EDS) technique. Although the XRD data shows that only Mn_2O_3 phase is

present without traces of Fe species, the standard-less EDS analysis gives the atomic ratio of Mn and Fe close to 1:2, as shown in following Table 4.1, which indicates co-deposition of Mn and Fe species.

Table 4.1 A qualitative standard-less EDS analysis results of $MnFe_2O_4$ deposit

Element	Wt%	% oxide	atom %	app. conc%	ZAF factor	3 sigma
O	22.37		50.00	0.05		
Mn	26.81	34.62	17.45	34.07	0.934	1.5585
Fe	50.82	65.38	32.55	65.88	0.953	2.4520

When increasing the annealing temperature to 1000 °C, the XRD results show the peaks of Fe_2O_3 phase. In the meanwhile, $MnFe_2O_4$ phase starts forming and after annealed at 1200 °C for 1 hour, only $MnFe_2O_4$ spinel phase is observed in the deposit.

4.3 Nanocomposite based on Chitosan

Chitosan is a natural cationic polysaccharide that can be produced by alkaline N-deacetylation of chitin. Important properties of this material, such as antimicrobial activity, chemical stability, biocompatibility, and advanced mechanical properties, have been utilized in biotechnology. Water soluble and positively charged chitosan can be prepared by the protonation of amine groups in acidic solutions:

$$CHIT\text{-}NH_2 + H_3O^+ \rightarrow CHIT\text{-}NH_3^+ + H_2O \qquad 4.9$$

At pH 6.5, the primary amine groups of CHIT become deprotonated. The charges of chitosan decreases with increase of pH and dissolved chitosan usually flocculates at pH above 6.5.

Electric field provides the motion of the charged chitosan macromolecules towards the cathode surface. It is suggested that the cathodic reactions, such as:

$$2H_2O + 2e^- \rightarrow H_2 + 2OH^- \qquad 4.10$$

result in an increase of pH value at the electrode surface. Therefore, chitosan loses its charge and forms an insoluble deposit on the cathode surface:

$$CHIT\text{-}NH_3^+ + OH^- \rightarrow CHIT\text{-}NH_2 + H_2O \qquad 4.11$$

The results of the current work demonstrate the possibility of the fabrication of composite films using a combined deposition method based on the electrolytic deposition (ELD) of metal oxide and electrophoretic deposition (EPD) of chitosan

4.3.1 Electrodeposition of γ-Fe_2O_3 using chitosan

Cathodic electrodeposition was developed for the fabrication of nanocomposites containing γ-Fe_2O_3 particles in the chitosan matrix. The proposed method was based on the electrosynthesis of γ-Fe_2O_3 and electrophoretic deposition of cationic chitosan macromolecules. The electrodeposition was performed from 5 mM $FeCl_3$ solution containing 0.2 – 0.3 g/l chitosan at a current density in the range of 1 – 5 mA/cm^2 for a deposition time of 0.5 – 5 min.

Structural characterization of γ-Fe_2O_3-Chitosan nanocomposite

The deposits were analyzed by XRD before and after annealing in air at different temperatures. Fig.4.49 shows X-ray diffraction pattern of the deposits prepared from 5mM $FeCl_3$ solutions containing 0.2 g/l chitosan. The fresh deposit and those annealed at 200 °C exhibited a small peak around $2\theta = 36°$. After annealing at 300 °C, broadened peaks, which can be attributed to γ-Fe_2O_3 or Fe_3O_4, were observed. However, it is difficult to distinguish between γ-Fe_2O_3 and Fe_3O_4 due to the similar spinel structure of the both phases and peak broadening. Moreover, the two phases can form solid solutions. After annealing at 400 °C, the X-ray diffraction pattern showed pure phase of α- Fe_2O_3.

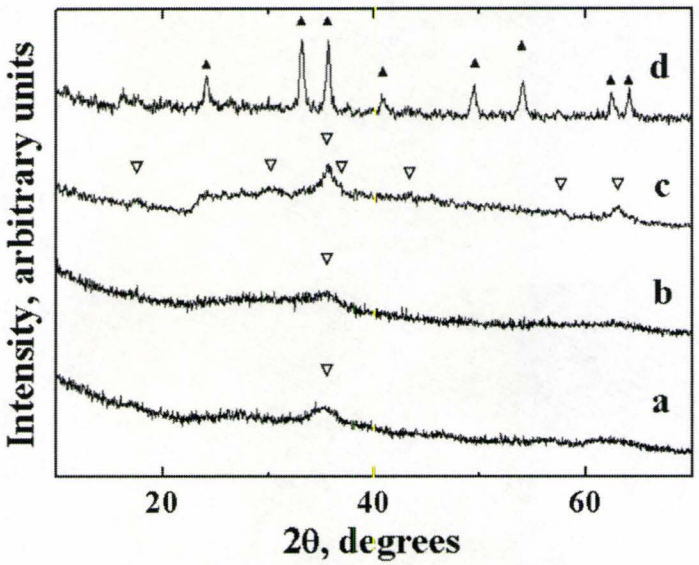

Figure 4.49 X-ray diffraction patterns for the deposits prepared from 5 mM FeCl3 solution containing 0.2 g/l chitosan: (a) as-prepared, and those annealed at (b) 200 (c) 300 and (d) 400 °C for 1 hour. ∇ - γ-Fe_2O_3 (JCPDS 39-1346), ▲ - α-Fe_2O_3 (JCPDS 33-664).

Fig.4.50 shows X-ray diffraction patterns of the deposits prepared from 5mM $FeCl_3$ solutions containing 0.3 g/l chitosan. The fresh deposit and those annealed at and below 200 °C exhibited a small peak around 2θ = 36 °. After annealing at 300 °C, Fig.4.50 d, the X-ray showed peaks of spinel iron oxide phase. The XRD pattern of the sample annealed at and above 400 °C exhibited the major peaks of α- Fe_2O_3.

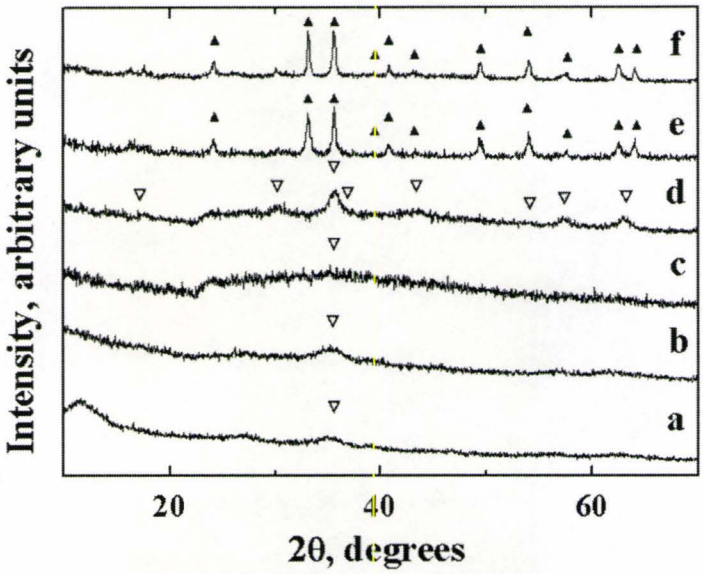

Figure 4.50 X-ray diffraction patterns for the deposits prepared from 5mM FeCl3 solution containing 0.3 g/l chitosan: (a) as-prepared, and those after annealing at (b) 100, (c) 200 (d) 300 (e) 400 and (f) 500 °C for 1 hour. ∇ - γ-Fe_2O_3 (JCPDS 39-1346), ▲ - α-Fe_2O_3 (JCPDS 33-664).

Fig.4.51 shows TG and DTA curves for the deposits prepared from 5 mM $FeCl_3$ solutions containing 0.2 g/l chitosan. The TG data (Fig.4.51 a) showed total weight loss of 41.2% of the initial weight, with three steps in the weight loss in the temperature ranges of 50-150 °C, 200-400 °C and 450-500 °C. The corresponding DTA data (Fig.4.51 b) showed one endotherm around 100 °C and several exotherms in the range of 200-500 °C.

The DTA data is in good agreement with the results of TG studies. The endotherm at 100 °C is associated with water evaporation and corresponding weight loss of 10% is observed in the TG. The exotherms in the range of 200-500 °C can be attributed to burning out of chitosan and the γ-$Fe_2O_3 \rightarrow \alpha$-$Fe_2O_3$ transformation. Considering the

composite material as a mixture of organic and inorganic components, the content of an organic phase was found to be 41.2 wt%, obtained from TG data.

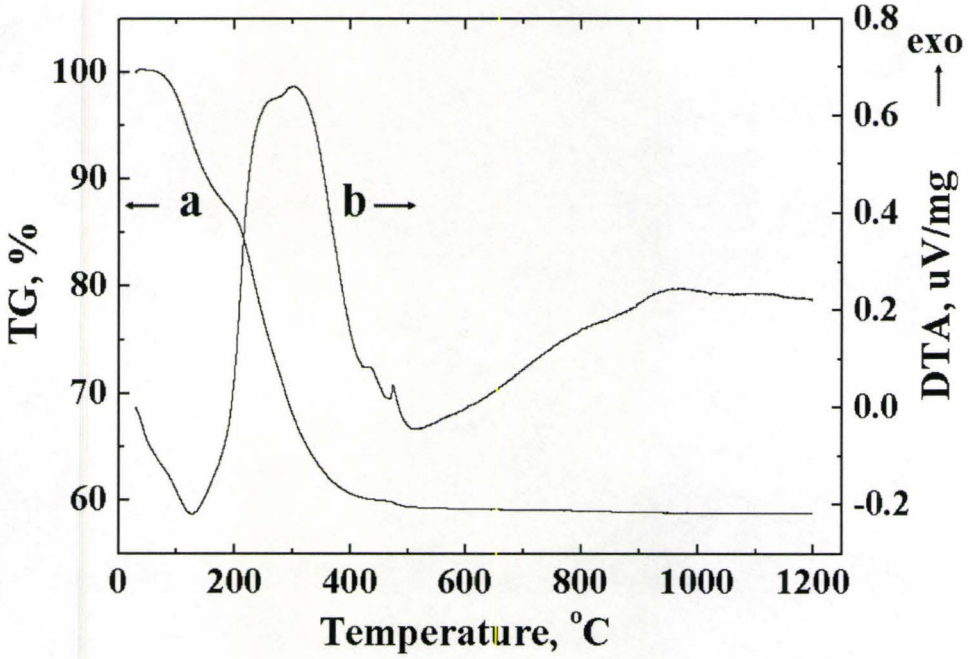

Figure 4.51 TG (a) and DTA (b) data for the deposits prepared from 5 mM $FeCl_3$ solutions containing 0.2 g/l chitosan.

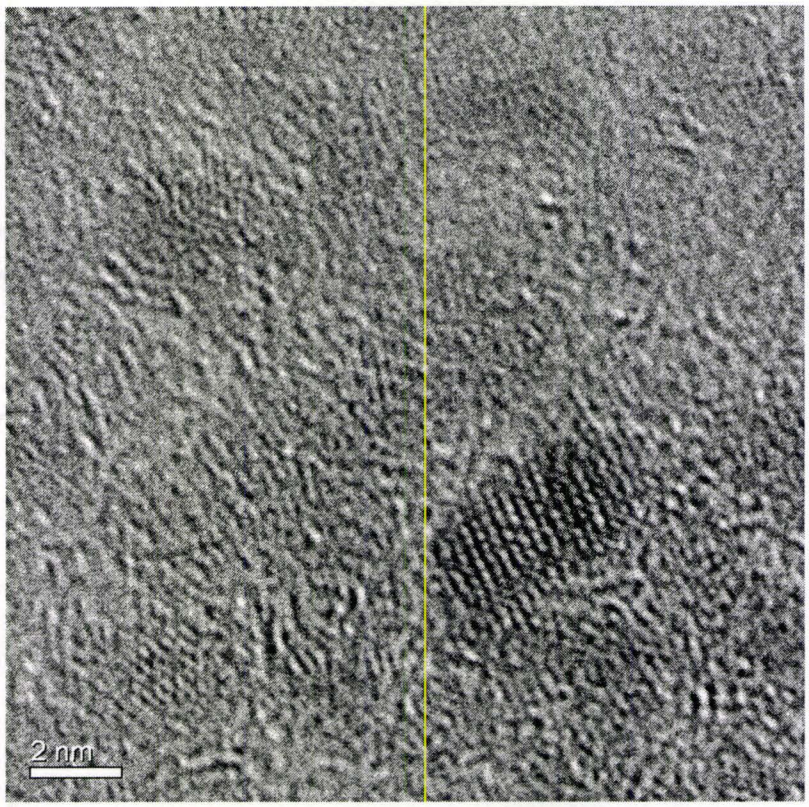

Figure 4.52 HRTEM images for the deposits prepared from the 5 mM $FeCl_3$ solutions containing 0.2 g/l chitosan

Fig.4.52 shows HRTEM images of the nanocomposite deposits obtained from the 5 mM $FeCl_3$ solutions containing 0.2 g/l chitosan. The γ-Fe_2O_3 nanoparticles were randomly distributed *in situ* within the chitosan. The average particle size was estimated around 3.2 ± 0.5 nm by counting numerous images.

Magnetic properties of γ-Fe_2O_3-chitosan nanocomposite

In the following chapters, the fresh deposit obtained from the 5 mM $FeCl_3$ solutions containing 0.2 g/l chitosan was labelled as FeChi-RT, and those annealed at 300°C for 1 hour as FeChi-300.

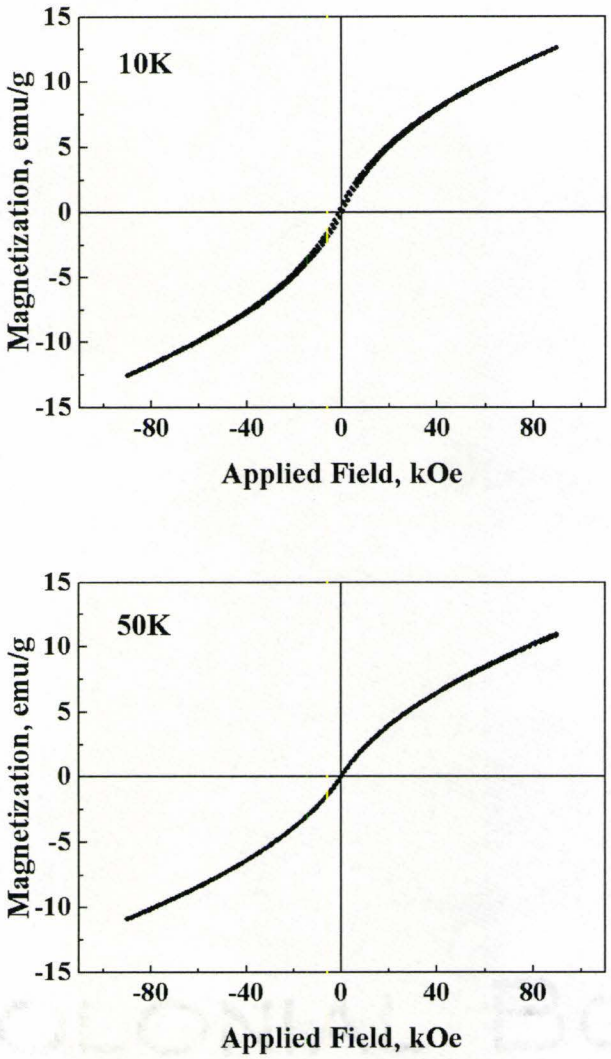

Figure 4.53 Magnetization versus applied field measured at temperatures of 10 K and 50 K for FeChi-RT.

Fig.4.53 shows the magnetization curve for FeChi-RT. The magnetization data obtained at 10 K exhibited the hysteresis loop with the small coercive force of less than 300 Oe. The curves measured at temperatures of 50 K and above indicate that the sample is in superparamagnetic state, with zero coercive force and zero remnant magnetization.

By fitting the magnetization versus applied field data in the superparamagnetic state, two approaches can be used to evaluate the magnetic moment per particle μ. In the first approach, the magnetization versus applied field in the superparamagnetic state is fitted by the Langevin function Eq. 4.6, as shown in Fig.4.54. It showed almost ideal Langevin-type behaviour of the paramagnetic materials, which gave $\mu = 39\ \mu_B$ per particle at 100 K.

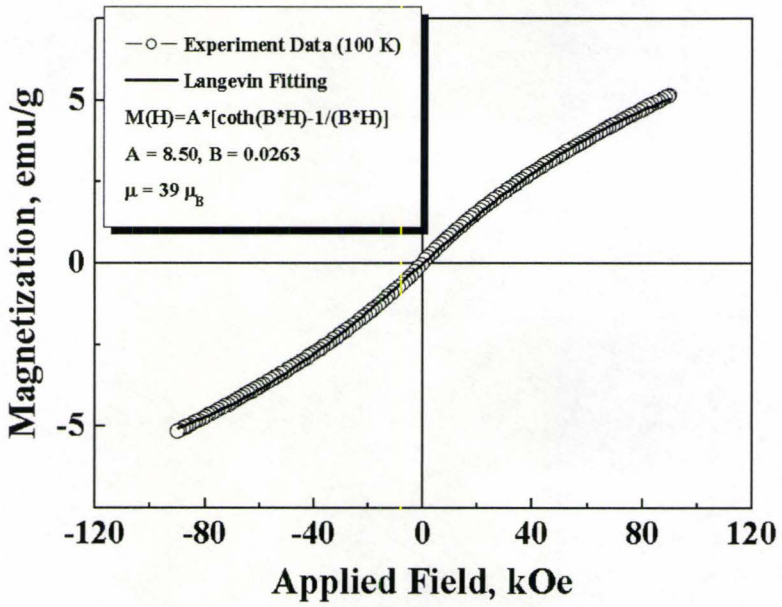

Figure 4.54 Magnetization versus applied field measured at 100 K for FeChi-RT. The solid line is the best fit of the experimental data using Langevin function

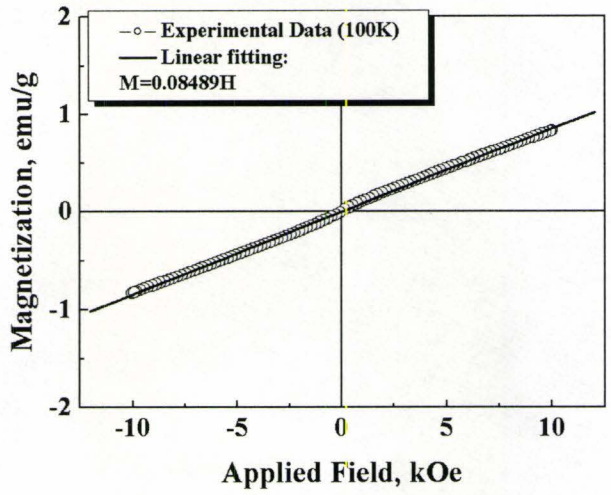

(a)

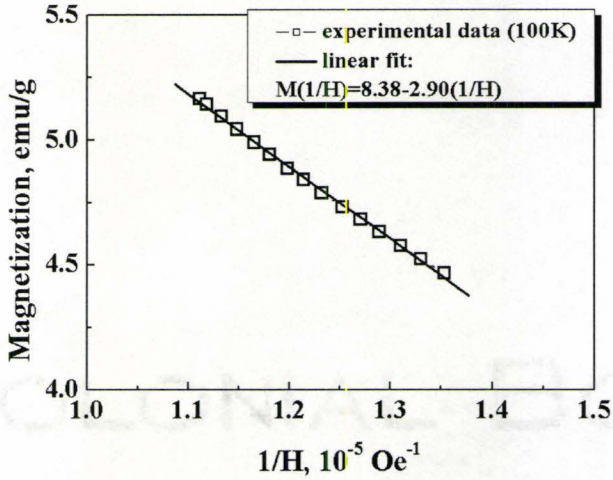

(b)

Figure 4.55 Experimental data for magnetization compared to the data calculated using Chantrell's (a) linear fitting of M versus H. (b) linear fitting of M versus 1/H. Both magnetization curves were measured at 100 K.

Alternatively, the magnetic moment per particle μ was estimated by utilizing Chantrell's model (Chapter 4.2.2). The initial susceptibility $\chi_i = 8.489*10^{-5}$ emu/gOe, was obtained by fitting the magnetization versus low field curve (Fig.4.55 a). Values of M_S

and $1/H_0$ were obtained from plotting the magnetization versus the inverse of the applied field (1/H) at the high field regime (Fig.4.55 b), which gave M_S = 8.38 emu/g and $1/H_0$ = $2.89*10^{-5}$ Oe^{-1}. The magnetic moment per particle was obtained as μ = 44 μ_B from Chantrell's equations.

Small deviation between the results obtained using these two approaches is expected because the Chantrell's model takes into account the particle size distribution, while the Langevin function assumes identical particle size.

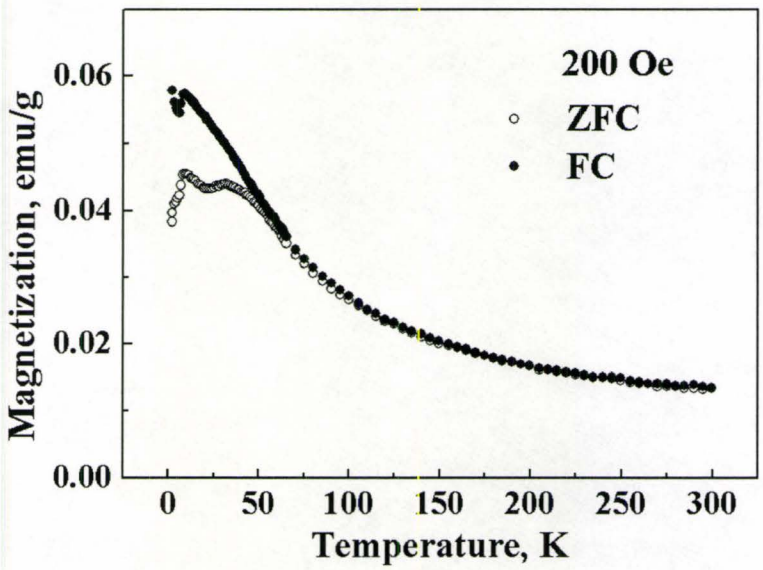

Figure 4.56 Temperature dependence of FC (solid circles) and ZFC (open circles) of DC magnetization measured at 200 Oe for FeChi-0.2g-RT

Fig.4.56 shows temperature dependence of DC magnetization for zero-field-cooled (ZFC) and field cooled (FC) FeChi-0.2g-RT sample, measured at low magnetic field of 200 Oe. On increasing the temperature from 2 K to 300 K, ZFC magnetization increased

with two maxima at T_{max1} = 8 K and T_{max2} = 31 K, and then decreased. The phenomenon of two peaks on ZFC curve reveals that the nanoparticle assembly contains two distinct sizes, which gives a double-peak particle size distribution. FC magnetization diverged from the ZFC curve at temperatures below T_{max2}. It is suggested that the particles are in a superparamagnetic state when FC and ZFC curves superimpose above T_{max2}.

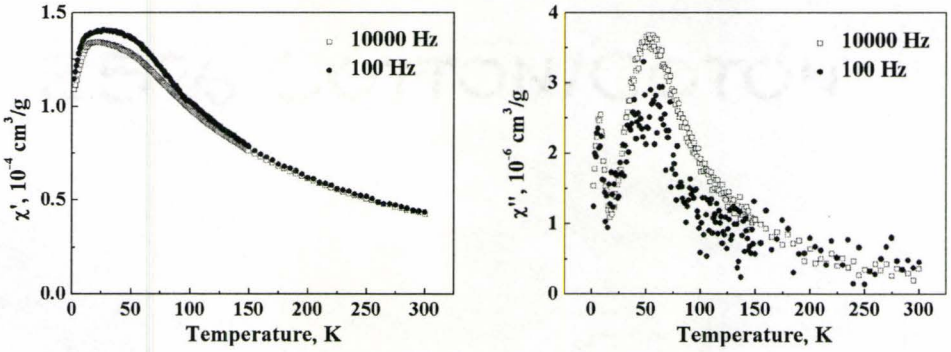

Figure 4.57 Temperature dependence of real (χ′) and imaginary parts (χ") of AC susceptibility measured at frequencies range of 10 Hz - 10 kHz for the FeChi-0.2g-RT

In Fig.4.57, AC susceptibility of FeChi-RT exhibited a broad maximum around T_{max} ~ 20 K in χ′ and two maxima at T_{max1} =8 K and T_{max2} = 52 K in χ", which all can be attributed to the superparamagnetic relaxation. The broad peak in the real part of χ, and two maxima in imaginary part of χ can be caused by the broad particle size distribution in the nanoparticle assembly.

Magnetic properties of FeChi-300

The Langevin function fitting to the magnetization data of FeChi-300, shown in Fig.4.58, gave μ = 205 μ_B per particle at 298 K. It is seen that the magnetization behaviour deviates from the ideal Langevin function for paramagnetic materials. Such deviation indicates that there can be strong interparticle interaction, or wide particle size distribution in FeChi-300 sample.

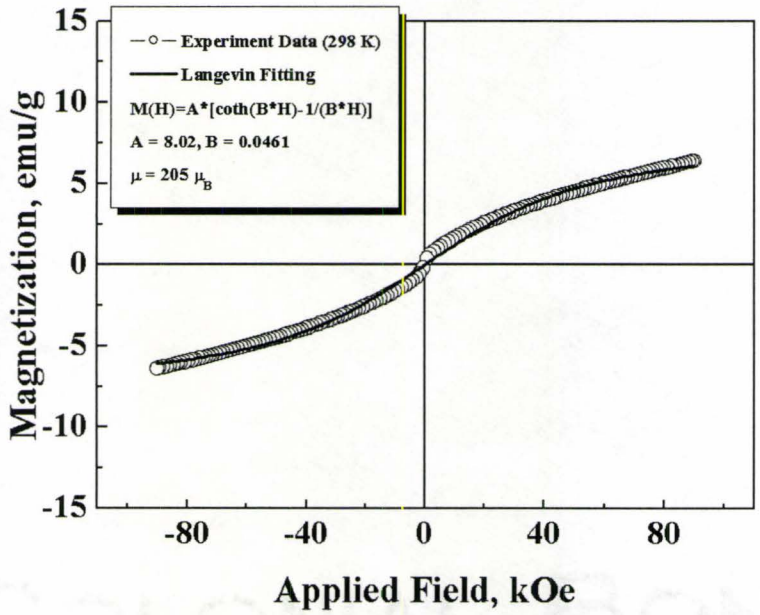

Figure 4.58 The Langevin fitting of magnetization versus applied field in 9 T at temperature of 298 K for FeChi-300. The solid line is the best fit of the experimental data using Langevin function

The fitting results for the magnetization data of FeChi-300 measured at 298 K (Fig.4.59) by Chantrell's model, gave the initial susceptibility $\chi_i = 7.587*10^{-4}$ emu/gOe, $M_S = 12.63$ emu/g and $1/H_0 = 3.92*10^{-5}$ Oe^{-1}, which yielded the magnetic moment per particle $\mu = 373\ \mu_B$.

The relatively high initial susceptibility χ_i value in magnetization curves shown in Fig.4.59 (a) indicates that larger particles might exist in the system, since χ_i is more sensitive to the larger particles. From the measured values of χ_i and $1/H_0$, it is possible to make two estimates of the diameter: D_i (Eq.1.31), which is derived from the initial susceptibility and D_u (Eq.1.32), which is calculated from the magnetization data at high field region.

$$D_i = \left(\frac{18 k_B T}{\pi} \cdot \frac{\chi_i}{\varepsilon M_S'^2} \right)^{\frac{1}{3}} \tag{1.31}$$

$$D_u = \left(\frac{6 k_B T}{\pi M_S'} \cdot \frac{1}{H_0} \right)^{\frac{1}{3}} \tag{1.32}$$

If the system has a distribution of particle sizes, the two diameters will differ, and in general, $D_i > D_u$, since χ_i is more sensitive to the larger particles, whilst the approach to saturation is more sensitive to the smaller particles [42].

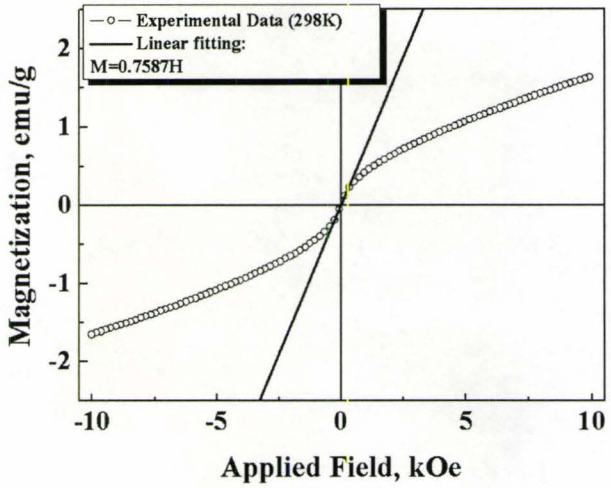

(a)

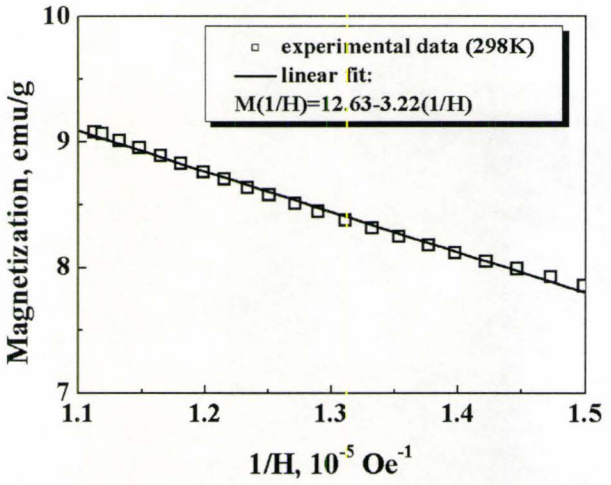

(b)

Figure 4.59 Chantrell's model to obtain the magnetic moment per particle: (a) the initial susceptibility obtained from the linear fitting of M versus H. (b) linear fitting of M versus 1/H. Both magnetization curves are measured at 298 K for FeChi-300

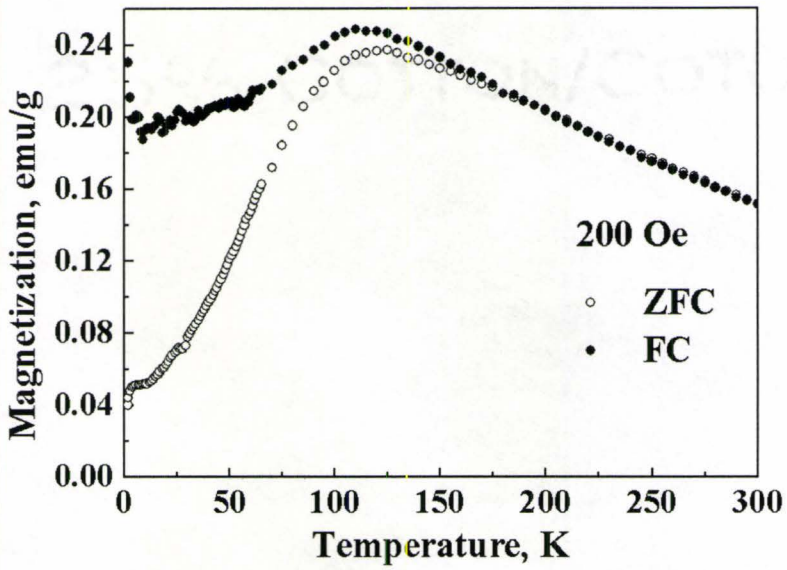

Figure 4.60 Temperature dependence of FC (solid circle) and ZFC (open circle) magnetization measured at 200 Oe for FeChi-300

Fig.4.60 shows temperature dependence of DC magnetization for zero-field-cooled (ZFC) and field cooled (FC) FeChi-300 samples measured at low magnetic fields of 200 Oe. On increasing the temperature from 2 K to 300 K, ZFC magnetization increased with a maximum at T_{max} = 125 K and then decreased. FC magnetization diverged from the ZFC curve at temperatures below T_{max}, and two curves merged and followed one superimposed characteristic at temperatures higher than about 175 K. This characteristic temperature is called breaking temperature T_{Br} and can be considered as a superparamagnetic blocking temperature of the largest particle in the assembly. Relatively large difference between T_B and T_{Br} suggests a broad distribution of particle sizes in the composite.

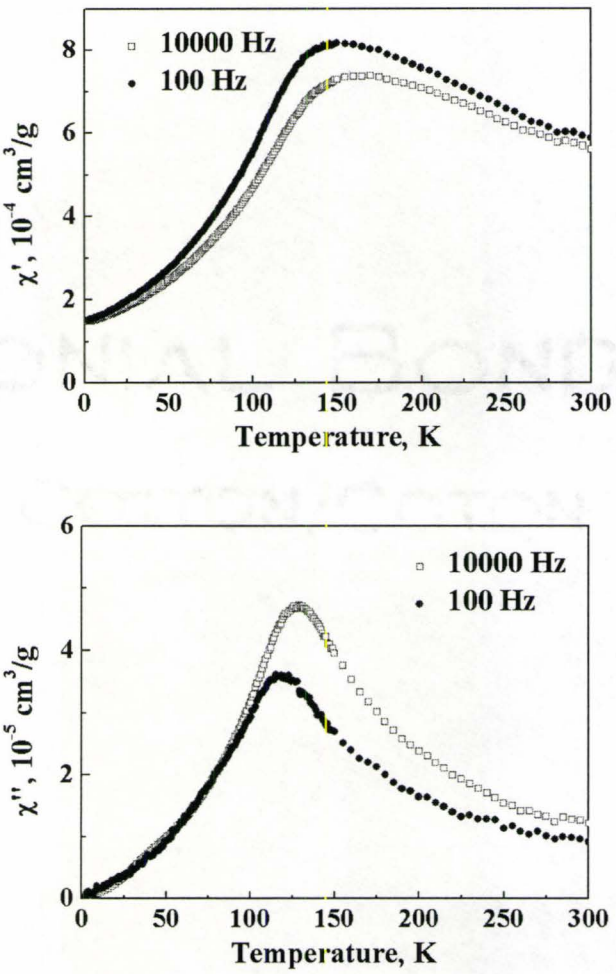

Figure 4.61 Temperature dependence of real part (χ') and imaginary part (χ") of AC susceptibility measured at frequencies 10 - 10 kHz for FeChi-300

In Fig.4.61, temperature dependence of AC susceptibility of FeChi-300 shows a broad maximum around $T_{max} \sim 150$ K in χ' and $T_{max} = 130$ K in χ", which was attributed to the superparamagnetic relaxation.

4.3.2 Electrodeposition of Mn_3O_4 using chitosan

The electrodeposition was performed from 5 mM $MnCl_2$ solution containing 0.2 g/l chitosan at a current density in the range of 1 – 5 mA/cm^2 for a deposition time of 0.5 – 5 min.

X-ray diffraction patterns of the deposits prepared from 5 mM $MnCl_2$ solution containing 0.2 g/l chitosan are shown in Fig.4.62. XRD of fresh deposit and those annealed at 300 °C and 400 °C, showed small peaks belonging to Mn_3O_4 (hausmannite-JCPDS file #24-0734) phase. The peak broadening can be caused by small particle size. Deposits annealed at 500 °C exhibited peaks attributed to Mn_2O_3 structure.

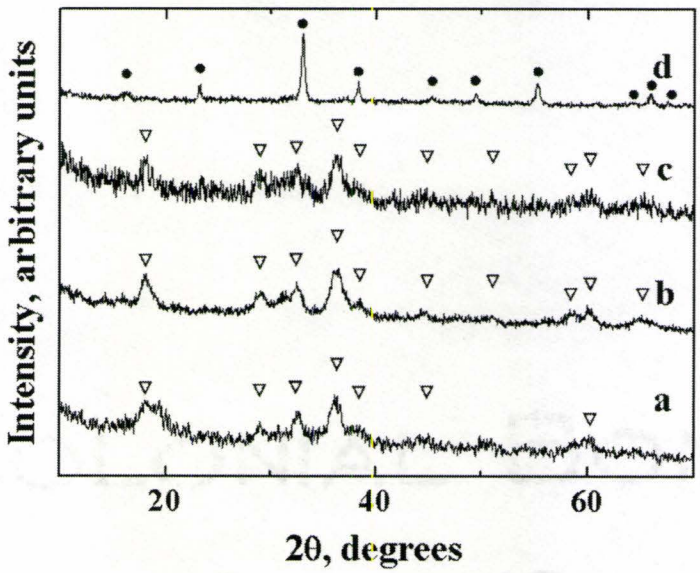

Figure 4.62 X-ray diffraction patterns for the deposits prepared from the 5 mM $MnCl_2$ solution containing 0.2 g/l chitosan: (a) as prepared and those annealed at (b) 300 (c) 400 and (d) 500 °C for 1 hour. • -Mn_2O_3 (JCPDS 41-1442), ∇ -Mn_3O_4 (JCPDS 24-0734)

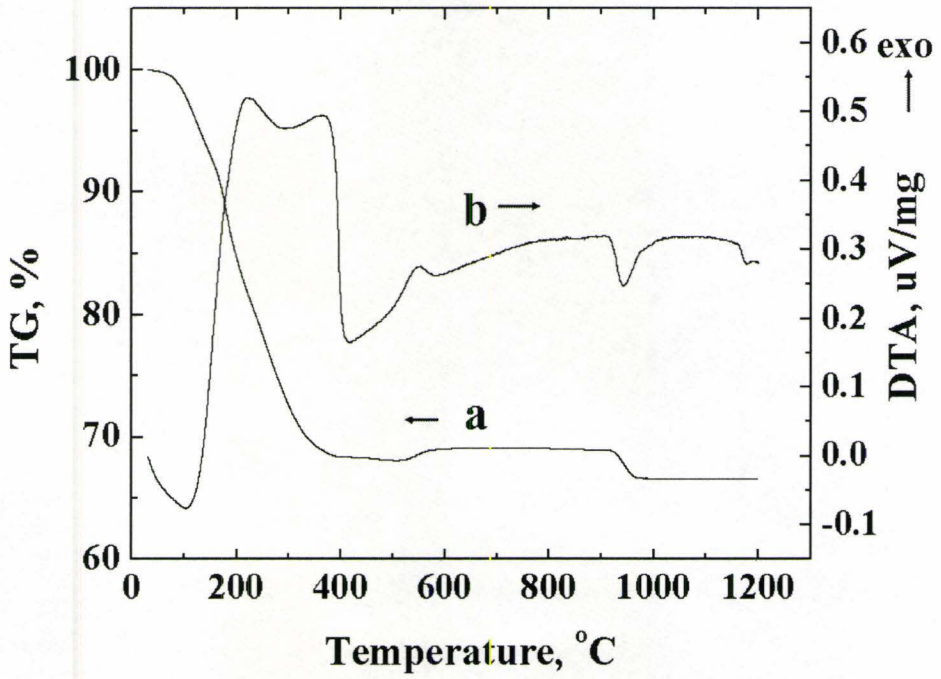

Figure 4.63 TG (a) and DTA (b) data for deposits prepared from the 5 mM $MnCl_2$ solutions containing 0.2 g/l Chitosan

Fig.4.63 shows TG and DTA curves for the deposits prepared from 5 mM $MnCl_2$ solutions containing 0.2 g/l chitosan. The TG data (Fig.4.63 a) indicated that essentially most of the weight loss occurred below 500 °C. The weight loss at 500 °C was 32.0% of initial sample weight. There was a weight gain of 1.0% in the temperature range 500-600 °C. Another weight loss of 2.4% occurred in 930-970 °C if further increase the temperature. It showed total weight loss of 33.4% of the initial weight. The corresponding DTA data (Fig.4.63 b) showed two endotherms around 100 °C and 950 °C, and exotherms in the range 200-600 °C.

There is a possible connection between the observed exothermic and endothermic effects in DTA data and the steps in TG data. The endotherm around 100 °C can be attributed to the liberation of the adsorbed water. The exotherms can be related to the burning out polymer. The weight gain in the temperature range 500-600 °C can be attributed to the oxygen uptake due to the phase transition from Mn_3O_4 to Mn_2O_3. The weight loss in the temperature range 930-970 °C can be related the phase transition from Mn_2O_3 to Mn_3O_4.

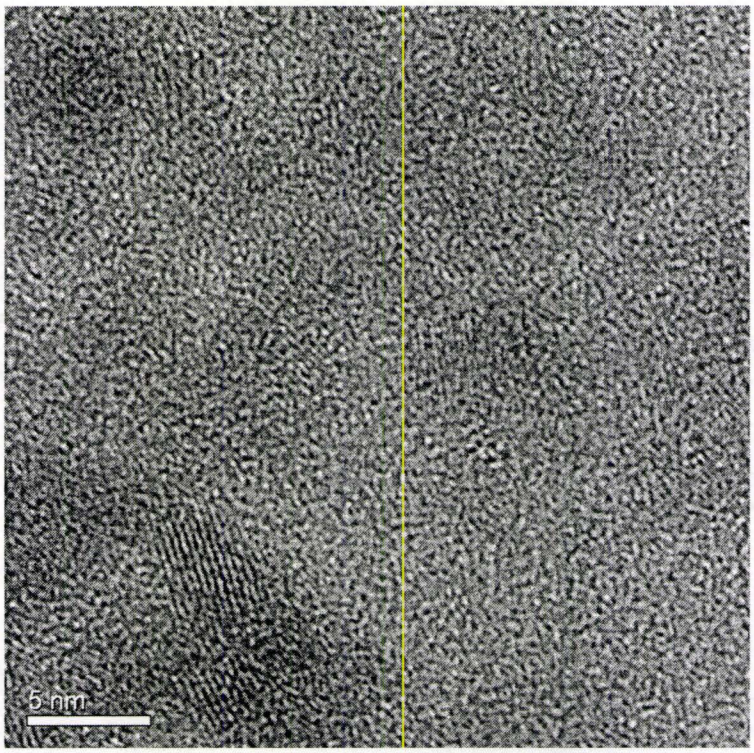

Figure 4.64 HRTEM images for the deposit prepared from the 5 mM $MnCl_2$ solution containing 0.2 g/l chitosan

Fig.4.64 shows high resolution TEM (HRTEM) images of the nanocomposite deposits obtained from the 5 mM $MnCl_2$ solutions containing 0.2 g/l chitosan. It is seen that

Mn_3O_4 nanoparticles are randomly distributed in a polymer matrix. The micrograph showed that the atomic fringes overlap with each other in some areas, indicating agglomeration of Mn_3O_4 nanoparticles. The effect is attributed to magnetic interaction of Mn_3O_4 nanoparticles. The average particle size determined from numerous areas analysed gave the particle diameter of 4.4 ± 0.5 nm.

Magnetic properties of Mn_3O_4 – chitosan nanocomposite

In this chapter, the fresh deposits prepared from 5 mM $MnCl_2$ solutions containing 0.2 g/l chitosan were labeled as *MnChi-0.2g-RT*, and those annealed at 300 °C for 1 hour as *MnChi-0.2g-300*.

Studies of the MnChi-0.2g-RT sample

Fig.4.65 shows magnetization versus applied field curve of MnChi-0.2g-RT in 9 T range at the temperatures 5 K and 20 K. The MnChi-0.2g-RT showed ferrimagnetism at the temperature below T_N. The remnant magnetization and coercive force decreased with increasing the temperature to T_N.

It is suggested that the observed magnetization behaviour comes from two contributions to the magnetization: the magnetically ordered particle core, and the structurally and magnetically disordered surface structure. The surface effect is significant in the magnetic behaviour of nanoparticles.

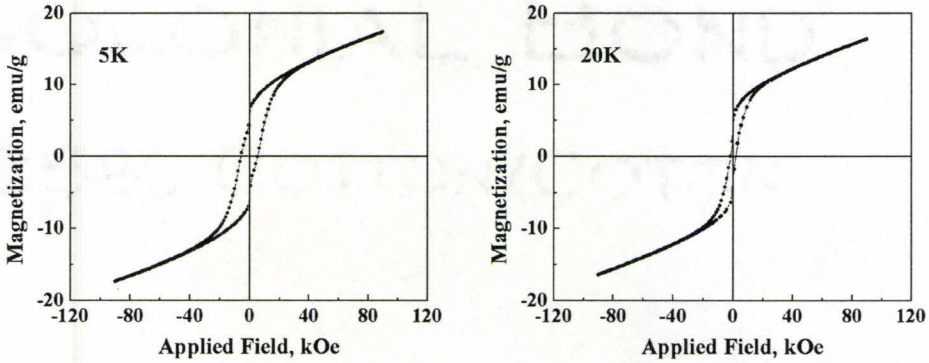

Figure 4.65 Magnetization versus applied field in 9 T range measured at temperatures 5 K and 20 K for MnChi-0.2g-RT

Fig.4.66 compares the magnetization versus applied field behaviour (1 T or 9 T range) measured at 10 K for MnChi-0.2g-RT. The magnetization curve of MnChi-0.2g-RT in 9 T range (Fig.4.66 a) showed a reversible linear part above 3 T, and an irreversible loop below 3 T. Only irreversible loop was observed in the magnetization in 1 T range (Fig.4.66 b). The irreversible loop behaviour is attributed to the magnetic reversal of magnetically ordered core, and the reversible linear part comes from the alignment of magnetization towards applied field, and also from the magnetically disordered surface layer. The coercive force obtained from the magnetization curve in 9 T range and in 1 T range was 3400 Oe and 250 Oe respectively.

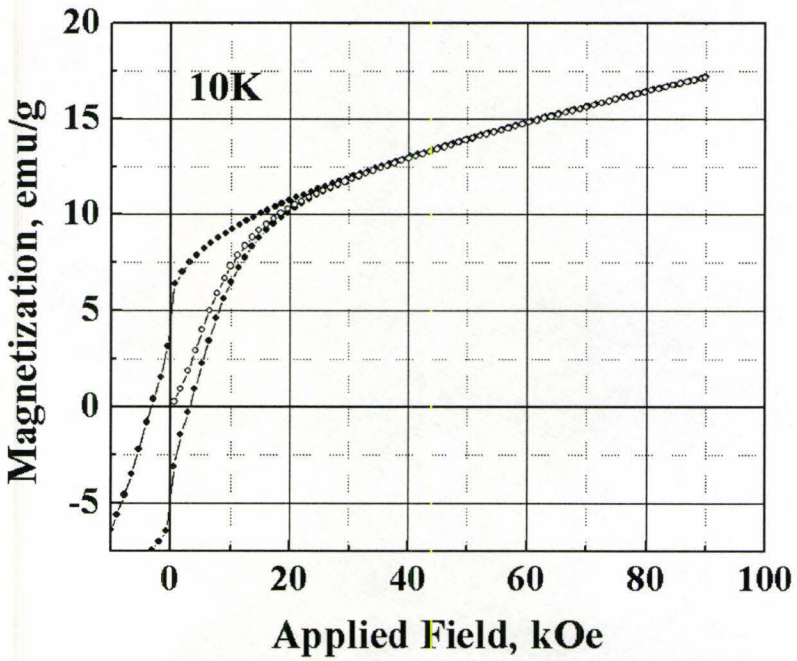

a

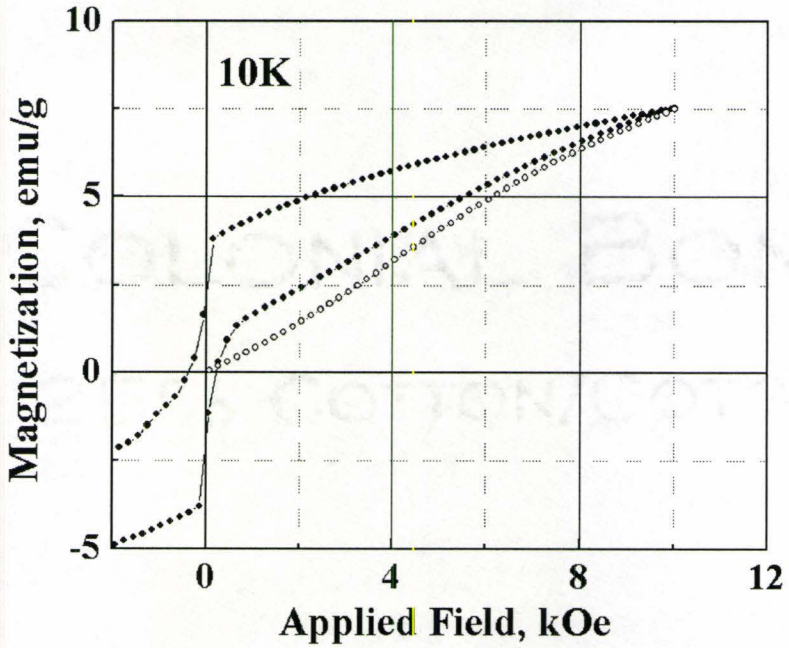

Figure 4.66 Magnetization versus high (9T) and low (1T) applied fields measured at 10 K for MnChi-0.2g-RT. Open circles show initial magnetization curve.

A relatively large change of magnetization near the zero applied field on the magnetization curves is shown in Fig.4.66. The magnitude of this change was recorded to be 3.2 emu/g·kOe, and 4.7 emu/g·kOe in 9 T and 1 T range respectively, and it decreased with increase of measuring temperature. This phenomenon might arise from the wide distribution of particles sizes. It is suggested that the smaller particles, which are in the superparamagnetic state, contribute to this large change in the magnetization curves.

Fig.4.67 shows the temperature dependence of the field cooling (FC) and zero field cooling (ZFC) magnetization of the MnChi-0.2g-RT deposit. On the increase of the temperature, ZFC magnetization increased with a maximum at T_{max} and then decreased. FC magnetization decreased with temperature over the whole temperature range. FC diverged from ZFC and two curves merged and followed one superimposed line at temperatures slightly higher than T_{max}. In the regime where FC and ZFC merged together, paramagnetic behaviour was observed by following the Curie-Weiss law. The ferrimagnetic Néel temperature T_N obtained from T_{max} of ZFC curves was 37 K for the fields of 200 Oe.

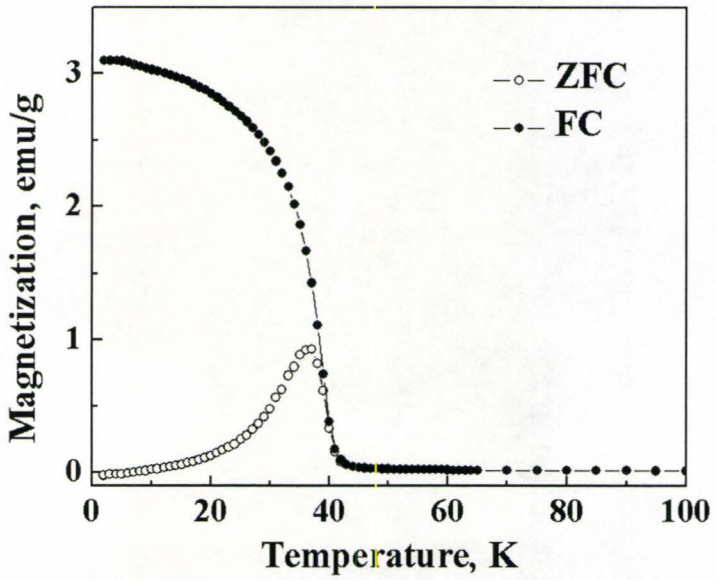

Figure 4.67 Temperature dependence of FC (solid) and ZFC (open) magnetization measured at 200 Oe for MnChi-0.2g-RT

The real and imaginary parts (χ' and χ'') of the AC complex susceptibility for MnChi-0.2g-RT are shown in Fig.4.68. On the increase of the temperature, real and imaginary parts of the susceptibility increased with a maximum at T_{max} and then decreased. The Néel temperature T_N, as marked by T_{max}, was found to be 37 K in the frequency range of 10 Hz - 10 kHz, and showed no frequency dependence. No evidence for the superparamagnetic transition was found in this sample.

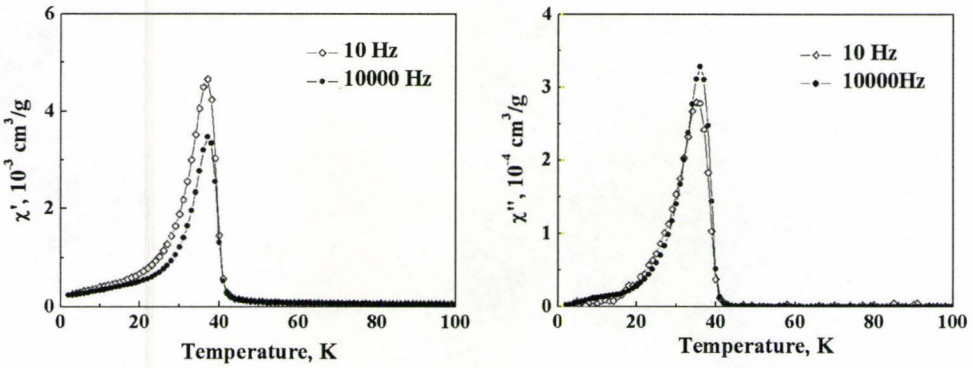

Figure 4.68 Temperature dependence of real and imaginary parts of AC complex susceptibility ($\chi=\chi'-i\chi''$) measured at frequency range 10 - 10 kHz for MnChi-0.2g-RT

Studies of MnChi-0.2g-300 sample

Fig.4.69 shows the temperature dependence of the field cooling (FC) and zero field cooling (ZFC) magnetization of the MnChi-0.2g-300 deposit. On the increase of temperature, ZFC increased with a maximum at T_{max} and then decreased. FC magnetization decreased with the temperature over the whole temperature region. FC diverged from ZFC and two curves merged and followed one superimposed line at the temperatures slightly higher than T_{max}. In the regime where FC and ZFC merged together, the paramagnetic behaviour was observed by following the Curie-Weiss law. The ferrimagnetic Néel temperature T_N obtained from T_{max} of ZFC curves was 39 K at the magnetic fields of 200 Oe.

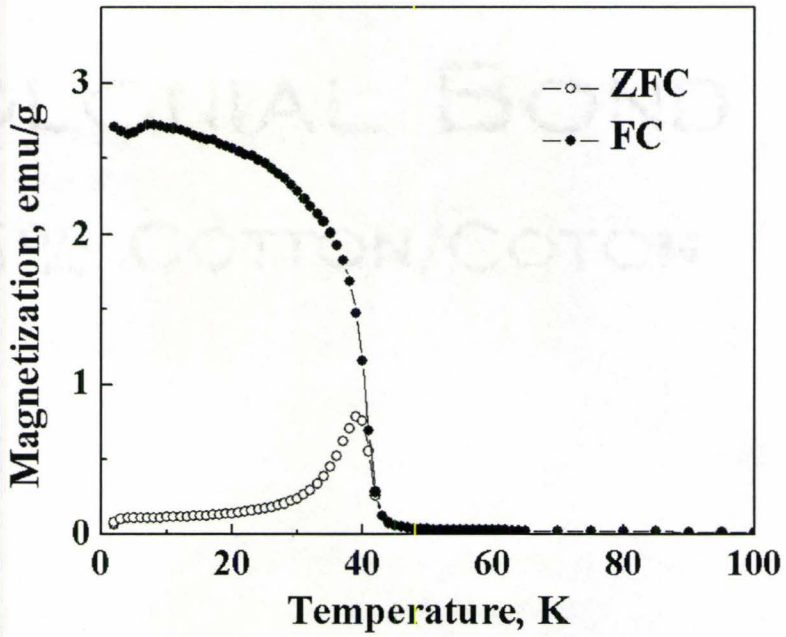

Figure 4.69 Temperature dependence of FC (solid) and ZFC (open) magnetization measured at 200 Oe for MnChi-0.2g-300

The real and imaginary parts (χ' and χ'') of the AC complex susceptibility for MnChi-0.2g-300 are shown in Fig.4.70. On the increase of the temperature, the real and imaginary parts of the susceptibility increased with a maximum at T_{max} and then decreased. The Néel temperature T_N, as marked by T_{max}, gave 40 K in the frequency range 10 Hz - 10 kHz, and showed no frequency dependence. No evidence for the superparamagnetic transition was found for this sample.

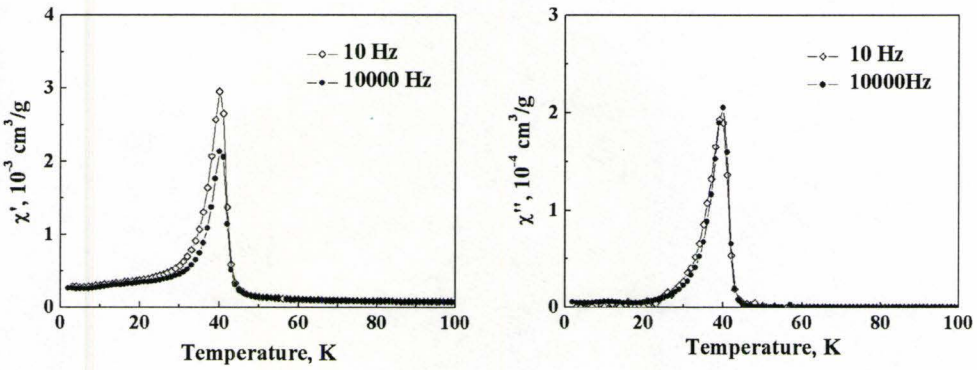

Figure 4.70 Temperature dependence of real and imaginary parts of AC complex susceptibility ($\chi=\chi'-i\chi''$) measured at the frequency range of 10 Hz to 10 kHz for MnChi-0.2g-300

4.4 Nanocomposites based on other strong and weak polyelectrolytes

4.4.1 Electrodeposition of γ-Fe_2O_3 using PDDA

Poly(diallyldimethylammonium chloride) (PDDA) is a strong polycation because of the quaternary amino group. The degree of dissociation of the ionic groups of PDDA is nearly pH independent in a wide pH range below pH 13.

The electrodeposition was performed from 5 mM $FeCl_3$ solution containing 0.1 – 0.3 g/l PDDA at a current density in the range of 1 – 5 mA/cm^2 for a deposition time of 0.5 – 5 min.

Magnetic properties of γ-Fe_2O_3 - PDDA nanocomposite

Fig.4.71 (a, b) compares the temperature dependence of AC susceptibility (χ' and χ") for the deposit prepared from 5 mM $FeCl_3$ solution containing 0.2 g/l and 0.3 g/l PDDA, respectively (Fe_2O_3-PDDA-0.2g-RT, Fe_2O_3-PDDA-0.3g-RT).

The peaks in the real part (χ') of AC susceptibility arise from the superparamagnetic relaxation, and the T_{max} in the curves corresponds to the blocking temperature T_B. T_{max1} and T_{max2} were found to be 47 K and 130 K in the real part of AC susceptibility of Fe_2O_3-PDDA-0.2g-RT (Fig.4.71 a), and T_{max1} dropped to 25 K in Fe_2O_3-PDDA-0.3g-RT (Fig.4.71 b). It is found that the weight percentage of the polymer in the deposit increases while increasing the polymer concentration in the bath solution. Therefore smaller particle sizes and less particle agglomerations can be expected in the samples with higher polymer concentration, what in turn lowers the blocking temperature.

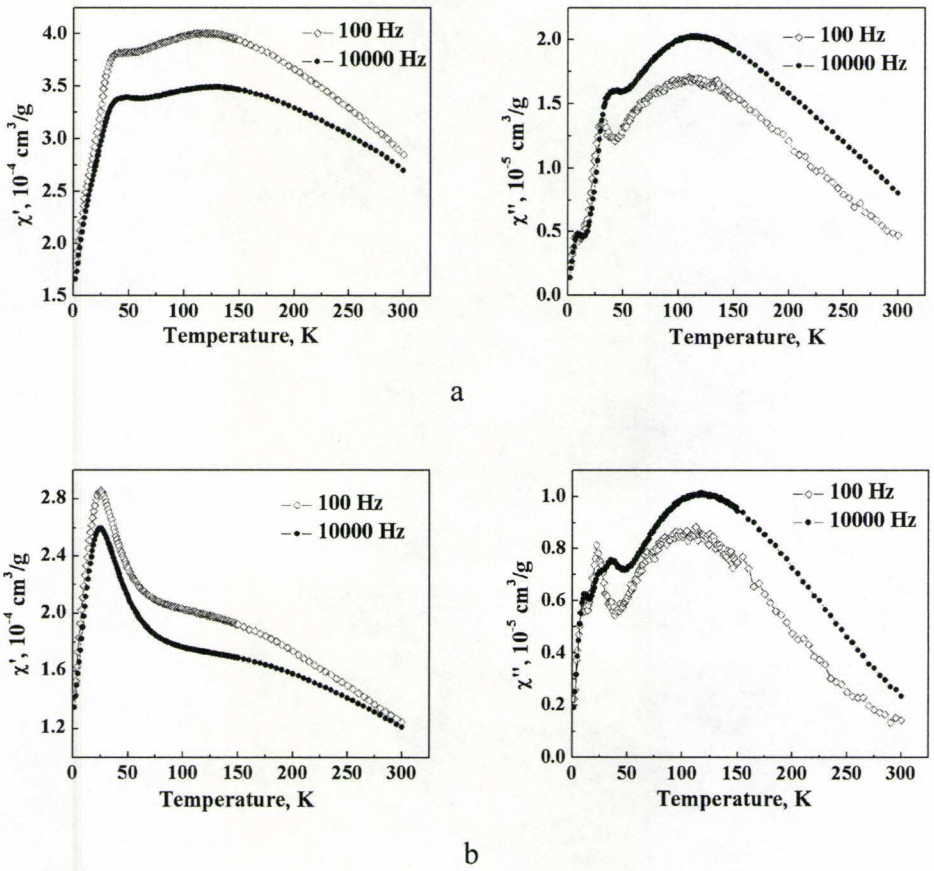

Figure 4.71 Temperature dependence of the AC susceptibility (real part χ' and imaginary part χ'') for the deposits from 5 mM $FeCl_3$ solutions containing (a)0.2 g/l and (b)0.3 g/l PDDA

Broad and multiple relaxation peaks were observed in both real and imaginary parts of AC susceptibility of the samples shown in Fig.4.71. This can be attributed to a broad particle size distribution and the effect of particle agglomeration. The partial agglomeration of particles can lead to two distinct sizes of the particles, having a fraction of separated individual particles gives a lower blocking temperature T_B marked by the T_{max1}, and the other fraction of the agglomeration gives the higher T_B marked by the T_{max2}.

Fig.4.72 (a, b) shows the temperature dependence of the zero-field-cooled (ZFC) and field cooled (FC) of DC magnetization curves measured at low magnetic fields of 200 Oe for the Fe_2O_3-PDDA-0.2g-RT and Fe_2O_3-PDDA-0.3g-RT deposits. On the increase of the temperature from 2 K to 300 K, ZFC magnetization of Fe_2O_3-PDDA-0.2g-RT (Fig.4.72 a) increased with a maximum at T_{max} = 29 K and then decreased, which gave an average blocking temperature T_B from the average particle size. FC magnetization diverged from the ZFC curve below the temperature T_{Br}, which is called breaking temperature, corresponding to the superparamagnetic blocking temperature of the largest particle in the assembly. Above T_{Br}, two curves merged and followed one superimposed characteristic. The breaking temperature T_{Br} of Fe_2O_3-PDDA-0.2g-RT was 85 K. Relatively large differences between T_B and T_{Br} suggests a broad particle size distribution. Similar curve trend was recorded for Fe_2O_3-PDDA-0.3g-RT (Fig.4.72 b), which gave T_B ~22 K and T_{Br} ~ 70 K. The broad particle size distribution may be caused by the agglomeration of the colloidal particles during the electrodeposition, which contains a fraction of the separate individual particles and also another fraction of the agglomerated larger particles.

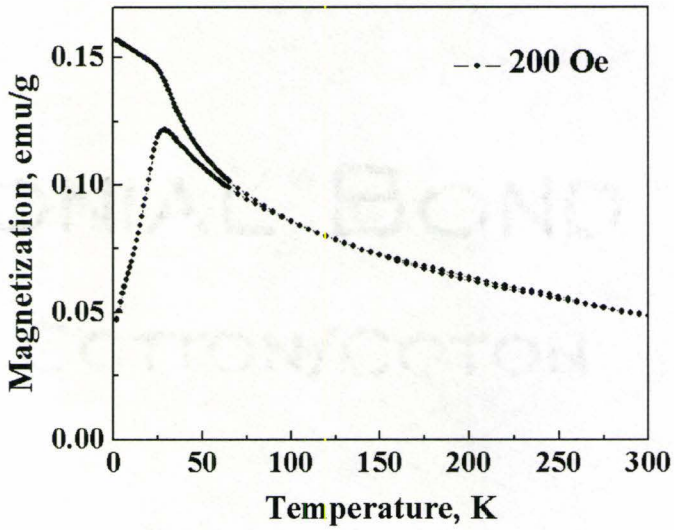

a

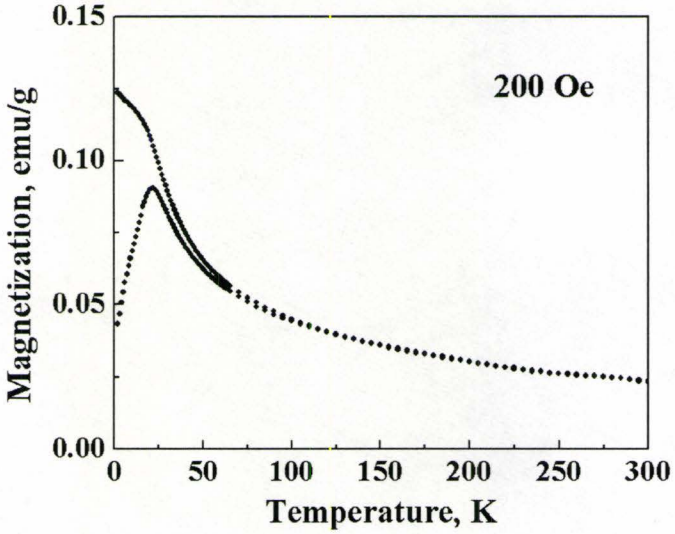

b

Figure 4.72 Temperature dependence of ZFC and FC magnetization measured at 200 Oe for the deposits prepared from 5 mM $FeCl_3$ solution containing (a) 0.2 g/l and (b) 0.3 g/l PDDA

4.4.2 Electrodeposition of– γ-Fe_2O_3 using P4VPy

Protonated poly(4-vinyl-pyridine) ($P4VPyH^+$) is a cationic weak polyelectrolyte, which can be used for the electrodeposition using combined method of ELD and EPD [95].

Cathodic electrodeposition was performed from 5 mM $FeCl_3$ solution containing 0.5 g/l P4VPy at a current density in the range of 1 – 5 mA/cm^2 for a deposition time of 0.5 – 5 min.

As shown in Fig.4.73, TG data for the deposits prepared from 5mM $FeCl_3$ solutions containing 0.5 g/l P4VPy showed several steps in the weight loss below 600 °C. The total weight loss at 1200 °C was found to be 29 wt%. The corresponding DTA data showed a broad endotherm in the range below 200 °C and exotherms in the range 200-600 °C. The endotherm was associated with evaporation of adsorbed water. The exotherms could be attributed to burning out of polymer P4VPy.

These results indicate the co-deposition of iron oxide and P4VPy. TG data is used to calculate the amount of an inorganic phase in the composite films. When the composite material was considered as a mixture of organic and inorganic components, the content of an inorganic phase was found to be 71 wt%. Therefore, the nanocomposite films are formed by the co-deposition method based on the EPD of polyelectrolyte P4VPy and cathodic electrosynthesis of iron oxide.

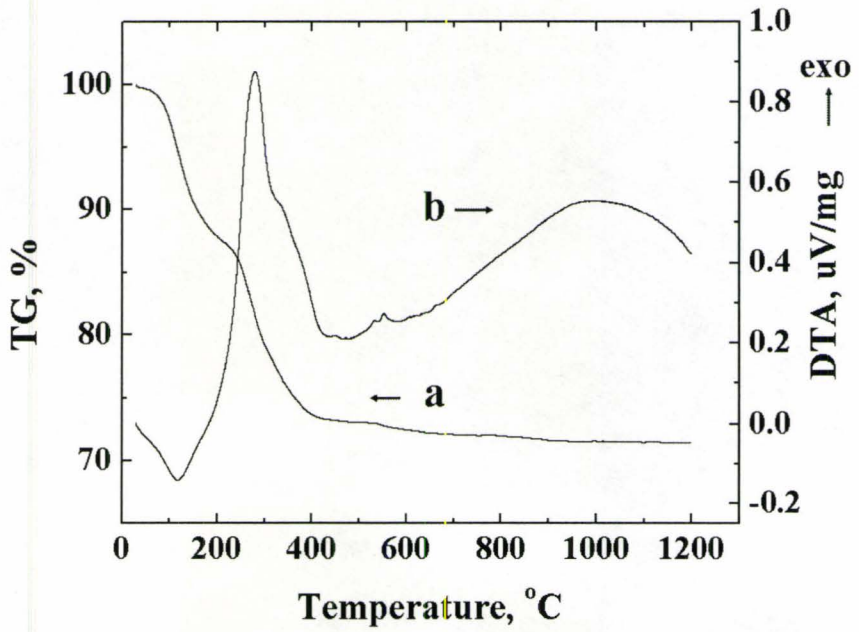

Figure 4.73 TG (a) and DTA (b) data for the deposit prepared from the 5 mM $FeCl_3$ solution containing 0.5g/l P4VPy

The present work started a new area in the electrodeposition of magnetic nanocomposite films. New electrochemical fabrication methods and deposition mechanisms for the electrodeposition of nanocomposite films have been developed. The new electrochemical strategies for the deposition and testing results will be discussed in chapter 5.

CHAPTER 5

DISCUSSION

The present chapter is dedicated to the discussion of the electrodeposition mechanisms and film properties. The main topics covered in this section include: deposition mechanisms of nanocomposite films using different polyelectrolytes, particle size distribution of magnetic nanoparticles and their effect on the magnetic properties, and the particle size dependence of the Néel temperature.

5.1 Deposition mechanisms of nanocomposites using various polyelectrolytes

Several different cationic polyelectrolytes were used in our experiments, such as PEI, PAH, Chitosan, PDDA and P4VPy. Among them, PDDA is a strong polyelectrolyte because it contains the quaternary amino group, while PEI, PAH, P4VPy and chitosan are weak polyelectrolytes, containing mainly primary and secondary amino group. Deposition mechanisms of various polyelectrolytes are different as a result of the polymer-metal ions or polymer-inorganic nanoparticle interactions.

Before discussing the deposition mechanisms of nanocomposite films using the above polyelectrolytes, it is worth mentioning a few basic aspects which are common for all experiments carried out in our work. Firstly, the electrochemical strategies used in our work combine the EPD of polyelectrolytes or polymer–metal ion complexes and cathodic electrosynthesis of inorganic materials for the electrosynthesis of nanoparticles *in situ* in a polymer matrix. Through this approach, particle agglomeration can be avoided. Secondly, cathodic electrodeposition is performed in either an ethanol-water, or methanol-water

solvent. The deposition process needs a certain amount of water for base generation in the cathodic reactions (Eq.2.22, 2.23). Methanol and ethanol are important solvents because they reduce gas evolution and the electrostatic repulsion of the polymer macromolecules [73, 76, 161, 226].

It is important to notice that the weight percentage of the inorganic phase in the deposits reduces with the increase of the polyelectrolyte concentration in the electrochemical bath solutions. These results imply that electrodeposition combines the EPD of polyelectrolytes or polymer–metal ion complexes and cathodic electrosynthesis of inorganic materials. In the solution containing 5 mM $FeCl_3$, when the PAH concentration increases from 0, 0.2, 0.3 to 0.5 g/l, the weight percentage of γ-Fe_2O_3 in the deposits reduces from 89.1%, 62.0%, 52.5% to 38.9%, respectively, as shown in the Fig.4.3 and Fig.4.4. In the solutions containing 5 mM $MnCl_2$, as PAH concentration increased from 0.5 to 1.0 g/l, the weight percentage of Mn_3O_4 in the Mn_3O_4–PAH deposits decreases from 60.4% to 47.9%, as shown in Fig.4.14 of Chapter 4. In the solution containing 5 mM $MnCl_2$, when the PEI concentration increases from 0.5 g/l, 1.0 g/l to 2.0 g/l, the weight percentage of Mn_3O_4 in the Mn_3O_4–PEI deposits drops from 61.6%, 50.4% to 38.7%, as it is shown in Fig.4.27.

5.1.1 Cathodic electrosynthesis of inorganic nanoparticles

Previous studies showed that, in the cathodic electrosynthesis of inorganic nanoparticles, the positively charged metal ions or polymer-metal ions complexes migrate

to the cathodic region where the high pH environment generated by the cathodic reactions (Eq.2.22, 2.23) allows for the formation of colloidal particles.

Our experiments showed that colloidal particles of hydroxide or oxide are formed, but that oxidation of the colloidal particles may occur in air at room temperature. Our results indicate that nanocrystalline Mn_3O_4 has been obtained from the 5 mM $MnCl_2$ solution containing different cationic polyelectrolytes, such as PEI, PAH, chitosan, which suggest that Mn^{2+} species are partially oxidized in air to form Mn_3O_4. Indeed, the oxidation of $Mn(OH)_2$ in air to form Mn_3O_4 is also reported for the powders prepared by chemical precipitation methods in other studies [227]. It is difficult, however, to distinguish between peaks of Mn_3O_4 (JCPDS file 24-0734) and γ-Mn_2O_3 (JCPDS file 18-803) because of the XRD peak broadening of the nanocrystalline oxides [228]. In our work, it has been confirmed by magnetic measurements that it is the Mn_3O_4 phase (JCPDS file 24-0734) that forms at room temperature. The fresh deposits obtained from $MnCl_2$-polyelectrolyte solution show a characteristic Néel temperature around 42 K, which is consistent with bulk Mn_3O_4, in AC susceptibility and DC magnetization measurements.

A previous study by Bon and Zhitomirsky [7] indicated that spinel phases γ-Fe_2O_3 or Fe_3O_4 were synthesised in the heat-treated deposits of composite iron oxide-polyelectrolyte films from an $FeCl_3$ solution containing PDDA or PEI. It is difficult to distinguish between γ-Fe_2O_3 and Fe_3O_4 due to the similar XRD pattern and peak broadening caused by the small crystal size.

In our experiments, the cathodic electrosynthesis of composite iron oxide-polyelectrolyte films were conducted from the 5 mM $FeCl_3$ solution containing different

cationic polyelectrolytes, such as PAH, chitosan, PDDA, and P4VPy. The same result occurs even without polyelectrolyte (Chapter 4). X-ray diffraction confirms the formation of spinel iron oxide nanoparticle in the fresh deposits obtained from $FeCl_3$ solution with or without polyelectrolytes. Moreover, our TG data show no weight gain in the phase transformation occurred at 400 °C when the room temperature spinel phase changes to α-Fe_2O_3, which suggests that the γ-Fe_2O_3 is formed in the fresh deposits (Fig.4.3). The reason for the formation of γ-Fe_2O_3 can be related to the nature of iron species formed in the mixed ethanol-water solution. It is known that various cationic species exist in $FeCl_3$ solutions, including monomers $FeOH^{2+}$, $Fe(OH)_2^{+}$, dimers $Fe_2(OH)_2^{4+}$ and other polynuclear species with the general formula $Fe_p^{III}O_r(OH)_s^{[3p-(2r+s)]+}$ [229]. Our results suggest that positively charged Fe species are hydrolyzed in the high pH cathodic region to form colloidal particles, which precipitate at the electrode. The hydroxide deposits are dehydrated and they convert to γ-Fe_2O_3 nanoparticles at room temperature.

Previous investigation [224] showed that the co-precipitation of Ni and Fe hydroxide colloidal particles could be achieved in the high pH region at the cathode surface. The precipitation resulted in the deposit formation on the cathode. The formation of spinel $NiFe_2O_4$ ferrite could be obtained by thermal dehydration of the hydroxide precursors, as indicated in [224]. Our experiments have been carried out to synthesize other spinel ferrites, such as $MnFe_2O_4$ by annealing the Mn/Fe hydroxide/oxide deposits electrochemically prepared from the solutions containing Mn^{2+} and Fe^{3+} ions and PEI polyelectrolyte (in Section 4.2). The present results reveal that $MnFe_2O_4$ ferrite is obtained after sintering at 1000 °C for 1 hour. As indicated by the results, the use of PEI

polychelates is beneficial for the co-deposition of oxides and paves the way for the electrosynthesis of other complex oxides.

5.1.2 Combined methods based on EPD of weak polyelectrolytes and electrosynthesis of inorganic nanoparticles

Previous studies showed that poly(allylamine hydrochloride) (PAH) is a weak polyelectrolyte and it is positively charged below pH 8 [88]. Polyallylamine was reported to form polymer-metal ion complexes in solutions of metal salts, such as Co^{2+}, Ni^{2+} and Cu^{2+} [230]. Shchukin and co-workers [10] obtained magnetic ferrite and magnetite particles inside the hollow PSS/PAH polyelectrolyte capsules using chemical precipitation methods. It was suggested the interaction between PAH molecules and aqua complexes of metal cations results in the formation of metal oxides.

Our studies show that cathodic electrosynthesis of γ-Fe_2O_3 or Mn_3O_4 nanoparticles *in situ* in the PAH polyelectrolyte can be achieved. The results suggest that the deposition mechanism can be as follows. Electric field resulted in accumulation of the particles and polymer macromolecules at the cathodic surface. The isoelectric point γ-Fe_2O_3 was found to be 6.7, and $Mn(OH)_2$ at 7.0 [231]. Therefore the colloidal particles formed in the high pH region at the cathode surface can be negatively charged and interact electrostatically with the cationic PAH macromolecules. It was found that the charge of PAH decreases with increasing pH [88]. Therefore non-electrostatic interactions, which are influenced by solvent, surface properties of the particles and other factors [9], also contribute to the interaction and heterocoagulation of the polymer and inorganic nanoparticles.

Poly(ethylenimine) (PEI) has been intensively studied in the literature. It is known that PEI is a polybase when dissolved in aqueous solution. The pH of an aqueous solution containing 1 wt% PEI was found to be about 11 and at this pH the PEI molecule has no charge. PEI adsorbs protons in acidic solutions and becomes charged positively through protonation of the secondary amine groups in acidic solutions, according to reaction Eq.4.5 [223].

Previous studies showed that PEI-metal ion complexes can be obtained by loading the polymer with different metals ions, such as Cu^{2+}, Zn^{2+}, Ni^{2+}, Co^{2+}, Mn^{2+} and Fe^{3+} [83, 232]. The extent of binding of the ions by PEI depends on the concentration of metal ions in solution, PEI concentration, pH, and other factors [233, 234]. The pH value is a very important factor in polymer binding since protons and metal ions compete to be bound to the polymer. In the case of metal binding with polybases, like PEI [83], amino groups become positively charged at low pH due to protonation and are thus unable to form chelates with cations. However, the binding capacity increases with increasing pH [83]. The evaporation of some PEI metal complex solutions can result in the formation of amorphous solids that are generally no longer soluble in water due to the cross-linking. A structure of a charged PEI-Cu^{2+} complex is shown in Fig.5.1.

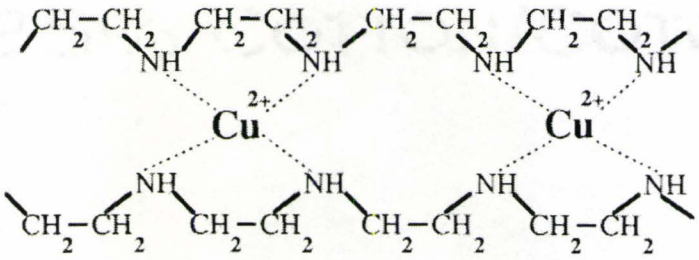

Figure 5.1 Idealized structure of the PEI-Cu^{2+} complex[235]

Our experiments clearly indicate the formation of PEI-Mn^{2+}, PEI-Ni^{2+}, and PEI-Fe^{3+} complexes by the strong coloration of mixed PEI and metal chloride solutions in the experiments. Our results show that the $MnCl_2$ dissolved in ethanol-water solution has no color. However after adding the PEI, the solution color changes to light brown. The addition of PEI to $NiCl_2$ solutions results in intensely blue colored solutions. The solutions of $FeCl_3$ turned from light brown to deep brown after the addition of PEI [224], indicating formation of complexes.

Previous investigations showed that nanocomposite films containing nanoparticles of Co, Fe, Ni, Ce, Zr, La oxides/hydroxides in a PEI matrix can be obtained [7, 224, 236-242]. The deposition mechanism has been discussed in several papers [7, 236, 237, 240].

Our experimental work has focused on the spinel structured manganese oxide and ferrites. The use of PEI polychelates enabled the formation of magnetic $NiFe_2O_4$, and $MnFe_2O_4$ ferrites. The EPD of PEI–Mn complex has been utilized for the deposition of nanocomposites containing Mn_3O_4 nanoparticles. Our results prove that polymer-metal ion complexes can be used for the electrodeposition of magnetic materials. In this process, PEI acquires positive charges by forming complexes with metal ions such as

Ni^{2+}, Mn^{2+}, Fe^{3+}, and Co^{2+}. Then, the electric field provides the electrophoretic motion of the PEI-metal ion complexes towards the electrode surface, the ions participate in cathodic reactions to form nanoparticles of metal oxide/hydroxides. The high pH value at the cathode surface reduces electrostatic repulsion of PEI macromolecules and promotes their deposition on the cathodic substrates. Free metal ions, which are not complexed by PEI also exist in solution and contribute to the electrosynthesis of inorganic phases [82].

Chitosan is a natural cationic polysaccharide and the N-deacetylated product of chitin where the degree of deacetylation is generally more than 60% [89]. Water soluble and positively charged chitosan can be prepared by the protonation of amine groups (Eq.4.9) in dilute organic acids such as acetic acid, formic acid, etc [92, 93, 243].

The properties of chitosan in solutions depend on the molecular weight, the degree of deacetylation, pH and ionic strength. At pH 6.5, the primary amine groups of chitosan become deprotonated. As a result of the decreasing charge with the pH increase, dissolved chitosan usually flocculates at pH above 6.5 [92, 93].

Our experiments have extended the combined method to deposit novel composite materials based on chitosan. Previous works have focused on the synthesis of hydroxide, oxide and metal particles, such as ZrO_2, $Al(OH)_3$ and Ag [228, 244-246]. The current work is focused on the fabrication of magnetic nanoparticles such as Mn_3O_4 and γ-Fe_2O_3 in the chitosan matrix. The present results suggest that the deposition mechanism is associated with the process in which the protonated chitosan loses its charges in the high pH region at the cathode surface and forms an insoluble deposit as indicated in Eq.4.11.

The metal ions or complexes are hydrolyzed by electrogenerated base to form colloidal particles at the cathode. Therefore, the cathodic precipitation of inorganic nanoparticles and EPD of chitosan can be combined together to form composite films, which is another interesting discovery arising from this work.

The chelating ability of chitosan and its derivatives for metal ions has been reviewed [243]. It is known that Ag^{+}, Fe^{3+}, Cu^{2+}, Hg^{2+}, Ni^{2+}, Zn^{2+} and some other ions have great binding affinity towards chitosan [247-250]. Therefore the chitosan-metal ion complex can form and behaves as a polyelectrolyte in the solutions. Our experiments also suggest the chitosan-Fe^{3+} and chitosan-Mn^{2+} complexes are formed in the solutions. The extent of binding of the ions by polymer depends on the concentration of metal ions in solution, chitosan concentration and pH values. The pH value is a very important factor in polymer binding because of the binding competition between protons and metal ions. The binding capacity to metal ions increases with increasing pH. The formation of chitosan-metal ion complexes can be enhanced in the high pH region at the cathode surface [245].

Part of the present work was dedicated to synthesize the nanocomposite utilizing poly(4-vinyl-pyridine) (P4VPy). P4VPy is a weak cationic polyelectrolyte and it was found [94] to form polychelates with Cu^{2+}, Zn^{2+}. Partially protonated P4VPy-H^{+} can be obtained by adding an appropriate amount HCl into polymeric solution [95]. In the present work we investigated the possibility to use combined method to deposit nanocomposite materials based on P4VPy. Our TG data show that the co-deposition of iron oxide and P4VPy can be achieved. The deposition mechanism is suggested to be

based on the similar process as discussed above for the case of PAH and chitosan. The protonated P4VPy migrates to the cathode in the electrical field, loses its charges in the high pH region near the cathode, and forms an insoluble deposit. In the meantime, the metal ions are driven to the cathode and are hydrolyzed to form colloidal particles. Therefore, the cathodic precipitation of inorganic nanoparticles and EPD of P4VPy can be combined to form composite films.

5.1.3 Combined methods based on EPD of strong polyelectrolytes and electrosynthesis of inorganic nanoparticles

PDDA is a strong polyelectrolyte because of the quaternary amino group [9]. The degree of dissociation of the ionic groups of PDDA is nearly pH independent in a wide pH range below pH 13.

Previous studies have reported results of the aqueous co-deposition of PDDA and inorganic materials with relatively low isoelectric points, such as oxides/hydroxides of Zr, Ce [77, 211, 214, 251]. Further investigations showed the possibility of co-deposition of other inorganic materials with larger isoelectric point, such as hydroxides of Ni and Co [236, 237]. The fabrication of superparamagnetic films based on Fe_3O_4 [8] was particularly interesting because of its magnetic properties.

The present work is allowed to develop better understanding of the co-deposition of nanocomposite films based on the PDDA and inorganic oxides. Our results show that composite films containing γ-Fe_2O_3 nanoparticles in the PDDA matrix can be obtained by electrodeposition.

The charge compensation mechanism has been developed for the fabrication of organic–inorganic nanocomposites containing PDDA [77]. It is known that PDDA macromolecules maintain a high positive charge in acidic bulk solutions as well as in basic conditions at the cathode surface. As a result of the strong electrostatic repulsion of the PDDA macromolecules, no deposit formation can be achieved from the aqueous PDDA solutions. However, co-deposition of PDDA and the colloidal particles of metal oxides or hydroxides was observed by other researchers [7, 8, 210-214, 236-238, 251-254]. For the inorganic materials with low isoelectric points, it was suggested that the deposit formation is driven by Coulombic attraction between two charged species: cationic PDDA and the negatively charged colloidal particles formed at the electrode surface [9]. For other inorganic materials with larger isoelectric point, the heterocoagulation of PDDA and inorganic nanoparticles is driven not only by charge attraction, but also by other interactions, such as hydrogen bonding and ion-dipole interactions. Present results reveal that such interactions are significant contributing factors in the deposit formation and in determining the stability and microstructure of the deposit.

5.2 Theoretical modeling of magnetic properties of γ-Fe_2O_3 nanoparticles

5.2.1 Particle separation ratio S/D

To understand the level of interparticle interactions of the nanoparticle assembly in our composites, one defines an important parameter, the ratio of the particle separation S and particle diameter D. It is determined by the volume fraction of the inorganic phase in the composite as plotted in the Fig.5.2.

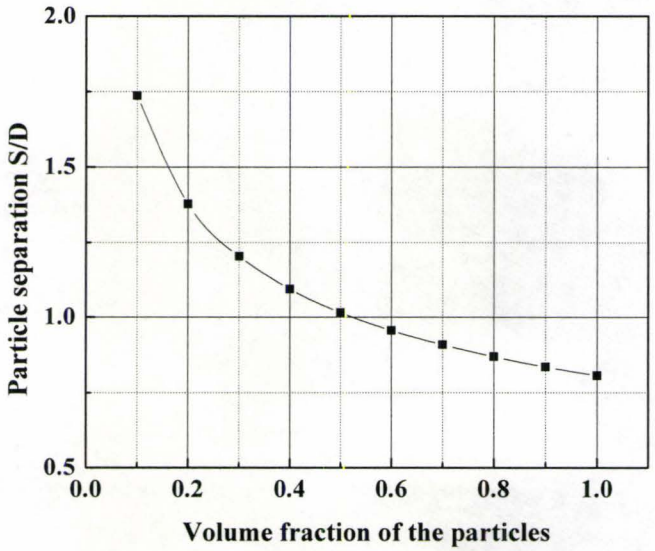

Figure 5.2 The relationship between the particle separation ratio S/D and volume fraction of the particles, assuming a cubic stacking of the particles.

Our studies showed that the weight percentage of inorganic phase in the deposit can be controlled by varying the polyelectrolyte concentration in the electrodeposition bath solution. Therefore, the particle separation ratio S/D can be tuned by the initial polyelectrolyte concentration. The S/D of γ-Fe_2O_3 – PAH and γ-Fe_2O_3 – chitosan

composites, comparing with the initial electrolyte concentration in the bath solution, mass and volume fraction of γ-Fe_2O_3 in the deposits are listed in Table 5.1.

Table 5.1 The particle separation ratios S/D of γ-Fe_2O_3 - PAH and γ-Fe_2O_3 – chitosan

PAH content (g/l)	Mass fraction	Volume fraction*	S/D
0	0.891	0.625	0.94
0.2	0.620	0.250	1.28
0.3	0.525	0.184	1.42
0.5	0.389	0.115	1.66
Chitosan (g/l)			
0.2	0.588	0.226	1.32

* consider polymer's bulk density ~1.0 g/cm^3

The particle separation ratio S/D indicates the interparticle interaction strength of superparamagnetic nanoparticles. Dormann [52, 55, 255] studied γ-Fe_2O_3 4.7 nm nanoparticle assembly dispersed in the polymer media with interparticle interactions of varying strength. The samples IF, IN, and Floc were dispersed in the polymer media, having a center-to-center separation distances S of 21 nm, 7.3 nm and 6.8 nm respectively. A powdered sample with no polymer media was also studied. According to Néel-Brown's model, variation of relaxation time as a function of the reciprocal of temperature i.e. $\log_{10}(\tau_m)$ versus $1/T_B$ in AC susceptibility, should show quasi-straight lines with a slope of $\frac{E_B}{k_B}$ and an intercept of $\log_{10}\tau_0$. Fig.5.3 shows that sample IF (S/D = 4.5) with very weak interparticle interaction fit very well with Néel-Brown's model, giving an appropriate τ_0 value ~10^{-10}. For the samples IN (S/D = 1.6) and Floc (S/D = 1.4) with weak and intermediate interaction, the Néel-Brown's model was still valid by taking

account of additional anisotropy energy term, giving a shift of τ_0 value, which depends on the number of nearest-neighbour particles (see chapter 1). Finally, for the powder sample, presumably S/D = 1 with a very strong interaction, the variation of T_{max} with frequency extremely slowed down, indicating a collective freezing of particle moments.

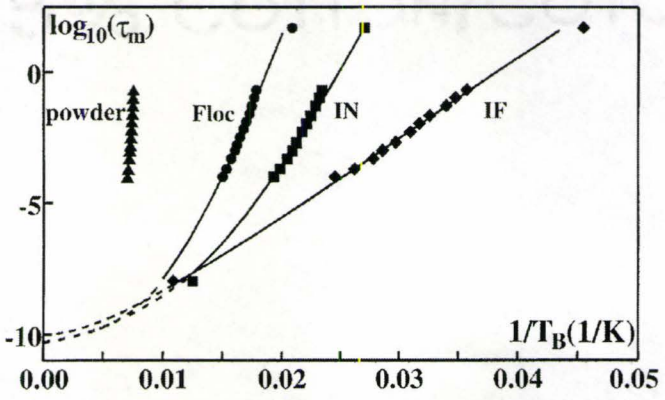

Figure 5.3 Frequency dependence of Tmax in AC susceptibility for γ-Fe_2O_3 with interparticle interactions of varying strength. Dispersions in a polymer (samples IF, IN and Floc) and powder particles [255].

It was concluded that interparticle interactions can be treated as very weak interaction when the particle separation ratio S/D > 4, and as weak and intermediate interaction when 1<S/D<4. The strong interaction occur when S/D ~ 1. All of the γ-Fe_2O_3/polymer nanocomposites in our experiments fell into the category of the weak and intermediate interactions and show slow variation of T_{max} with the frequency in the range of 10 Hz – 10 kHz, for instance, γ-Fe_2O_3 nanoparticles in the polyelectrolytes PAH, PDDA or chitosan. When the samples are prepared without any polyelectrolyte, or being heat treated to remove the polyelectrolyte, their interparticle interaction fell into the category of the strong interaction.

5.2.2 Estimating the average particle sizes by Langevin fitting

Langevin function fitting can been used to estimate the average size of superparamagnetic particles. The criteria have been discussed in Chapter 1. Assuming the particles in the assembly are all of the same size, the magnetization vs. magnetic field curve can be described by Langevin function when the nanoparticle assembly is in the superparamagnetic state:

$$M = M_S L\left(\frac{\mu H}{k_B T}\right) = M_S\left[\coth\left(\frac{\mu H}{k_B T}\right) - \frac{k_B T}{\mu H}\right] \qquad (5.1)$$

By fitting the magnetization curve with the Langevin function, M_S, μ, and the average particle size can be calculated.

Langevin function fitting, however, is an oversimplified model and care has to be taken to apply the fitting appropriately and to interpret the results properly. For instance, in the γ-Fe_2O_3/PAH nanocomposite obtained from the solution containing 0.5g/l PAH (FePAH-0.5g-RT), the magnetic moment per particle μ rose as the temperature increased from 20 to 100 K and then fell with increasing temperature from 150 K to 300 K, as shown in Fig.5.4. A slightly decreasing μ with increasing temperature should be expected ($\mu = M_S * V$, M_S decreases with increasing temperature). It was observed that, at the low temperature range, slightly above the blocking temperature T_B, the magnetization curve of the system could not be represented by the Langevin function because a fraction of the particles was still in the blocked state. On the other hand, in the high temperature range where $\mu H/kT \ll 1$, the magnetization curve was far from being saturated, almost linear in the entire magnetic field range up to 9 T, and the Langevin function fitting gave only poor

fitting parameters. It is concluded that the Langevin function fitting obtained better accuracy when the magnetization curve is taken at the median range temperatures, e.g. 5-10 times of the T_B. For instance, the median temperature range was 70 K – 140 K for the FePAH-0.5g-RT in Fig.5.4 because it had a T_B around 14 K.

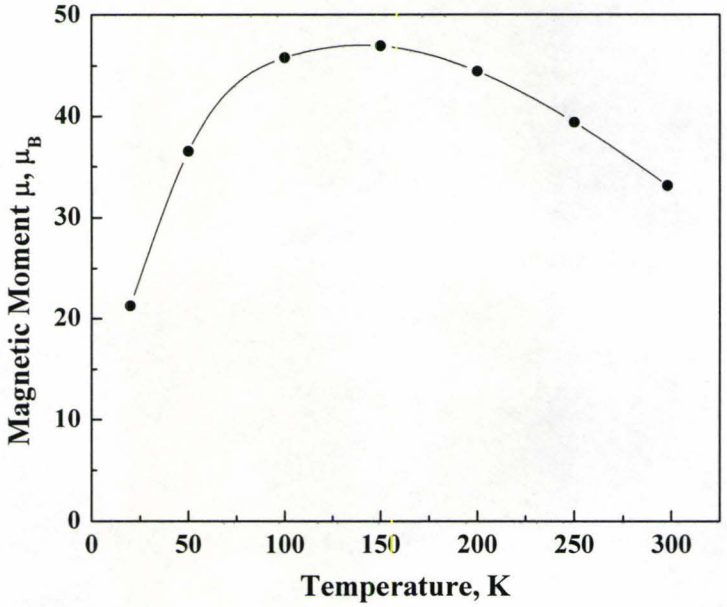

Figure 5.4 Variation of the magnetic moment per particle μ as a function of temperature for the FePAH-0.5g-RT sample. μ was obtained by Langevin fitting to the magnetization data.

Table 5.2 summarizes the average particle sizes calculated from Langevin function for the samples deposited from 5 mM $FeCl_3$ containing 0.5 g/l PAH and those heat-treated at 200 and 300 °C. In Table 5.2, the values of T_B were obtained from T_{max} in the AC susceptibility measurements. The KV/kT ratio in the Table 5.2 indicated whether the system was in the superparamagnetic state, which normally requires $E_B/k_BT << \ln(\tau_m/\tau_0) \sim 10$. The anisotropy constant K of γ-Fe_2O_3 was taken as $4 \cdot 10^5$ by considering magnetostatic, surface, and magnetocrystalline anisotropy as in the Dormann's

experiment [55]. It was shown that the saturation magnetization M_S of γ-Fe_2O_3 nanoparticles was less than that of the bulk γ-Fe_2O_3 value, M_S = 360 emu/cm^3. This reduction of M_S with decreasing the nanoparticle sizes were studied by others [256]. It was believed to be caused by the surface spin canting and related surface effects.

Table 5.2 The average particle sizes of γ-Fe_2O_3/PAH nanocomposites by fitting magnetization curves with Langevin function

γ-Fe_2O_3/PAH	Fitting parameters		Particle size	T_B (K)	KV/kT
	Magnetic moment per particle μ (μ_B)	M_S [1] (emu/cm^3)	D (nm)		
No polymer, RT[2]	5329@298K[3]	282	6.9	260	1.7
0.2 g/l, RT	45@150K	77	2.2	7, 38	0.10
0.3 g/l, RT	36@150K	83	2.0	7, 36	0.08
0.5 g/l, RT	46@100K	94	2.0	14	0.13
0.5 g/l, 200°C	85@200K	100	2.5	25	0.11
0.5 g/l, 300°C	3052@298K	142	7.2	195	1.9

(1) M_S is the volume saturation magnetization of nanoparticles (different from those of the composite or bulk magnetic materials).
(2)RT means the fresh deposit obtained at room temperature, no heat treatment.
(3)@298K means the magnetization curve was measured at 298 K.

Table 5.3 summarized the average particle sizes calculated from Langevin function for the samples deposited from 5 mM $FeCl_3$ containing 0.2 g/l chitosan and that heat-treated at 300 °C.

Table 5.3 The average particle sizes of γ-Fe_2O_3/chitosan nanocomposites by fitting magnetization curves with Langevin function

γ-Fe_2O_3/chitosan	Fitting parameters		Particle size D (nm)	T_B (K)	KV/kT
	Magnetic moment per particle μ (μ_B)	M_S (emu/cm^3)			
(a) 0.2 g/l, RT	39@100K	71	2.1	20	0.15
(b) 0.2 g/l, 300°C	204@298K	60	3.9	150	0.30

Fig.5.5 and Fig.5.6 show Langevin function fitting to the magnetization curves of FePAH-0.5g-RT and FeChi-0.2g-RT. The results were well represented by the Langevin function, assuming a simplified superparamagnetic model of identical particle sizes with no interaction. In practice, the FePAH-0.5g-RT and FeChi-0.2g-RT samples exhibit particle size distributions and interparticle interaction could not be avoided, even it if it had a small S/D ratio. These two effects could account for the slight deviation between the magnetization data and the Langevin behaviour. They were, however, very narrow distributions (the lognormal distribution of D/D_v with standard deviation $\sigma < 0.1$ obtained by Chantrell's method in Table 5.4 and Table 5.5) in the FePAH-0.5g-RT and FeChi-0.2g-RT samples.

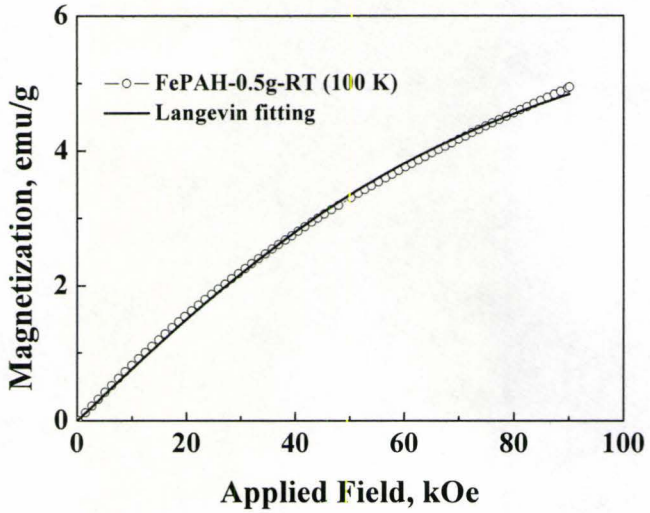

Figure 5.5 The Langevin function fitting to the magnetization curve of FePAH-0.5g-RT measured at 100 K. The fitting parameters were listed in Table 5.2

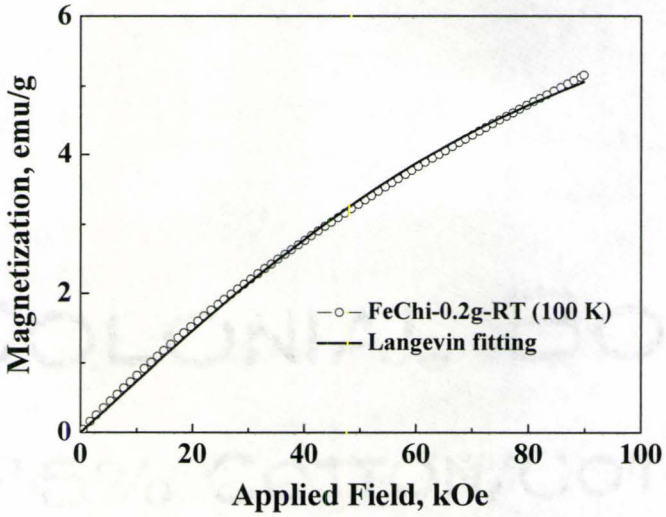

Figure 5.6 The Langevin function fitting to the magnetization curve of FeChi-0.2g-RT measured at 100 K. The fitting parameters were listed in Table 5.3

Langevin function fitting is invalid when there is either a distribution of particle sizes or a strong interparticle interaction. Instead, if the distribution of the nanoparticle

assembly can be described as the lognormal distribution, Chantrell [42] interpreted the magnetization versus the magnetic field curves by the sum of individual particle weighted by the distribution, and derived the equations to get mean and variance of the sample distribution. Later on, it was showed if the sample had a normal distribution, it could be well approximated by the lognormal one when the standard deviation was small, e.g. $\sigma < 0.35$ [50]. In the case of strong interparticle interaction, the superparamagnetic models fail, and the nanoparticle assembly behaves as a spin glass, a collective state observed in some systems [255].

5.2.3 Estimating the particle size distributions of γ-Fe_2O_3 nanoparticles

A critical parameter of an assembly of magnetic nanoparticles is *particle size distribution*. In the present work, two common techniques were used to analyze particle size distribution in the obtained nanocomposite films: electron microscopy (HRTEM) and magnetization characteristics utilizing Chantrell's method, Langevin function fitting or Néel-Brown model.

The advantage of the HRTEM method is that it is straightforward. Not only particle sizes but also morphology can be observed. However, since the particle size is only a few nanometers, the magnification has to be set high in order to obtain good-quality images to accurately identify the particle edges. Thus, the number of particles in one image is reduced. Also, the manual counting can be very time consuming because the images are not suitable for the automatic counting with available computer software. Therefore in the present work only about 100 particles were counted.

Magnetization curves can also be used to calculate the particle size distribution. The principle of Chantrell's method is explained in the literature review (Chap.1). Assuming a lognormal distribution, the magnetic diameter of a particle (D_{Vm}) and a standard deviation (σ) can be calculated from Eq.5.2.

$$D_{Vm} = \left(\frac{18 k_B T}{\pi M_S'} \sqrt{\frac{\chi_i}{3\varepsilon M_S'} \frac{1}{H_O}} \right)^{\frac{1}{3}} \qquad (5.2\ a)$$

$$\sigma = \frac{1}{3} \sqrt{\ln\left(\frac{3\chi_i H_O}{\varepsilon M_S'} \right)} \qquad (5.2\ b)$$

However, the disadvantage of Chantrell's method is that the assumption of the particle size distribution might not describe the real physical structure of the system, so that independent verification by other methods such as TEM observations are required to provide direct information about the size and distribution of the particles.

Table 5.4 summarized the parameters when fitting the magnetization curves of γ-Fe_2O_3 /PAH with the Chantrell's method by assuming a lognormal distribution of the particle diameter D. The standard deviation σ was dimensionless because it was using a normalized diameter D/D_V, where D_V was the mean value of the diameter.

Table 5.4 Chantrell's method to obtain the lognormal distribution parameters of γ-Fe_2O_3 /PAH samples

γ-Fe_2O_3 /PAH	Fitting parameters			Dv (nm)	Standard deviation σ
	χi (emu/gOe)	Ms (emu/g)	1/Ho (Oe^{-1})		
(a) 0.5 g/l, RT	8.35E-5	7.80	3.02E-5	2.0	0.08
(b) 0.5 g/l, 300°C	0.0299	34.0	1.05E-4	6.3	0.60
(c) No polymer, RT*	0.0517	61.2	2.59E-4	6.0	0.50

Table 5.5 summarizes the parameters when fitting the magnetization curves of γ-Fe_2O_3 /chitosan with Chantrell's method by assuming a lognormal distribution of particle sizes.

Table 5.5 Chantrell's method to obtain the lognormal distribution parameters of γ-Fe_2O_3 /chitosan samples

γ-Fe_2O_3 /chitosan	Fitting parameters			Dv (nm)	Standard deviation σ
	χi (emu/gOe)	Ms (emu/g)	1/Ho (Oe^{-1})		
(a) 0.2 g/l, RT	1.21E-4	8.42	2.86E-5	2.4	0.21
(b) 0.2 g/l, 300°C	7.59E-4	8.70	3.27E-5	4.6	0.48

Fig.5.7 compares the fitting results to the magnetization curves of FePAH-0.5g-300C by applying different particle size distributions. Fig.5.7(a) shows the Langevin function fitting result applied to the system with a single particle size. The very poor fitting indicates that the material can not be treated as a system containing particles of the same size, but as a system containing a distribution of particle sizes. By considering a lognormal distribution of the particles sizes with the parameters showed in Table 5.4, Chantrell's method gives a good fitting of the magnetization data at the high field region as shown in Fig.5.7(b). Moreover, if using a double-lognormal distribution, a better fitting can be obtained as shown in Fig.5.7(c). Two lognormal distributions assumed Dv=5.1 nm and 10.2 nm respectively, and $\sigma = 0.6$. The numbers of particles in these two distributions had a ratio 2:1.

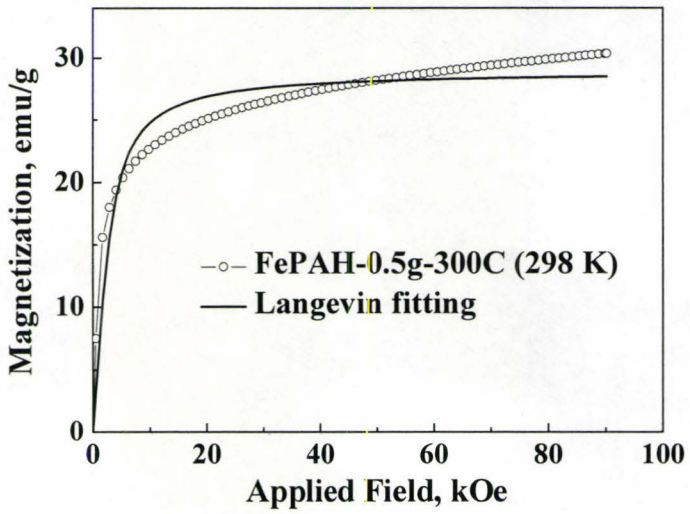
Magnetization, emu/g
Applied Field, kOe
FePAH-0.5g-300C (298 K)
Langevin fitting
0
10
20
30
0
20
40
60
80
100

(a)

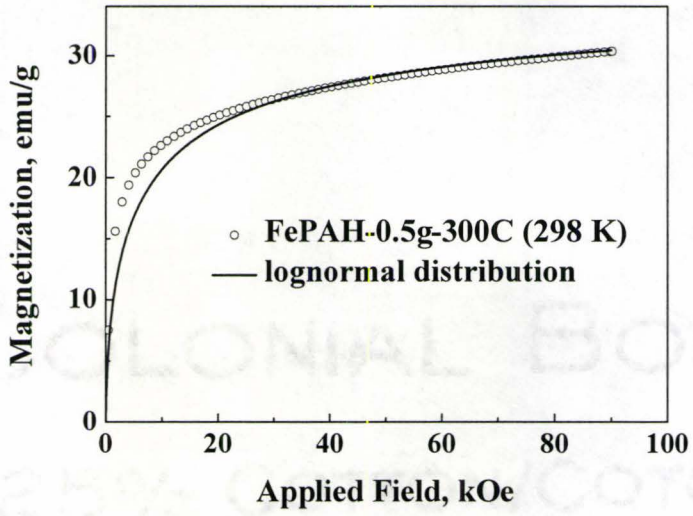
Magnetization, emu/g
Applied Field, kOe
FePAH-0.5g-300C (298 K)
lognormal distribution
0
10
20
30
0
20
40
60
80
100

(b)

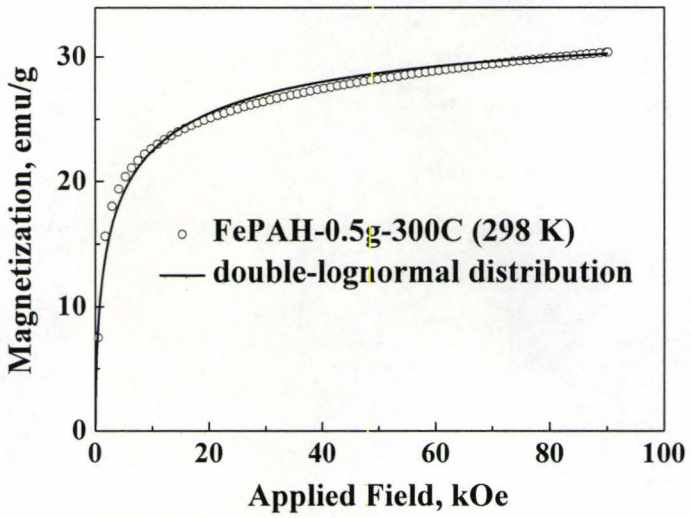

(c)

Figure 5.7 Magnetization curve fitting for FePAH-0.5g-300C composite with different particle size distribution. (a) identical sizes of particles without distribution, (b) lognormal distribution, (c) double lognormal distribution

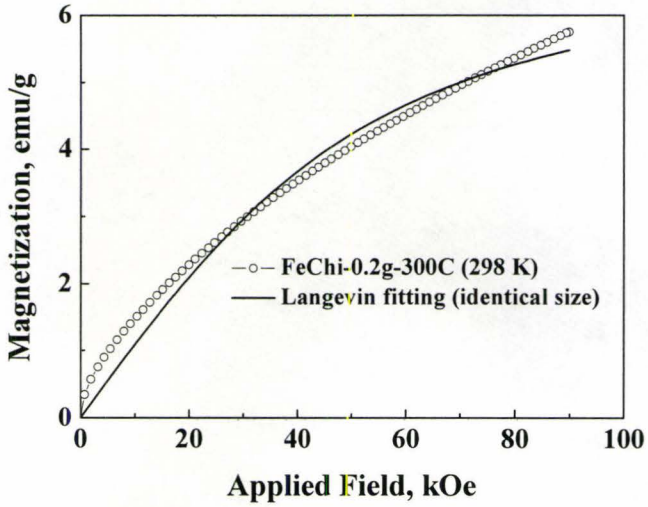
Magnetization, emu/g
Applied Field, kOe
FeChi-0.2g-300C (298 K)
Langevin fitting (identical size)
0
2
4
6
0
20
40
60
80
100

(a)

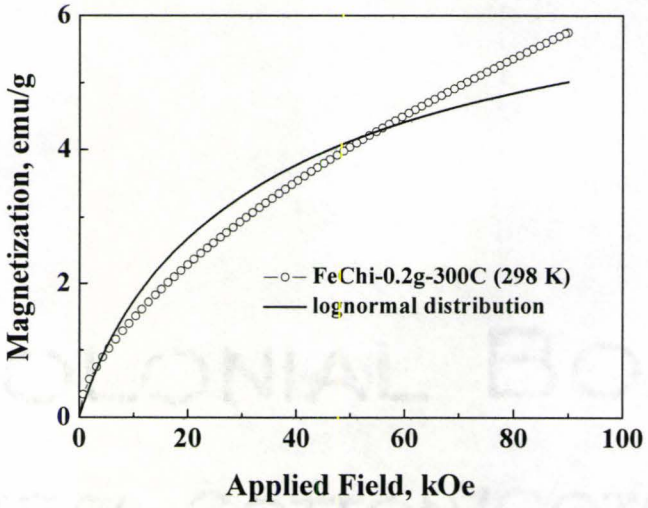
Magnetization, emu/g
Applied Field, kOe
FeChi-0.2g-300C (298 K)
lognormal distribution
0
2
4
6
0
20
40
60
80
100

(b)

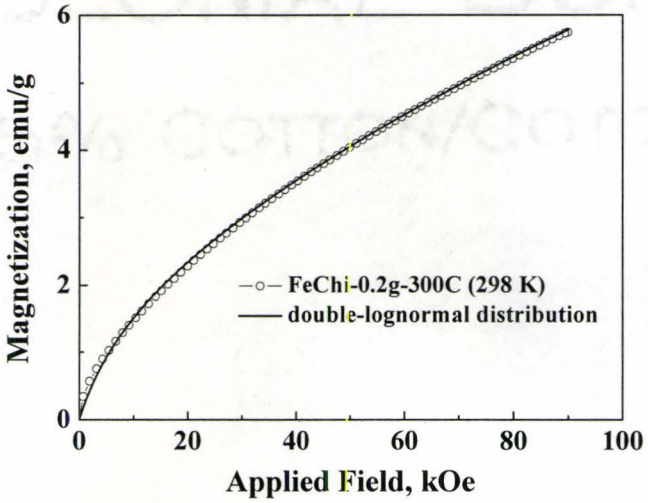

Figure 5.8 Magnetization curve fitting for FeChitosan-0.2g-300C with different particle size distributions (a) identical sizes of particles without distribution, (b) lognormal distribution, (c) double lognormal distribution

Fig.5.8 shows the fitting results to the magnetization curves of FeChi-0.2g-300C by applying different particle size distributions. The composite was in a form of a powder sample with the polymer burnt out. The best fitting was given by considering a double-lognormal distribution, having the Dv of 2 nm and 4.7 nm respectively, σ = 0.1 and 0.4 respectively. The number of particles in these two distributions was assumed in a ratio of 5:1.

It was found that the double-lognormal distribution can describe very well the magnetization curves of the powder samples showing the strong interparticle interaction, such as those of the FePAH-0.5g-300C and FeChi-0.2g-300C samples. The results are attributed to the agglomeration and strong interaction in the powder samples.

HRTEM images were used to count a sampling of the particle sizes of the γ-Fe_2O_3 nanoparticles in the selected deposits. For instance, the histogram of γ-Fe_2O_3 nanoparticle size distribution in the 5 mM $FeCl_3$ solutions containing 0.2 g/l chitosan (FeChi-0.2g-RT) was plotted in Fig.5.9, overlaid with a lognormal distribution fitting curve, having the mean diameter D = 3.2 nm and the standard deviation σ = 0.53 nm. On the other hand, the Langevin function fitting showed an average particle size of 2.1 nm, shown as a straight line in Fig.5.9. From Chantrell's method of fitting the magnetization curves (Fig.4.55 and Table 5.5), the mean diameter D_V and standard deviation σ of the lognormal distribution in FeChi-0.2g-RT were 2.4 nm and 0.21, respectively. The lognormal distribution of Chantrell's method was plotted as the dashed line in Fig.5.9.

The difference between TEM observation and Chantrell's method may be caused by the nature of the methods. As it was explained by Chantrell [42], the physical particle size D_p, which is measured from HRTEM images, should be larger than the magnetic particle size D_m, which is calculated from the magnetization data, because of the magnetically disordered surface layer caused by surface spin canting and other surface effects. Also, miscounts occurred when the individual particles distributed in the volume of the film might be counted as one particle because their images were superimposed one on the other in the HRTEM studies, which gave larger values of the average particle size and standard deviation in the distribution. Nonetheless the two methods were still in a good agreement.

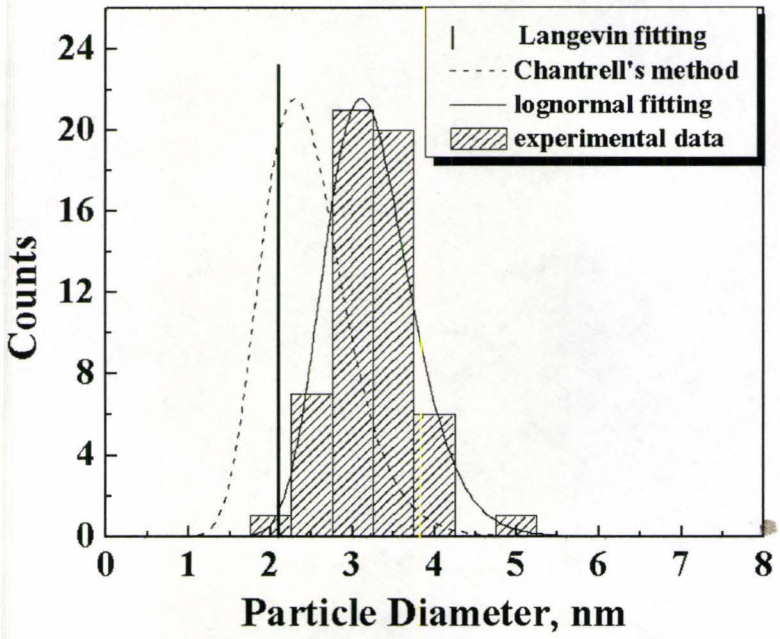

Figure 5.9 TEM observation of the histogram of γ-Fe_2O_3 nanoparticle size distribution in the FeChi-0.2g-RT. The solid and dash lines were the lognormal distributions observed from the TEM and calculated from Chantrell's method, respectively. The straight line showed Langevin function fitting result.

5.2.4 Modeling the AC susceptibility of γ-Fe_2O_3 nanoparticles

AC susceptibility studies the dynamic properties of magnetic nanoparticles. The shape of the temperature dependence of the susceptibility yields the information about particle size distribution.

According to Gittleman [62] the complex susceptibility of an assembly of isolated single-domain particles is given by (Chapter 1):

$$\chi = \frac{\chi_0 + i\varpi\tau\chi_1}{1 + i\varpi\tau} \qquad (5.3\ a)$$

The real part is given by $\chi' = \chi_1 + \frac{\chi_0 - \chi_1}{1+(\varpi\tau)^2}$ (5.3 b)

the imaginary part is given by $\chi'' = \varpi\tau\left(\frac{\chi_1 - \chi_0}{1+(\varpi\tau)^2}\right)$ (5.3 c)

where $\chi_0 = \frac{M_S^2 Vx}{3kT}$ (5.3 d)

χ_0 is the superparamagnetic susceptibility corresponding to thermal equilibrium, and x is the volume fraction occupied by the particles. And

$$\chi_1 = \frac{aM_S^2 x}{|K|} \quad (5.3\text{ e})$$

χ_1 is the ferrimagnetic susceptibility of the system in the "blocked" state, and $a = \frac{1}{2}\langle \sin^2\theta \rangle$ is the average of random oriented easy direction, θ is the angle between the applied field and the easy direction of magnetization.

We also know that relaxation time $\tau = \tau_o \exp\left(\frac{KV}{kT}\right)$. (5.4)

Eqs.5.3-5.4 define the relaxation process in a superparamagnetic particle. A simulation run by the MATLAB software used the above equations and applied different particle size distributions to show how the particle size distribution determines the shape of the temperature dependence of the susceptibility. As shown in the Fig.5.10. In the simulation, some parameters were taken as the following, the relaxation time $\tau_o = 10^{-10}$, the anisotropy constant $K = 5*10^5$, the measurement were taken at the angular frequency $\omega = 2\pi*10^{-5}$. Assuming the average particle diameter was 4 nm. Therefore the identical particle diameter was taken as 4 nm. The uniform distribution function is defined as

$f(D) = \overline{D}/2, \qquad D \le 2\overline{D}$

$= 0, \qquad D > 2\overline{D}$

In the simulation, the average diameter $\overline{D}$ of the uniform distribution was chosen as 4 nm.

The lognormal distribution function is defined as

$$f(y) = \frac{1}{y\sigma\sqrt{2\pi}} \exp\left(\frac{-(\ln y)^2}{2\sigma^2}\right), \text{ where } y = \frac{D}{\overline{D}}.$$

In the simulation, the average diameter $\overline{D}$ and σ of the lognormal distribution were taken as 4 nm and 0.2, respectively.

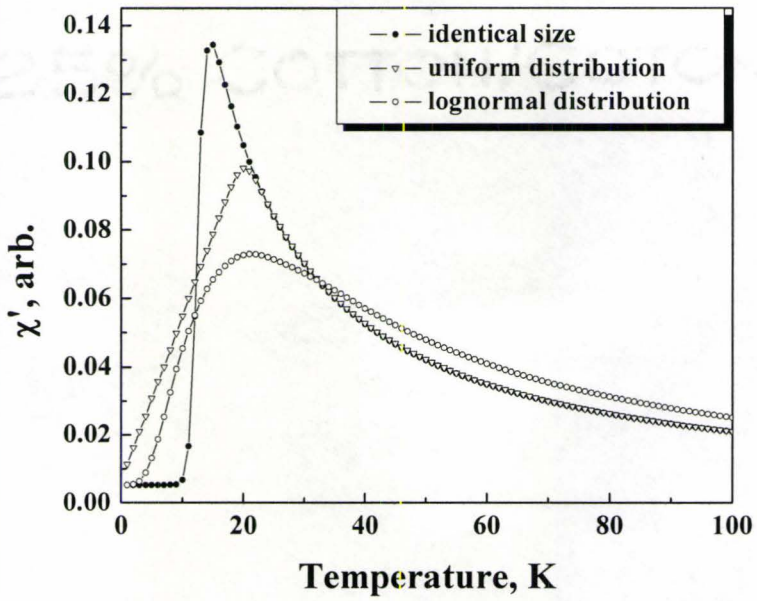

(a)

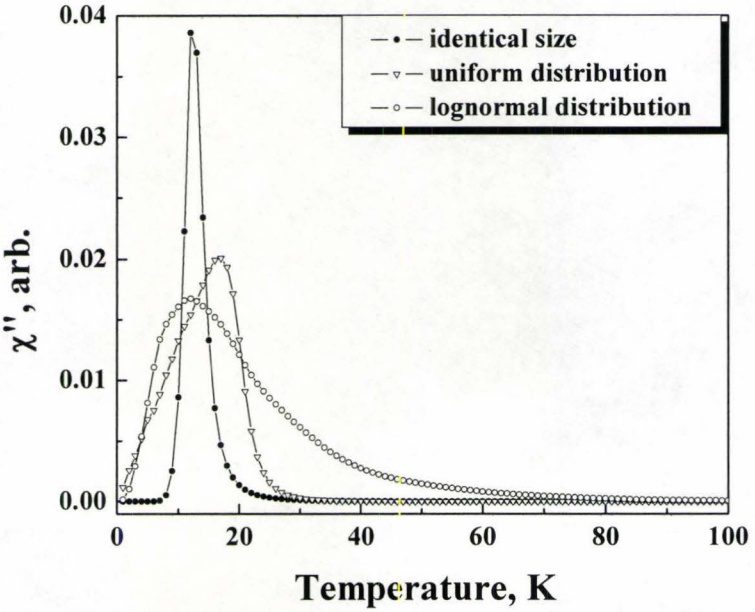

(b)

Figure 5.10 A modeling of the susceptibility versus temperature as a function of the particle size distribution, (a) real part and (b) imaginary part of the susceptibility.

From the simulation in Fig.5.10 and Eqs.5.3-5.4, it is concluded that the value of the T_{max} is determined by the anisotropy energy E_B, which is product of anisotropy constant K and the average volume of the particles V. The shape of the curve is determined by the particle size distribution. Therefore, by fitting the temperature dependence of the AC susceptibility, one can extract the particle size distribution in the system. On the other hand, if the particle size distribution is known, the fitting results can give the value of anisotropy constant K.

For instance, in the FePAH-0.5g-RT sample, the magnetization data studied by Chantrell's method revealed that there was a lognormal distribution of the particle size with the average diameter D_V = 2.0 nm, and σ = 0.08.

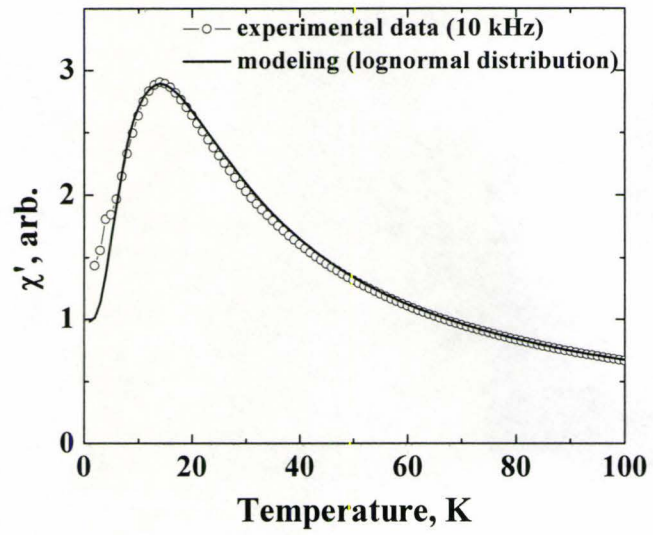

(a)

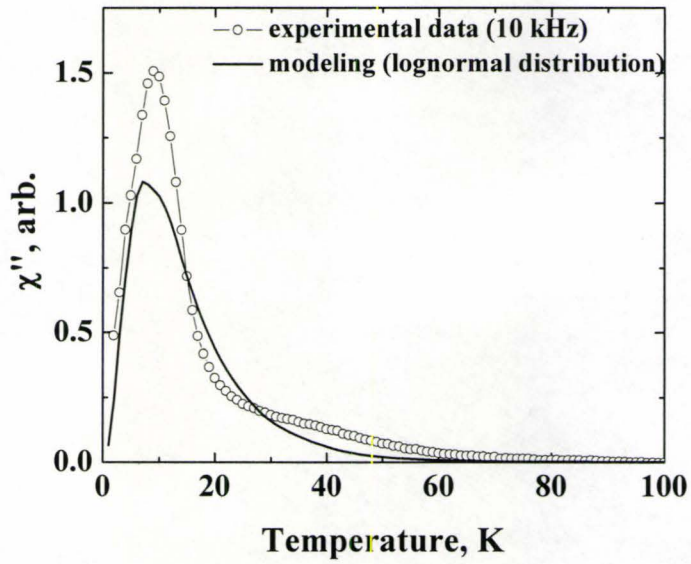

(b)

Figure 5.11 The best fitting to the temperature dependence of (a) real part and (b) imaginary part of AC susceptibility of the FePAH-0.5g-RT with a lognormal distribution of particle sizes.

Fig.5.11 shows the best fitting to the temperature dependence of AC susceptibility of the FePAH-0.5g-RT sample with a lognormal distribution of the particle sizes. The average particle diameter was fixed at 2.0 nm, and then the anisotropy constant was chosen as $27*10^5$ erg/cm^3 to best fit the T_{max}. Finally the standard deviation σ was chosen as 0.20 to best fit the shape of the curve. The magnitude of the susceptibility was controlled by the M_S, volume fraction of the particle x, and were taken as 51 emu/g and 0.2, respectively. The results reveal good fitting of the real part of the susceptibility, however some deviation for the imaginary part is observed.

The anisotropy constant obtained from the fitting K = $27*10^5$ erg/cm^3 was much larger than one can expect realistically in such system. Other workers obtained K ~ $4\cdot10^5$ erg/cm^3 after taking the surface anisotropy and shape anisotropy into account [55]. Our sample showed weak interparticle interactions, which could also contribute to the anisotropy energy. It is difficult to quantify how much these interactions contribute to the anisotropy energy and further investigations of the origin of the high anisotropy constant are required, but are beyond the scope of the present work. This high anisotropy constant in our sample could explain the very slow frequency dependence of the T_B.

The imaginary part of the susceptibility in FePAH-0.5g-RT showed a hump around 40 K in addition to the T_{max} peak around 14 K. Assuming a double-lognormal distribution of the particle sizes, a better fitting to the imaginary part is expected. This double-lognormal distribution was proven to be very common distribution of the particle sizes in the samples obtained by electrodeposition in our experiments. For instance, the reduction of the polymer PAH amount in the electrochemical bath solution from 0.5 g/l to 0.3 g/l,

changes clearly the characteristics of the susceptibility. It introduces double-peak in the imaginary part of the susceptibility, as shown in Fig.5.12, having the T_{max1} and T_{max2} around 7 K and 36 K, respectively. The reason for the double-lognormal distribution may lie in the nature of the electrodeposition, there was chance to have some level of agglomeration. As the polymer amount reduces, there is more agglomeration formed.

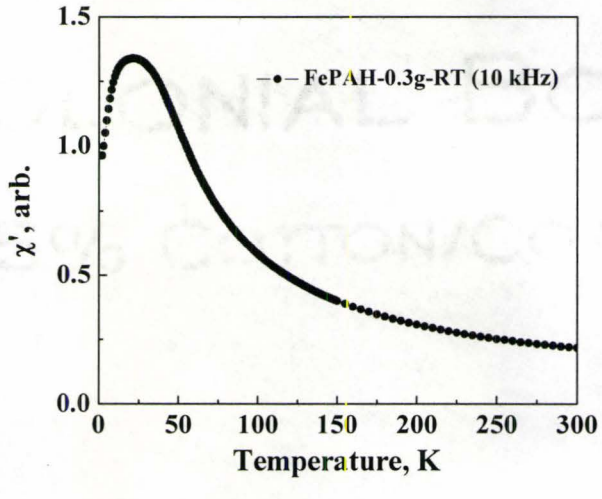

(a)

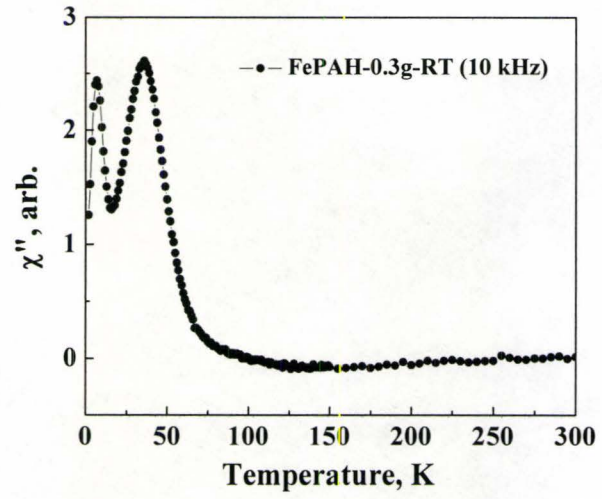

(b)

Figure 5.12 The temperature dependence of AC susceptibility of the FePAH-0.3g-RT samples showing a double-peak on the imaginary part (b).

As shown in Fig.4.57, the temperature dependence of AC susceptibility of the FeChi-0.2g-RT again showed the double-lognormal distribution of the particle sizes. HRTEM result however didn't show such double-lognormal distribution. The reason is that during the counting of particle sizes, the area which contains the agglomeration of γ-Fe_2O_3 particles was excluded.

Based on the simulation of the temperature dependence of the susceptibility of some samples obtained in our experiments, it is concluded that there is a broad distribution of the particle sizes, and in some case, a double-lognormal distribution. These distributions are required to describe the observed double-peak phenomenon in the imaginary part of the susceptibility.

5.3 Magnetic properties of Mn_3O_4 nanoparticles

5.3.1 Curie-Weiss behaviour of Mn_3O_4

Previous studies indicated that Mn_3O_4 has a tetragonal spinel structure below 1443 K, and a cubic spinel above 1443 K [257]. The ionic structure is $Mn^{2+}[Mn_2^{3+}]O_4$, so that Mn^{2+} ions occupy the tetrahedral interstices (A sites), and Mn^{3+} are in the octahedral ones (B sites). Above the Néel temperature T_N = 42 K, Mn_3O_4 is magnetically disordered. Below 42 K, the ferrimagnetic structure of Mn_3O_4 changes as a function of temperature in the regions 42-39 K, 39-33 K, and below 33 K. A detailed description of the magnetic structure in the temperature below 42 K is available in the literature [222, 257, 258].

Several papers discussed the temperature dependence of reciprocal susceptibility of Mn_3O_4 in the paramagnetic region $T > T_N$. It was shown that it follows a hyperbolic curve, which is described by the relation (Eq.1.12 a) [258]:

$$\frac{1}{\chi} = \frac{T}{C} + \frac{1}{\chi_0} - \frac{\sigma}{T-\Theta} \qquad (1.12\ a)$$

Here, C is the Curie constant, and can be calculated by the following equations [259]:

$$C = C_A(Mn^{2+}) + 2C_B(Mn^{3+}), \qquad (5.1)$$

$$C_{A,B} = N\mu^2_{eff(A,B)}/3k_B, \qquad (5.2)$$

N is the Avogadro number, k is the Boltzmann constant, $\mu_{eff(A,B)}$ is the effective magnetic moment of the A and B sublattice,

$$\mu^2_{eff(A,B)} = g^2_{(A,B)}S(S+1)\,\mu_B{}^2 \qquad (5.3)$$

g(A, B) is the g factor of the A or B sublattice, and μ_B is the Bohr magneton. Based on the electron-spin-resonance (ESR) experiments, Srinivasan [258] used g_A= 2.0 for Mn^{2+} (S_A=5/2) and g_B = 2.017 for Mn^{3+} (S_B=2), so that the magnetic moments of manganese ions and the Curie constant are $\mu^2_{effA} = 35\mu_B^2$, $\mu^2_{effB} = 24.41\mu_B^2$ and C_A=4.37, C_B=3.03. As a result, the Curie constant C = 10.43. In this calculation, it is convenient to use the cgs units because the following relationship:

$$\mu_{eff} = 2.827\sqrt{\chi_m^{cgs}T} = 2.827\sqrt{C}\ \text{(cgs)}\ [260] \qquad (5.4)$$

Where χ_m^{cgs} is measured in emu/mol.

Srinivasan [258] has fitted T-1/χ to Eq.1.12 a with Curie constant C=10.43, and obtained the following parameters: Θ=10.2 K, σ=1700, $1/\chi_0$=57.5. Therefore, all the Weiss coefficients can be calculated by Eq.1.12 b-d, such that N_{AA} = 26.0, N_{BB} = 78.9,

N_{AB} =54.3. Thus, the ferrimagnetic Néel temperature T_{FN} = 37.6 K was obtained from Eq.1.14, comparing with the experimental value of 41.9 K [261]. The small discrepancy was most likely due to the expected failure of the molecular field model close to T_N. The paramagnetic Curie point θ = 600 K [258] was in the experimental range from 540 K [222] to 640 K [220, 221].

In the present work, the temperature dependence of reciprocal susceptibility of Mn_3O_4 in the paramagnetic region T > 150 K until 300 K has been linearly fitted to $\frac{1}{\chi} = \frac{T}{C} + \frac{1}{\chi_0}$ (Eq.1.13) to obtain the Curie coefficient C and paramagnetic Curie point θ. As discussed in Chapter 4, the following Mn_3O_4 nanocomposite samples have been studied (Table 5.6).

Table 5.6 The fitting parameters of Eq.1.13 to the temperature dependence of reciprocal susceptibility of Mn_3O_4 in the paramagnetic region 150 K -300 K

Sample	$1/\chi_0$	C (emuK/mol)	θ	μ_{eff}/formula
Mn_3O_4-PAH-0.5g-RT	37.7	15.62	589	11.2
Mn_3O_4-PEI-0.5g-RT	33.9	6.14	208	7.0

5.3.2 Particle Separation Ratio S/D of Mn_3O_4 Nanoparticles

The particle separation ratios S/D of the Mn_3O_4 – PEI, the Mn_3O_4 – PAH, and the Mn_3O_4 – chitosan composites, comparing with the initial electrolyte concentration in the bath solution, mass and volume fraction of the inorganic phases (Mn_3O_4) in the deposits, were calculated in the Table 5.7.

All of the Mn_3O_4/polymer nanocomposites in our experiments fell into the category of the weak and intermediate interaction because the S/D ratios were in the range of 1.2-1.7.

Table 5.7 The particle separation ratios S/D of the Mn_3O_4 – PEI, the Mn_3O_4 – PAH, and the Mn_3O_4 – chitosan composites

PEI content (g/l)	Mass fraction	Volume fraction(1)	S/D
0.5	0.616	0.254	1.27
1.0	0.504	0.178	1.43
2.0	0.387	0.118	1.64
PAH content (g/l)			
0.5	0.604	0.245	1.29
1.0	0.479	0.164	1.47
Chitosan content (g/l)			
0.2	0.666	0.298	1.21

(1) consider polymer's bulk density ~1.0 g/cm^3

5.3.3 Particle size distributions of Mn_3O_4 nanoparticles

Mn_3O_4 has ferrimagnetic Néel temperature at 42 K. In order to observe the superparamagnetic behaviour in Mn_3O_4 nanoparticle, from the Néel-Brown model $\tau = \tau_0 \exp[KV / k_B T]$ (Eq.1.25), the critical superparamagnetic volume V_C at T_B = 42 K equals to 1.6×10^{-19} cm^3, so that the particle diameter φ_C = 6.7 nm. This estimation was given by assuming the anisotropy constant of bulk Mn_3O_4, K ~ 1×10^6 erg/cm^3, τ = 100 s, which was the measurement time (τ is frequency dependent in AC measurement), $\tau_O = 10^{-10}$ s, the characteristic relaxation time, and k_B = 1.38×10^{-16} erg/K, the Boltzmann constant.

In our work, Fig.4.32 showed AC magnetic susceptibility of Mn_3O_4 – PEI nanocomposites. A superparamagnetic relaxation occurred below T_N (42 K) for the deposits prepared from the 5 mM $MnCl_2$ solution containing (a) 1.0 g/l PEI and (b) 0.5 g/l PEI due to the extremely small particle sizes. This was the first experimental evidence of

the superparamagnetic behaviour being observed below T_N = 42 K. The average particle size can be estimated using the Néel-Brown model. From the experimental values, T_B are 7 K and 14 K for the deposits prepared from the 5 mM $MnCl_2$ solution containing 1.0 g/l PEI and 0.5 g/l PEI, respectively at the measurement frequency of 10 kHz ($\tau = 10^{-5}$ s), so that the estimated particle size φ is found to be 2.8 nm and 3.5 nm, respectively.

HRTEM (e.g. Fig.4.29) images of the Mn_3O_4 nanocomposite deposits obtained from the 5 mM $MnCl_2$ solutions containing 0.5 g/l PEI (sample b) were used for particle sizes counting. The histogram of Mn_3O_4 nanoparticle size distribution in the MnPEI-0.5-RT was plotted in Fig.5.13, overlaid with a lognormal distribution fitting curve, having the mean diameter D = 3.0 nm and standard deviation σ = 0.08. The estimated particle size (3.5 nm) was in a good range with the experimental results.

By counting the HRTEM images (e.g. Fig.4.16) of the Mn_3O_4 nanocomposite deposits obtained from the 5 mM $MnCl_2$ solutions containing 0.5 g/l PAH, Fig.5.14 shows that the histogram of MnPAH-0.5g-RT is fitted with a lognormal distribution, having the mean diameter D = 4.5 nm and standard deviation σ = 0.22. Fig.5.15 shows the histogram of the MnChi-0.2g-RT overlaid with a lognormal distribution of the mean diameter D = 4.4 nm, and standard deviation σ = 0.11 nm. A summary of various Mn_3O_4 nanocomposites is shown in Table 5.8.

In Fig.4.66, large change of magnetization near the zero applied field was suggested to be related to smaller particles in the superparamagnetic state, and the hysteresis loop was contributed by larger particles. It is however not shown in HRTEM results here two different sizes in the distribution. The reason is that only separated individual particles

were chosen, however, there existed a large area of agglomeration of Mn_3O_4 nanoparticles which was not chosen and counted. So the HRTEM results only determines the distribution of the separated individual particles

Table 5.8 The particle size distribution observed by HRTEM for Mn_3O_4-polymer composites, comparing with the estimation from Neel-Brown model

Samples	HRTEM observation		Neel-Brown model
	Average D (nm)	Standard deviation σ	D (nm)
MnPEI-0.5g-RT	3.0	0.08	3.5
MnPAH-0.5g-RT	4.5	0.22	-
MnChi-0.2g-RT	4.4	0.11	-

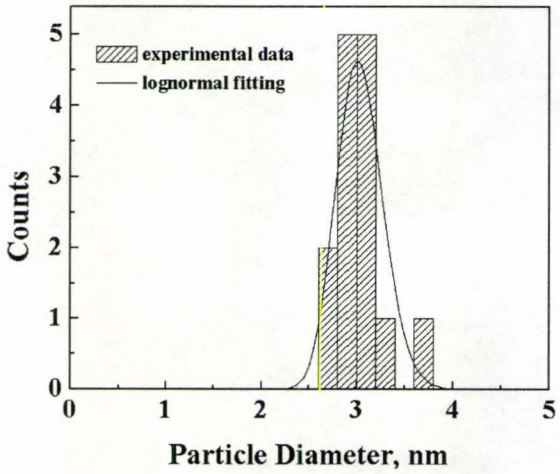

Figure 5.13 Histogram of Mn_3O_4 nanoparticle size distribution of the fresh deposit obtained from the solution containing 5 mM $MnCl_2$ and 0.5 g/l PEI. The solid line is the lognormal distribution fitting curve.

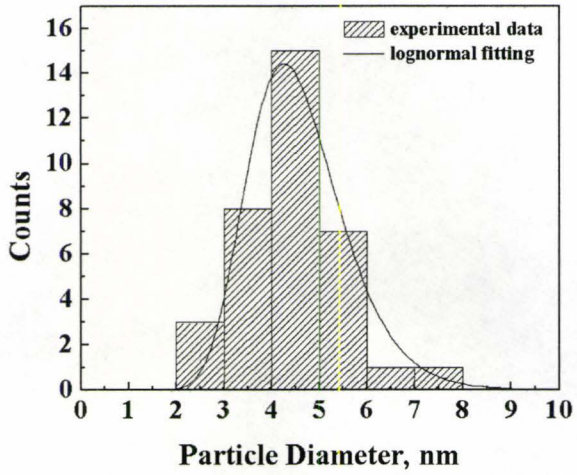

Figure 5.14 Histogram of Mn_3O_4 nanoparticle size distribution of the fresh deposit obtained from the solution containing 5 mM $MnCl_2$ and 0.5 g/l PAH. The solid line is the lognormal distribution fitting curve.

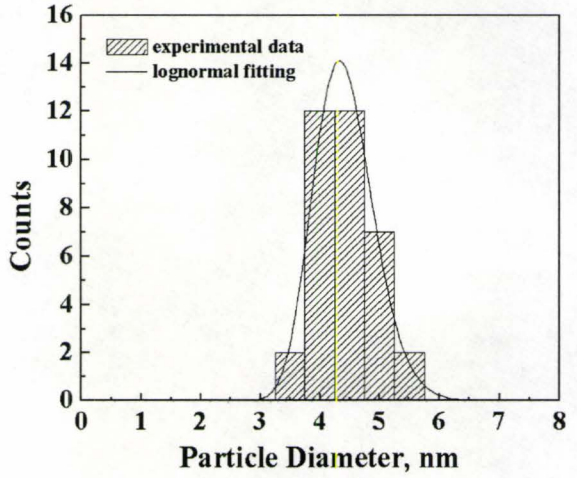

Figure 5.15 Histogram of Mn_3O_4 nanoparticle size distribution of the fresh deposit obtained from the solution containing 5 mM $MnCl_2$ and 0.2 g/l chitosan. The solid line is the lognormal distribution fitting curve.

5.3.4 Size dependence of the Néel temperature of Mn_3O_4 nanoparticles

Fig.4.31 shows the temperature dependence of field cooling (FC) and zero field cooling (ZFC) magnetization for the selected four Mn_3O_4/PEI samples, which were the

deposits prepared from the 5 mM $MnCl_2$ solutions containing 1.0 g/l PEI and 0.5g/l PEI and those annealed at 200 and 300 °C. A decrease of the Néel temperature was observed with reducing the average Mn_3O_4 particle size. The Néel temperature T_N values obtained from T_{max} of AC susceptibility measured at 10 kHz (Fig.4.32 a, b, c, d) gave 31 K, 36 K, 39 K, and 43 K from samples a to d, respectively. The estimated average particle sizes of Mn_3O_4 nanoparticles in the fresh deposits, samples a and b, were 3.5 nm and 2.8 nm, respectively. After annealing at 200 and 300 °C, the narrowed and sharpened XRD Mn_3O_4 characteristic peaks indicated the increase of crystalline sizes.

A similar particle size dependence of Néel temperature was reported in some other works. It was found that Mn_3O_4 nanoparticles with diameters of 6, 10, and 15 nm showed a T_N = 36, 40, and 41 K, respectively [262]. It was suggested that Mn_3O_4 nanoparticles had reduced Néel temperature comparing to the bulk value T_N = 42 K. This phenomenon could be related to surface effects due to the large surface to volume ratio in the nanoparticles. The surface effects, which include the surface spins canting, surface anisotropy, core-surface exchange interaction, could result in the reduced spontaneous magnetization and Néel temperature [46, 263].

CHAPTER 6

CONCLUSIONS

The present work was dedicated to fabricate new nanocomposite materials by using electrodeposition and to investigate deposition mechanisms, film composition, structure and magnetic properties of these materials. A combined method based on the electrophoretic deposition (EPD) of cationic polyelectrolytes and cathodic electrosynthesis of inorganic phases has been developed to prepare spinel structured oxide nanoparticles *in situ* in the polymer matrix. Various electrochemical strategies have been developed, which are based on the use of weak polyelectrolytes, strong polyelectrolytes and polymer-metal ion complexes. Deposited films have been characterized using XRD, TG, DTA, SEM, TEM and AFM. Magnetic properties have been studied by measurement of AC susceptibility at the frequency range of 10 Hz to 10 kHz and the temperature range of 2 to 298 K, ZFC/FC magnetization at different magnetic fields in the temperature range of 2 to 298 K. The major conclusions are as following:

The electrodeposition is conducted in ethanol-water mixed solvent containing metal chloride salts and polyelectrolytes. Strong polyelectrolyte, such as PDDA, and weak polyelectrolytes, such as PEI, PAH, chitosan, and P4VPy, have been utilized in the combined method. SEM investigations show good uniformity and adhesion to the substrates with thickness range up to 5 μm. When the electrodeposition is conducted on a carefully polished substrate, AFM studies show very smooth film surface with a root-mean-square (rms) surface roughness of 1.6 nm.

It has been shown that the weight percentage of inorganic phase in the deposits can be reduced by increasing the polyelectrolyte concentration in the electrodeposition bath solutions. In the solution containing 5 mM $MnCl_2$, when the PEI concentration increases from 0.5 g/l, 1.0 g/l to 2.0 g/l the weight percentage of Mn_3O_4 in the Mn_3O_4–PEI deposits drops from 61.6%, 50.4% to 38.7%; and as PAH concentration increases from 0.5 to 1.0 g/l, the weight percentage of Mn_3O_4 in the Mn_3O_4–PAH deposits also decreases from 60.4% to 47.9%. In the solution containing 5 mM $FeCl_3$, as the PAH concentration increases from 0.0, 0.2, 0.3 to 0.5 g/l, the weight percentage of γ-Fe_2O_3 in the γ-Fe_2O_3–PAH deposits reduces from 90.0%, 62.0%, 52.5% to 39.0%.

XRD and HRTEM studies have shown the crystal structure and morphology of the magnetic nanoparticles in the nanocomposites obtained at different experimental conditions. It is shown that nearly spherical Mn_3O_4 or γ-Fe_2O_3 nanoparticles are formed *in situ* in the polymer matrix when the electrodeposition is conducted in the solutions containing 5 mM $MnCl_2$ or 5 mM $FeCl_3$ and one type of the polyelectrolytes, such as PAH, PEI, PDDA, chitosan, or P4VPy.

HRTEM images have been used to study the average particle sizes. The results show that the particle sizes are mainly controlled by the polymer properties, e.g. molecular weights or functional groups. The average particle sizes of Mn_3O_4 are 3.0 ± 0.2 nm for Mn_3O_4–PEI (61.6 wt% of Mn_3O_4, 0.5 g/l PEI in the solution), 4.6 ± 1.0 nm for Mn_3O_4–PAH (60.4 wt% of Mn_3O_4, 0.5 g/l PAH in the solution), and 4.4 ± 0.5 nm for Mn_3O_4–chitosan (66.6 wt% of Mn_3O_4, 0.2 g/l chitosan in the solution). The smaller particle sizes for Mn_3O_4 in the PEI matrix may be caused by a different electrodeposition mechanism,

which is based on the use of PEI-metal ion complexes in the electrochemical bath solution. HRTEM shows that the average particle size of γ-Fe_2O_3 in chitosan matrix (0.2 g/l chitosan in the solution) is 3.2 nm. The particle size distributions in various nanocomposites obtained in the present work are proven to be close to the normal distribution.

It is found that the average particle size of inorganic nanoparticles can be controlled by the polymer concentration in the electrochemical bath solution. The increase in the polymer concentration in solutions and deposits results in smaller size of the inorganic nanoparticles formed in a polymer matrix. In the solution containing 5 mM $FeCl_3$, as the PAH concentration increases from 0 to 0.5 g/l, the estimated particle size is reduced from 6.9 nm to 2.0 nm (Table 5.2). In the solution containing 5 mM $MnCl_2$, when PEI concentration increases from 0.5 g/l to 1.0 g/l, the estimated particle size drops from 3.5 nm to 2.8 nm.

Heat treatment is also used to modify the particle size. When the annealing temperature is below the burning temperature of polymer, usually in the temperature below 300 °C, only small increase in the particle sizes is observed. However, when the annealing temperature is at 300 °C where the polymer is burnt out, significant increase in the particle sizes can be found. In the γ-Fe_2O_3–PAH nanocomposites (Table 5.2), the particle sizes are 2.5 nm and 7.2 nm after annealing at 200 and 300 °C, comparing to 2.0 nm of the fresh deposit. When the annealing temperature is at 400 °C and above, the phase transformation occurs from spinel phase to non-magnetic oxide phase, such as Mn_3O_4 to Mn_2O_3 or γ-Fe_2O_3 to α- Fe_2O_3.

It is discovered that the polyelectrolytes promote the room temperature crystallization of Mn_3O_4, γ-Fe_2O_3 and other spinel structured nanoparticles.

DC magnetization and AC susceptibility measurements have been used to study the superparamagnetic behavior and ferrimagnetic phase transitions in γ-Fe_2O_3 and Mn_3O_4. It is found that blocking temperature T_B is mainly controlled by the particle sizes, and that increasing the particle size results in shift of the T_B to higher temperature, which agrees with the Néel-Brown's model. With the estimated particle sizes increase from 2.0 nm, 2.5 nm to 7.2 nm, the experimental data give T_B of 14 K, 25 K, and 195 K, respectively (Table 5.2). Moreover, there is almost no frequency dependence of T_B in the frequency range of 10 Hz – 10 kHz, this phenomenon is attributed to the strong interparticle interaction similar to the results reported in the literature for other materials[255]. It is the first time to observe superparamagnetism in Mn_3O_4 nanoparticles below the ferrimagnetic Néel temperature T_N, the T_B is found to be 7 K and 14 K, and therefore the estimated average particle sizes are 3.5 nm and 2.8 nm, for the fresh deposit prepared from the 5 mM $MnCl_2$ solutions containing 1.0 g/l and 0.5 g/l PEI, respectively. It is found that the T_N depends on the average particle size. When the estimated average particle size of Mn_3O_4 changes from 3.5 nm to 2.8 nm, the Néel temperature T_N decreases from 36 K to 31 K.

Various theoretical models have been used to calculate the average particle size of the magnetic nanoparticles based on the magnetic measurement data, such as Chantrell's model, Langevin function fitting, Néel-Brown model. The particle separation ratio S/D was used to describe the level of the interparticle interaction. Langevin function fitting is

found to be valid only when the interaction is weak and the system has a very narrow particle size distribution. When the system contains a lognormal distribution of particle sizes, the Chantrell's method is used to estimate the parameters of the lognormal distribution. When the system has a strong interparticle interaction, a double-lognormal distribution is required to describe the magnetization data. The criteria to apply these models have been discussed.

The double-lognormal distribution is also found to be useful to explain the double-peak phenomenon observed in the imaginary part of AC susceptibility versus temperature curves in some nanocomposites.

HRTEM observation of the particle size distribution shows larger average particle size D than the one calculated from the magnetization data. It is concluded that a magnetically dead layer is found on the surface of the magnetic nanoparticle because of the surface spin canting and other related surface effects.

FUTURE WORK

PEI has shown good binding capacity with metal ions to form PEI-metal ion complexes. It will be interesting to investigate chemically modified PEI and other chelating polyelectrolytes which have other functional groups to obtain novel superparamagnetic nanocomposites.

In Chapter 4.4.2, co-deposition of iron oxide and P4VPy has been achieved. In order to characterize microstructure and magnetic properties of the nanocomposite material, some further experiments will be necessary. X-ray diffraction will be important to study the crystal structure of the inorganic phase. SEM and HRTEM are needed to study the film morphology and particle size distribution. Magnetic characterization is needed in order to investigate the relationship between microstructure and magnetic properties

The double-lognormal distribution was considered for some samples in order to explain the double peaks occurred in the imaginary part of the susceptibility versus temperature curves. It will be interesting to study the best fitting parameters of the double-lognormal distribution to the temperature dependence of AC susceptibility.

The interparticle interaction is usually treated as an extra term applied to the energy barrier in the superparamagnetic particles by other workers. It will be interesting to see how the interparticle interaction modifies the magnetic properties of superparamagnetic particles.

APPENDIX A MATLAB SOURCE CODE

1. Calculating the AC susceptibility

```
%calculate the AC susceptibility based on the superparamagnetic model
%reference paper Physical Review B, vol 9, number 9, P3891
%assume a lognormal distribution of the diameters of the particles

clear all; close all;
%generate a lognormal distribution of the diameter D

mu=log(2.03); sigma=0.2; counts=10000;
d=lognrnd(mu,sigma,counts,1); %d, the diameter, nm.
D=d*10^(-7); %D is the diameter of the particles, cm.
V=1/6*pi*D.^3;

%define the constants
omiga=2*pi*10^5; tau0=1E-10; Ms=51.5; k=1.38*10^(-16); K=27*10^5;
a=0.5; vf=0.2;

%Energy barrier caused by the anisotropy engergy
Eb=K*V;

%temperature range is from 1 K to 300 K
M=300;
T=linspace(1,300,M);
%calculate the real and imaginary part of the susceptibility
for i=1:M
   x0=Ms^2*V*vf/(3*k*T(i));
   x1=a*Ms^2*vf/K;
   tau=tau0*exp(Eb/(k*T(i)));
   xr(i)=mean(x1+(x0-x1)./(1+(omiga*tau).^2));
   xi(i)=mean((omiga*tau).*(x0-x1)./(1+(omiga*tau).^2))/5;
end

%load the experimental data
load tfepahrt.txt;
load xfepahrt.txt;
load xifepahrt.txt

%plot the simulation curve over the experimental curve
subplot(1,2,1)
```

```
plot(tfepahrt,xfepahrt,'r:.');
hold on;
plot(T,xr,'b:.');
xlabel('TEMPERATURE (K)');
ylabel('SUSCEPTIBILITY {\chi} real part (ARB.)');
hold off;

subplot(1,2,2)
plot(tfepahrt,xifepahrt,'r:.');
hold on;
plot(T,xi,'b:.');
xlabel('TEMPERATURE (K)');
ylabel('SUSCEPTIBILITY {\chi} imaginary part (ARB.)');

hold off;

%output the simulation results
tem=T';
realsus=xr';
imgsus=xi';
save fepahtemp.out tem -ascii;
save fepahreallog.out realsus -ascii;
save fepahimglog.out imgsus -ascii;
```

2. Calculating the magnetization versus applied field

```
%calculate the Magnetization versus applied field of the superparamagnetic nanoparticles
%assuming a lognormal distribution of particle sizes D

clear all; close all;
%generate a lognormal distribution of particle sizes D
mu=log(2.2); sigma=0.08; counts=10000;
d=lognrnd(mu,sigma,counts,1); %d, the diameter, nm.
D=d*10^(-7); %D is the diameter of the particles, cm.
V=1/6*pi*D.^3;

%define the constants
%m: mass fraction
Ms=8.38; den=4.9; m=0.588;
Isp=Ms*den/m;
k=1.38*10^(-16); T=100;
```

```
load mFechiRT100K.txt;
load hFechiRT100K.txt;
plot(hFechiRT100K,mFechiRT100K,'r:.');
hold on;
%applied field is between -90000 Oe and 90000 Oe
M=1000;
h=linspace(-90,90,M);
H=h*10^3;
for i=1:M
   b=Isp*V*H(i)/(k*T);
   L=coth(b)-1./b;
   mag(i)=Ms*mean(L);
end
plot(h,mag);
xlabel('applied field, Oe');
ylabel('magnetization, emu/g');

save mFechiRTlog.out mag -ascii;
save hFechiRTlog.out h -ascii
hold off;
```

REFERENCES

1. Andres, R.P., Averback, R.S., Brown, W.L., Brus, L.E., Goddard, W.A., *Research Opportunities on Clusters and Cluster-Assembled Materials - a Department of Energy, Council on Materials Science Panel Report.* Journal of Materials Research, 1989. **4**(3): p. 704-736.
2. LesliePelecky, D.L. and R.D. Rieke, *Magnetic properties of nanostructured materials.* Chemistry of Materials, 1996. **8**(8): p. 1770-1783.
3. Pankhurst, Q.A., Connolly, J., Jones, S.K., Dobson, J., *Applications of magnetic nanoparticles in biomedicine.* Journal of Physics D-Applied Physics, 2003. **36**(13): p. R167-R181.
4. Tartaj, P., Morales, M.D., Veintemillas-Verdaguer, S., Gonzalez-Carreno,T., *The preparation of magnetic nanoparticles for applications in biomedicine.* Journal of Physics D-Applied Physics, 2003. **36**(13): p. R182-R197.
5. Sun, S.H., Murray, C.B., Weller, D., Folks, L., Moser, A., *Monodisperse FePt nanoparticles and ferromagnetic FePt nanocrystal superlattices.* Science, 2000. **287**(5460): p. 1989-1992.
6. Ziolo, R.F., Giannelis, E.P., Weinstein, B.A., Ohoro, M.P., *Matrix-Mediated Synthesis of Nanocrystalline Gamma-Fe_2O_3 - a New Optically Transparent Magnetic Material.* Science, 1992. **257**(5067): p. 219-223.
7. Bon, P., I. Zhitomirsky, and J.D. Embury, *Electrodeposition of composite iron oxide-polyelectrolyte films.* Materials Chemistry and Physics, 2004. **86**(1): p. 44-50.
8. Zhitomirsky, I., M. Niewczas, and A. Petric, *Electrodeposition of hybrid organic-inorganic films containing iron oxide.* Materials Letters, 2003. **57**(5-6): p. 1045-1050.
9. Zhitomirsky, I., *Cathodic electrodeposition of ceramic and organoceramic materials. Fundamental aspects.* Advances in Colloid and Interface Science, 2002. **97**(1-3): p. 279-317.
10. Shchukin, D.G., I.L. Radtchenko, and G.B. Sukhorukov, *Synthesis of nanosized magnetic ferrite particles inside hollow polyelectrolyte capsules.* Journal of Physical Chemistry B, 2003. **107**(1): p. 86-90.
11. Shchukin, D.G., I.L. Radtchenko, and G.B. Sukhorukov, *Micron-scale hollow polyelectrolyte capsules with nanosized magnetic Fe_3O_4 inside.* Materials Letters, 2003. **57**(11): p. 1743-1747.
12. Aharoni, A., *Introduction to the Theory of Ferromagnetism.* 1996.
13. Jiles, D., Introduction to Magnetism and Magnetic Materials, 1991.
14. Weiss, P., *L'hypothese du champ moleculaire et la propriete ferromagnetique.* J. de Phys, 1907. **6**: p. 661-690.
15. Kittel, C., *Physical theory of ferromagnetic domains.* Reviews of Modern Physics, 1949. **21**: p. 541-583.

16. Landau, L. and E. Lifshitz, *On the theory of the dispersion of magnetic permeability in ferromagnetic bodies.* Physik. Zeits. Sowjetunion, 1935. **8**: p. 153-169.
17. Bloch, F., *Zur theorie des Austauschproblems und der Remanen-zerscheinung der ferromagnetika.* Zeits. f. Physik, 1932. **74**: p. 295-335.
18. Kittel, C., *Theory of the structure of ferromagnetic domains in films and small particles.* Physical Review, 1946. **70**(11,12): p. 965-971.
19. http://www.aacg.bham.ac.uk/magnetic_materials/domains.htm.
20. Néel, L., *Quelques properietes des parois de domaines elementaires ferromagnetiques.* Cahiers de Physique, 1944. **25**: p. 1-20.
21. Herring, C. and C. Kittel, *On the Theory of Spin Waves in Ferromagnetic Media.* Physical Review, 1951. **81**(5): p. 869-880.
22. Morrish, A.H., The Physical Principles of Magnetism, 1965.
23. Coey, J.M.D., *Louis Néel: Retrospective (invited).* Journal of Applied Physics, 2003. **93**(10): p. 8224-8229.
24. Sickafus, K.E., J.M. Wills, and N.W. Grimes, *Structure of spinel.* Journal of the American Ceramic Society, 1999. **82**(12): p. 3279-3292.
25. Kramers, H.A., *L'interaction Entre les Atomes Magnétogènes dans un Cristal Paramagnétique.* Physica, 1934. **1**(1-6): p. 182-192.
26. Anderson, P.W., *Antiferromagnetism theory of superexchange interaction.* Physical Review, 1950. **79**(2): p. 350-356.
27. Kurti, N., *Saturation magnetization of certain ferrites.* The selected works of Louis Néel (English translation), 1988: p. 93-94.
28. Stoner, E.C. and E.P. Wohlfarth, *A mechanism of magnetic hystersis in hetrogeneous alloys.* Phil. Trans. Roy. Soc. London Ser. A, 1948. **240**: p. 599-642.
29. Néel, L., *Propriétés d'un ferromagnétique cubique en grains fins.* Comptes rendus, 1947. **224**: p. 1488-1490.
30. Stoner, E.C. and E.P. Wohlfarth, *Interpretation of high coercivity in ferromagnetic materials.* Nature, 1947. **160**: p. 650.
31. Zijlstra, H., *Chapter 2 Permanent Magnets.* Ferromagnetic Materials, Vol. 3, 1982: p. 37.
32. Dormann, J.L., D. Fiorani, and E. Tronc, *Magnetic relaxation in fine-particle systems.* Advances in Chemical Physics, Vol 98, 1997. **98**: p. 283-494.
33. Néel, L., *Anisotropie magnetique superficielle et surstructures d'orientation.* J. Phys. Rad., 1954. **15**: p. 225-239.
34. Néel, L., *Theorie du trainage magnetique des ferromagnetiques en grains fins avec applications aux terres cuites.* Ann. Géophys, 1949. **5**: p. 99-136.
35. Brown, W.F., *Thermal fluctuations of a single-domain particle.* Physical Review, 1963. **130**(5): p. 1677-1686.
36. Brown, W.F., *Time Constants of Superparamagnetic Particles.* Physica B & C, 1977. **86**(Jan-M): p. 1423-1424.
37. Brown, W.F., *Thermal Fluctuations of Fine Ferromagnetic Particles.* IEEE Transactions on Magnetics, 1979. **15**(5): p. 1196-1208.

38. Coffey, W.T., Cregg, P.J., Crothers, D.S.F., Waldron, J.T. Wickstead, A.W., *Simple Approximate Formulas for the Magnetic-Relaxation Time of Single-Domain Ferromagnetic Particles with Uniaxial Anisotropy.* Journal of Magnetism and Magnetic Materials, 1994. **131**(3): p. L301-L303.
39. Coffey, W.T., Crothers, D.S.F., Kalmykov, Y.P., Massawe, E.S., *Exact Analytic Formula for the Correlation Time of a Single-Domain Ferromagnetic Particle.* Physical Review E, 1994. **49**(3): p. 1869-1882.
40. Fiorani, D., Dormann, J.L., Lucari, F., Dorazio, F., Tronc, E., *Dynamic properties of interacting gamma-Fe_2O_3 particles.* Philosophical Magazine B-Physics of Condensed Matter Statistical Mechanics Electronic Optical and Magnetic Properties, 1997. **76**(4): p. 457-462.
41. Dormann, J.L., Dorazio, F., Lucari, F., Spinu, L., Tronc, E., *Dynamical properties of gamma-Fe_2O_3 nanoparticles dispersed in a polymer.* Synthesis and Properties of Mechanically Alloyed and Nanocrystalline Materials, Pts 1 and 2 - Ismanam-96, 1997. **235-**: p. 669-674.
42. Chantrell, R.W., J. Popplewell, and S.W. Charles, *Measurements of Particle-Size Distribution Parameters in Ferrofluids.* IEEE Transactions on Magnetics, 1978. **14**(5): p. 975-977.
43. Godovsky, D.Y., Varfolomeev, A.V., Efremova, G.D., Cherepanov, V.M., Kapustin, G.A., Volkov, A.V., Moskvina, M.A. *Magnetic properties of polyvinyl alcohol-based composites containing iron oxide nanoparticles.* Advanced Materials for Optics and Electronics, 1999. **9**(3): p. 87-93.
44. Kodama, R.H., Berkowitz, A.E., McNiff, E.J., Foner, S., *Surface spin disorder in ferrite nanoparticles (invited).* Journal of Applied Physics, 1997. **81**(8): p. 5552-5557.
45. Kodama, R.H., Berkowitz, A.E., McNiff, E.J., Foner, S., *Surface spin disorder in $NiFe_2O_4$ nanoparticles.* Physical Review Letters, 1996. **77**(2): p. 394-397.
46. Winkler, E., R.D. Zysler, and D. Fiorani, *Surface and magnetic interaction effects in Mn_3O_4 nanoparticles.* Physical Review B, 2004. **70**(17): p. -.
47. Kodama, R.H., S.A. Makhlouf, and A.E. Berkowitz, *Finite size effects in antiferromagnetic NiO nanoparticles.* Physical Review Letters, 1997. **79**(7): p. 1393-1396.
48. Hennion, M., Bellouard, C., Mirebeau, I., Dormann, J.L., *Dual-Spin Dynamics of Small Fe Particles.* Europhysics Letters, 1994. **25**(1): p. 43-48.
49. Kodama, R.H., *Magnetic nanoparticles.* Journal of Magnetism and Magnetic Materials, 1999. **200**(1-3): p. 359-372.
50. O'Grady, K. and A. Bradbury, *Particle size analysis in ferrofluids.* Journal of Magnetism and Magnetic Materials, 1983. **39**: p. 91-94.
51. Shtrikman, S. and E.P. Wohlfarth, *The Theory of the Vogel-Fulcher Law of Spin-Glasses.* Physics Letters A, 1981. **85**(8-9): p. 467-470.
52. Dormann, J.L., D. Fiorani, and E. Tronc, *On the models for interparticle interactions in nanoparticle assemblies: comparison with experimental results.* Journal of Magnetism and Magnetic Materials, 1999. **202**(1): p. 251-267.

53. Tholence, J.L., *On the Frequency-Dependence of the Transition-Temperature in Spin-Glasses.* Solid State Communications, 1980. **35**(2): p. 113-117.
54. Dormann, J.L., L. Bessais, and D. Fiorani, *A Dynamic Study of Small Interacting Particles - Superparamagnetic Model and Spin-Glass Laws.* Journal of Physics C-Solid State Physics, 1988. **21**(10): p. 2015-2034.
55. Dormann, J.L., Dorazio, F., Lucari, F., Tronc, E., Prene, P., *Thermal variation of the relaxation time of the magnetic moment of gamma-Fe_2O_3 nanoparticles with interparticle interactions of various strengths.* Physical Review B, 1996. **53**(21): p. 14291-14297.
56. Wenger, L.E. and J.A. Mydosh, *Nonuniqueness of $H^{2/3}$ and H^2 Field-Temperature Transition Lines in Spin-Glasses.* Physical Review B, 1984. **29**(7): p. 4156-4158.
57. Dormann, J.L., D. Fiorani, and M. Elyamani, *Field-Dependence of the Blocking Temperature in the Superparamagnetic Model - $H^{2/3}$ Coincidence.* Physics Letters A, 1987. **120**(2): p. 95-99.
58. Elhilo, M., K. Ogrady, and R.W. Chantrell, *Susceptibility Phenomena in a Fine Particle System.1. Concentration-Dependence of the Peak.* Journal of Magnetism and Magnetic Materials, 1992. **114**(3): p. 295-306.
59. Elhilo, M., K. Ogrady, and R.W. Chantrell, *Susceptibility Phenomena in a Fine Particle System.2. Field-Dependence of the Peak.* Journal of Magnetism and Magnetic Materials, 1992. **114**(3): p. 307-313.
60. Ogrady, K., Bradbury, A., Charles, S.W., Menear, S., Popplewell, J., Chantrell, R.W., *Curie-Weiss Behavior in Ferrofluids.* Journal of Magnetism and Magnetic Materials, 1983. **31-4**(Feb): p. 958-960.
61. Chantrell, R.W. and E.P. Wohlfarth, *Dynamic and Static Properties of Interacting Fine Ferromagnetic Particles.* Journal of Magnetism and Magnetic Materials, 1983. **40**(1-2): p. 1-11.
62. Gittleman, J.I., B. Abeles, and S. Bozowski, Physical Review B, 1974. **9**: p. 3891.
63. Beck, P.A., *Remanence and Relaxation in a Mictomagnet.* Physical Review B, 1981. **24**(5): p. 2867-2869.
64. Tronc, E., Prene, P., Jolivet, J.P., Fiorani, D., *Magnetic dynamics of gamma-Fe_2O_3 nanoparticles.* Nanostructured Materials, 1995. **6**(5-8): p. 945-948.
65. Dormann, J.L., Spinu, L., Tronc, E., Jolivet, J.P., Lucari, F., *Effect of interparticle interactions on the dynamical properties of gamma-Fe_2O_3 nanoparticles.* Journal of Magnetism and Magnetic Materials, 1998. **183**(3): p. L255-L260.
66. Willard, M.A., Kurihara, L.K., Carpenter, E.E., Calvin, S., Harris, V.G., *Chemically prepared magnetic nanoparticles.* International Materials Reviews, 2004. **49**(3-4): p. 125-170.
67. Rockenberger, J., E.C. Scher, and A.P. Alivisatos, *A new nonhydrolytic single-precursor approach to surfactant-capped nanocrystals of transition metal oxides.* Journal of the American Chemical Society, 1999. **121**(49): p. 11595-11596.
68. Sun, S.H., Zeng, H., Robinson, D.B., Raoux, S. Rice, P.M., *Monodisperse MFe_2O_4 (M = Fe, Co, Mn) nanoparticles.* Journal of the American Chemical Society, 2004. **126**(1): p. 273-279.

69. Sun, S.H. and H. Zeng, *Size-controlled synthesis of magnetite nanoparticies.* Journal of the American Chemical Society, 2002. **124**(28): p. 8204-8205.
70. Pascal, C., *Electrochemical synthesis for the control of gamma-Fe_2O_3 nanoparticle size. Morphology, microstructure, and magnetic behavior.* Chemistry of Materials, 1999. **11**(1): p. 141-147.
71. Dierstein, A., Natter, H., Meyer, F., Stephan, H.O., *Electrochemical deposition under oxidizing conditions (EDOC): A new synthesis for nanocrystalline metal oxides.* Scripta Materialia, 2001. **44**(8-9): p. 2209-2212.
72. Besra, L. and M. Liu, *A review on fundamentals and applications of electrophoretic deposition (EPD).* Progress in Materials Science, 2007. **52**(1): p. 1-61.
73. Van der Biest, O.O. and L.J. Vandeperre, *Electrophoretic deposition of materials.* Annual Review of Materials Science, 1999. **29**: p. 327-352.
74. Heavens, S.N., *Chapter 7.* Advanced Ceramic Processing and technology, J.G.P Binner (Ed.), 1990.
75. Sarkar, P. and P.S. Nicholson, *Electrophoretic deposition (EPD): Mechanisms, kinetics, and application to ceramics.* Journal of the American Ceramic Society, 1996. **79**(8): p. 1987-2002.
76. Moreno, R. and B. Ferrari, *Advanced ceramics via EPD of aqueous slurries.* American Ceramic Society Bulletin, 2000. **79**(1): p. 44-48.
77. Zhitomirsky, I., *Ceramic Films Using Cathodic Electrodeposition.* JOM-e The Minerals, Metals & Materials Society, 2000. **52**: p. 1.
78. Zhitomirsky, I. and L. Gal-Or, *Chapter 3.* Intermetallic and Ceramic Coatings, N.B.Dahotre, T.S.Sudarshan (Eds.), 1999.
79. Zhitomirsky, I., *New developments in electrolytic deposition of ceramic films.* American Ceramic Society Bulletin, 2000. **79**(9): p. 57-63.
80. Zhitomirsky, I., *Electrophoretic and electrolytic deposition of ceramic coatings on carbon fibers.* Journal of the European Ceramic Society, 1998. **18**(7): p. 849-856.
81. Mandel, M., *Polyelectrolytes.* Encyclopedia of Polymer Science and Engineering, edited by F.H. Mark, N.M. Bikales, C.G. Overberger, G. Menges, 2nd edn, 1988. **11**: p. 739.
82. Zhitomirsky, I., *Electrophoretic deposition of organic-inorganic nanocomposites.* Journal of Materials Science, 2006. **41**(24): p. 8186-8195.
83. Rivas, B.L. and K.E. Geckeler, *Synthesis and Metal Complexation of Poly(Ethyleneimine) and Derivatives.* Advances in Polymer Science, 1992. **102**: p. 171-188.
84. Griffiths, P.C., Paul, A., Stilbs, P., Petterson, E., *Charge on poly(ethylene imine): Comparing electrophoretic NMR measurements and pH Titrations.* Macromolecules, 2005. **38**(8): p. 3539-3542.
85. Baklouti, S., Pagnoux, C., Chartier, T., Baumard, J.F., *Processing of aqueous alpha-Al_2O_3, alpha-SiO_2 and alpha-SiC suspensions with polyelectrolytes.* Journal Of The European Ceramic Society, 1997. **17**(12): p. 1387-1392.

86. Zhu, X.W., Tang, F.Q., Suzuki, T.S., Sakka, Y., *Role of the initial degree of ionization of polyethylenimine in the dispersion of silicon carbide nanoparticles.* Journal of the American Ceramic Society, 2003. **86**(1): p. 189-191.
87. Caruso, F., *Nanoengineering of particle surfaces.* Advanced Materials, 2001. **13**(1): p. 11.
88. Radtchenko, I.L., M. Giersig, and G.B. Sukhorukov, *Inorganic particle synthesis in confined micron-sized polyelectrolyte capsules.* Langmuir, 2002. **18**(21): p. 8204-8208.
89. Kampf, N., U. Raviv, and J. Klein, *Normal and shear forces between adsorbed and gelled layers of chitosan, a naturally occurring cationic polyelectrolyte.* Macromolecules, 2004. **37**(3): p. 1134-1142.
90. Shepherd, R., S. Reader, and A. Falshaw, *Chitosan functional properties.* Glycoconjugate Journal, 1997. **14**(4): p. 535-542.
91. Rabea, E.I., Badawy, M.E.T., Stevens, C.V., Smagghe, G., Steurbaut, W., *Chitosan as antimicrobial agent: Applications and mode of action.* Biomacromolecules, 2003. **4**(6): p. 1457-1465.
92. Sorlier, P., Denuziere, A., Viton, C., Domard, A., *Relation between the degree of acetylation and the electrostatic properties of chitin and chitosan.* Biomacromolecules, 2001. **2**(3): p. 765-772.
93. Bartkowiak, A. and D. Hunkeler, *Alginate-oligochitosan microcapsules: A mechanistic study relating membrane and capsule properties to reaction conditions.* Chemistry of Materials, 1999. **11**(9): p. 2486-2492.
94. Seguel, G.V., B.L. Rivas, and C. Novas, *Polychelates of poly(4-vinylpyridine) with Cu(II) and Zn(II). Synthesis, characterization, and semi-empirica calculations.* Journal of the Chilean Chemical Society, 2006. **51**(1): p. 801-807.
95. Hong, H., Sfez, R., Vaganova, E., Yitzchaik, S., Davidov, D, *Electrostatically self-assembled poly(4-vinylpyridine-co-vinylpyridinium-chloride)-based LED.* Thin Solid Films, 2000. **366**(1-2): p. 260-264.
96. Verwey, E.J.W. and J.T.G. Overbeek, Theory of the stability of Lyophotic Colloids, 1948.
97. Derjaguin, B.V. and L. Landau, Acta Physicochim USSR, 1941. **14**: p. 633.
98. Zhitomirsky, I., Chaim, R., GalOr, L., Bestgen, H., *Electrochemical Al_2O_3-Cr_2O_3 alloy coatings on non-oxide ceramic substrates.* Journal of Materials Science, 1997. **32**(19): p. 5205-5213.
99. Peulon, S. and D. Lincot, *Cathodic electrodeposition from aqueous solution of dense or open-structured zinc oxide films.* Advanced Materials, 1996. **8**(2): p. 166-&.
100. Hirata, Y., A. Nishimoto, and Y. Ishihara, *Forming of Alumina Powder by Electrophoretic Deposition.* Nippon Seramikkusu Kyokai Gakujutsu Ronbunshi-Journal of the Ceramic Society of Japan, 1991. **99**(2): p. 108-113.
101. Matsuda, Y., Imahashi, K. Yoshimoto, N., Morita, M. Haga, M., *Formation of Yttrium-Oxide by Electrodeposition in Organic Electrolyte.* Journal of Alloys and Compounds, 1993. **193**(1-2): p. 277-279.

102. Zhitomirsky, I., Galor, L., Kohn, A., Hennicke, H.W., *Electrodeposition of Ceramic Films from Nonaqueous and Mixed-Solutions.* Journal of Materials Science, 1995. **30**(20): p. 5307-5312.
103. Zhitomirsky, I., *Cathodic electrosynthesis of titanium and ruthenium oxides.* Materials Letters, 1998. **33**(5-6): p. 305-310.
104. Zhitomirsky, I. and A. Petric, *Electrolytic and electrophoretic deposition of CeO_2 films.* Materials Letters, 1999. **40**(6): p. 263-268.
105. Hayashi, S., Nakagawa, Z.E., Yasumori, A., Okada, K., *Effects of H_2O in EtOH-H_2O disperse medium on the electrophoretic deposition of $CaSiO_3$ fine powder.* Journal of the European Ceramic Society, 1999. **19**(1): p. 75-79.
106. Ducheyne, P., Radin, S., Heughebaert, M., Heughebaert, J.C., *Calcium-Phosphate Ceramic Coatings on Porous Titanium - Effect of Structure and Composition on Electrophoretic Deposition, Vacuum Sintering and Invitro Dissolution.* Biomaterials, 1990. **11**(4): p. 244-254.
107. Zhitomirsky, I., *Electrophoretic hydroxyapatite coatings and fibers.* Materials Letters, 2000. **42**(4): p. 262-271.
108. Abolmaali, S.B. and J.B. Talbot, *Synthesis of Superconductive Thin-Films of $YBa_2Cu_3O_7$-X by a Nonaqueous Electrodeposition Process.* Journal of the Electrochemical Society, 1993. **140**(2): p. 443-445.
109. Yamashita, K., M. Nagai, and T. Umegaki, *Fabrication of green films of single- and multi-component ceramic composites by electrophoretic deposition technique.* Journal of Materials Science, 1997. **32**(24): p. 6661-6664.
110. Van Tassel, J. and C.A. Randall, *Electrophoretic deposition and sintering of thin/thick PZT films.* Journal of the European Ceramic Society, 1999. **19**(6-7): p. 955-958.
111. Nicholson, P.S., P. Sarkar, and X. Huang, *Electrophoretic Deposition and Its Use to Synthesize ZrO_2/Al_2O_3 Micro-Laminate Ceramic-Ceramic Composites.* Journal of Materials Science, 1993. **28**(23): p. 6274-6278.
112. Foissy, A.A. and G. Robert, *Electrophoretic Forming of Beta-Alumina from Dichloromethane Suspensions.* American Ceramic Society Bulletin, 1982. **61**(2): p. 251-255.
113. Ishihara, T., K. Sato, and Y. Takita, *Electrophoretic deposition of Y_2O_3-stabilized ZrO_2 electrolyte films in solid oxide fuel cells.* Journal of the American Ceramic Society, 1996. **79**(4): p. 913-919.
114. Andrews, J.M., A.H. Collins, and D.C. Cornish, Proc. Brit. Ceram. Soc., 1969. **12**: p. 211.
115. Jones, S.L. and C.J. Norman, *Dehydration of Hydrous Zirconia with Methanol.* Journal of the American Ceramic Society, 1988. **71**(4): p. C190-C191.
116. Zhitomirsky, I., *Cathodic electrosynthesis of titania films and powders.* Nanostructured Materials, 1997. **8**(4): p. 521-528.
117. Kosmulski, M., Durand-Vidal, S., Gustafsson, J., *Charge interactions in semi-concentrated titania suspensions at very high ionic strengths.* Colloids and Surfaces a-Physicochemical and Engineering Aspects, 1999. **157**(1-3): p. 245-259.

118. Biesheuvel, P.M. and H. Verweij, *Theory of cast formation in electrophoretic deposition.* Journal of the American Ceramic Society, 1999. **82**(6): p. 1451-1455.
119. Ohshima, H., *On the general expression for the electrophoretic mobility of a soft particle.* Journal of Colloid and Interface Science, 2000. **228**(1): p. 190-193.
120. Ohshima, H., *Electrophoretic Mobility of Soft Particles.* Colloids and Surfaces a-Physicochemical and Engineering Aspects, 1995. **103**(3): p. 249-255.
121. Ohshima, H., *Electrophoretic Mobility of Soft Particles.* Journal of Colloid and Interface Science, 1994. **163**(2): p. 474-483.
122. Ohshima, H., *Electrophoretic mobility of spherical colloidal particles in concentrated suspensions.* Journal of Colloid and Interface Science, 1997. **188**(2): p. 481-485.
123. Ohshima, H., *Electrophoretic mobility of soft particles in concentrated suspensions.* Journal of Colloid and Interface Science, 2000. **225**(1): p. 233-242.
124. Levine, S. and G.H. Neale, Journal of Colloid and Interface Science, 1974. **47**: p. 520.
125. Galor, L., I. Silberman, and R. Chaim, *Electrolytic ZrO_2 Coatings.1. Electrochemical Aspects.* Journal of the Electrochemical Society, 1991. **138**(7): p. 1939-1942.
126. Matsumoto, Y., H. Adachi, and J. Hombo, *New Preparation Method for PZT Films Using Electrochemical Reduction.* Journal of the American Ceramic Society, 1993. **76**(3): p. 769-772.
127. Matsumoto, Y., Morikawa, T., Adachi, H., Hombo, J., *A New Preparation Method of Barium-Titanate Perovskite Film Using Electrochemical Reduction.* Materials Research Bulletin, 1992. **27**(11): p. 1319-1327.
128. Switzer, J.A., *Electrochemical Synthesis of Ceramic Films and Powders.* American Ceramic Society Bulletin, 1987. **66**(10): p. 1521-1525.
129. Lee, G.R. and J.A. Crayston, *Studies on the electrochemical deposition of niobium oxide.* Journal of Materials Chemistry, 1996. **6**(2): p. 187-192.
130. Therese, G.H.A. and P.V. Kamath, *Electrochemical synthesis of metal oxides and hydroxides.* Chemistry of Materials, 2000. **12**(5): p. 1195-1204.
131. Indira, L. and P.V. Kamath, *Electrogeneration of Base by Cathodic Reduction of Anions - Novel One-Step Route to Unary and Layered Double Hydroxides (Ldhs).* Journal of Materials Chemistry, 1994. **4**(9): p. 1487-1490.
132. Gal-Or, L., I. Silberman, and R. Chaim, *Electrolytic ZrO_2 Coatings.1. Electrochemical Aspects.* Journal of the Electrochemical Society, 1991. **138**(7): p. 1939-1942.
133. Hughes, A.E., *XPS and SEM Characterization of Hydrated Cerium Oxide Conversion Coatings.* Surface and Interface Analysis, 1995. **23**(7-8): p. 540-550.
134. Ulberg, Z.R. and Y.F. Deinega, Electrophoretic Composite Coatings, 1992.
135. Kuhn, A.T. and C.Y. Chan, *pH Changes at near-Electrode Surfaces.* Journal of Applied Electrochemistry, 1983. **13**(2): p. 189-207.
136. Ban, S. and S. Maruno, *Deposition of Calcium-Phosphate on Titanium by Electrochemical Process in Simulated Body-Fluid.* Japanese Journal of Applied Physics Part 2-Letters, 1993. **32**(10B): p. L1577-L1580.

137. Chaim, R., Zhitomirsky, I., GalOr, L., Bestgen, H., *Electrochemical Al_2O_3-ZrO_2 composite coatings on non-oxide ceramic substrates.* Journal of Materials Science, 1997. **32**(2): p. 389-400.
138. Izaki, M., *Preparation of transparent and conductive zinc oxide films by optimization of the two-step electrolysis technique.* Journal of the Electrochemical Society, 1999. **146**(12): p. 4517-4521.
139. Jayashree, R.S. and P.V. Kamath, *Factors governing the electrochemical synthesis of alpha-nickel (II) hydroxide.* Journal of Applied Electrochemistry, 1999. **29**(4): p. 449-454.
140. Li, F.B., R.C. Newman, and G.E. Thompson, *In situ atomic force microscopy studies of electrodeposition mechanism of cerium oxide films: Nucleation and growth out of a gel mass precursor.* Electrochimica Acta, 1997. **42**(16): p. 2455-2464.
141. Matsumoto, Y., H. Ohmura, and T. Goto, *Effect of lanthanide ions on the electrodeposition of cobalt and manganese oxides.* Journal of Electroanalytical Chemistry, 1995. **399**(1-2): p. 91-96.
142. Meulenkamp, E.A., *Mechanism of WO_3 electrodeposition from peroxy-tungstate solution.* Journal of the Electrochemical Society, 1997. **144**(5): p. 1664-1671.
143. Shacham, R., D. Avnir, and D. Mandler, *Electrodeposition of methylated sol-gel films on conducting surfaces.* Advanced Materials, 1999. **11**(5): p. 384-388.
144. Shirkhanzadeh, M., *Bioactive Calcium-Phosphate Coatings Prepared by Electrodeposition.* Journal of Materials Science Letters, 1991. **10**(23): p. 1415-1417.
145. Therese, G.H.A. and P.V. Kamath, *Cathodic reduction of different metal salt solutions - Part I: Synthesis of metal hydroxides by electrogeneration of base.* Journal of Applied Electrochemistry, 1998. **28**(5): p. 539-543.
146. Zhang, J.M., Lin, C.J., Feng, Z.D., Tian, Z.W., *Mechanistic studies of electrodeposition for bioceramic coatings of calcium phosphates by an in situ pH-microsensor technique.* Journal of Electroanalytical Chemistry, 1998. **452**(2): p. 235-240.
147. Zhitomirsky, I., *Electrolytic deposition of oxide films in the presence of hydrogen peroxide.* Journal of the European Ceramic Society, 1999. **19**(15): p. 2581-2587.
148. Zhitomirsky, I., *Electrolytic TiO_2-RuO_2 deposits.* Journal of Materials Science, 1999. **34**(10): p. 2441-2447.
149. Zhitomirsky, I., L. Galor, and S. Klein, *Electrolytic Deposition of $ZrTiO_4$ Films.* Journal of Materials Science Letters, 1995. **14**(1): p. 60-62.
150. Zhitomirsky, I., Galor, L., Kohn, A, Hennicke, H.W., *Electrochemical Preparation of PbO Films.* Journal of Materials Science Letters, 1995. **14**(11): p. 807-810.
151. Zhitomirsky, I., GalOr, L., Kohn, A., Spang, M.D., *Electrolytic PZT films.* Journal of Materials Science, 1997. **32**(3): p. 803-807.
152. Zhitomirsky, I., A. Kohn, and L. GalOr, *Cathodic electrosynthesis of PZT films.* Materials Letters, 1995. **25**(5-6): p. 223-227.

153. Monk, P.M.S., R. Janes, and R.D. Partridge, *Speciation analysis applied to the electrodeposition of precursors of neodymium cuprate and related phases - First application of speciation modelling to a solution not at equilibrium.* Journal of the Chemical Society-Faraday Transactions, 1997. **93**(22): p. 3985-3990.
154. Monk, P.M.S., R. Janes, and R.D. Partridge, *Speciation modelling of the electroprecipitation of rare-earth cuprate and nickelate materials - Speciation of aqueous solutions not at equilibrium.* Journal of the Chemical Society-Faraday Transactions, 1997. **93**(22): p. 3991-3997.
155. Koelmans, H., *Suspensions in Non-aqueous Media.* Philips Research Reports, 1955. **10**: p. 161.
156. Brown, D.R. and F.W. Salt, *The Mechanism of Electrophoretic Deposition.* J. Appl. Chem, 1965. **15**: p. 40.
157. Hamaker, H.C., *Formation of a deposit by electrophoresis.* Transactions of the Faraday Society, 1940. **36**: p. 279.
158. Hamaker, H.C. and E.J.W. Verwey, *The Role of the Forces between the Particles in Electrodeposition and Other Phenomena.* Transactions of the Faraday Society, 1940. **36**: p. 180.
159. Shane, M.J., Talbot, J.B., Kinney, B.G., Sluzky, E. Hesse, K.R., *Electrophoretic Deposition of Phosphors.2. Deposition Experiments and Analysis.* Journal of Colloid and Interface Science, 1994. **165**(2): p. 334-340.
160. Kaya, C., A.R. Boccaccini, and K.K. Chawla, *Electrophoretic deposition forming of nickel-coated-carbon-fiber-reinforced borosilicate-glass-matrix composites.* Journal of the American Ceramic Society, 2000. **83**(8): p. 1885-1888.
161. Kaya, C., A.R. Boccaccini, and P.A. Trusty, *Processing and characterisation of 2-D woven metal fibre-reinforced multilayer silica matrix composites using electrophoretic deposition and pressure filtration.* Journal of the European Ceramic Society, 1999. **19**(16): p. 2859-2866.
162. Koelmans, H. and J.T.G. Overbeek, *Stability and electrophoretic deposition of suspensions in non-aqueous media.* Discuss. Faraday Society, 1954. **18**: p. 52.
163. Ferrari, B., Moreno, R., Sarkar, P., Nicholson, P.S., *Electrophoretic deposition of MgO from organic suspensions.* Journal of the European Ceramic Society, 2000. **20**(2): p. 99-106.
164. Russ, B.E. and J.B. Talbot, *A study of the adhesion of electrophoretically deposited phosphors.* Journal of the Electrochemical Society, 1998. **145**(4): p. 1245-1252.
165. Koura, N., Tsukamoto, T., Shoji, H., Hotta, T., *Preparation of Various Oxide-Films by an Electrophoretic Deposition Method - a Study of the Mechanism.* Japanese Journal of Applied Physics Part 1-Regular Papers Short Notes & Review Papers, 1995. **34**(3): p. 1643-1647.
166. Zhang, J.P. and B.I. Lee, *Electrophoretic deposition and characterization of micrometer-scale $BaTiO_3$ based X7R dielectric thick films.* Journal of the American Ceramic Society, 2000. **83**(10): p. 2417-2422.
167. Verwey, E.J.W. and J.T.G. Overbeek, Theory of the Stability of Lyophobic Colloids, 1948.

168. Trau, M., D.A. Saville, and I.A. Aksay, *Field-induced layering of colloidal crystals.* Science, 1996. **272**(5262): p. 706-709.
169. Giersig, M. and P. Mulvaney, *Formation of Ordered 2-Dimensional Gold Colloid Lattices by Electrophoretic Deposition.* Journal of Physical Chemistry, 1993. **97**(24): p. 6334-6336.
170. Zhitomirsky, I., *Cathodic electrophoretic deposition of diamond particles.* Materials Letters, 1998. **37**(1-2): p. 72-78.
171. Shimbo, M., Tanzawa, K., Miyakawa, M., Emoto, T., *Electrophoretic Deposition of Glass Powder for Passivation of High-Voltage Transistors.* Journal of the Electrochemical Society, 1985. **132**(2): p. 393-398.
172. Bouyer, F. and A. Foissy, *Electrophoretic deposition of silicon carbide.* Journal of the American Ceramic Society, 1999. **82**(8): p. 2001-2010.
173. Mizuguchi, J., K. Sumi, and T. Muchi, *A Highly Stable Non-Aqueous Suspension for the Electrophoretic Deposition of Powdered Substances.* Journal of the Electrochemical Society, 1983. **130**(9): p. 1819-1825.
174. Zhitomirsky, I., *Electrophoretic deposition of chemically bonded ceramics in the system CaO-SiO_2-P_2O_5.* Journal of Materials Science Letters, 1998. **17**(24): p. 2101-2104.
175. Harbach, F. and H. Nienburg, *Homogeneous functional ceramic components through electrophoretic deposition from stable colloidal suspensions - I. Basic concepts and application to zirconia.* Journal of the European Ceramic Society, 1998. **18**(6): p. 675-683.
176. Siracuse, J.A., Talbot, J.B., Sluzky, E., Hesse, K.R., *The Adhesive Agent in Cataphoretically Coated Phosphor Screens.* Journal of the Electrochemical Society, 1990. **137**(1): p. 346-348.
177. Russ, B.E. and J.B. Talbot, *An analysis of the binder formation in electrophoretic deposition.* Journal of the Electrochemical Society, 1998. **145**(4): p. 1253-1256.
178. Aslanidis, D., J. Fransaer, and J.P. Celis, *The electrolytic codeposition of silica and titania modified silica with zinc.* Journal of the Electrochemical Society, 1997. **144**(7): p. 2352-2357.
179. De, D. and P.S. Nicholson, *Role of ionic depletion in deposition during electrophoretic deposition.* Journal of the American Ceramic Society, 1999. **82**(11): p. 3031-3036.
180. Cinibulk, M.K., *Deposition of oxide coatings on fiber cloths by electrostatic attraction.* Journal of the American Ceramic Society, 1997. **80**(2): p. 453-460.
181. Lee, D.G. and R.K. Singh, *Synthesis of (111) oriented diamond thin films by electrophoretic deposition process.* Applied Physics Letters, 1997. **70**(12): p. 1542-1544.
182. Valdes, J.L., Mitchel, J.W., Mucha, J.A., *Selected-Area Nucleation and Patterning of Diamond Thin-Films by Electrophoretic Seeding.* Journal of the Electrochemical Society, 1991. **138**(2): p. 635-636.
183. Lavrov, I.S. and O.V. Smirnov, J. Appl. Chem USSR, 1969. **42**: p. 1459.

184. Grillon, F., D. Fayeulle, and M. Jeandin, *Quantitative Image-Analysis of Electrophoretic Coatings.* Journal of Materials Science Letters, 1992. **11**(5): p. 272-275.
185. Solomentsev, Y., M. Bohmer, and J.L. Anderson, *Particle clustering and pattern formation during electrophoretic deposition: A hydrodynamic model.* Langmuir, 1997. **13**(23): p. 6058-6068.
186. Trau, M., D.A. Saville, and I.A. Aksay, *Assembly of colloidal crystals at electrode interfaces.* Langmuir, 1997. **13**(24): p. 6375-6381.
187. Bohmer, M., *In situ observation of 2-dimensional clustering during electrophoretic deposition.* Langmuir, 1996. **12**(24): p. 5747-5750.
188. Derjaguin, B.V. and L. Landau, *Theory of the stability of strongly charged lyophobic sols and of the adhesion of strongly charged.* Acta Physicochim. URSS, 1941: p. 633.
189. Sogami, I. and N. Ise, *On the Electrostatic Interaction in Macroionic Solutions.* Journal of Chemical Physics, 1984. **81**(12): p. 6320-6332.
190. Larsen, A.E. and D.G. Grier, *Like-charge attractions in metastable colloidal crystallites.* Nature, 1997. **385**(6613): p. 230-233.
191. Crocker, J.C. and D.G. Grier, *When like charges attract: The effects of geometrical confinement on long-range colloidal interactions.* Physical Review Letters, 1996. **77**(9): p. 1897-1900.
192. Sader, J.E. and D.Y.C. Chan, *Electrical double-layer interaction between charged particles near surfaces and in confined geometries.* Journal of Colloid and Interface Science, 1999. **218**(2): p. 423-432.
193. Kralchevsky, P.A. and K. Nagayama, *Capillary Forces between Colloidal Particles.* Langmuir, 1994. **10**(1): p. 23-36.
194. Asakura, S. and F. Oosawa, *Interaction between particles suspended in solutions of macromolecules.* Journal of Polymer Science, 1958. **33**: p. 183-192.
195. Chu, X.L., A.D. Nikolov, and D.T. Wasan, *Thin Liquid-Film Structure and Stability - the Role of Depletion and Surface-Induced Structural Forces.* Journal of Chemical Physics, 1995. **103**(15): p. 6653-6661.
196. Valleau, J.P., R. Ivkov, and G.M. Torrie, *Colloid Stability - the Forces between Charged Surfaces in an Electrolyte.* Journal of Chemical Physics, 1991. **95**(1): p. 520-532.
197. Henderson, D., *An Explicit Expression for the Solvent Contribution to the Force between Colloidal Particles Using a Hard-Sphere Model.* Journal of Colloid and Interface Science, 1988. **121**(2): p. 486-490.
198. Chu, X.L. and D.T. Wasan, *Attractive interaction between similarly charged colloidal particles.* Journal of Colloid and Interface Science, 1996. **184**(1): p. 268-278.
199. Delville, A., R.J.M. Pellenq, and J.M. Caillol, *A Monte Carlo (N, V, T) study of the stability of charged interfaces: A simulation on a hypersphere.* Journal of Chemical Physics, 1997. **106**(17): p. 7275-7285.

200. Kjellander, R., Marcelja, S., Pashley, R.M., Quirk, J.P., *Double-Layer Ion Correlation Forces Restrict Calcium Clay Swelling.* Journal of Physical Chemistry, 1988. **92**(23): p. 6489-6492.
201. Kjellander, R., Akesson, T., Jonsson, B., Marcelja, S., *Double-Layer Interactions in Monovalent and Divalent Electrolytes - a Comparison of the Anisotropic Hypernetted Chain Theory and Monte-Carlo Simulations.* Journal of Chemical Physics, 1992. **97**(2): p. 1424-1431.
202. Walz, J.Y. and A. Sharma, *Effect of Long-Range Interactions on the Depletion Force between Colloidal Particles.* Journal of Colloid and Interface Science, 1994. **168**(2): p. 485-496.
203. Qian, Y.X. and W.R. Bowen, *Long-range electrostatic interaction between a charged wall and two similarly charged colloidal spheres at low surface potentials.* Journal of Colloid and Interface Science, 1999. **213**(2): p. 316-321.
204. Sader, J.E. and D.Y.C. Chan, *Long-range electrostatic attractions between identically charged particles in confined geometries and the Poisson-Boltzmann theory.* Langmuir, 2000. **16**(2): p. 324-331.
205. Winslow, W.M., *Induced Fibration of Suspensions.* Journal of Applied Physics, 1949. **20**: p. 1137.
206. Zhitomirsky, I. and L. GalOr, *Electrophoretic deposition of hydroxyapatite.* Journal of Materials Science-Materials in Medicine, 1997. **8**(4): p. 213-219.
207. Hu, Y., Glass, J.L., Griffith, A.E., Fraden, S., *Observation and Simulation of Electrohydrodynamic Instabilities in Aqueous Colloidal Suspensions.* Journal of Chemical Physics, 1994. **100**(6): p. 4674-4682.
208. Hughes, M.P., *AC electrokinetics: applications for nanotechnology.* Nanotechnology, 2000. **11**(2): p. 124-132.
209. Velegol, D., J.D. Feick, and L.R. Collins, *Electrophoresis of spherical particles with a random distribution of zeta potential or surface charge.* Journal of Colloid and Interface Science, 2000. **230**(1): p. 114-121.
210. Zhitomirsky, I. and A. Petric, *Electrochemical deposition of yttrium oxide.* Journal of Materials Chemistry, 2000. **10**(5): p. 1215-1218.
211. Zhitomirsky, I. and A. Petric, *Electrolytic deposition of zirconia and zirconia organoceramic composites.* Materials Letters, 2000. **46**(1): p. 1-6.
212. Zhitomirsky, I. and A. Petric, *Electrolytic deposition of Gd_2O_3 and organoceramic composite.* Materials Letters, 2000. **42**(5): p. 273-279.
213. Zhitomirsky, I. and A. Petric, *Cathodic electrodeposition of polymer films and organoceramic films.* Materials Science and Engineering B-Solid State Materials for Advanced Technology, 2000. **78**(2-3): p. 125-130.
214. Zhitomirsky, I. and A. Petric, *Electrochemical deposition of ceria and doped ceria films.* Ceramics International, 2001. **27**(2): p. 149-155.
215. Zhitomirsky, I. and A. Petric, *Electrophoretic deposition of ceramic materials for fuel cell applications.* Journal of the European Ceramic Society, 2000. **20**(12): p. 2055-2061.

216. Hasegawa, K., M. Tatsumisago, and T. Minami, *Preparation of thick silica films by the electrophoretic sol-gel deposition using a cationic polymer surfactant.* Journal of the Ceramic Society of Japan, 1997. **105**(7): p. 569-572.
217. Digital_Instruments, *Practical Guide to Scanning probe Microscopy.* http://www.veeco.com/library/resources.php.
218. Digital_Instruments, *Scanning Probe Microscopy Training Notebook.* http://www.eng.yale.edu/uelm/Document%5Cafm.pdf, 2000.
219. Quantum_Design, *AC Susceptibility.* http://www.qdusa.com/resources/index.html.
220. Nielsen, O.V., J.Phys. (Paris) Colloq., 1971. **32**: p. suppl. C1-51.
221. Rosenberg, M. and I. Nicolae, Proceedings of the International Conference on Magnetism, 1965: p. 651.
222. Dwight, K. and N. Menyuk, *Magnetic properties of Mn_3O_4 and the canted spin problem.* Physical Review, 1960. **119**(5): p. 1470-9.
223. Baklouti, S., Pagnoux, C., Chartier, T., *Processing of aqueous alpha-Al_2O_3, alpha-SiO_2 and alpha-SiC suspensions with polyelectrolytes.* Journal of the European Ceramic Society, 1997. **17**(12): p. 1387-1392.
224. Bon, P., I. Zhitomirsky, and J.D. Embury, *Electrochemical preparation of Ni and Fe hydroxide/oxide films using polyethylenimine.* Surface Engineering, 2004. **20**(1): p. 5-10.
225. Prene, P., Tronc, E., Jolivet, J.P., Livage, J., Fiorani, D., *Magnetic-Properties of Isolated Gamma-Fe_2O_3 Particles.* IEEE Transactions on Magnetics, 1993. **29**(6): p. 2658-2660.
226. Boccaccini, A.R. and P.A. Trusty, *Electrophoretic deposition infiltration of metallic fabrics with a boehmite sol for the preparation of ductile-phase-toughened ceramic composites.* Journal of Materials Science, 1998. **33**(4): p. 933-938.
227. Moon, J., Awano, M., Takai, H., Fujishiro, Y., *Synthesis of nanocrystalline manganese oxide powders: Influence of hydrogen peroxide on particle characteristics.* Journal of Materials Research, 1999. **14**(12): p. 4594-4601.
228. Nagarajan, N., M. Cheong, and I. Zhitomirsky, *Electrochemical capacitance of MnOx films.* Materials Chemistry and Physics, 2007. **103**(1): p. 47-53.
229. Cornell, R.M. and U. Schwertmann, *The Iron Oxides.* 1996.
230. Rivas, B.L. and G.V. Seguel, *Synthesis, characterization of poly(allylamine)chelates with Cu(II), Co(II) and Ni(II).* Polymer Bulletin, 1996. **37**(4): p. 463-468.
231. Parks, G.A., *The Isoelectric Points of Solid Oxides, Solid Hydroxides, and Aqueous Hydroxo Complex Systems.* Chemical Reviews, 1965. **65**: p. 177.
232. Vonzelewsky, A., L. Barbosa, and C.W. Schlapfer, *Poly(Ethylenimines) as Bronsted Bases and as Ligands for Metal-Ions.* Coordination Chemistry Reviews, 1993. **123**(1-2): p. 229-246.
233. Kislenko, V.N. and L.P. Oliynyk, *Complex formation of polyethyleneimine with copper(II), nickel(II), and cobalt(II) ions.* Journal of Polymer Science Part a-Polymer Chemistry, 2002. **40**(7): p. 914-922.

234. Takagishi, T., Okuda, S., Kuroki, N., Kozuka, H. *Binding of Metal-Ions by Polyethylenimine and Its Derivatives.* Journal of Polymer Science Part a-Polymer Chemistry, 1985. **23**(8): p. 2109-2116.
235. Geckeler, K.E. and K. Volchek, *Removal of hazardous substances from water using ultrafiltration in conjunction with soluble polymers.* Environmental Science & Technology, 1996. **30**(3): p. 725-734.
236. McNally, E.A., I. Zhitomirsky, and D.S. Wilkinson, *Cathodic electrodeposition of cobalt oxide films using polyelectrolytes.* Materials Chemistry and Physics, 2005. **91**(2-3): p. 391-398.
237. Zhitomirsky, I., *Composite nickel hydroxide - polyelectrolyte films prepared by cathodic electrosynthesis.* Journal of Applied Electrochemistry, 2004. **34**(2): p. 235-240.
238. Zhitomirsky, I., *Electrochemical processing and characterization of nickel hydroxide-polyelectrolyte films.* Materials Letters, 2004. **58**(3-4): p. 420-424.
239. Nagarajan, N., H. Humadi, and I. Zhitomirsky, *Cathodic electrodeposition of MnOx films for electrochemical supercapacitors.* Electrochimica Acta, 2006. **51**(15): p. 3039-3045.
240. Pang, X. and I. Zhitomirsky, *Fabrication of composite films containing zirconia and cationic polyelectrolytes.* Langmuir, 2004. **20**(7): p. 2921-2927.
241. Zhitomirsky, I., *Electrodeposition of lanthanum hydroxide-polyethylenimine films.* Materials Letters, 2003. **57**(24-25): p. 3761-3766.
242. Zhitomirsky, I., *Electrodeposition of composite ceria-polyethylenimine films.* Surface Engineering, 2004. **20**(1): p. 43-47.
243. Varma, A.J., S.V. Deshpande, and J.F. Kennedy, *Metal complexation by chitosan and its derivatives: a review.* Carbohydrate Polymers, 2004. **55**(1): p. 77-93.
244. Pang, X. and I. Zhitomirsky, *Electrodeposition of composite hydroxyapatite-chitosan films.* Materials Chemistry and Physics, 2005. **94**(2-3): p. 245-251.
245. Zhitomirsky, I. and A. Hashambhoy, *Chitosan-mediated electrosynthesis of orgarlic-inorganic nanocomposites.* Journal of Materials Processing Technology, 2007. **191**(1-3): p. 68-72.
246. Nagarajan, N. and I. Zhitomirsky, *Cathodic electrosynthesis of iron oxide films for electrochemical supercapacitors.* Journal of Applied Electrochemistry, 2006. **36**(12): p. 1399-1405.
247. Deans, J.R. and B.G. Dixon, *Uptake of Pb^{2+} and Cu^{2+} by Novel Biopolymers.* Water Research, 1992. **26**(4): p. 469-472.
248. Randall, J.M., Randall, V.G., Mcdonald, G.M., *Removal of Trace Quantities of Nickel from Solution.* Journal of Applied Polymer Science, 1979. **23**(3): p. 727-732.
249. Udaybhaskar, P., L. Iyengar, and A.V.S.P. Rao, *Hexavalent Chromium Interaction with Chitosan.* Journal of Applied Polymer Science, 1990. **39**(3): p. 739-747.
250. Penichecovas, C., L.W. Alvarez, and W. Arguellesmonal, *The Adsorption of Mercuric Ions by Chitosan.* Journal of Applied Polymer Science, 1992. **46**(7): p. 1147-1150.

251. Zhitomirsky, I. and A. Petric, *Cathodic electrodeposition of ceramic coatings for oxidation protection of materials at elevated temperatures.* Canadian Metallurgical Quarterly, 2002. **41**(4): p. 497-505.
252. Zhitomirsky, I. and A. Petric, *The electrodeposition of ceramic and organoceramic films for fuel cells.* Jom-Journal of the Minerals Metals & Materials Society, 2001. **53**(9): p. 48-50.
253. Zhitomirsky, I., A. Petric, and M. Niewczas, *Nanostructured ceramic and hybrid materials via electrodeposition.* Jom-Journal of the Minerals Metals & Materials Society, 2002. **54**(9): p. 31-34.
254. Pang, X., I. Zhitomirsky, and M. Niewczas, *Cathodic electrolytic deposition of zirconia films.* Surface & Coatings Technology, 2005. **195**(2-3): p. 138-146.
255. Dormann, J.L., Fiorani, D., Cherkaoui, R., Tronc, E., *From pure superparamagnetism to glass collective state in gamma-Fe_2O_3 nanoparticle assemblies.* Journal of Magnetism and Magnetic Materials, 1999. **203**: p. 23-27.
256. Martinez, B., X. Obradors, and L. Balcells, *Low Temperature Surface Spin-Glass Transition in r-Fe_2O_3 Nanoparticles.* Physical Review Letters, 1998. **80**(1): p. 181.
257. Jensen, G.B. and O.V. Nielsen, *The magnetic structure of Mn_3O_4 (Hausmannite) between 4.7 K and the Neel point, 41 K.* Journal of Physics C-Solid State Physics, 1974. **7**: p. 409-424.
258. Srinivasan, G. and M.S. Seehra, *Magnetic Properties of Mn_3O_4 and a Solution of the Canted-Spin Problem.* Physical Review B, 1983. **28**(1): p. 1-7.
259. Arbuzova, T.I., Naumov, S.V., Kozlov, E.A., *Influence of structural defects on magnetic properties of the submicrometer ceramic Mn_3O_4.* Journal of Experimental and Theoretical Physics, 2006. **102**(6): p. 931-937.
260. Blundell, S.J., *Magnetism in Condensed Matter.* 2001: p. Appendix A.
261. Borovik-Romanov, A.S. and M.P. Orlova, J.Exptl.Theoret.Phys. (U.S.S.R.) [translation: Soviet Phys.-JETP 5, 1023 (1957)], 1957. **32**: p. 1255.
262. Seo, W.S., Jo, H.H., Lee, K., Kim, B., Oh, S.J., Park, J.T., *Size-dependent magnetic properties of colloidal Mn_3O_4 and MnO nanoparticles.* Angewandte Chemie-International Edition, 2004. **43**(9): p. 1115-1117.
263. Binder, K. and P.C. Hohenberg, *Surface effects on magnetic phase transitions.* Physical Review B, 1974. **9**(5): p. 2194-2214.